This is to certify that the
dissertation entitled

ENGINEERING INTERFACES FOR BIOELECTRONIC APPLICATIONS

presented by

BRIAN LLOYD HASSLER

has been accepted towards fulfillment
of the requirements for the

Doctoral degree in Chemical Engineering

Robert Mark Worden
Major Professor's Signature

Sept 4, 2009
Date

ENGINEERING INTERFACES FOR BIOELECTRONIC APPLICATIONS

BY

BRIAN LLOYD HASSLER

A DISSERTATION

Submitted to
Michigan State University
in partial fulfillment of the requirements
for the degree of

DOCTOR OF PHILOSOPHY

Chemical Engineering

2009

ABSTRACT

ENGINEERING INTERFACES FOR BIOELECTRONIC APPLICATIONS

By

Brian Lloyd Hassler

Bioelectronic interfaces that facilitate electron transfer between the electrode and a dehydrogenase enzyme have potential applications in biosensors, biocatalytic reactors, and biological fuel cells. Secondary alcohol dehydrogenase (2° ADH) from *Thermoanaerobacter ethanolicus* is well suited for the development of such bioelectronic interfaces because of its thermostability and facile production and purification. The development of bioelectronic interfaces could lead to significant advances in biosensors, biocatalytic reactors, and biological fuel cells.

Development of a bioelectronic interface is especially challenging for cofactor-dependent dehydrogenase enzymes, whose activity requires the presence of an electron carrying cofactor. Direct electron transfer between the cofactor and the electrode is not kinetically favored, requiring the use of high overpotentials which may lead to cofactor degradation. These problems can be circumvented by using an electron mediator to shuttle electrons between the electrode and cofactor at moderate potentials. We capitalized upon the formation of an amide linkage to form a bioelectronic interface capable of electron transfer at moderate potentials while providing greater flexibility in the assembly of the bioelectronic interfaces. However, enzymes and cofactors have limited useful lifetimes, due to natural degradation processes. The abovementioned

interface fabrication method involved the covalent linkage of the enzyme to the surface making no provision for removal and replacement of degraded components. However, for long-term operation, new interface-assembly methods must be developed that allow facile removal and replacement of the cofactor and enzyme.

We present the fabrication of a renewable bioelectronic interface in which poly(ethyleneimine) (PEI) was used to couple the cofactor and enzyme to the electrode. By decreasing the pH the surface-bound carboxylic acid group protonates disrupting the ionic bonds and releasing the enzyme and cofactor. After neutralization, fresh PEI, enzyme, and cofactor can be reassembled, allowing the interface to be reconstituted. Renewable bioelectronic interfaces were also fabricated on a glassy carbon electrode. To increase the performance parameters (saturation current and sensitivity) exfoliated graphite nanoplatelets were incorporated into the bioelectronic interface. However, these interfaces are limited in their reaction capacity, because it contains a single enzyme monolayer. A novel approach, in which multiple, nanostructured bioelectronic cassettes are stacked in series to yield multilayered bioelectronic interfaces having higher reaction capacities is also described. An approximate analytical solution for bioelectronic interfaces containing reversible enzymes and mediators; the general approach developed takes into account reversible enzyme kinetics, reversible mediator kinetics, substrate diffusion, product diffusion, and electron diffusion was also developed.

DEDICATION

TO MY FAMILY

TABLE OF CONTENTS

LIST OF TABLES

LIST OF FIGURES

LIST OF SCHEMES

NOMENCLATURE

Chemicals

CBA	3-carboxyphenyl boronic acid
Cys	Cysteine
DTT	Dithiothreitol
EDC	1-ethyl-3-(3-dimethylaminopropyl) carbodiimide
Hcy	Homocysteine
IPTG	isopropyl-β-D-thiogalactopyranoside
MB	Medola's blue
MPA	3-mercaptopropanoic acid
NAD^+	β-nicotinamide adenine dinucleotide
$NADP^+$	β-nicotinamide adenine dinucleotide phosphate
NBA	Nile blue A
NHS	N-hydroxysuccinimide
NR	Neutral Red
PAA	Poly(acrylic acid)
PAH	Poly(allylamine hydrochloride)
PEI	Poly(ethyleneimine)
PBS	Phosphate buffer solution
PQQ	pyrroloquinoline quinone

TBO	Toluidine blue O
X-gal	5'-bromo-4-chloro-3-indolyl-β-D-galactopyranoside

Enzymes

2° ADH	Secondary alcohol dehydrogenase
ADH	Alcohol Dehydrogenase
TmMtDH	Mannitol dehydrogenase

Techniques

CVD	Chemical vapor deposition
LbL	Layer-by-layer
PCR	Polymerase chain reaction
PVD	Physical vapor deposition

Materials

GCE	Glassy carbon electrode
PEI/xGnP	PEI-coated expholiated graphite nanoplatelets
RMS	Root mean squared
RVC	Reticulated vitreous carbon
xGnP	Expholiated graphite nanoplatelets

Symbols

A	Electrode area
C_1	Redox form 1 of the cofactor

C_2	Redox form 2 of the cofactor
C_F	Faradic capacitance
C_{DL}	Double layer capacitance
CPE	Constant phase element
C_{TBO}	Concentration of TBO
D_{app}	Apparent electron transfer diffusion coefficient
D_S	Diffusion rate of the substrate
D_P	Diffusion rate of the product
D_M	Diffusion rate of the mediator
E	Enzyme
EC_1	Redox form 1 of the enzyme/cofactor complex
EC_1S	Enzyme/cofactor/substrate complex
EC_2	Redox form 2 of the enzyme/cofactor complex
F	Faradays constant
I	Current
I_0	Background current
I_P	Peak current
I_c	Charging current
I_{cat}^{sat}	Saturation current

J_{obs}	Observed flux
K	Ratio of mediator reaction rates
K_m	Michaels Menten constant
M_1	Redox form 1 of the electron mediator
M_2	Redox form 2 of the electron mediator
P	Product concentration
Q	Charge transferred during oxidation/reduction
Q_i	Charge transferred during oxidation/reduction for binding mode *i*
Q'	Charge transferred during oxidation/reduction for binding mode 1
Q''	Charge transferred during oxidation/reduction for binding mode 2
R_{CT}	Charge transfer resistance
R_S	Solution resistance
S	Substrate concentration
TR_{max}	Maximum turnover rate
V_{max}	Maximum reaction rate
Y	Admittance
Z_D	Finite diffusion element
Z_{im}	Imaginary impedance
Z_{re}	Real impedance

Z_D	Finite diffusion impedance
$f(\eta)$	Potential dependence
d	Film thickness
j_o	Dimensionless observed flux
k_1	Second order reaction rate of E and C_1 forming EC_1
k_2	Second order reaction rate of EC_1 and S forming EC_1S
k_3	Second order reaction rate describing EC_1 break down to form EC_2 and P
k_4	Second order reaction rate describing EC_2 break down to form E and C_2
k_{-1}	Second order reaction rate describing EC_1 break down to form E and C_1
k_{-2}	Second order reaction rate describing EC_1S break down to form EC_1 and S
k_{-3}	Second order reaction rate of EC_2 and P forming EC_2P
k_{-4}	Second order reaction rate of E and C_2 forming EC_2
k_{et}	Electron transfer rate constant
k'_{et}	Electron transfer rate constant for binding mode 1
k''_{et}	Electron transfer rate constant for binding mode 2
m	Dimensionless mediator concentration
n	Number of electrons transferred during oxidation/reduction
p	Dimensionless product concentration
s	Dimensionless substrate concentration

t	Time
ν_P	Reaction rate with respect to the product
ν_S	Reaction rate with respect to the substrate
ν_M	Reaction rate with respect to the mediator

Greek Symbols

Φ_S	Observable substrate Thiele modulus
Φ_P	Observable product Thiele modulus
Φ_M	Observable mediator Thiele Modulus
Γ'_{enz}	Enzyme surface coverage for bindining mode 1
Γ''_{enz}	Enzyme surface coverage for bindining mode 2
Γ'_{enz}	Enzyme surface coverage
Γ^i_{enz}	Enzyme surface coverage for binding mode *i*
Γ_{med}	Mediator surface coverage
Γ_{TBO}	Toluidine blue O surface coverage
θ	Ratio of the mediator to product diffusion
σ	Ratio of the mediator to substrate diffusion
χ	Dimensionless length of the film
γ	Dimensionless variable presented by Bartlett and Pratt
ρ	Ratio of the reverse enzyme to the forward mediator reaction rate

ε	Dimensionless potential
η	Effectiveness factor
κ	Apparent Thiele modulus
λ	Concentration of product to the Michaelis constant for the product
μ	Concentration of substrate to the Michaelis constant for the substrate
ω	Osicallation Frequency
ω_{tr}	Transition frequency
ω	Ratio of the forward enzyme to the forward mediator reaction rate
τ	Thiele modulus for the Bartlett and Pratt model
η	Dimensionless variable presented by Bartlett and Pratt
τ_{Cys}	2° ADH adsorption on a Cys-TBO-$NADP^+$-modified electrode
τ_{Hcy}	2° ADH adsorption on a Hcy-TBO-$NADP^+$-modified electrode
τ_{NAD}	2° ADH adsorption on a Cys-TBO-NAD^+-modified electrode
τ_{PAH}	2° ADH adsorption on a MPA-TBO-PAH-$NADP^+$-modified electrode
τ_{PEI}	2° ADH adsorption on a MPA-TBO-PEI-$NADP^+$-modified electrode
τ_{PS}	2° ADH adsorption on a Cys-TBO-$NADP^+$-modified polystyrene electrode
τ_{xGnP}	2° ADH adsorption on a MPA-TBO-PEI/xGnP-$NADP^+$-modified electrode
τ_{Y218}	Y218F2° ADH adsorption on a Cys-TBO-NAD^+-modified electrode

Dimensionless Groups

$\overline{v_P}$	Dimensionless reaction rate
$\overline{V_{\max}}$	Dimensionless maxium reaction rate
$\overline{K_{eq}}$	Dimensionless equilibrium rate constant
$\overline{K_{ii}}$	Inhibition constant
$\overline{K_{ms}}$	Dimensionless Michaelis constant for the substrate
$\overline{K_{mp}}$	Dimensionless Michaelis constant for the product

Equipment

AFM	Atomic Force Microscopy
DLS	Dynamic light scattering
EDS	Electron dispersive x-ray spectroscopy
EIS	Electrochemical impedance spectroscopy
FE-SEM	Field emission scanning electron microscopy
FTIR	Fourier transform infrared spectroscopy
JEOL	Japan electronic optics laboratories
RMS	Root mean square

1. INTRODUCTION

1.1. Significance of the problem

Bioelectronic interfaces that facilitate electron transfer between the electrode and a dehydrogenase enzyme have potential applications as biosensors, biocatalytic reactors, and biological fuel cells. However, there are several challenges for commercialization including the (1) *in situ* regeneration of the cofactor, (2) high cost and low stability of nicotinamide adenine dinucleotide phosphate ($NADP^+$), and (3) low stability of some dehydrogenases.

This dissertation describes the fabrication and characterization of functional, three dimensional bioelectronic interfaces consisting of electron mediators, enzymatic cofactors, enzymes, and other nanostructured components. Establishing efficient electrical communication between redox enzymes and the electrode is a major challenge. Dehydrogenases, which are of interest for bioelectronic applications because of their ability to catalyze electron transfer reactions, use using either β-nicotinamide adenine dinucleotide (NAD^+) (EC 1.1.1.1), $NADP^+$ (EC 1.1.1.2), or both (EC 1.1.1.71) as a cofactor. However, difficulties associated with *in situ* regeneration of these cofactors have hindered commercial development of dehydrogenase-based biosensors and biocatalytic reactors. One complicating factor is that direct electrochemical oxidation or reduction of $NAD(P)^+$ is kinetically unfavorable, requiring the use of high overpotentials, which leads to cofactor degradation, as well as interference from compounds such as ascorbic acid and molecular oxygen. Problems with cofactor degradation due to high overpotentials can be circumvented by using an electron mediator to shuttle electrons between the electrode and cofactor at moderate voltages. Several approaches have been

developed to achieve mediated electron exchange between the electrode and enzyme, including the use of a diffusional mediator, immobilization of the enzymes in conductive polymers, and the construction of a redox relay, which conducts electrons between the enzyme and electrode. None of these approaches have proven entirely satisfactory; for example, some enzyme-immobilization methods result in the random orientation of the redox centers with respect to the electrode, leading to inefficient electrical communication.

The formation of multilayered films via the layer-by-layer (LbL) deposition, of first introduced by Decher, is becoming a well-established technique for the deposition of films on charged surfaces. LbL assembly was initially based on alternating electrostatic adsorption, but has been extended to encompass hydrogen bonding, covalent bonding, and other weak intermolecular interactions. Polyelectrolye multilayer films formed using LbL techniques are economical to produce and could be extended to templates for colloidal self-assembly. The self-assembly of colloidal metal particles has generated interest as a powerful method for the fabrication of macroscopic surfaces with well-defined and controllable nanostructures.

While each chapter addresses a unique architecture or issue, the underlying theme of this dissertation is the development of improved bioelectronic interfaces that express protein activity. The bioelectronic interfaces have outstanding potential for conducting fundamental studies of biological and electrochemical activity and for the developing new protein-based technologies, including electrochemical bioreactors and novel biosensors.

1.2. Dissertation overview

Chapter 2 of this dissertation presents the common expiremental methods. Chapter 3 presents a novel bioelectronic interface based on heterotrifunctional linking molecules. Chapter 4 discussed the mutation of tyrosine-218 (Tyr^{218}) to Phenylalanine in Thermoanaerobacter ethanolicus secondary alcohol dehydrogenase: effects on bioelectronic interface performance. Chapter 5 discusses the design, fabrication and characterization of bioelectronic interfaces on flexible non-conductive substrates. Chapter 6 discusses the design, fabrication, and characterization of a renewable dehydrogenase based interface. Chapter 7 describes the design, fabrication, characterization, and optimization of novel multilayer interfaces. Chapter 8 presents the design, fabrication and characterization of aversatile bioelectronic interface containing exfoliated graphite supports. Chapter 9 describesthe theoretical study of reversible enzymes at an electrode surface. Chapter 10 discusses the covalent modification of glassy carbon electrodes with mannitol dehydrogenase. The electrodes were characterized using Cyclic voltammetry, electrochemical impedance spectroscopy, and chronoamperometry were used to demonstrate the sequential assembly steps and the electrical activity of the resulting bioelectronic interface.

1.2.1. Bioelectronic interfaces based on heterotrifunctional linking molecules

The fabrication of a versatile, new method that uses heterotrifunctional linking molecules in an orientation where multistep electron transfer is achieved is described. The fabrication of bioelectronic interfaces using heterotrifunctional linking molecules provides greater flexibility in assembling complex bioelectronic interfaces than previously reported approaches that bind the enzyme, cofactor, and mediator in a linear

chain. Cysteine and homocysteine were bound to the gold electrode through the sulfhydryl groups to the electron mediator through the carboxyl group, and to the cofactor through the amino group. Multiple electron mnediators were studied including: neutral red, Nile bule A, and toluidine blue O. Cyclic voltammetry, impedance spectroscopy, and chronoamperometry were used to demonstrate the sequential assembly steps and the electrical activity of the resulting bioelectronic interface. The studies also examined tethering molecules of different length (cysteine and homocysteine).

1.2.2. Mutation of tyrosine -218 to phenylalanine in secondary alcohol dehydrogenase from Thermoanoerobactor Ethanolicus: effects on bioelectronic interface performance

Dehydrogenase enzymes are of particular interest for bioelectronic applications because they catalyze reactions that involve direct electron transfer. Secondary alcohol dehydrogenase (2° ADH) from *Thermoanaerobacter ethanolicus* is especially well suited for the development of such bioelectronic interfaces because of its thermostability and facile production and purification. However, β-nicotinamide adenine dinucleotide phosphate ($NADP^+$) the natural cofactor for 2° ADH is more expensive and less stable than β-nicotinamide adenine dinucleotide (NAD^+). Korkhin *et al.* (1998) suggested that Tyr^{218} might be the most important determinant of *Thermoanaerobacter brockii* 2° ADH's specificity for NADP(H) (Korkhin, Kalb et al. 1998) because upon NADP(H) binding, the sidechain of Tyr^{218} rotates by 120°, enabling Tyr^{218} to stack against the adenine moiety of the cofactor and to form a hydrogen bond between its hydroxyl and one oxygen atom of the ribose phosphate. Site-directed mutagenesis was performed on 2° ADH in an attempt to modify the cofactor specificity towards NAD^+ by mutating Tyr^{218}

to Phe. This mutation increased the K_m(app) for $NADP^+$ 200-fold, while decreasing the K_m(app) for NAD^+ 2.5-fold. The mutant and wild-type enzymes along with different electron mediators, and different heterotrifunctional linking molecule were incorporated into a bioelectronic interface were the sensitivity, turnover rate, and peak current were compared.

1.2.3. Versatile bioelectronic interfaces on non-conductive substrates

Bioelectronic interfaces are commonly formed on gold coated silicon wafers deposited using either physical vapor deposition (PVD) or chemical vapor deposition (CVD). PVD and CVD require deposition of a primer layer, such as titanium or chromium. PVD and CVD are expensive, cannot be used on a wide range of substrates, and requires the use of equipment not found in most labs. Electroless metal deposition is a convenient, bench-top metal-deposition technique which uses colloidal self-assembly to deposit metal nanoparticles (Supriya and Claus 2004).

Chapter 5 describes the fabrication of a versatile new bench-top method to form a bioelectronic interface containing a heterotrifunctional linking molecule, electron mediator, cofactor, and enzyme on previously nonconductive substrates such as polystyrene, Permanox®, and glass. Interfaces formed on flexible polystyrene slides retained activity after bending to a radius of curvature of 18 mm. The fabrication of the electrode combined layer-by-layer deposition of polyelectrolytes, electroless metal deposition, and directed molecular self-assembly. The gold films were characterized using field atomic force microscopy, emission x-ray dispersive spectroscopy, and scanning electron microscopy.

1.2.4. Renewable dehydrogenase based interfaces for bioelectronic applications

Several approaches have been used to achieve mediated electron exchange, including immobilization of the enzymes in conductive polymers (Emr and Yacynych 1995; Chen, Barton et al. 2001), fabrication of redox relays that conduct electrons between the enzyme and electrode (Degani and Heller 1987; Zimmermann, Lindgren et al. 2000), and the direct immobaliziation of the mediator, cofactor, and enzyme were bound directly to the surface of the electrode (Zayats, Katz et al. 2002; Hassler and Worden 2006; Willner, Katz et al. 2006; Hassler, Dennis et al. 2007). However, many enzymes and cofactors have limited useful lifetimes, due to natural degradation processes (Burdette, Tchernajencko et al. 2000; Wang, Feng et al. 2003; De Temino, Hartmeier et al. 2005). For long-term operation, new interface-assembly methods must be developed that allow facile removal and replacement of the cofactor and enzyme. This chapter describes a versatile new fabrication approach that binds the enzymes and cofactors using reversible ionic interactions

The LbL deposition of polyelectrolytes provides a mechanism by which target molecules can be reversibly bound to an interface and later released (Wu, Guan et al. 2002; Yun, Song et al. 2005). Poly(ethyleneimine) and poly(allylamine hydrochloride) were used to couple the electron mediator, cofactor, and enzyme to a carboxylic-acid-modified gold electrode in such a way that mediated electron transfer was achieved. Decreasing the pH of the solution protonated the surface-bound carboxylic acid groups disrupting the ionic bonds and releasing the enzyme and cofactor. After neutralization, fresh enzyme and cofactor could be bound, allowing the interface to be reconstituted. The

regenerated interface exhibited the similar surface coverage, electron transfer coefficient, and turnover rate as the original interface.

1.2.5. Characterization of renewable multilayered dehydrogenase-based bioelectronic interfaces

Several molecular architectures covalently bind the cofactors and enzymes to the electrode making no provision for periodic removal and replacement of cofactors and enzymes, whose activities degrade over time (Burdette, Tchernajencko et al. 2000; Wang, Feng et al. 2003; De Temino, Hartmeier et al. 2005). To address this need, we developed a renewable bioelectronic interface in which the enzyme and cofactor can be easily removed by reducing the pH, and then replaced to regenerate the bioelectronic activity (Hassler, Kohli et al. 2007). The renewable interface was fabricated via LbL self assembly polyelectrolytes. In LbL self assembly, alternating layers of oppositely charged polyelectrolytes are sequentially adsorbed to create a polyelectrolyte multilayer (PEM) film.

PEM films have been shown to be well suited for encapsulating enzymes, including catalase (Shi, Lu et al. 2003; Wang and Caruso 2005; Shutava, Kommireddy et al. 2006), glucose oxidase (Antipov and Sukhorukov 2004; Zhao, Xu et al. 2005), and polyphenol oxidase (Forzani, Teijelo et al. 2003; Coche-Guerente, Desbrieres et al. 2005). Deposition of multiple enzyme layers has been shown to increase the reaction rate for interfaces containing glucose oxidase, polyphenol oxidase, or L-proline dehydrogenase. However, the strategy of using multiple enzyme layers has not been investigated for more complex systems, such as multicomponent bioelectronic cassettes that include a mediator, a cofactor, and a cofactor-dependent dehydrogenase.

1.2.6. Versatile bioelectronic interfaces on exfoliated graphite supports

LbL-self assembly is a versatile approach based on the alternating adsorption of materials containing oppositely charged functional groups (Decher and Hong 1991; Decher and Hong 1991; Decher, Hong et al. 1992). Recently, The LbL approach has been extended to the incorporation of colloidal particles (Chen, Yuan et al. 2006; Qi, Honma et al. 2006), cells (Kidambi, Lee et al. 2004), fullerenes (Guldi, Zilbermann et al. 2004), carbon nanotubes (Huang, Wang et al. 2006), fullerenes, and exfoliated graphite nanoplatelets (xGnP) (Du, Xiao et al. 2004). The incorporation of graphene-based nanoparticles, including exfoliated graphite xGnP, carbon nanotubes, and fullerenes into polyelectrolyte films is significant due to their unique chemical, physical, and electronic properties (Luo, Killard et al. 2006). The xGnP have chemical, physical, and electronic properties consistent with carbon nanotubes and fullerenes. The low production cost ($5/pound) and chemical, physical, and electronic properties make xGnP a suitable replacement for carbon nanotubes and fullerenes. In this chapter we present a novel assembly method that incorporates polyelectrolyte-modified xGnP into bioelectronic interfaces. Poly(ethyleneimine) was used to couple the xGnP, cofactor, and enzyme to the mediator-modified gold electrode in a configuration that allows electron transfer.

1.2.7. Theoretical study of bioelectronic interfaces containing reversible enzymes and mediators at an electrode surface

Bioelectronic interfaces containing dehydrogenases have potential utility in important applications including biosensors, biocatalytic reactors and biofuels cells. Engineering these systems is challenging, because their performance properties depend on a complex set of simultaneous molecular processes, including multistep electron

exchange between an electrode, an electron mediator, a cofactor, and the enzyme; interphase and intraphase transport of the substrates, products, and electrons; and reversible bi-bi enzyme kinetics involving substrates, products, and electrons. This chapter presents a mathematical model that captures these simultaneous processes and predicts their effects on the overall system performance. The steady-state model was expressed in terms of natural dimensionless groups and solved numerically to explore the effects of reversible enzyme and mediator kinetics, substrate, product, and electron diffusion, and substrate, product, and mediator concentration, and electrode potential on the overall reaction rate. The effects of substrate, product, and electron transport resistance on the overall reaction rate were correlated in terms of an effectiveness factor and an observable Thiele modulus. These results have utility in design and optimization of practical bioelectronic processes.

1.2.8. Covalent modification of glassy carbon electrodes with mannitol dehydrogenase for detection of fructose

The most popular chemistries for the formation of bioelectronic interfaces are alkane thiol self-assembly onto gold (Ulman 1996), silanes on metal oxides (Ulman 1996), and alkenes on highly doped silicon (Barrelet, Robinson et al. 2001). The attractiveness of the gold-thiol interaction is that well ordered monolayers are formed easily and high diversity of functional that can bound to the surface. However, the high cost of gold, which restricts the commercial application of these interfaces. Alkoxy-terminated silanes can react with surface hydroxyl groups on metal-oxide electrodes to form a polysiloxane linkage (Quan, Kim et al. 2004; Curran, Chen et al. 2005). Kraft has reported that metal oxide substrates are not stable during anodic potential cycling, due to the anodic dissolution of the metal-oxide coating (Kraft, Hennig et al. 1994). The

abovementioned problems can be circumvented by fabricating the bioelectronic interface on vitreous carbon [glassy carbon electrode (GCE)] using a carbon-nitrogen bond (Adams 1969; Woodward 1985). Reticulated vitreous carbon (RVC) is an open pore material with a foam structure (Friedrich, Ponce-De-Leon et al. 2004). RVC has been used in flow injection systems because of its low electrical resistance, large surface area, and its mechanical and hydrodynamic properties (Strohl and Curran 1979; Strohl and Curran 1979). This chapter presents a novel method based on molecular self assembly to fabricate renewable bioelectronic interfaces on a GCE. Glycine and poly(ethyleneimine) were used to couple the electron mediator, cofactor, and enzyme to a GCE in such a way that mediated electron transfer was achieved. Fresh cofactor and enzyme could then be reattached to regenerate bioelectronic activity.

2. EXPERIMENTAL METHODS

2.1. Enzyme preparation

2.1.1. Media and strains

Escherichia coli DH5α cells containing the recombinant plasmids expressing *Thermoanaerobacter ethanolicus* secondary alcohol dehydrogenase (2° ADH) were grown in a 10 L fermentor (Bioflo 3000, New Brunswick Scientific, Edison, NJ) in a rich complex medium (20 g L^{-1} tryptone, 10 g L^{-1} yeast extract, 5 g L^{-1} NaCl) under constant stirring at 37°C in the presence of 25 μg mL^{-1} kanamycin and 100 μg mL^{-1} ampicillin.

Escherichia coli BL21(DE3) (Novagen, Madison, WI) cells containing the recombinant plasmids expressing *Thermotoga maritima* mannitol dehydrogenase (TmMtDH), were grown in a 10 L fermentor in Luria-Bertani medium (10 g L^{-1} tryptone, 5 g L^{-1} yeast extract, 10 g L^{-1} NaCl) under constant stirring at 37°C in the presence of 25 μg mL^{-1} kanamycin. TmMtDH expression was induced at an OD_{600} of 1.4 by adding 0.6 mM isopropyl-B-D-thiogalactoside (IPTG) and the culture was grown for an additional 16 hours.

2.1.2. Enzyme purification

The recombinant 2° ADH and TmMtDH were purified from *E. coli* aerobically. After cell recovery via centrifugation, the pelleted cells were re-suspended (0.5 g wet cell wt mL^{-1}) in Buffer A [50 mM Tris/HCl, pH 8.0, 5 mM dithiothreitol (DTT), and 10 μM $ZnCl_2$]. The resuspended cells were lysed in a French press using a pressure of 15,000 psi. The cell lysate was treated with DNAse I, incubated on ice for 15 min and centrifuged for 30 min at 15,000 *g* to obtain the initial cell extract; upon centrifugation the supernatant was recovered. The clarified lysate was then heat-treated at 85°C for 15

min to denature the non-thermostable protein. The lysate was then cooled on ice for 30 min, and centrifuged for 30 min at 15,000 *g*; upon centrifugation the supernatant was recovered. $(NH_4)_2SO_4$ was added to the supernatant to give a concentration of 29.1 g L^{-1} (50% saturation) and stirred at 4°C for 30 min to precipitate the denatured protein. The mixture was centrifuged at 15,000 *g* for 30 min, and the supernatant was recovered. To precipitate the enzyme, an additional 15.9 g L^{-1} of $(NH_4)_2SO_4$ was added to the supernatant to achieve 70% saturation, and the solution was continuously stirred at 4°C for 30 min. The resulting suspension was centrifuged at 15,000 *g* for 30 min, and the pellet was dissolved in Buffer A and stored in sealed plastic tubes at -80°C.

2.2. Cleaning procedures

2.2.1. Gold electrodes

Gold wafers (LGA Thin Films, Santa Clara, CA) were cut into 1 cm × 1.5 cm rectangular electrodes and cleaned by immersion in piranha solution (7 parts by volume concentrated sulfuric acid and 3 parts by volume 30% aqueous hydrogen peroxide) for 30 s. The electrodes were treated with a Harrick plasma cleaner (Harrick Scientific Corporation, Ossining, NY) for 1 min under 50 sccm flow of oxygen at a pressure of 0.15 Torr and then rinsed with deionized water for 10 min.

2.2.2. Glassy carbon electrodes

The glassy carbon electrodes (GCEs) (3 mm diameter, CH Instruments, Austin, TX) were polished on microcloth pads using 0.05 μm alumina powder (CH Instruments) and rinsed thoroughly with distilled water in an ultrasonic bath for 10 minutes.

2.3. Electrochemical techniques

A conventional three-electrode cell consisting of the enzyme-modified gold working electrode, a platinum auxiliary electrode, and a silver/silver chloride (Ag/AgCl) reference electrode was used for electrochemical measurement. Cyclic voltammetry, chronoamperometry, and electrochemical impedance spectroscopy (EIS) were performed using an electrochemical analyzer (CHI660B, CH Instruments). Electrochemical measurements were made in a 100 mM phosphate buffer solution (PBS, pH 7.4) at room temperature (25±2°C) for 2° ADH and in 100 mM PBS (pH 6.0) at 60±2°C for TmMtDH. Electrochemical measurements on gold and glassy carbon electrodes were made with a controlled surface area of 0.16 and 0.07 cm^2, respectively. To evaluate the reproducibility, three bioelectronic interfaces were fabricated, and the properties of each were measured.

2.3.1. Chronoamperometry

Chronoamperometric experiments were conducted by stepping the potential of the working electrode from a potential where no reaction occurs to a potential that drives the desired reaction. Origin 7.5 software (OriginLab, Northampton, MA) was used to fit kinetic models to the resulting current vs. time data. Redox species differing in their spatial orientations relative to the electrode reveal a different electron-transfer rate constant for each spatial orientation (Katz and Willner 1997) suggesting that the redox components with multiple binding modes may exhibit a rate constant for each mode (Zayats, Katz et al. 2002). β-nicotinamide adenine dinucleotide phosphate ($NADP^+$) has a single ribose unit available for the reaction with the boronic acid ligand an exponential decay model (Eq. 2.1) was used to model the transient current response of the system (Bard and Faulkner 2001; Zayats, Katz et al. 2002).

$$I = k_{et} Q \exp(-k_{et} t) + I_c \quad \textbf{(2.1)}$$

I, k_{et}, Q, t, and I_c are the current, electron transfer rate constant, charge associated with oxidation following the change in potential, time, and the charging current, respectively. Unlike $NADP^+$, β-nicotinamide adenine dinucleotide (NAD^+) has two ribose units available for the reaction. Accordingly, two binding modes are possible, thus a biexponential decay model (Eq. 2.2) describes the data:

$$I = k'_{et} Q' \exp(-k'_{et} t) + k''_{et} Q'' \exp(-k''_{et} t) + I_c \quad \textbf{(2.2)}$$

where k'_{et} and k''_{et} are the electron transfer rate constants for the two binding modes, and Q' and Q'' are the corresponding amounts of charge transferred by each binding mode. The surface coverage of active enzyme for each binding mode i (Γ^i_{enz}) can be calculated using Eq. 2.3 (Zayats, Katz et al. 2002):

$$\Gamma^i_{enz} = \frac{Q_i}{nFA} \quad \textbf{(2.3)}$$

where Q_i, F, A, and n are the charge associated with with binding mode i, Faraday's constant, electrode area, and number of electrons transferred in the reaction (n=2), respectively.

2.3.2. Cyclic voltammetry

Cyclic voltammetric experiments were conducted by sweeping the potential of the working electrode between a potential where no reaction occurs and a potential in which oxidation/reduction reactions occur causing analyte in the vicinity of the electrode to be oxidized in the positive direction and reduced in the negative direction. The slope of the calibration plot (peak current vs. analyte concentration) is a measure of the biosensor's

sensitivity. The maximum turnover rate (TR_{max}), the number of analyte molecules oxidized per enzyme molecule per second, can be calculated using Eq. 2.4 (Eisenwiener and Schulz 1969).

$$TR_{\max} = \frac{I_{cat}^{sat} - I_0}{nFA\Gamma_{enz}} \tag{2.4}$$

where I_0 and I_{cat}^{sat} are the background current (the current when no substrate is present) and saturation current, respectively.

2.3.3. *Electrochemical impedance spectroscopy*

2.3.3.1. Interface fabrication

Electrochemical impedance spectroscopy (EIS) was used to investigate the sequential assembly of mediators, cofactors, and enzymes onto a gold electrode. To follow interface assembly, EIS measurements were made in 100 mM PBS (pH 6.0) containing 10 mM $K_3[Fe(CN)_6]$, 10 mM $K_4[Fe(CN)_6]$, and 10 mM NaCl over six frequency decades (10^4 Hz to 10^{-2} Hz) at the system's open circuit potential. The data were displayed as a Nyquist plot [imaginary impedance ($-Z_{im}$) *vs.* real impedance (Z_{re})]. A modified Randles equivalent circuit model (Figure 2.1) containing a solution resistance (R_S), charge transfer resistance (R_{CT}), and constant phase element (CPE) (Brug, Vandeneeden et al. 1984). The modified Randles equivalent circuit was fit to data using commercial software (Z-view, Version 2.1b, Scribner Associates Inc., Southern Pines, NC).

2.3.3.2. Determination of redox site concentration

Several models have been developed to analyze the electrochemical impedance spectra of redox polymer films (Gabrielli, Haas et al. 1987; Lindholm, Sharp et al. 1987;

Lang and Inzelt 1991; Mathias and Haas 1992). Calvo and coworkers have shown that the surface coverage of the mediator (Γ_{med}), and apparent electron transfer diffusion coefficient (D_{app}) can be determined using EIS (Tagliazucchi and Calvo 2007). A modified Randles equivalent circuit (Figure 2.2) consisting of R_S in series with impedance given by a double layer capacitance (C_{DL}) in parallel with R_{CT} and a finite diffusion impedance (Z_D) was used to analyze the data. In the high frequency region, Z_D behaves as a semi-infinite Warburg element, and in the low frequency region, Z_D exhibits pseudo-capacitive behavior. The high and low frequency limits of the Faradaic capacitance (Y/ω) are given by Eqs. 2.5 and 2.6, respectively (Tagliazucchi and Calvo 2007).

$$Y/\omega \;\; \omega \to \infty \;\; = \frac{-\sqrt{2}}{f\;\eta}\left(\frac{\omega}{\omega_{tr}}\right)^{-1/2} C_F \qquad \textbf{(2.5)}$$

$$Y/\omega \;\; \omega \to 0 \;\; = \frac{1}{f\;\eta} C_F \qquad \textbf{(2.6)}$$

Y, ω, ω_{tr}, and $f(\eta)$ are the admittance, angular frequency, angular transition frequency, and potential dependence, respectively. The Faradic capacitance (C_F) is given by Eq. 2.7 (Liu, Jin et al. 2004).

$$C_F = \frac{n^2 A \Gamma_{med}}{4RT} \qquad \textbf{(2.7)}$$

Γ_{med} is the concentration of the mediator in the film. The characteristic transition angular frequency (ω_{tr}) is defined by Eq. 2.8 (Tagliazucchi and Calvo 2007),

$$\omega_{tr} = \frac{D_{app}}{d^2} \tag{2.8}$$

where d is the film thickness. Plots of $\log(Y/\omega)$ vs $\log(\omega)$ can be used to visualize ω_{tr}.

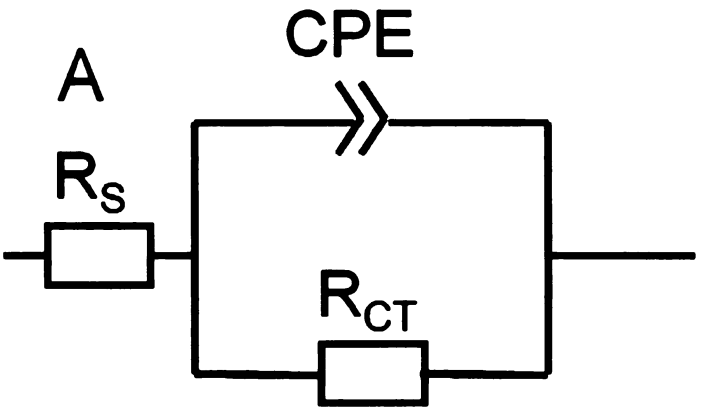

Figure 2.1: Modified Randles electrical equivalent circuit containing a solution resistance (R_S) in series with a constant phase element (CPE) in parallel with the charge transfer resistance (R_{CT}).

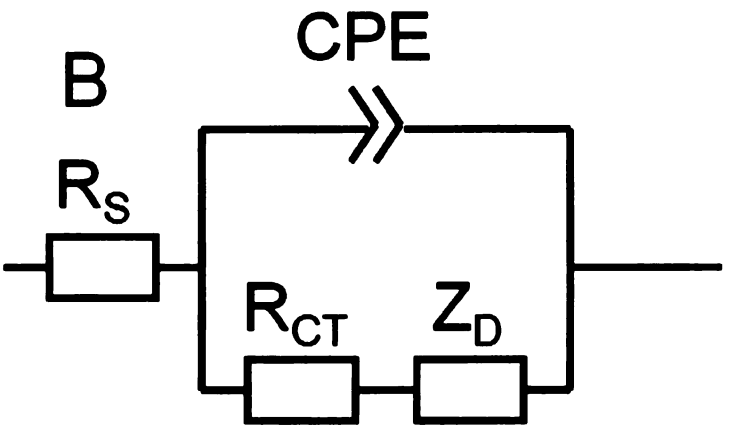

Figure 2.2: Modified Randles equivalent circuit containing a solution resistance (R_S) in series with interfacial a constant phase element (CPE) in parallel with the charge transfer resistance (R_{CT}) and a finite diffusion impedance (Z_D) element.

3. VERSATILE BIOELECTRONIC INTERFACES BASED ON HETEROTRIFUNCTIONAL LINKING MOLECULES

3.1. Abstract

Bioelectronic interfaces that allow dehydrogenase enzymes to communicate with electrodes have potential applications such as biosensors and biocatalytic reactors. A major challenge in creation of such bioelectronic interfaces is the orientation of the enzyme, its cofactor, and electron mediator properly with respect to the electrode in order to achieve efficient, multistep electron transfer. This chapter describes a versatile, new method that uses cysteine, an inexpensive, branched amino acid having sulfhydryl, amino, and carboxyl functional groups, to achieve such an orientation. This approach provides greater flexibility in assembling complex bioelectronic interfaces than previously reported approaches that bind the enzyme, cofactor, and mediator in a linear chain. Cysteine (Cys) and Homocysteine (Hcy) were assembled on a gold electrode through the sulfhydryl group, to the electron mediator [Toluidine blue O (TBO), neutral red (NR), and Nile Blue A (NBA)] through the carboxyl group, and to the cofactor [(β-nicotinamide adenine dinucleotide phosphate ($NADP^+$)] through the amino group. Chronoamperometry, cyclic voltammetry, and electrochemical impedance spectroscopy (EIS) were used to demonstrate the sequential assembly steps and the electrical activity of the resulting bioelectronic interface.

3.2. Introduction

Biosensors can be fabricated using a variety of molecular recognition elements, including enzymes, microbes, and antibodies. Redox enzymes are of particular interest because electrons produced or consumed in the reaction can be directly measured with an

electrode. Establishing electrical communication between redox enzymes and an electrode is a challenge in the development of biosensors (Armstrong, Heering et al. 1997; Armstrong and Wilson 2000; Habermuller, Mosbach et al. 2000), biocatalytic systems (Park, Laivenieks et al. 1999; Park and Zeikus 1999; Park and Zeikus 2000), and biofuel cells (Chen, Barton et al. 2001; Tsujimura, Fujita et al. 2001). Development of bioelectronic interfaces is especially challenging for cofactor-dependent dehydrogenase enzymes because their activity often requires diffusion of a cofactor (e.g., $NADP^+$) into the protein. Difficulties associated with *in situ* regeneration of the enzyme's cofactor have also hindered commercial development of dehydrogenase-based biosensors and biocatalytic reactors (Prodromidis and Karayannis 2002).

One complicating factor is that direct electrochemical oxidation or reduction of $NADP^+$ at an electrode is kinetically unfavored, requiring the use of high overpotentials (Blaedel and Jenkins 1975; Schmakel, Santhanam et al. 1975), which can cause cofactor degradation. Electron mediators, such as TBO (Lu, Jiang et al. 2004), meldola blue (MB) (Serban and El Murr 2004), NR (Park and Zeikus 1999; Park and Zeikus 2000) and NBA (Ramesh, Sivakumar et al. 2003), which shuttle electrons between the electrode and cofactor at moderate voltages can be used to circumvent this problem. Several approaches have been developed to achieve mediated electron exchange between an electrode and a dehydrogenase enzyme, including the use of diffusional mediators to shuttle electrons between the electrode and cofactor (Barlett, Tebutt et al. 1991), immobilization of the enzymes in conductive polymers (Heller 1990; Emr and Yacynych 1995), and construction of a redox relay which conducts electrons between the enzyme and electrode (Degani and Heller 1987; Schuhmann, Ohara et al. 1991). None of these

approaches has proven entirely satisfactory; for example, some enzyme-immobilization methods result in random orientations of the redox centers with respect to the electrode, leading to inefficient electrical communication.

Willner and co-workers assembled a linear molecular chain consisting of the electrode, mediator, cofactor, and enzyme (Riklin, Katz et al. 1995; Zayats, Katz et al. 2002). This approach was shown to work for flavoenzymes (Zayats, Katz et al. 2002), hemoproteins (Zimmermann, Lindgren et al. 2000), and pyrroloquinoline quinone (PQQ) (Raitman, Patolsky et al. 2002) containing enzymes. In one example system (Zayats, Katz et al. 2002), a self-assembled monolayer of cystamine was assembled on the gold electrode. One carboxyl group of the mediator PQQ was then covalently bound to the amino groups of cystamine via an amide bond. Next, an amino-functionalized 3-aminophenylboronic acid molecule was covalently bound to a second carboxyl group on the PQQ through an amide bond. The cofactor $NAD(P)^+$ was then bound to the phenylboronic acid through an affinity linkage between the boronic acid and dihydroxyl functionality of the cofactor (Ozdemir and Tuncel 2000; Senel, Camli et al. 2002). This arrangement allowed unimpeded access of the cofactor to its binding site on the enzyme, providing multistep electron transfer while preventing component loss due to diffusion.

One disadvantage of this approach is that the mediator lies in the middle of the linear molecular chain and must therefore form two chemical bonds. Since PQQ has two carboxylic acid groups, it can react with both the cystamine and the 3-aminophenylboronic acid. However, PQQ's high cost (about $30,000 per gram) may make it prohibitively expensive for many commercial applications. While difunctional

mediators are rare, many monofunctional mediators are both inexpensive and able to efficiently regenerate $NAD(P)^+$.

This chapter presents a novel approach that overcomes the above-mentioned need for a difunctional mediator, thereby greatly expanding the range suitable mediators. A branched heterotrifunctional-linking molecule is used to couple a mediator and cofactor to an electrode in such a way that mediated electron transfer is achieved between the electrode and the dehydrogenase enzyme. The fabrication of the bioelectronic interface was characterized using External reflection Fourier-transform infrared spectroscopy (FTIR). Chronoamperometry, cyclic voltammetry, and EIS were used to characterize the electrical properties of the resulting bioelectronic interface. To demonstrate the versatility of this approach, results are presented for bioelectronic interfaces formed using two trifunctional linking molecules (Cys and Hcy), and multiple electron mediators (TBO, NR, and NBA).

3.3. Materials and methods

3.3.1. Media and strains

Escherichia coli (DH5α pADH B1M1-kan) culture containing a recombinant plasmid for 2° ADH from *Thermoaneorbactor ethanolicus* was grown and purified as described in Chapter 2 (Hassler, Dennis et al. 2007).

3.3.2. Chemicals

β-nicotinamide adenine dinucleotide phosphate ($NADP^+$), Cys, Hcy, TBO, NR, NBA, 3-carboxyphenyl boronic acid (CBA), 1-ethyl-3-(3-dimethylaminopropyl)carbodiimide (EDC), n-hydroxysuccinimide (NHS), glutaric dialdehyde (25% in water), ethanol, 2-propanol, 2-butanol, and pentanol were purchased

from Sigma-Aldrich (St. Louis, MO). Ultrapure water (18.2 MΩ) was supplied by a Barnstead Nanopure-UV four-stage purifier (Barnstead International Dubuque, Iowa).

3.3.3. Interface formation

Gold electrodes were cleaned using pirahana solution as described in Chapter 2. Clean gold electrodes were soaked in 100 mM Cys for 1 h at room temperature (25±2°C) and thoroughly rinsed with water to remove weakly adsorbed Cys. The Cys-modified gold electrodes were incubated for 1 h in a 100 mM phosphate buffer solution (PBS) (pH 7.4) containing 10 mM NHS and 10 mM EDC. The EDC and NHS react with the carboxylic acid branch of the Cys forming a better leaving group. The EDC/NHS-modified electrode was then reacted with the amine branch of TBO (1 mM TBO) resulting in the formation of an amide linkage between the TBO and the carboxylic group of the Cys (Cys-TBO). A 5 mM CBA solution was activated at room temperature with 10 mM NHS and 10 mM EDC in 100 mM PBS (pH 7.4) for 1 h. The activated CBA was then reacted with the Cys-TBO-modified electrodes for 1 h at room temperature (Riklin, Katz et al. 1995) and rinsed with deionized water to remove weakly adsorbed CBA. The CBA-modified electrodes were reacted with a 1 mM solution of $NADP^+$ in 100 mM PBS (pH 7.4) for 1 h and then washed with water to remove any weakly bound $NADP^+$ resulting in a gold electrode functionalized with Cys, TBO, and $NADP^+$ (Cys-TBO-$NADP^+$). The Cys-TBO-$NADP^+$-functionalized gold electrodes were reacted with a 4.4 mg mL^{-1} solution of 2° ADH in 100 mM PBS (pH 7.4) for 1 h at room temperature and cross-linked with 25 % (v/v) glutaric dialdehyde in water for 20 min. Scheme 3.1 illustrates the steps involved in functionalizing the electrode with Cys, TBO, $NADP^+$,

and 2° ADH. The resulting bioelectronic interfaces were rinsed with water and used for the biocatalytic oxidation of 2-propanol. Electrodes containing different linking molecules (Hcy) and electron mediators (NR and NBA) were fabricated in the manner described above, replacing Cys and TBO, respectively.

3.3.4. Electrochemical measurements

Chronoamperometry, cyclic voltammetry, and EIS were performed using an electrochemical analyzer (CHI660B) as described in Chapter 2.

3.3.5. Surface characterization techniques

FTIR was performed with a Nicolet Magna 560 FTIR spectrometer using a PIKE grazing angle (80°) attachment. A background spectrum of each uncoated electrode was obtained prior to electrode modification.

3.4. Results

3.4.1. Interface formation

Figure 3.1 shows the impedance spectra for the Cys, Cys-TBO, Cys-TBO-$NADP^+$, and Cys-TBO-$NADP^+$-2° ADH-modified electrodes (Curves 1-5, respectively). Fitting the equivalent-circuit model (Figure 2.1) to EIS data gave charge transfer resistance (R_{CT}) values of 12.8±2.4, 30.6±2.4, 39.1±1.7, and 64.0±2.3 Ω cm^2, for the Cys, Cys-TBO, Cys-TBO-$NADP^+$, and Cys-TBO-$NADP^+$-2° ADH-modified electrodes, respectively. The increase in R_{CT} provides evidence of interface-fabrication.

Figure 3.2 shows the FTIR spectra of gold electrodes with Cys, Cys-TBO, Cys-TBO-$NADP^+$-2° ADH-modified interfaces. The Cys-modified electrode (Figure 3.2A) shows peaks at 1710 and 1580 cm^{-1} corresponding to the stretching mode of the carboxylic acid group (C=O) vibration (Ihs and Liedberg 1991) and NH_2/NH_3^+

symmetric deformation modes (Uvdal and Vikinge 2001), respectively, confirming Cys adsorption to the electrode surface. The Cys-TBO-modified electrode (Figure 3.2B) shows absorption peaks at 1626 and 1450 cm^{-1}, which correspond to the amide I' (C=O) stretching and amide II' (N-H) bending (Meersman, Wang et al. 2005), respectively, suggesting that Cys and TBO are linked by an amide bond. The Cys-TBO-$NADP^+$-2° ADH-modified electrode (Figure 3.2C) shows peaks at 1655 and 1540 cm^{-1}, corresponding to the carboxylic acid (C=O) vibration and amine (N-H) bending, respectively. These peaks are consistent with enzyme adsorption (Masuda, Hasegawa et al. 2004). The small shifts of amide I (1626-1655 cm^{-1}) and amide II (1450-1540 cm^{-1}) peaks upon 2° ADH adsorption suggest that the Cys-TBO-$NADP^+$-modified electrode surface does not undergo conformation changes upon 2° ADH adsorption (Liu and Cai 2007).

3.4.2. Electrochemical Characterization

3.4.2.1. Cys-TBO-$NADP^+$-2° ADH-modified electrodes

Figure 3.3A shows the cyclic voltammograms at different times of 2° ADH adsorption on a Cys-TBO-$NADP^+$-modified electrode obtained at a constant 2-propanol concentration (25 mM) in 100 mM PBS at room temperature. Figure 3.3B shows the peak anodic current as a function of adsorption time. A pseudo-first-order absorption time constant (τ_{Cys}) of 49.2±1.0 min was derived from the data.

Figure 3.4 shows the chronoamperometric response for the Cys-TBO-$NADP^+$-2° ADH-modified electrode. Fitting Eqs. 2.1 and 2.3 to the chronoamperometric data gave values for the an electron transfer rate constant (k_{et}) and an apparent enzymatic surface

coverage (Γ_{enz}) of 130.0±19.1 s^{-1} and 2.6±0.1×10^{-11} mol cm^{-2}, respectively. Figure 3.5A shows the cyclic voltammograms of the Cys-TBO-$NADP^+$-2° ADH-modified electrode at various 2-propanpol concentrations in 100 mM PBS (pH 7.4) at room temperature. The peak anoidic current increased linearly with 2-propanol concentration (Figure 3.5B) below 30 mM, with a slope of 3.8±0.0 μA mM^{-1} cm^{-2} which is a measure of the biosensor's sensitivity. At 2-propanol concentrations above 30 mM, the anodic current reached a saturation current (I_{cat}^{sat}) of 129.0±3.0 μA cm^{-2}. The maximum turnover rate (TR_{max}) was determined to be 19.8±1.1 s^{-1} using Eq. 2.4.

The selectivity of the Cys-TBO-$NADP^+$-2° ADH-modified electrode was examined by testing alternative substrates. Table 3.1 shows the values of I_{cat}^{sat}, sensitivity, and TR_{max} for the Cys-TBO-$NADP^+$-2° ADH-modified electrode in the presence of 2-propanol, ethanol, 2-butanol, and pentanol. These data are consistent with the literature values for 2° ADH (Burdette, Secundo et al. 1997).

3.4.2.2. Hcy-TBO-$NADP^+$-2° ADH-modified electrodes

Figure 3.6A shows the cyclic voltammograms at different times of 2° ADH adsorption on an Hcy-TBO-NAD^+-modified electrode obtained at a constant 2-propanol concentration (25 mM) in 100 mM PBS at room temperature. Figure 3.6B shows the peak anodic current as a function of adsorption time. The pseudo-first-order absorption time constant (τ_{Hcy}) derived from the data was 45.5±0.6 min. τ_{Hcy} is consistent with τ_{Cys} (49.2±1.0 min) suggesting that the enzyme adsorption kinetics are independent of the linking molecule.

Figure 3.7 shows the chronoamperometric response of the Hcy-TBO-$NADP^+$-2° ADH-modified electrode in 100 mM PBS (pH 7.4) at containing 25 mM 2-propanol at room temperature. Fitting Eqs. 2.1 and 2.3 to the chronoamperometric data gave values for k_{et} and Γ_{enz} of 90.0±9.3 s^{-1} and 3.5±0.4×10^{-11} mol cm^{-2}, respectively. The value of k_{et} for the Hcy-TBO-$NADP^+$-2° ADH-modified electrode are smaller than those measured for the Cys-TBO-$NADP^+$-2° ADH-modified electrode (130.0±19.1 s^{-1}); however the Γ_{enz} for the Hcy-TBO-$NADP^+$-2° ADH-modified electrode was comparable to the Cys-TBO-$NADP^+$-2° ADH-modified electrode (2.6±0.1×10^{-11} mol cm^{-2})

Figure 3.8A shows the cyclic voltammograms of the Hcy-TBO-$NADP^+$-2° ADH-modified electrode at various 2-propanpol concentrations in 100 mM PBS (pH 7.4) at room temperature. The peak anoidic current increased linearly with 2-propanol concentration (Figure 3.8B) below 30 mM, with a slope of 1.4±0.0 μA mM^{-1} cm^{-2} which is a measure of the biosensor's sensitivity. At 2-propanol concentrations above 30 mM, the anodic current reached an I_{cat}^{sat} value of 55.8±1.1 μA cm^{-2}. The calculated TR_{max} value was found to be 5.6±0.6 s^{-1}. The values of I_{cat}^{sat}, sensitivity and TR_{max} for the Hcy-TBO-$NADP^+$-2° ADH-modified electrode are smaller than those measured for the Cys-TBO-$NADP^+$-2° ADH-modified electrode (129.0±3.0 μA cm^{-2}, 3.8±0.0 μA mM^{-1} cm^{-2}, and 19.8±1.1 s^{-1}, respectively). The decrease in the performance parameters (k_{et}, I_{cat}^{sat}, sensitivity and TR_{max}) suggests that the distance the interface (mediator, cofactor, and enzyme) is bound away from the interface plays an important role in interface performance.

3.4.2.3. Different electron mediators

While TBO was used as the primary electron mediator for this study, other electron mediators such as NR and NBA were also evaluated. Table 3.2 shows the performance of the 2°ADH biosensors prepared using TBO, NR, and NBA. An ideal electron mediator should allow the bioelectronic interface to (1) catalyze the oxidization/reduction of the desired analyte at a low overpotential, (2) allow a high current density, (3) exhibit high turnover rate, (4) promote fast electron transfer (i.e., relatively high values of k_{et}), and (5) be sensitive to small changes in analyte concentration. The Cys-NR-$NADP^+$-2° ADH modified electrode exhibited an I_{cat}^{sat} and sensitivity of 139.0±12.1 μA cm^{-2} and 2.8±0.2 μA mM^{-1} cm^{-2}, respectively. While the electrode containing NR as the electron mediator expresses a high current density, NR oxidizes at a relatively high overpotential (560 mV), which is close to the oxidation potential of common interferents including molecular oxygen and ascorbic acid (800 and 910 mV, respectively). The Cys-NBA-$NADP^+$-2° ADH modified electrode exhibited a I_{cat}^{sat} and sensitivity of 93.8±9.2 μA cm^{-2} and 1.9±0.2 μA mM^{-1} cm^{-2}, respectively. Even though NBA exhibited electron transfer, the current density, turnover rate, and the overpotential were less than that for TBO.

3.5. Discussion

We introduced a novel molecular architecture containing a branched, heterotrifunctional linking molecule that binds an electron mediator, cofactor, and enmzyme to the electrode such that electrons are transferred between the electrode and emzyme. Willner and co-workers assembled a linear molecular chain consisting of the electrode, bi-functional electron mediator, cofactor, and enzyme (Riklin, Katz et al. 1995;

Zayats, Katz et al. 2002). However, the high cost of the bi-functional electron mediator (PQQ) (about $30,000 per gram) makes it prohibitively expensive for commercial applications. The novel architectures discussed show the fabrication of bioelectronic interfaces using monofunctional electron mediators (TBO, NR, and NBA). The low cost of the monofunction electron mediators (~$4.78 per gram) compared to that of PQQ (~$40,000 per gram) suggests that the cost of fabrication of these interfaces can be reduced by 99% by replacing the PQQ with a monofunctional electron mediator.

We also investigated the fabrication of the bioelectronic interfaces using different trifunctional linking molecules. Changes in performance parameters (I_{cat}^{sat}, sensitivity and TR_{max}) upon changing the linking molecule from Cys to Hcy suggests the distance the redox center of the electron mediator is located from the surface is relevant in determination of the bioelectronic interfaces electrochemical properties. The fabrication of the bioelectronic interface has been focused on the use of branched hetero-trifunctional linking molecules, with different tethering lengths, on the surface of the electrode; the work could be extended to the use of linking molecules with branches of different lengths. It is believed that linking molecules with different branch lengths would exhibit similar characteristics as varying tether lengths. Understanding the effects of linking molecule size will allow investigators to tailor the bioelectronic interface for the desired application.

3.6. Conclusions

This chapter introduces a novel molecular architecture for mediated, bioelectronic interfaces using dehydrogenase enzymes. The use of branched, heterotrifunctional linking molecules allows the electrode, mediator, and cofactor to be tightly bound in such a way

that electron transfer is achieved between the electrode and dehydrogenase enzymes. This versatile approach greatly extends the range of mediators that can be used compared to previously reported linear architectures. The ability to use monofunctional mediators allows a greater degree of customization while reducing costs. Bioelectronic interfaces interfaces incorporating the monofunctional mediator TBO, $NADP^+$, and a 2° ADH enzyme exhibited high stability and may be suitable for applications as biosensors and biocatalytic reactors.

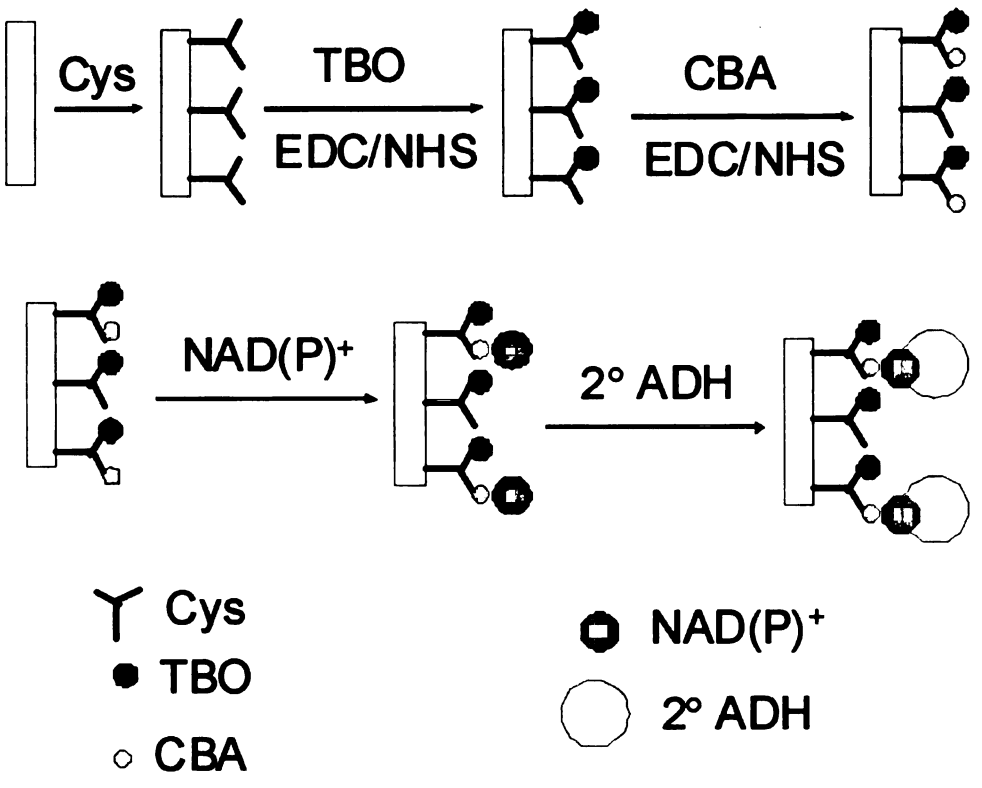

Scheme 3.1: Fabrication of the Cys-TBO-$NADP^+$-2^o ADH-modified electrode.

Table 3.1: Selectivity of the Cys-TBO-$NADP^+$-2^o ADH-modified electrode to the substrates 2-propanol, ethanol, 2-butanol, and 2-pentanol

Compound	I_{cat}^{sat} ($\mu A\ cm^{-2}$)	Sensitivity ($\mu A\ mM^{-1}\ cm^{-2}$)	TR_{max} (s^{-1})
2-propanol	129.0±3.0	3.8±0.1	19.8±1.1
Ethanol	78.5±1.4	1.6±0.1	9.2±0.8
2-Butanol	57.0±0.9	0.6±0.1	3.5±0.3
2-Pentanol	53.3±0.2	0.6±0.0	3.3±0.3

Table 3.2: Performance properties of 2° ADH-based bioelectronic interfaces containing toluidine blue O, neutral red, and Nile blue A.

Compound	I_{cat}^{sat} ($\mu A\ cm^{-2}$)	Sensitivity ($\mu A\ mM^{-1}\ cm^{-2}$)	Oxidation Potential (mV)
Toludine Blue O	129.0±3.0	3.8±0.1	175
Neutral Red	139.2±12.1	2.8±0.2	560
Nile Blue A	93.8±9.2	1.9±0.2	380

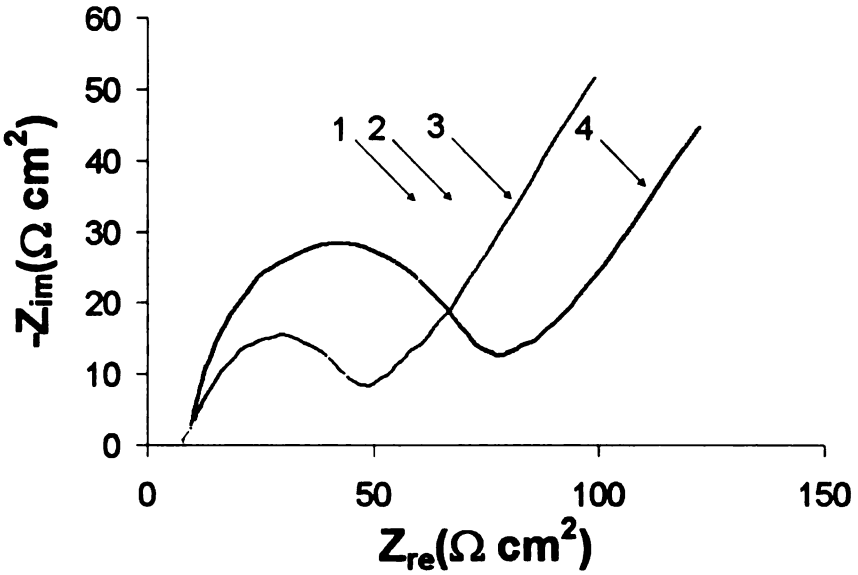

Figure 3.1: Nyquist plots of (1) Cys, (2) Cys-TBO, (3) Cys-TBO-$NADP^+$, and (4) Cys-TBO-$NADP^+$-2° ADH-modified electrodes an equimolar 5 mM solution of $K_3[Fe(CN)_6]/K_4[Fe(CN)_6]$ in 100 mM PBS (pH 7.4) recorded at the electrodes open circuit potential (210 mV) and room temperature (25±2°C).

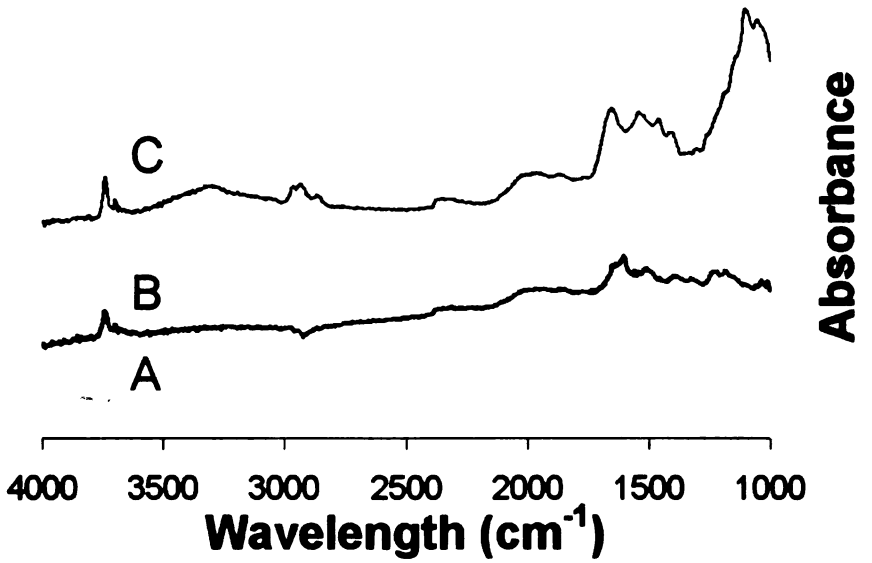

Figure 3.2: Average FTIR adsorption spectra of the (A) Cys, (B) Cys-TBO, and (C) Cys-TBO-$NADP^{+}$-2° ADH-modified electrodes

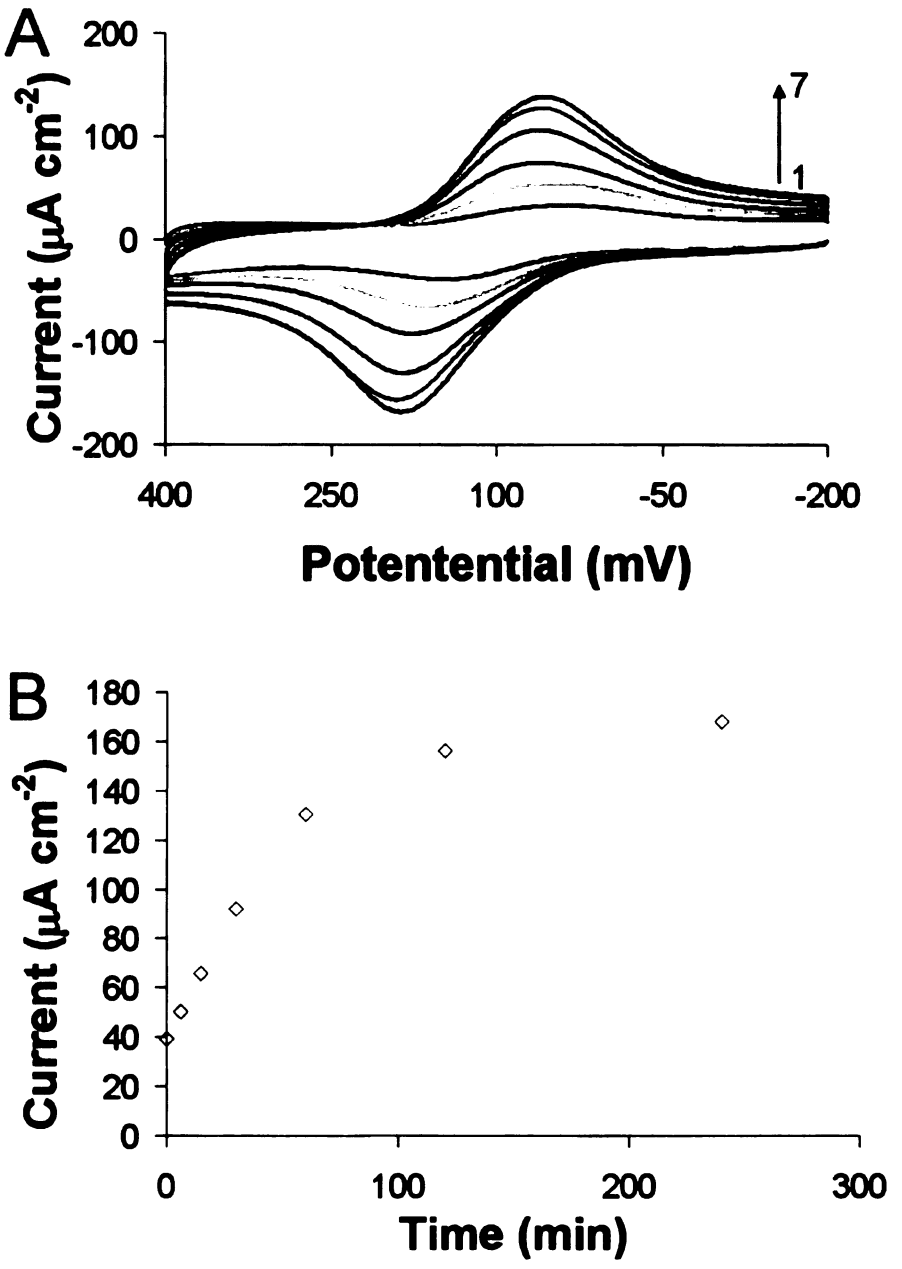

Figure 3.3: (A) Cyclic voltammograms of the Cys-TBO-$NADP^+$-functionalized electrode following various times of 2° ADH adsorption: (1) 0, (2) 6, (3) 15, (4) 30, (5) 60, (6) 120, and (7) 240 min. The data were recorded in room-temperature (25±2°C) 100 mM PBS (pH 7.4) containing 25 mM 2-propanol, at a potential scan rate of 100 mV s^{-1}. (B) Peak electrocatalytic current vs. time of adsorption.

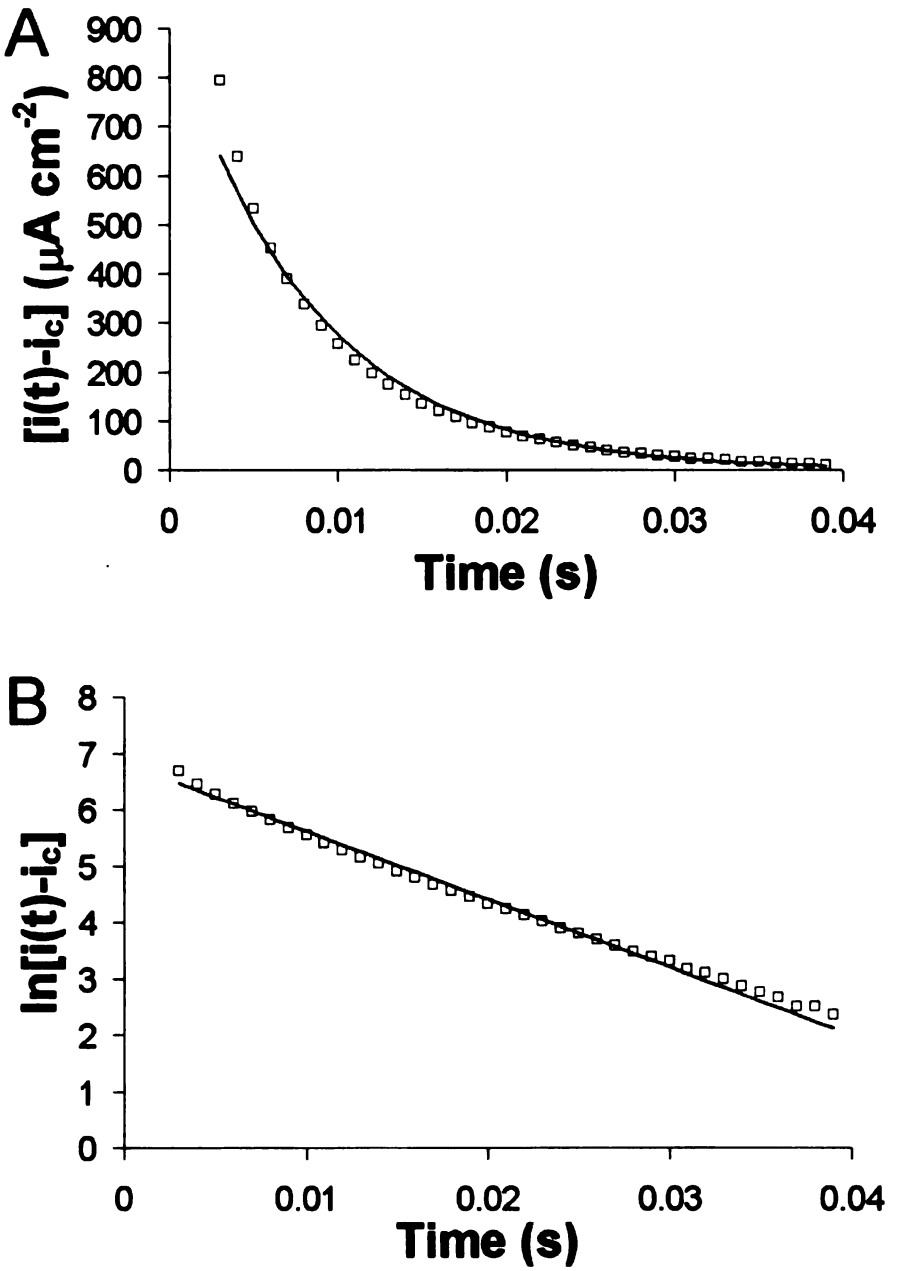

Figure 3.4: (A) Current transient for a potential step from -200 mV to 400 mV for a Cys-TBO-$NADP^+$-2° ADH-functionalized electrode in 100 mM PBS (pH 7.4) containing 25 mM 2-propanol at room temperature (25±2°C). (B) Shows the plots of $\log[i(t)-i_c]$ after double layer charging. The solid line represents the curve of best fit to the data.

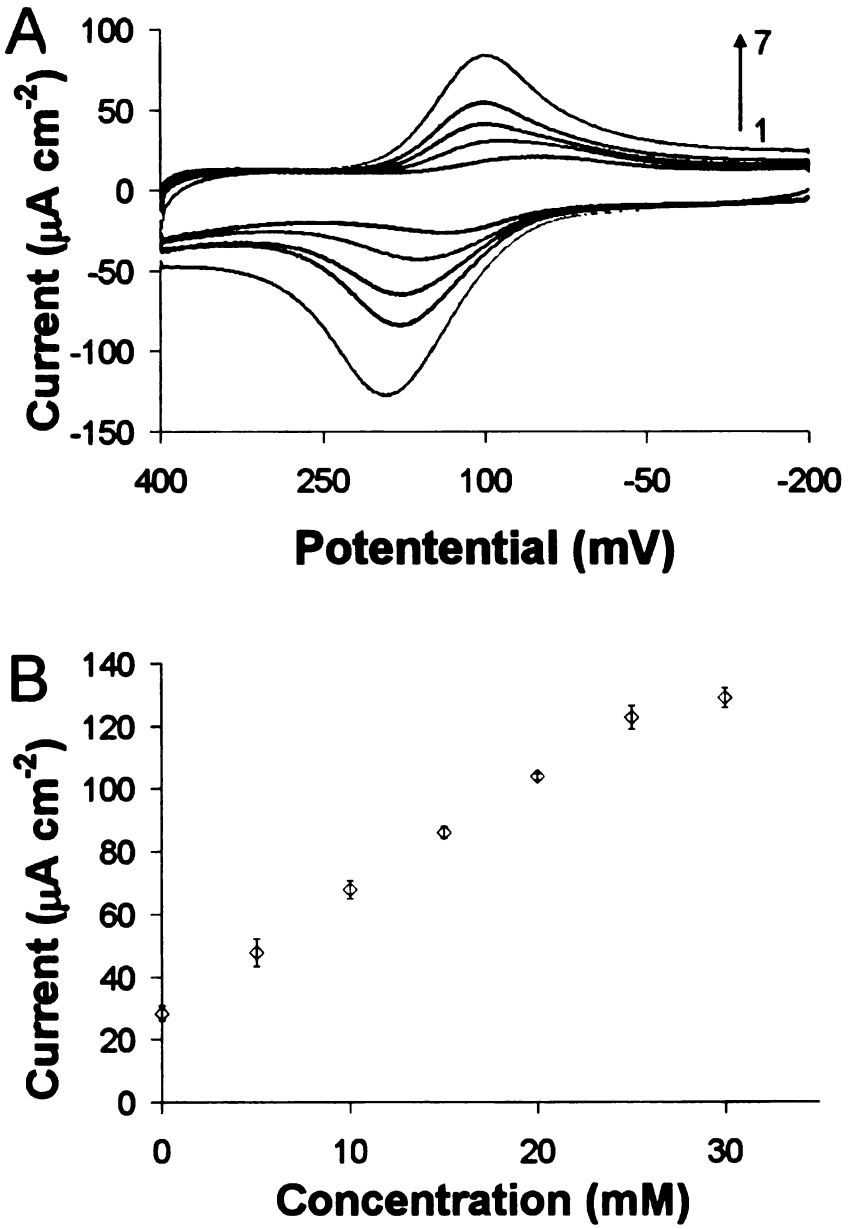

Figure 3.5: (A) Cyclic voltammograms for the Cys-TBO-$NADP^+$-2° ADH-functionalized electrode. The data were recorded in 100 mM PBS (pH 7.4) at room temperature (25±2°C) containing (1) 0, (2) 5, (3) 10, (4) 15, (5) 20, (6) 25, and (7) 30 mM 2-propanol at a potential scan rate of 100 mV s^{-1}. (B) Peak electrocatalytic current at various 2-propanol concentrations. The error bars indicate the mean ± the standard deviation (n=3).

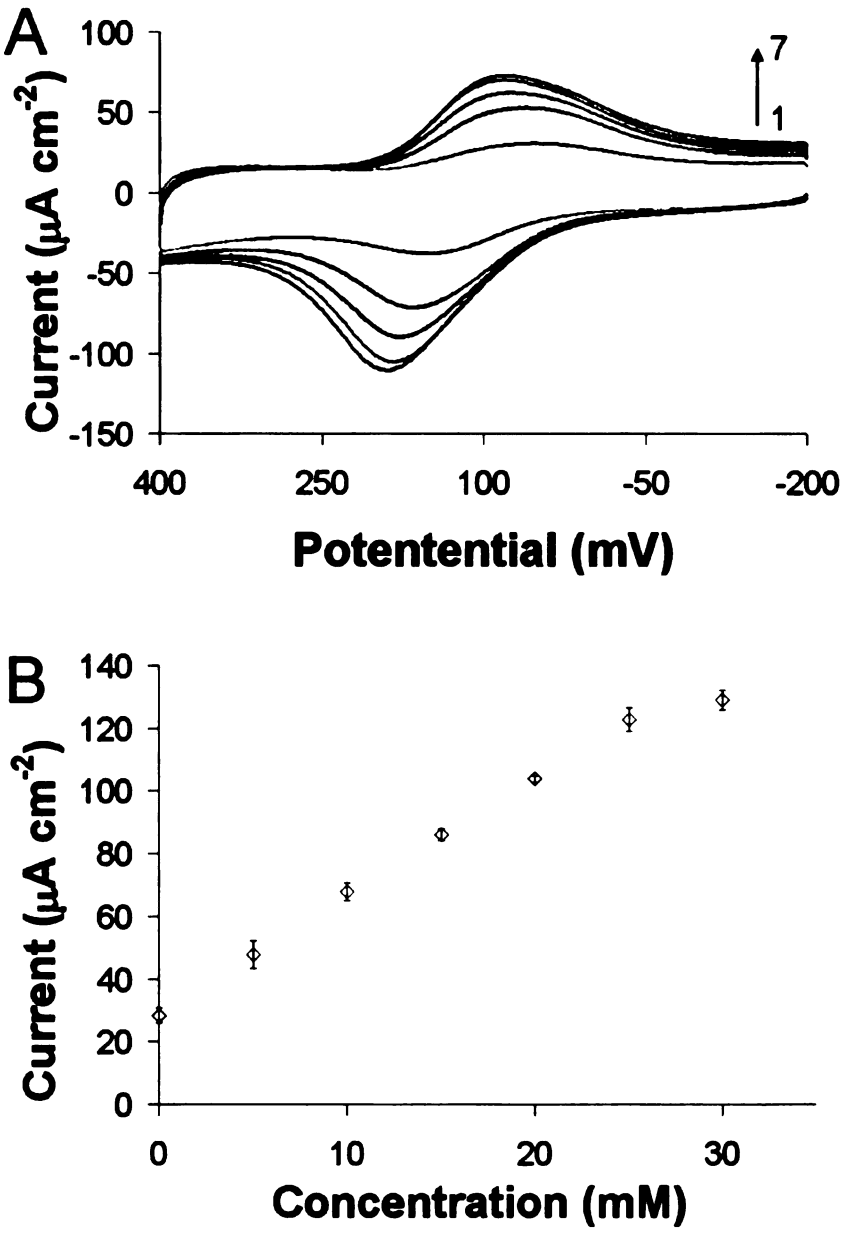

Figure 3.6: (A) Cyclic voltammograms of the Hcy-TBO-$NADP^+$-functionalized electrode following various times of 2^o ADH adsorption: (1) 0, (2) 6, (3) 15, (4) 30, (5) 60, (6) 120, and (7) 240 min. The data were recorded in room-temperature (25±2°C) 100 mM PBS (pH 7.4) containing 25 mM 2-propanol, at a potential scan rate of 100 mV s^{-1}. (B) Peak electrocatalytic current vs. time of adsorption.

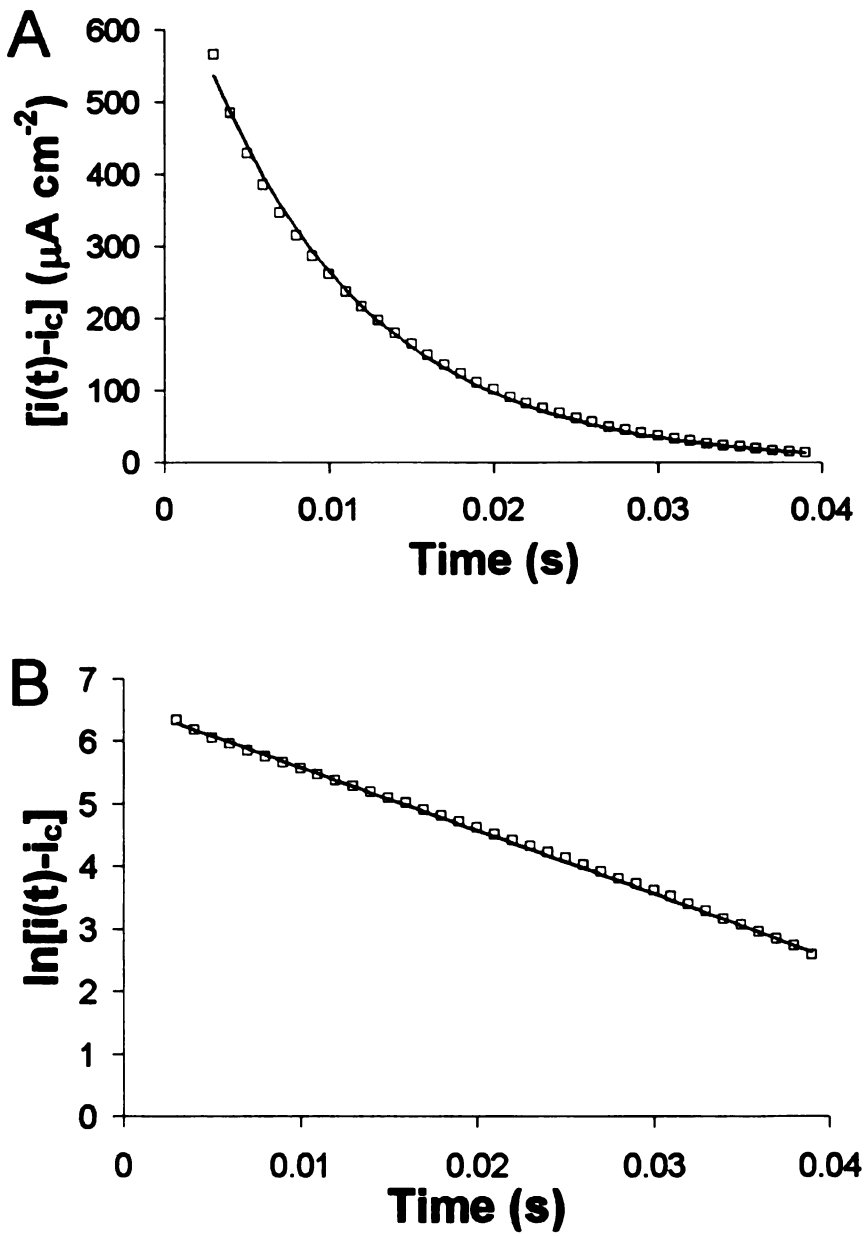

Figure 3.7: (A) Current transient for a potential step from -200 mV to 400 mV for a Hcy-TBO-$NADP^+$-2° ADH-functionalized electrode in 100 mM PBS (pH 7.4) containing 25 mM 2-propanol at room temperature (25±2°C). (B) Shows the plots of $\log[i(t)-i_c]$ after double layer charging. The solid line represents the curve of best fit to the data.

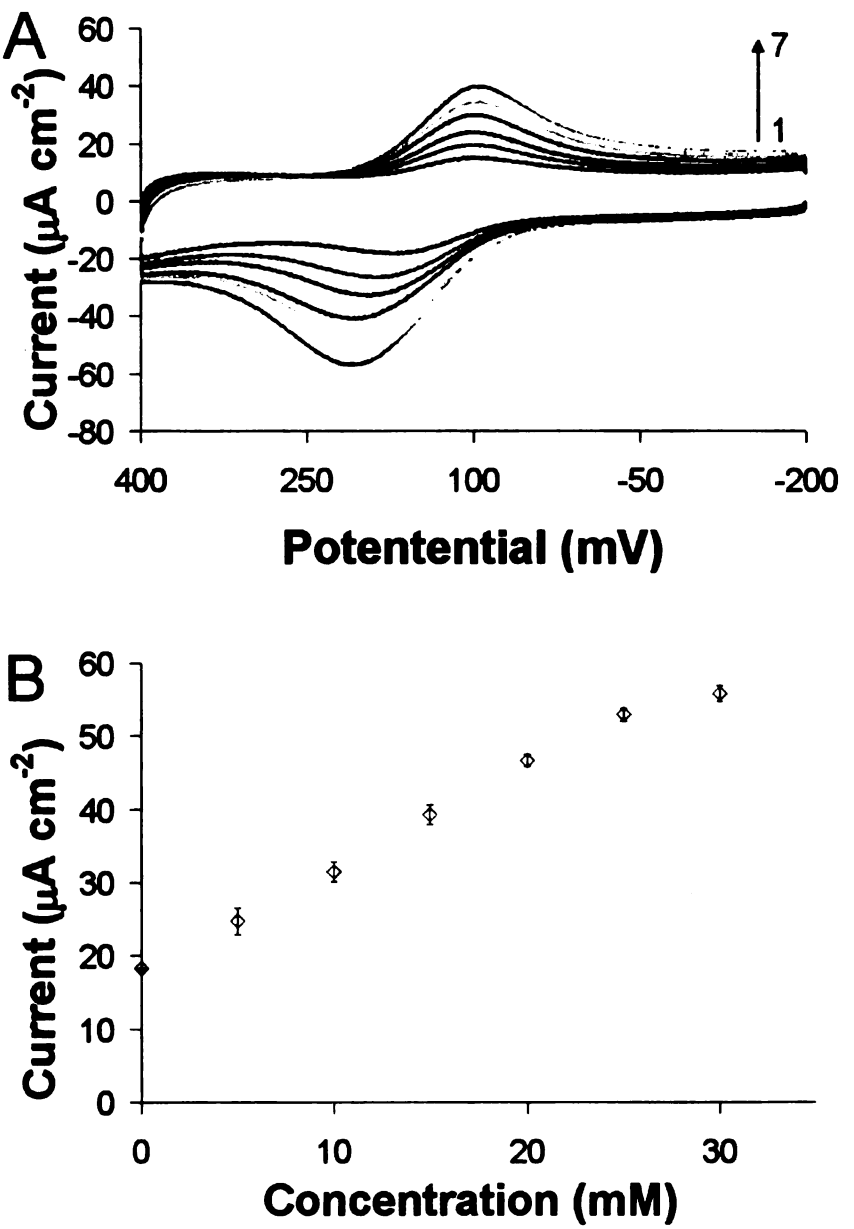

Figure 3.8: (A) Cyclic voltammograms for the Hcy-TBO-$NADP^+$-2^o ADH-functionalized electrode. The data were recorded in 100 mM PBS (pH 7.4) at room temperature (25±2°C) containing (1) 0, (2) 5, (3) 10, (4) 15, (5) 20, (6) 25, and (7) 30 mM 2-propanol at a potential scan rate of 100 mV s^{-1}. (B) Peak electrocatalytic current at various 2-propanol concentrations. The error bars indicate the mean ± the standard deviation (n=3).

4. MUTATION OF TYRISINE-218 TO PHENYLALANINE IN THERMOANAEROBACTER ETHANOLICUS SECONDARY ALCOHOL DEHYDROGENASE: EFFECTS ON BIOELECTRONIC INTERFACE PERFORMANCE

4.1. Abstract

Bioelectronic interfaces that facilitate electron transfer between the electrode and a dehydrogenase enzyme have potential applications in biosensors, biocatalytic reactors, and biological fuel cells. Secondary alcohol dehydrogenase (2° ADH) from *Thermoanaerobacter ethanolicus* is especially well suited for the development of such bioelectronic interfaces because of its thermostability and facile production and purification. However, the natural cofactor for 2° ADH, β-nicotinamide adenine dinucleotide phosphate ($NADP^+$) is more expensive and less stable than β-nicotinamide adenine dinucleotide (NAD^+). Polymerase chain reaction (PCR)-based site-directed mutagenesis was performed on 2° ADH in an attempt to adjust the cofactor specificity toward NAD^+ by mutating Tyr^{218} to Phe (Y218F 2° ADH). The mutation of Tyr^{218} to Phe increased the K_m(app) for $NADP^+$ 200-fold, while decreasing the K_m(app) for NAD^+ 2.5-fold. Both the wild-type and mutant enzyme were incorporated into a bioelectronic interface that established electrical communication between the enzyme, cofactor (e.g., $NADP^+$), the electron mediator [toluidine blue O (TBO)], and a gold electrode. Y218F 2° ADH exhibited a four-fold increase in the turnover ratio compared to the wild-type in the presence of NAD^+. The electrochemical and kinetic measurements support the prediction that Tyr218 is a strong determinant of *T. ethanolicus* 2° ADH's specificity for $NADP^+$. Chronoamperometry, cyclic voltammetry and electrochemical impedance spectroscopy

(EIS) were used to characterize the bioelectronic interfaces where the mutant and wild type enzymes are incorporated.

4.2. Introduction

Bioelectronic interfaces that allow electrons to be exchanged between an enzyme and an underlying electrode have potential industrial applications, including biosensors (Armstrong, Heering et al. 1997; Halbhuber, Petrmichlova et al. 2003), biocatalytic reactors (Park, Laivenieks et al. 1999; Park and Zeikus 1999), and biological fuel cells (Chen, Barton et al. 2001; Tsujimura, Fujita et al. 2001). Dehydrogenase enzymes are of particular interest for bioelectronic applications because they catalyze reactions that involve direct electron transfer. Alcohol dehydrogenases (ADHs) are zinc-containing enzymes that use NAD^+ (EC 1.1.1.1), $NADP^+$ (EC 1.1.1.2), or both (EC 1.1.1.71) as a cofactor (Jornvall, Eklund et al. 1978). The ADHs are classified as either primary (1^o) or secondary (2^o) based on their efficiency in reacting with either primary or secondary alcohols, respectively.

The $NADP^+$-dependent 2° ADH from *Thermoanaerobacter ethanolicus* is an especially attractive enzyme for bioelectronic interface development because of its thermostability, ease of production, and ability to function in the presence of molecular oxygen (Keinan, Hafeli et al. 1986; Keinan, Seth et al. 1987). The cloning, purification, crystallization, and reaction properties of this 2° ADH have previously been reported (Peretz, Bogin et al. 1997; Tripp, Burdette et al. 1998; Heiss, Laivenieks et al. 2001; Kosjek, Stampfer et al. 2004). However, since NAD^+ is more stable and less expensive

than $NADP^+$ (Schuhmann, Ohara et al. 1991), research is underway to engineer this enzyme to make it use NAD^+ as a cofactor.

Thermoanaerobacter ethanolicus 2° ADH belongs to the majority of dehydrogenases that bind the nicotinamide cofactor through a Rossmann fold (Burdette, Vieille et al. 1996). Recent *T. ethanolicus* 39E genome sequencing results (Genbank # EAO63648) and repeated sequencings in the Zeikus lab (Laivenieks, unpublished results) indicate that *T. ethanolicus* 2° ADH is identical to that of *Thermoanaerobacter brockii*. However in the NAD^+-dependent horse liver primary ADH (Genbank # P00327), the Gly^{198} in the Rossmann fold is replaced by Asp^{223}. The side chain of the Asp^{223} occupies the volume otherwise occupied by the ribose phosphate of NADPH in *T. brockii* 2° ADH. A Gly198Asp mutation in *T. ethanolicus* 2° ADH (Burdette, Secundo et al. 1997) yielded an enzyme with a 3-fold increased specificity for NAD^+ and a 6.7-fold increased k_{cat} with NAD^+. The catalytic efficiency (i.e., k_{cat}/K_m) of that mutant enzyme is 6.6 times higher with NAD^+ than with $NADP^+$, but it still shows only ~35% of the wild-type enzyme activity with $NADP^+$, showing that Gly^{198} is not the only amino acid responsible for determination of cofactor specificity in this enzyme. Korkhin *et al.* (1998) suggested that Tyr^{218} might be the most important determinant of *Thermoanaerobacter brockii* 2° ADH's specificity for $NADP^+$ (Korkhin, Kalb et al. 1998). Upon $NADP^+$ binding, the sidechain of Tyr^{218} rotates by 120°, enabling Tyr^{218} to stack against the adenine moiety of the cofactor and to form a hydrogen bond between its hydroxyl and one oxygen atom of the ribose phosphate. Other residues involved in determining *T. brockii* 2° ADH's

specificity for $NADP^+$ include Ser^{199} and Arg^{200}, whose side chains also form hydrogen bonds with the oxygens of the ribose phosphate. In the horse liver primary ADH, Ser^{199}, Arg^{200}, and Tyr^{218} are replaced with Ile^{224}, Asn^{225}, and Pro^{243}, respectively. The role of residues Ser^{199} and Arg^{200} as cofactor specificity determinants in *T. ethanolicus* 2° ADH is the subject of parallel study in the Zeikus lab. Here we characterize *T. ethanolicus* 2° ADH mutant Tyr218Phe to determine the function of Tyr^{218} in cofactor specificity. Substitution of Tyr^{218} with Phe is designed to remove the hydrogen bond between Tyr^{218} and $NADP^+$'s ribose phosphate, while maintaining the stacking of Tyr's phenyl ring with $NADP^+$'s adenine.

Ideal dehydrogenases should not only have a desirable profile of cofactor and product specificities, they should also function effectively when incorporated into bioelectronic interfaces suitable for industrial applications. Development of such interfaces has been hampered by challenges associated with regenerating the enzyme's cofactor *in situ* (Blaedel and Jenkins 1975; Schmakel, Santhanam et al. 1975; Prodromidis and Karayannis 2002). Methods have been developed to immobilize mediators, cofactors, and dehydrogenase enzymes at the electrode surface including the use of diffusional electron mediators (Serban and El Murr 2004), immobilization of the enzymes in conductive polymers (Heller 1990; Emr and Yacynych 1995), and construction of a redox relay conducting electrons between the enzyme and electrode (Degani and Heller 1987; Schuhmann, Ohara et al. 1991). However, these electrodes result in the enzyme binding to the surface in a random orientation possibly resulting in inefficient electrical communication (Badia, Carlini et al. 1993; Zayats, Katz et al. 2002).

To overcome this problem, Zayats et al. developed a linear molecular chain consisting of the electrode, mediator, cofactor, and enzyme (Riklin, Katz et al. 1995; Zayats, Katz et al. 2002). However, this approach requires the use of an electron mediator that forms two bonds: one with the surface, and the other with the cofactor. We recently developed an electron transfer scaffold using a heterotrifunctional linking molecule [i.e., cysteine (Cys)] (Hassler and Worden 2006). The electron mediator and cofactor were bound to opposite branches of the linking molecule, allowing greater flexibility in scaffold formation and permitting the use of electron mediators having a single reactive group.

This chapter describes the site-directed mutagenesis of *T. ethanolicus* 2° ADH to replace Tyr^{218} with Phe, and the characterization of the mutant enzyme, Y218F 2° ADH. The K_m(app) and V_{max} values of the mutant and wild-type enzymes were measured. The performance of Y218F 2° ADH immobilized in a bioelectronic interface was also characterized using cyclic voltammetry and chronoamperometry.

4.3. Materials and methods

4.3.1. Chemicals

The kanamycin-resistance GenBlock DNA cartridge used in the construction of the expression vector was purchased from GE Healthcare (Pittsfeild, MA) (Oka, Sugisaki et al. 1981). DNA for sequencing was isolated using the Wizard miniprep kit (Promega, Madison, WI). PCR products were cloned using the TOPO TA PCR product cloning kit (Invitrogen, Carlsbad, CA). Excised DNA from agarose gels was purified using the QIAEX II Gel extraction kit (Qiagen, Valencia, CA). Tryptone, yeast extract, dithiothreitol, isopropyl-β-D-thiogalactopyranoside (IPTG), and 5'-bromo-4-chloro-3-indolyl-β-D-galactopyranoside (X-gal) were purchased from Fisher Scientific (Pittsburgh,

PA). All other chemicals, including NAD^+, $NADP^+$, Cys, TBO, 3-carboxyphenyl boronic acid (CBA), 1-ethyl-3-(3-dimethylaminopropyl) carbodiimide (EDC), n-hydroxysuccinimide (NHS), glutaric dialdehyde (25% in water), 2-propanol, ammonium sulfate, sodium phosphate monobasic, and sodium phosphate dibasic, were purchased from Sigma-Aldrich (St. Louis, MO). Ultrapure water (18.2 MΩ) was supplied by a Barnstead Nanopure-UV four-stage purifier (Barnstead International, Dubuque, IA).

4.3.2. Media and strains

Escherichia coli (DH5α pADH B1M1-kan) culture containing a recombinant plasmids for 2° ADH and Y218F 2° ADH from *Thermoaneorbactor ethanolicus* were grown and purified as described in Chapter 2 (Hassler, Dennis et al. 2007).

4.3.3. Mutagensis

All DNA manipulations were done using established protocols (Sambrook and Russell. 1989; Ausubel, Brent et al. 1993). A point mutation was introduced into the *T. ethanolicus* 39E *adhB* gene by PCR-based site-directed mutagenesis (Sambrook and Russell. 1989). An oligonucleotide primer (P1) complementary to the non-coding strand was synthesized, including a *KpnI* restriction site, the native *adhB* ribosome assembly site, and the *adhB* translation initiation codon. A second oligonucleotide primer (P2) was designed to include the complement to the *adhB* termination codon and an *ApaI* restriction site. The complementary 25-45 base oligonucleotide primers containing the mutant bases (coding strand [P3] 5'-GATATTGTAAACTTTAAAGATGGTCC-3', and the non-coding strand [P4] 5'-GGACCATCTTTAAAGTTTACAATATC-3') were used in conjunction with primers P1 and P2 to mutate and amplify the N-terminal (primers P1 and P4) and C-terminal segments (primers P2 and P3) of the *adhB* gene separately. The

two amplified segments were combined as the template in a final PCR reaction, using primers P1 and P2, to assemble the whole mutated *adhB* gene. The mutated *adhB* gene was cloned into the pCR 2.1-TOPO vector. The plasmid was then transformed into *E. coli* TOP 10 and grown on Luria-Bertani plates containing 50 μg L^{-1} kanamycin, 1.2 mg mL^{-1} IPTG, and 0.5 mg mL^{-1} X-gal. After sequence verification, the correct clone was expressed in pBluescriptII KS(+) containing a kanamycin-resistance cartridge introduced in the *Eco*RI site.

4.3.4. Enzyme kinetics

The activity of 2° ADH in the presence of $NAD(P)^+$ during the enzymatic oxidation of 2-propanol at 60°C (Burdette and Zeikus 1994) was measured using a spectrophotometer at a wavelength of 340 nm. The enzyme was incubated at 55°C for 15 min before the activity assay. The pH of Tris buffer was adjusted to be 8.0 at 60°C using a thermal correction factor of -0.031 ΔpH/°C. Assays to determine K_m(app) and V_{max}(app) for $NAD(P)^+$ were conducted at 60°C using a 2-propanol concentration 20 times the K_m(app) value. Kinetic parameters were calculated from non-linear best fits of the activity data to the Michaelis-Menten equation using Origin 7.5 (OriginLab, Northampton, MA) (Brooks 1992). Protein concentrations were determined using the modified Bradford assay.

4.3.5. Interface fabrication

Clean gold electrodes were soaked in 100 mM Cys for 1 h at room temperature (25±2°C) and thoroughly rinsed with water to remove weakly adsorbed Cys. The Cys-modified gold electrodes were incubated for 2 h in a 100 mM phosphate buffer solution (PBS) (pH 7.4) containing 10 mM NHS and 10 mM EDC. The EDC and NHS react with

the carboxylic acid branch of the Cys forming a better leaving group on the surface of the Cys. The EDC/NHS-modified electrode was then reacted with the amine branch of TBO (1 mM TBO) resulting in the formation of an amide linkage between the TBO and the carboxylic group of the Cys (Cys-TBO). A 5 mM CBA solution was activated at room temperature with 10 mM NHS and 5 10 mM EDC in 100 mM PBS (pH 7.4) for 2 h. The activated CBA was then reacted with the Cys-TBO-modified electrodes for 1 h at room temperature (Riklin, Katz et al. 1995) and rinsed with deionized water to remove weakly adsorbed CBA. The CBA-modified electrodes were reacted with a 1 mM solution of NAD^+ in 100 mM PBS (pH 7.4) for 1 h and then washed with water to remove any weakly bound cofactor resulting in a gold electrode functionalized with Cys, TBO, and NAD^+. The Cys-TBO-NAD^+ functionalized gold electrodes were reacted with a 4.4 mg mL^{-1} solution of 2° ADH in 100 mM PBS (pH 7.4) for 1 h and then cross-linked with 25% (v/v) glutaric dialdehyde in water for 20 min. Scheme 4.1 illustrates the steps involved in functionalizing the electrode with Cys, TBO, NAD^+, and 2° ADH. The resulting bioelectronic interfaces were rinsed with water and used for the biocatalytic oxidation of 2-propanol. Electrodes containing different enzymes (Y218F 2°ADH) were fabricated in the manner described above, replacing 2°ADH.

4.3.6. Electrochemical measurements

Cyclic voltammetry and chronoamperometry were performed as described in Chapter 2 using an electrochemical analyzer (CHI660B, CH Instruments).

4.4. Results

4.4.1. Cofactor specificity

Kinetic parameters for the wild-type and Y218F 2° ADHs are given in Table 4.1. 2° ADH exhibited a 150-fold lower K_m(app) for $NADP^+$ than for NAD^+ and a V_{max}(app) that was 16.5 times greater for $NADP^+$ than for NAD^+. Y218F 2° ADH exhibited a 2.7-fold lower K_m(app) and 5.5-fold higher V_{max}(app) than 2° ADH in the presence of NAD^+ indicating that Y218F 2° ADH has greater activity in the presence of NAD^+ then does 2° ADH. In the presence of $NADP^+$, Y218F 2° ADH exhibited a 200-fold greater K_m(app) and a 3-fold lower V_{max}(app) than 2° ADH suggesting that 2° ADH is more active then Y218F 2° ADH. These trends are consistent with the results of Kleifeld and co-workers (Kleifeld, Frenkel et al. 2000).

4.4.2. Electrochemical characterization

4.4.2.1. Cys-TBO-NAD^+-2° ADH-modified electrode

Figure 4.1A shows the cyclic voltammograms at different times of 2° ADH adsorption on a Cys-TBO-NAD^+-modified electrode obtained at a constant 2-propanol concentration (25 mM) in 100 mM PBS (pH 7.4) at room temperature. Figure 4.1B shows the peak anodic current as a function of adsorption time. The pseudo-first-order absorption time constant (τ_{NAD}) derived from the data was 67.6±1.0 min. The higher the value of τ_{NAD} compared to τ_{Cys} (49.2±1.0 min) suggests that 2° ADH has a great affinity for $NADP^+$ than NAD^+.

Figure 4.2 shows the chronoamperometric response of the Cys-TBO-NAD^+-2° ADH modified electrode following a potential step from -200 mV to 400 mV measured

in 100 mM PBS (pH 7.4) containing 25 mM 2-propanol at room temperature. Fitting Eq. 2.2 to the chronoamperometric data gave values for the electron transfer rate constants for the two binding modes for NAD^+ (k'_{et} and k''_{et}), of 382.2±1.7 and 36.1±0.2 s^{-1}. The resulting surface coverage of the two binding domains (Γ'_{enz} and Γ''_{enz}, respectively) were determined to be $1.6\pm0.0\times10^{-12}$ and $2.0\pm0.0\times10^{-12}$ mol cm^{-2}, respectively using Eq. 2.3. Figure 4.3A shows the cyclic voltammograms of the Cys-TBO-NAD^+-2° ADH-modified electrode at various 2-propanpol concentrations in 100 mM PBS (pH 7.4) at room temperature. The peak anoidic current increased linearly with 2-propanol concentration (Figure 4.3B) below 30 mM, with a slope of 0.4±0.0 μA mM^{-1} cm^{-2} which is a measure of the biosensor's sensitivity. At 2-propanol concentrations above 30 mM, the anodic current reached a saturation current (I_{cat}^{sat}) of 28.6±3.0 μA cm^{-2}. TR_{max} value was found to be 2.9±0.8 s^{-1}, according to Eq. 2.4. The values of I_{cat}^{sat}, sensitivity, and TR_{max} for the Cys-TBO-NAD^+-2° ADH-modified electrode are considerably lower than those for the Cys-TBO-$NADP^+$-2° ADH-modified electrode (129.0±3.0 μA cm^{-2}, 3.8±0.0 μA mM^{-1} cm^{-2}, and 19.8±1.1 s^{-1}, respectively) indicating that 2° ADH has greater activity in the presence of $NADP^+$ compared to NAD^+.

4.4.2.2. Cys-TBO-NAD^+-Y218F 2° ADH-modified electrode

Figure 4.4A shows the cyclic voltammograms at different times of Y218F 2° ADH adsorption on a Cys-TBO-NAD^+-modified electrode obtained at a constant 2-propanol concentration (25 mM) in 100 mM PBS (pH 7.4) at room temperature. Figure 4.4B shows the peak anodic current as a function of adsorption time. The pseudo-first-order absorption time constant (τ_{Y218}) derived from the data was 50.7±1.4 min. The lower

value of τ_{Y218} compared to τ_{NAD} (67.6±1.0 min.) suggests that the Y218F 2° ADH has a greater affinity for NAD^+ than does the 2° ADH.

Figure 4.5 shows the chronoamperometric response of the Cys-TBO-NAD^+-Y218F 2° ADH-modified electrode in 100 mM PBS containing 25 mM 2-propanol at room temperature. Fitting Eq. 2.2 and 2.3 to the chronoamperometric data gave k'_{et} and $k''_{et,}$ values of 564.6±23.8 and 63.5±6.8 s^{-1}, respectively and Γ'_{enz} and Γ''_{enz} were determined to be $2.9\pm0.1\times10^{-12}$ and $2.1\pm0.2\times10^{-11}$ mol cm^{-2}, respectively. Figure 4.6A shows the cyclic voltammograms of the Cys-TBO-NAD^+-Y218F 2° ADH-modified electrode at various 2-propanpol concentrations in 100 mM PBS (pH 7.4) at room temperature. The peak anoidic current increased linearly with 2-propanol concentration (Figure 4.6B) below 30 mM, with a slope of 2.6±0.0 μA mM^{-1} cm^{-2} which is a measure of the biosensor's sensitivity. At 2-propanol concentrations above 30 mM, the anodic current reached an I_{cat}^{sat} value of 95.5±3.5 μA cm^{-2}. The calculated TR_{max} value was found to be 18.8±1.5 s^{-1}. The values of I_{cat}^{sat}, sensitivity and TR_{max} suggests that Y218F 2° ADH has a greater activity towards NAD^+ compared to 2° ADH. However, the values of I_{cat}^{sat}, sensitivity, and TR_{max} is still lower than the activity of 2° ADH in the presence of a Cys-TBO-$NADP^+$-modified electrode (129.0±3.0 μA cm^{-2}, 3.8±0.0 μA mM^{-1} cm^{-2}, and 19.8±1.1 s^{-1}, respectively) suggesting more work needs to be done in order to get a complete mutation of 2° ADH from $NADP^+$-dependce to NAD^+-dependence.

4.5. Discussion

NAD^+ has increased stability and has a lower price $56 per gram compared to $NADP^+$ $437.50 per gram (Banta and Anderson 2002). The difference in cost between $NADP^+$ and NAD^+ led us to develop a novel mutant of secondary alcohol dehydrogenase (2° ADH) whose cofactor would be NAD^+ as opposed to the wild-type's $NADP^+$. Kinetic and electrochemical measurements provide evidence that the Tyr^{218} to Phe mutation adjusted the 2° ADH cofactor specificity towards NAD^+. The ability to use an NAD^+-dependent enzymes compared to $NADP^+$-dependent enzymes offers potential for commercial biosensors and biocatalytic reactors having increased stability and reduced costs. Since cofactor specificity was not completely transformed the work could be extended to continue the mutagenesis of the 2° ADH. It is believed that mutation of Ile^{224}, Asn^{225}, and Pro^{243} will adjust 2° ADH cofactor specificity towards NAD^+.

4.6. Conclusions

This study described the catalytic properties, cofactor specificity, and biosensor and bioreactor applicability of thermophilic *T. ethanolicus* 2° ADH mutant Y218F. Using NAD^+ as the cofactor, the Y218F mutant enzyme exhibited a 5.5-fold higher V_{max} and a 2.7-fold lower K_m for NAD^+ than the wild-type. When immobilized on the Cys-TBO-NAD^+-modified interface, the electron transfer coefficients for the Y218F mutant enzyme were 564.6±23.8 and 63.5±6.8 s^{-1} compared to 382.2±1.7 and 36.1±0.2 s^{-1} for the wild-type. The sensitivity, I_{sat}^{cat}, and TR_{max} for the NAD^+-containing bioelectronic interface containing the Y218F mutant were 2.6±0.0 μA cm^{-2} mM^{-1}, 95.5±3.5 μA cm^{-2}, and

18.8±1.5 s^{-1}, respectively, compared to 0.4±0.0 μA cm^{-2} mM^{-1}, 30.3±2.5 μA cm^{-2}, and 2.9±0.8 s^{-1}, respectively, for the wild-type. Collectively, these results provide strong evidence that the Tyr^{218} to Phe mutation adjusted the 2° ADH cofactor specificity towards NAD^+. The ability to use an NAD^+-dependent 2° ADH offers potential for commercial biosensors and biocatalytic reactors having increased stability and reduced costs.

Table 4.1: Apparent K_m and V_{max} values for 2° ADH and Y218F 2° ADH. 2-propanol was used as the co-substrate in all cases. The values of K_m and V_{max} for 2° ADH (wild type) and Y218F 2° ADH mutant were determined for each cofactor.

Enzyme	$NADP^+$		NAD^+	
	V_{max}(app) (units mg^{-1})	K_m(app) (mM)	V_{max}(app) (units mg^{-1})	K_m(app) (mM)
Wild-type	69±5.2	0.017±0.001	4.2±3.1	2.5±1.9
Y218F-mutant	21±2.3	3.4±2.4	23±2.6	0.93±0.08

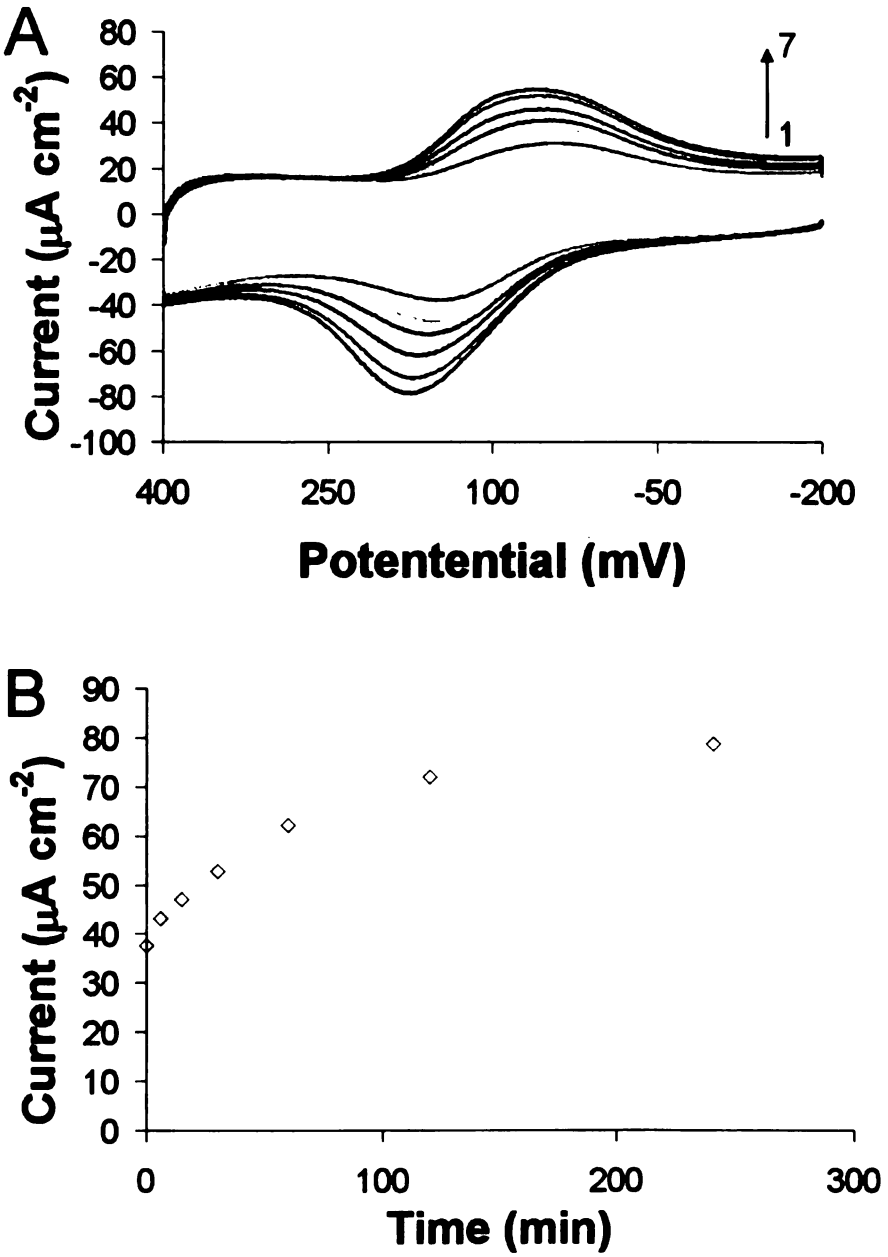

Figure 4.1: (A) Cyclic voltammograms of the Cys-TBO-NAD^+-functionalized electrode following various times of 2° ADH adsorption: (1) 0, (2) 6, (3) 15, (4) 30, (5) 60, (6) 120, and (7) 240 min. The data were recorded in room-temperature 100 mM PBS (pH 7.4) containing 25 mM 2-propanol, at a potential scan rate of 100 mV s^{-1}. (B) Peak electrocatalytic current vs. time of adsorption.

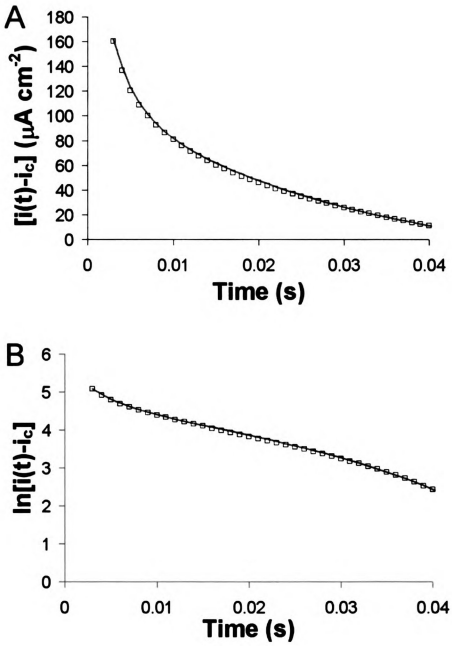

Figure 4.2: (A) Current transient for a potential step from -200 mV to 400 mV for a Cys-TBO-NAD^{+}-2° ADH-functionalized electrode in 100 mM PBS (pH 7.4) containing 25 mM 2-propanol at room temperature. (B) Shows the plots of $\log[i(t)-i_c]$ after double layer charging. The solid line represents the curve of best fit to the data.

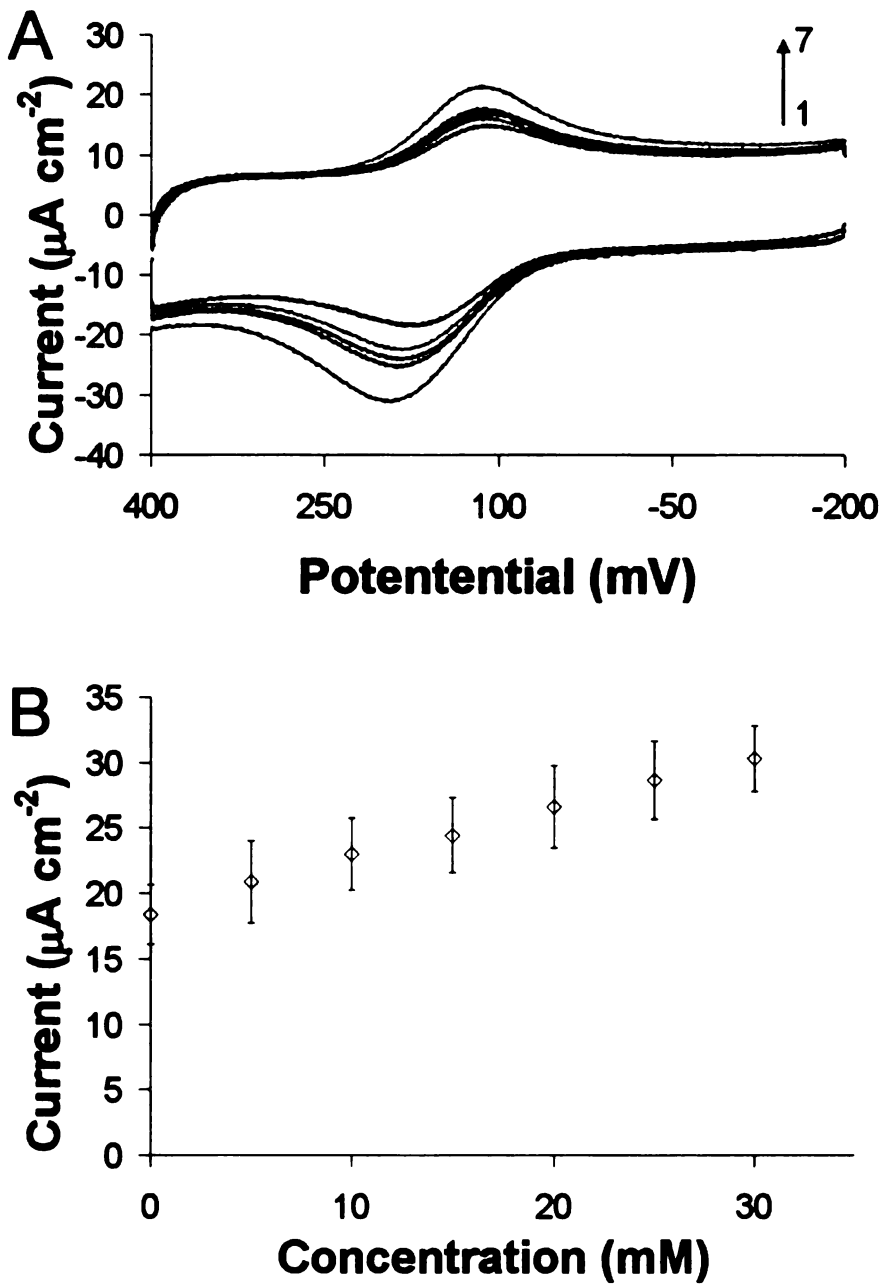

Figure 4.3: (A) Cyclic voltammograms for the Cys-TBO-NAD^+-2^o ADH-functionalized electrode. The data were recorded in 100 mM PBS (pH 7.4) at room temperature containing (1) 0, (2) 5, (3) 10, (4) 15, (5) 20, (6) 25, and (7) 30 mM 2-propanol at a potential scan rate of 100 mV s^{-1}. (B) Peak electrocatalytic current at various 2-propanol concentrations. The error bars indicate the mean ± the standard deviation (n=3).

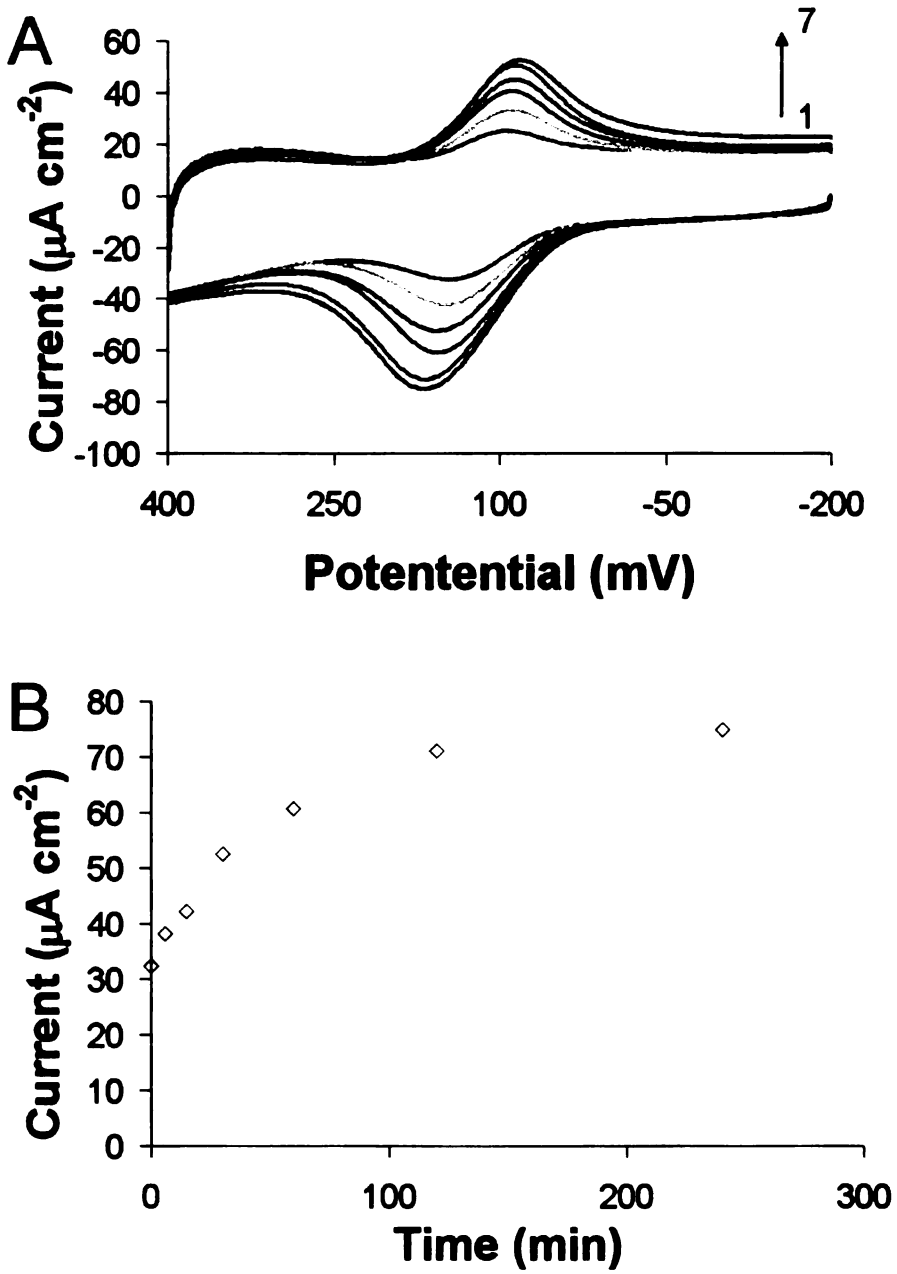

Figure 4.4: (A) Cyclic voltammograms of the Cys-TBO-NAD^+-functionalized electrode following various times of Y218F 2^o ADH adsorption: (1) 0, (2) 6, (3) 15, (4) 30, (5) 60, (6) 120, and (7) 240 min. The data were recorded in room-temperature 100 mM PBS (pH 7.4) containing 25 mM 2-propanol, at a potential scan rate of 100 mV s^{-1}. (B) Peak electrocatalytic current vs. time of adsorption.

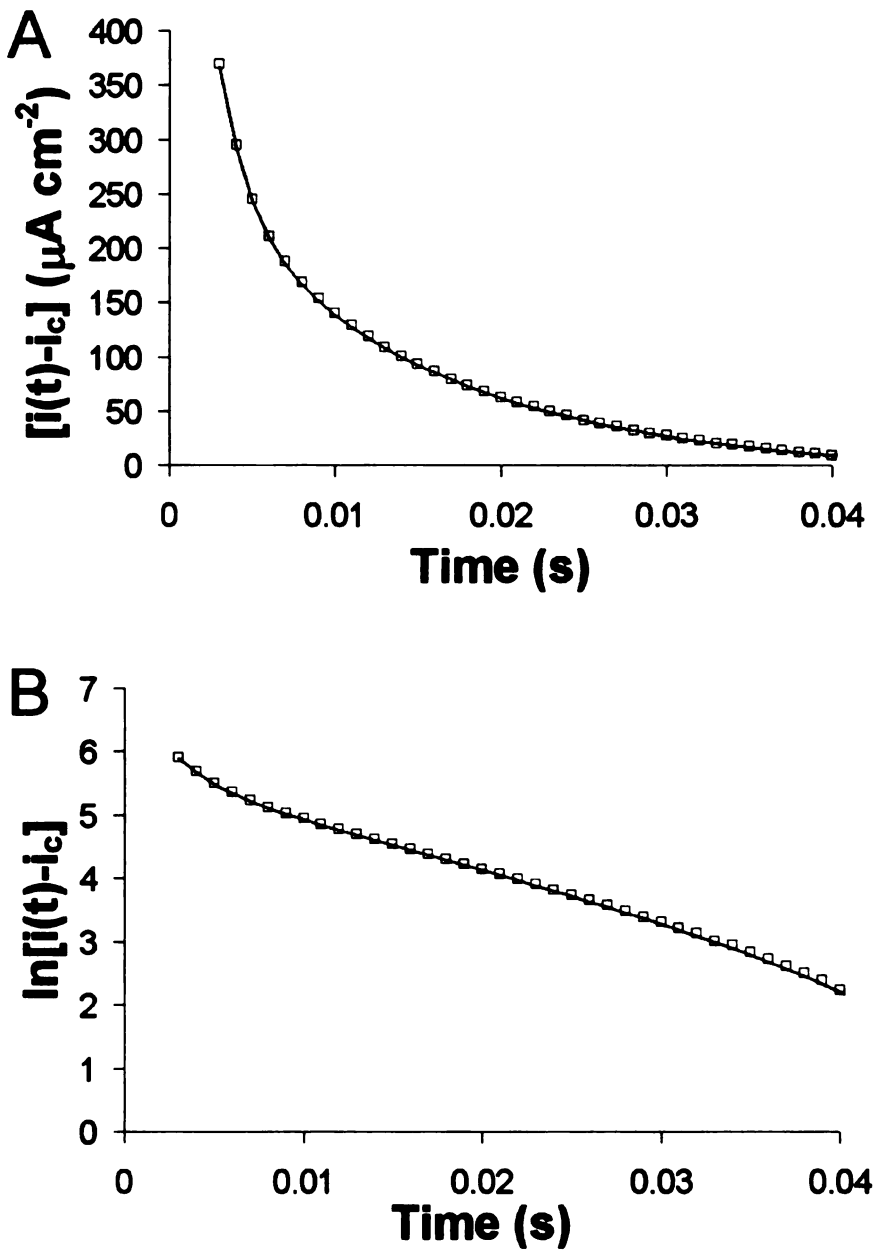

Figure 4.5: (A) Current transient for a potential step from -200 mV to 400 mV for a Cys-TBO-NAD^+-Y218F 2° ADH-functionalized electrode in 100 mM PBS (pH 7.4) containing 25 mM 2-propanol at room temperature. (B) Shows the plots of $\log[i(t)-i_c]$ after double layer charging. The solid line represents the curve of best fit to the data.

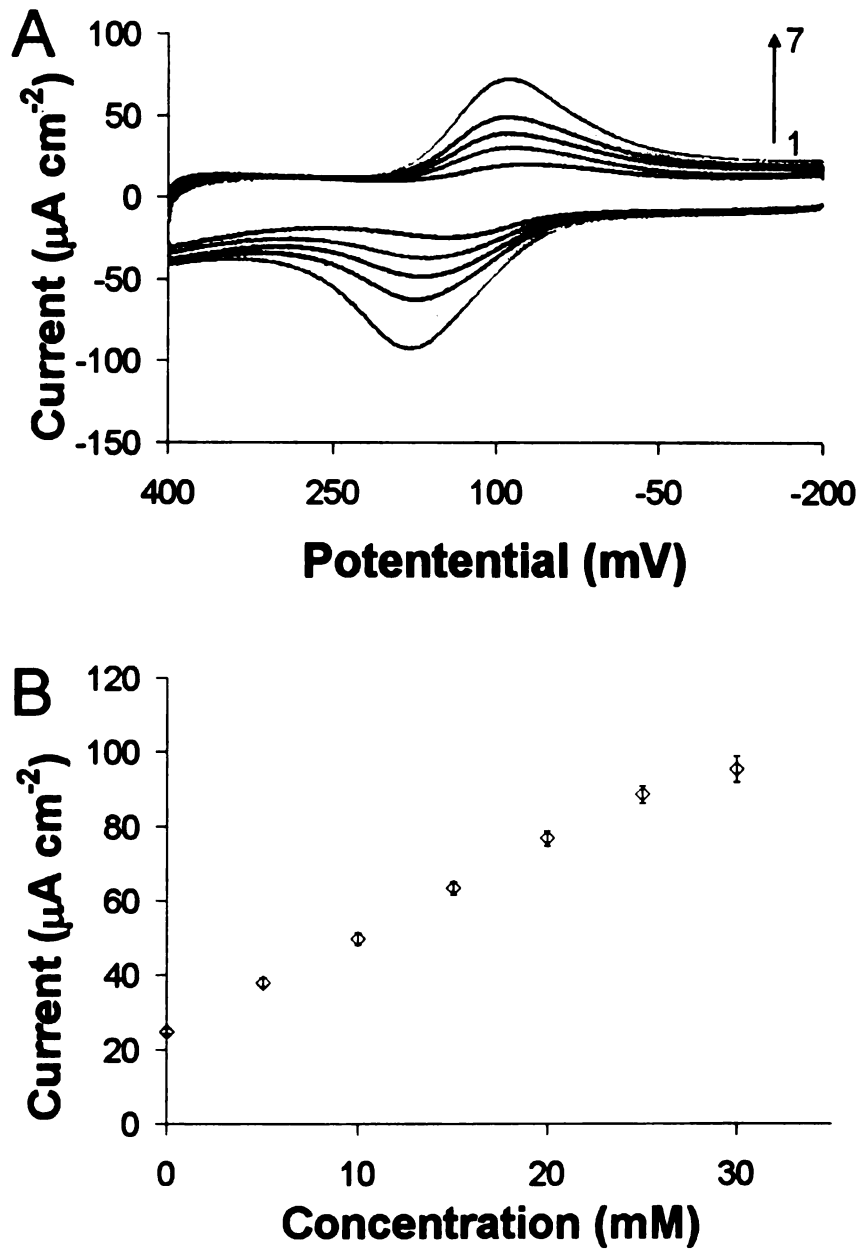

Figure 4.6: (A) Cyclic voltammograms for the Cys-TBO-NAD^+-Y218F 2^o ADH-functionalized electrode. The data were recorded in 100 mM PBS (pH 7.4) at room temperature containing (1) 0, (2) 5, (3) 10, (4) 15, (5) 20, (6) 25, and (7) 30 mM 2-propanol at a potential scan rate of 100 mV s^{-1}. (B) Peak electrocatalytic current at various 2-propanol concentrations. The error bars indicate the mean ± the standard deviation (n=3).

5. VERSATILE BIOELECTRONIC INTERFACES ON FLEXIBLE NON-CONDUCTIVE SUBSTRATES

5.1. Abstract

Bioelectronic interfaces that establish electrical communication between redox enzymes and electrodes have potential applications as biosensors, biocatalytic reactors, and biological fuel cells. These interfaces are commonly formed on gold films deposited using physical vapor deposition (PVD) or chemical vapor deposition (CVD). PVD and CVD require deposition of a primer layer, such as titanium or chromium, and require the use of expensive equipment and cannot be used on a wide range of substrates. This chapter describes a versatile new bench-top method to form bioelectronic interfaces containing a gold film, electron mediator, cofactor, and dehydrogenase enzyme [secondary alcohol dehydrogenase (2° ADH)] on nonconductive substrates such as polystyrene and glass. The method combines layer-by-layer deposition of polyelectrolytes, electroless metal deposition, and directed molecular self-assembly. The gold particles were characterized using dynamic light scattering (DLS). The gold film was characterized using field emission scanning electron microscopy (FE-SEM), field emission x-ray dispersive spectroscopy (EDS), and atomic force microscopy (AFM). Chronoamperometry and cyclic voltammetry were used to characterize the bioelectronic interfaces. Interfaces formed on flexible polystyrene slides were shown to retain their activity after bending to a radius of curvature of 18 mm, confirming that the approach can be applied on cheap and flexible substrates for applications where traditional wafer-scale electronics is not suitable, such as personal or structural health monitors and rolled microtube biosensors.

5.2. Introduction

Bioelectronic interfaces that achieve electrical communication between redox enzymes and an electrode have potential applications as biosensors (Kurita, Tabei et al. 2000; Zayats, Katz et al. 2002; Hassler and Worden 2006; Hassler, Dennis et al. 2007; Hassler, Kohli et al. 2007), biocatalysts (Park, Vieille et al. 2003), and fuel cells (Katz, Heleg-Shabtai et al. 1998; Park and Zeikus 2000; Park and Zeikus 2003). Dehydrogenase enzymes are of particular interest for bioelectronic applications because they catalyze reactions involving direct electron transfer between an electrode and the enzyme's cofactor.

For bioelectronic applications to be economically viable for a wide range of applications, facile, inexpensive methods are needed to fabricate the bioelectronic interfaces on a wide range of substrates. Traditional methods to deposit conductive gold films, such as CVD and PVD, use expensive equipment and often require deposition of primer layers, such as titanium or chromium, to improve adhesion of the gold to the substrate (Tisone and Drobek 1972). CVD and PVD are expensive, cannot be used on a wide range of substrates, and require the use of equipment not found in most labs. Electroless metal deposition is a convenient, bench-top metal-deposition technique which uses colloidal self-assembly to deposit metal nanoparticles (Supriya and Claus 2004). Seeding, the deposition of additional metal through chemical reduction of a metal salt from an aqueous solution can give a conductive metal film having electrical properties comparable to those of bulk gold film deposited using conventional methods (Brown, Lyon et al. 2000). Supriya and Claus have shown that gold can electrolessly deposit on surfaces containing -SH, $-NH_2$, and -CN-functional groups (Supriya and Claus 2004).

Layer-by-layer (LbL) assembly of polyelectrolytes provides an alternative method to deposit a conductive metal layer on a much broader range of substrates. The LBL assembly technique, introduced by Decher in 1991 (Decher and Hong 1991; Decher and Hong 1991; Decher, Hong et al. 1992), is a versatile approach based on the alternating adsorption of materials containing complementary functional groups. Polyelectrolyte multilayer (PEM) films can be formed by LbL deposition of oppositely charged poly-ion species. Recently, the assembly of PEMs has been extended to include hydrogen bonding, covalent bonding, and other weak intermolecular interactions, allowing PEMs to be assembled on virtually any surface (Hammond 2004).

This chapter describes a novel bench-top fabrication method to deposit gold, and then overlay high-performance bioelectronic interfaces containing dehydrogenase enzymes, on a variety of nonconductive surfaces. The method integrates LbL deposition of polyelectrolytes, colloidal gold deposition, and molecular self-assembly. The gold particles were characterized using DLS. The gold film was characterized using FE-SEM, EDS, and AFM. The performance of the bioelectronic interface on multiple substrates including glass, polystyrene, and Permanox® were characterized using cyclic voltammetry, and chronoamperometry. The effects of flexing on the properties of the interface were also characterized.

5.3. Materials and methods

5.3.1. Media and strains

Escherichia coli (DH5α pADH B1M1-kan) culture containing a recombinant plasmid for 2° ADH from *Thermoaneorbactor ethanolicus* was grown and purified as described in Chapter 2 (Hassler, Dennis et al. 2007).

5.3.2. Chemicals

Polystyrene and Permanox® slides were purchased from Nalge Nuc International (Rochester, NY). All other chemicals, including poly(acrylic acid) (PAA), poly(allylamine hydrochloride) (PAH), sodium citrate, tertachloroaurate(III) trihydrate ($HAuCl_4 \cdot 3\ H_2O$), hydroxylamine, cysteine (Cys), 1-ethyl-3-(3-dimethylaminopropyl) carbodiimide (EDC), n-hydroxysuccinimide (NHS), toluidine blue O (TBO), 3-carboxy phenylboronic acid (CBA), β-nicotinamide adenine dinucleotide phosphate ($NADP^+$), glutaric dialdehyde (25% in water), 2-propanol, ethanol, 2-butanol, and 2-pentanol were obtained from Sigma-Aldrich (St. Louis, MO). Ultrapure water (18.2 MΩ) was supplied by a Barnstead Nanopure-UV four-stage purifier (Barnstead International, Dubuque, IA).

5.3.3. Surface modification

5.3.3.1. Polyelectrolyte mulitlayer formation

Polystyrene, Permanox®, and glass slides were cleaned by sonication in an Alconox (New York, NY) soap solution for 20 min then treated in a Harrick plasma cleaner (Harrick Scientific Corporation, Broading Ossining, NY) for 1 min under 50 sccm flow of O_2, at a vacuum pressure of 0.15 Torr. The polystyrene slides were soaked in a 10 mM aqueous solution of PAH for 15 min and rinsed with deionized water. They were then placed in a 10 mM aqueous solution of PAA for 20 min and again rinsed with water. The slides were cleaned for 5 min in an ultrasonic bath to remove the weakly bound polyelectrolytes (Clark, Montague et al. 1997; Kidambi, Chan et al. 2004). Deposition of PAH and PAA was then alternated until 10.5 bilayers (i.e., 21 total layers) were formed, with the topmost layer being PAH.

5.3.3.2. Synthesis of colloidal gold particles

A 100 mL aqueous solution of sodium citrate (2.2 mM) was brought to a rapid boil under vigorous stirring, and 1 mL of 24 mM $HAuCl_4 \cdot 3\ H_2O$ was rapidly added. The solution was boiled for 15 min, cooled to room temperature (25±2°C), and stored at 4°C (Supriya and Claus 2004).

5.3.3.3. Formation of gold film

The PAH-modified polystyrene slides were immersed into the colloidal gold solution at room temperature for 2 h and rinsed with water. Additional gold was deposited onto the bound colloidal gold particles via chemical reduction by suspending the gold-coated slides in 200 mL aqueous solution containing 20 mM hydroxylamine and 30 mM of $HAuCl_4 \cdot 3\ H_2O$ under constant agitation for 30 min. The seeding procedure was repeated to achieve a conductive gold film. The conductivities of the polystyrene modified electrodes were measured using a digital multimeter (AM-15, Amprobe Test Tools, Everett, WA). Scheme 5.1 depicts the electrode formation process (Supriya and Claus 2004).

5.3.3.4. Interface formation

Clean gold electrodes were soaked in 100 mM Cys for 1 h at room temperature and thoroughly rinsed with water to remove weakly adsorbed Cys. The Cys-modified gold electrodes were incubated for 2 h in a 100 mM phosphate buffer solution (PBS) (pH 7.4) containing 10 mM NHS and 10 mM EDC, the EDC and NHS react with the carboxylic acid branch of the Cys forming a better leaving group on the surface of the Cys. The EDC/NHS-modified electrode was then reacted with the amine branch of TBO (1 mM TBO) resulting in the formation of an amide linkage between the TBO and the carboxylic group of the Cys (Cys-TBO). A 5 mM CBA solution was activated at room

temperature with 10 mM NHS and 5 10 mM EDC in 100 mM PBS for 2 h. The activated CBA was then reacted with the Cys-TBO-modified electrodes for 1 h at room temperature and rinsed with deionized water to remove weakly adsorbed CBA. The resulting Cys-TBO-CBA-modified electrodes were reacted with a 1 mM solution of $NADP^+$ in 100 mM PBS for 1 h and then washed with water to remove any weakly bound cofactor resulting in a gold electrode functionalized with Cys, TBO, and $NADP^+$ (Cys-TBO-$NADP^+$). The Cys-TBO-$NADP^+$ functionalized gold electrodes were reacted with a 4.4 mg mL^{-1} solution of 2° ADH in 100 mM PBS for 1 h and then cross-linked with 25% (v/v) glutaric dialdehyde in water for 20 min. Electrodes fabricated on Permanox® and glass slides were fabricated in the manner described above, replacing polystyrene.

5.3.4. Electrochemical measurements

Chronoamperometry and cyclic voltammetry were performed as described in Chapter 2 using an electrochemical analyzer (CHI660B, CH Instruments).

5.3.5. Surface characterization

5.3.5.1. Particle size analysis

The sizes and size distributions of the gold nanoparticles were determined on a 90Plus/BI-MAS (Brookhaven Instruments, Holtsville, NY) photon correlation spectrophotometer with a BI-9000AT digital correlator. The instrument was equipped with a 15 mW solid state laser (Lasermax Inc., Rochester, NY) that was used at a wavelength of 660 nm. Dust-free solution vials were used for the aqueous gold solutions, and measurements were performed at an angle of 90° at room temperature. The Non-negative least squared algorithm was used to analyze the DLS data.

5.3.5.2. Scanning Electron Microscopy

The gold films were imaged using a JEOL (Japan Electronic Optics Laboratories, Peabody, MA) JSM-6400 FE-SEM operating at 5 kV. Analysis of the film composition was found using a LaB6 emitter (Noran EDS, Boston, MA) connected to a JEOL JSM-6400 SEM.

5.4. Results

5.4.1. Characterization of gold film

Figure 5.1 depicts gold film growth on polyelectrolyte multilayers as examined by FE-SEM. Figure 5.1A shows the colloidal gold particles attached to the PAH-modified polystyrene, where the spherical gold particles are visible. The size of the gold nanoparticles is consistent with the size obtained by DLS (10.1±3.1 nm) suggesting that a single gold nanoparticle is adsorbed on the surface of the polystyrene. Seeding for 30 min induced growth of the gold particles (Figure 5.1B). Seeding the layer a second time led to the formation of a densely packed, electrically conductive film (Figure 5.1C). The addition of gold to the surface was confirmed by the Au peaks in the EDS plot (Figure 5.1D).

5.4.2. Electrochemical characterization

5.4.2.1. Polystyrene-modified electrodes

Figure 5.2A shows the cyclic voltammograms at different times of 2° ADH adsorption on a Cys-TBO-$NADP^+$-modified polystyrene electrode obtained at a constant 2-propanol concentration (25 mM) in 100 mM PBS at room temperature. Figure 5.2B shows the peak anodic current as a function of adsorption time. The pseudo-first-order adsorption time constant (τ_{PS}) derived from the data was 43.8±1.0 min. The value of τ_{PS}

consistent with τ_{Cys} (49.2±1.0 min) suggesting that the enzyme adsorption kinetics are independent of the underlying substate.

Figure 5.3 shows the chronoamperometric response for the Cys-TBO-$NADP^+$-modified polystyrene electrode in 100 mM PBS containing 25 mM 2-propanol at room temperature. Fitting Eqs. 2.1 and 2.3 to the chronoamperometric data gave values for the an electron transfer rate constant (k_{et}) and an apparent enzymatic surface coverage (Γ_{enz}) of 130.0±5.4 s^{-1} and 5.6±0.1×10^{-11} mol cm^{-2}, respectively. The measured Γ_{enz} is twice that measured for the Cys-TBO-$NADP^+$-2° ADH-modified gold coated silicon wafer (2.6±0.1×10^{-11} mol cm^{-2}) (Hassler, Dennis et al. 2007). Figure 5.4A shows the cyclic voltammograms of the Cys-TBO-$NADP^+$-modified polystyrene electrode at various 2-propanpol concentrations in 100 mM PBS at room temperature. The peak anoidic current increased linearly with 2-propanol concentration (Figure 5.4B) below 30 mM, with a slope of 7.5±0.1 μA mM^{-1} cm^{-2} which is a measure of the biosensor's sensitivity. At 2-propanol concentrations above 30 mM, the anodic current reached a saturation current (I_{cat}^{sat}) of 237.5±6.0 μA cm^{-2}. The I_{cat}^{sat} and sensitivity values are nearly twice that measured for a Cys-TBO-$NADP^+$-2° ADH-modified gold coated silicon wafer (3.8±0.1 μA mM^{-1} cm^{-2} and 129.0±3.0 μA cm^{-2}, respectively) (Hassler, Dennis et al. 2007). The TR_{max} (19.3±0.7 s^{-1}) is comparable to the Cys-TBO-$NADP^+$-2° ADH-modified electrode (19.8±1.1 s^{-1}) (Hassler, Dennis et al. 2007) suggesting the activity of the 2° ADH is unaffected by the presence of the electrolessly deposited gold.

The selectivity of the Cys-TBO-$NADP^+$-2° ADH-modified polystyrene electrode was examined by testing alternative substrates. Table 5.1 shows the values of I_{cat}^{sat}, sensitivity, and TR_{max} for the Cys-TBO-$NADP^+$-2° ADH-modified polystyrene electrode in the presence of 2-propanol, ethanol, 2-butanol, and pentanol. These data are consistent with the literature values for 2° ADH (Burdette, Secundo et al. 1997). These data are consitent with literature values for 2° ADH (Burdette and Zeikus 1994; Burdette, Secundo et al. 1997).

To determine whether the bioelectronic activity of the interface was stable after flexing, the Cys-TBO-$NADP^+$-2° ADH-modified polystyrene electrode was flexed to a radius of curvature of 18 mm, returned to its original shape, and then performance properties were measured (Table 5.2). The values of Γ_{enz}, k_{et}, I_{cat}^{sat}, sensitivity, and TR_{max} values after flexing were virtually identical to those for the Cys-TBO-$NADP^+$-2° ADH-modified polystyrene electrode before flexing, suggesting the interface could be flexed without any loss in performance.

5.4.2.2. Permanox®-modified electrodes

Figure 5.5 shows the chronoamperometric response for the Cys-TBO-$NADP^+$-2° ADH-modified Permanox® electrode. Fitting Eqs. 2.1 and 2.3 to the chronoamperometric data gave k_{et} and Γ_{enz} values of 107.4±8.7 s^{-1} and 5.8±0.4×10^{-11} mol cm^{-2}, respectively. Figure 5.6A shows the cyclic voltammograms for the Cys-TBO-$NADP^+$-2° ADH-modified Permanox® electrode at various 2-propanpol concentrations in 100 mM PBS at room temperature. The peak anoidic current increased linearly with 2-propanol

concentration (Figure 5.6B) below 30 mM, with a slope of 4.2±0.1 μA mM^{-1} cm^{-2} which is a measure of the biosensor's sensitivity. At 2-propanol concentrations above 30 mM, the anodic current reached an I_{cat}^{sat} value of 139.4±0.7 μA cm^{-2}. The TR_{max} was calculated to be 9.7±0.8 s^{-1} using Eq. 2.4. The values of k_{et}, Γ_{enz}, sensitivity, I_{cat}^{sat}, and TR_{max} for the Cys-TBO-$NADP^+$-2° ADH-modified Permanox® interface were approximetly half the values of then Cys-TBO-$NADP^+$-2° ADH-modified polystyrene electrode (130.0±5.4 s^{-1}, 5.6±0.1×10^{-11} mol cm^{-2}, 7.5±0.1 μA mM^{-1} cm^{-2}, 237.5±6.0 μA cm^{-2}, and 19.3±0.7 s^{-1}, respectively).

5.4.2.3. Glass-modified electrodes

Figure 5.7 shows the chronoamperometric response of the Cys-TBO-$NADP^+$-2° ADH-modified glass electrode. Fitting Eqs. 2.1 and 2.3 to the chronoamperometric data gave k_{et} and Γ_{enz} values of 98.8±5.0 s^{-1} and 5.5±0.9×10^{-11} mol cm^{-2}, respectively. Figure 5.8A shows the cyclic voltammograms for the Cys-TBO-$NADP^+$-2° ADH-modified glass electrode at various 2-propanpol concentrations in 100 mM PBS at room temperature. The peak anoidic current increased linearly with 2-propanol concentration (Figure 5.BB) below 30 mM, with a slope of 3.1±0.1 μA mM^{-1} cm^{-2} which is a measure of the biosensor's sensitivity. At 2-propanol concentrations above 30 mM, the anodic current reached an I_{cat}^{sat} value of 118.4±3.4 μA cm^{-2}. The value for TR_{max} was calculated to be 7.6±1.3 s^{-1} using Eq. 2.4. The values of k_{et}, Γ_{enz}, sensitivity, I_{cat}^{sat}, and TR_{max} for the Cys-TBO-$NADP^+$-2° ADH-modified Glass are lower then Cys-TBO-$NADP^+$-2° ADH-

modified polystyrene electrode (130.0±5.4 s^{-1}, 5.6±0.1×10^{-11} mol cm^{-2}, 7.5±0.1 μA mM^{-1} cm^{-2}, 237.5±6.0 μA cm^{-2}, and 19.3±0.7 s^{-1}, respectively).

5.5. Discussion

Bioelectronic interfaces are commonly formed on gold films deposited using either PVD or CVD, these techniques require the deposition of a primer layer of titanium or chromium, to improve adhesion of the gold to the substrate (Tisone and Drobek 1972). The deposition of a primer layer is expensive and requires the use of equipment not found in most labs. Polyelectrolyte multilayers were deposited on glass, polystyrene, and Permanox® using the LbL-deposition technique. The deposition of gold was confirmed by FE-SEM and EDS. The bench-top fabrication technique eliminates the requirement of primer layer and expensive equipment, making the deposition of gold on any surface more cost effective.

Chronoamperometry and cyclic voltammetry confirm that the fabrication of bioelectronic interfaces on virtually any surface. The sensitivity of the bioelectronic interface formed using electroless deposition of gold on polystyrene (7.5±0.1 μA mM^{-1} cm^{-2}) is higher than that for the PVD deposited gold (3.8±0.1 μA mM^{-1} cm^{-2}). The increase in the sensivity has potential applications for this interface include personal structural health monitors, biosensors inside microfluidic devices, biofuel cells, and high density biosensor arrays. The bioelectronic interface formed on polystyrene retained its activity after being flexed to a radius of curvature of 18 mm. The deposition of polyelectrolytes and colloidal gold can be expanded to fabricate bioelectronic interfaces on more flexible and thinner substrates applicable for rolled microtube biosensors (Li, Han et al. 2007).

The work on the fabrication of bioelectronic interfaces on non-conductive substrtates has been focused on the use of gold colloidal self-assembly. The work could be extended to the use of other metals including silver, copper, platinum, and palladium. It is believed that interfaces containing different metals would exhibit similar characteristics.

5.6. Conclusions

This study introduces a facile, benchtop method to fabricate mediated bioelectronic interfaces containing dehydrogenase enzymes on flexible and non-conductive substrates. The method uses LbL assembly of polyelectrolytes along with colloidal self-assembly of gold nanoparticles to form a conductive gold film without the need for expensive equipment or the use of primers. A film containing an electron mediator, cofactor, and dehydrogenase enzyme is then deposited that achieves efficient electron transfer between the gold film and the enzyme. This interface retains its activity after being flexed to a radius of curvature of 18 mm. This versatile approach greatly extends the range of substrates that can be used in bioelectronic applications. Bioelectronic interfaces formed on polystyrene exhibited a higher peak current and sensitivity than those formed on glass, Permanox®, and a gold coated silicon wafer.

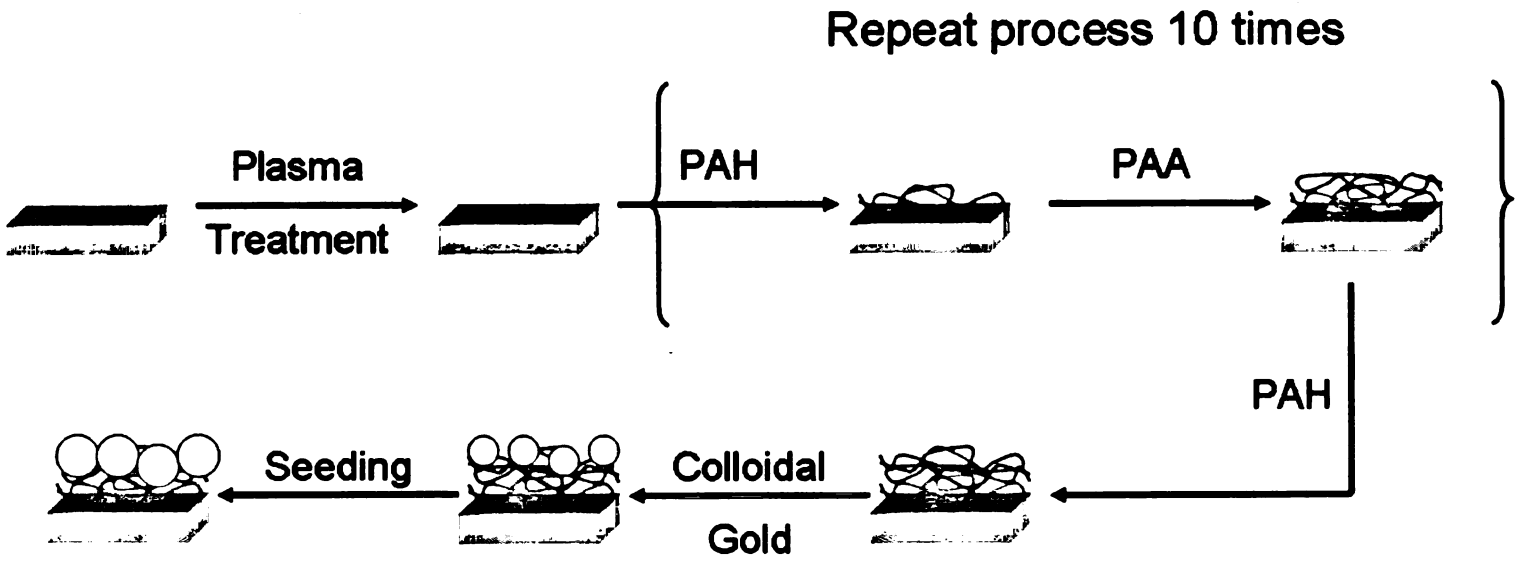

Scheme 5.1: Schematic of process used to deposit gold on the PEM-modified polystyrene substrate.

Table 5.1: Selectivity of the Cys-TBO-$NADP^+$-2°ADH-modified gold coated polystyrene electrode to the substrates 2-propanol, ethanol, 2-butanol, and 2-pentanol

Compound	I_{cat}^{sat} ($\mu A\ cm^{-2}$)	Sensitivity ($\mu A\ mM^{-1}\ cm^{-2}$)	TR_{max} (s^{-1})
2-propanol	237.5±6.0	7.5±0.1	19.2±0.7
Ethanol	138.0±7.3	4.4±0.4	10.7±1.1
2-Butanol	116.3±2.1	3.6±0.1	8.2±0.4
2-Pentanol	113.6±8.0	3.7±0.1	8.4±0.8

Table 5.2: Comparison of performance of the Cys-TBO-$NADP^{+}$-2^{o} ADH-modified gold coated polystyrene electrode before and after flexing to a radius of curvature of 18 mm.

	Γ_{enz} ($\times 10^{-11}$ mol cm^{-2})	k_{et} (s^{-1})	I_{cat}^{sat} ($\mu A\ cm^{-2}$)	Sensitivity ($\mu A\ mM^{-1}\ cm^{-2}$)	TR_{max} (s^{-1})
Before Bending	5.6±0.1	130.0±5.4	237.5±6.0	7.5±0.1	19.2±0.7
After Bending	5.6±0.0	128.2±2.0	231.1±5.5	7.4±0.3	18.0±0.6

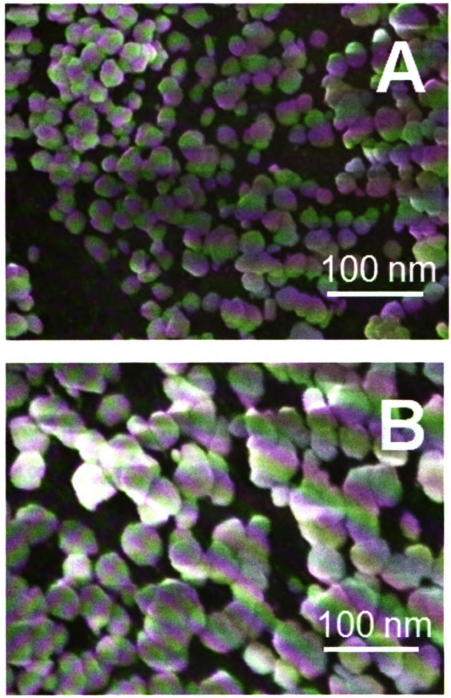

Figure 5.1: FE-SEM images showing the growth of gold film on PEM: (A) after deposition of the colloidal particles, (B) after seeding with $HAuCl_4 \cdot 3\ H_2O$, (C) after seeding twice with $HAuCl_4 \cdot 3\ H_2O$, (D) field emission X-ray dispersive spectroscopy analysis of the electrolessly deposited gold film on the PEM film. All scale bars are 100 nm.

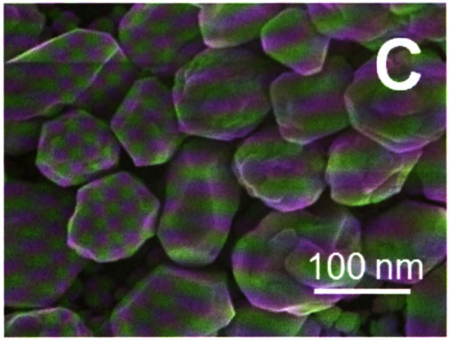

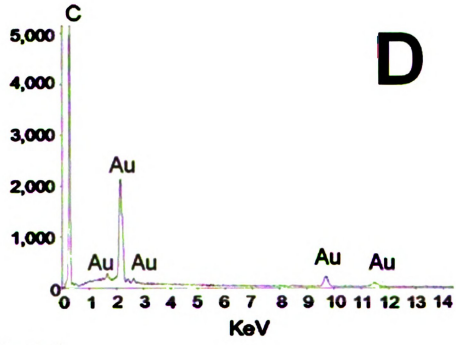

Figure 5.1 continued.

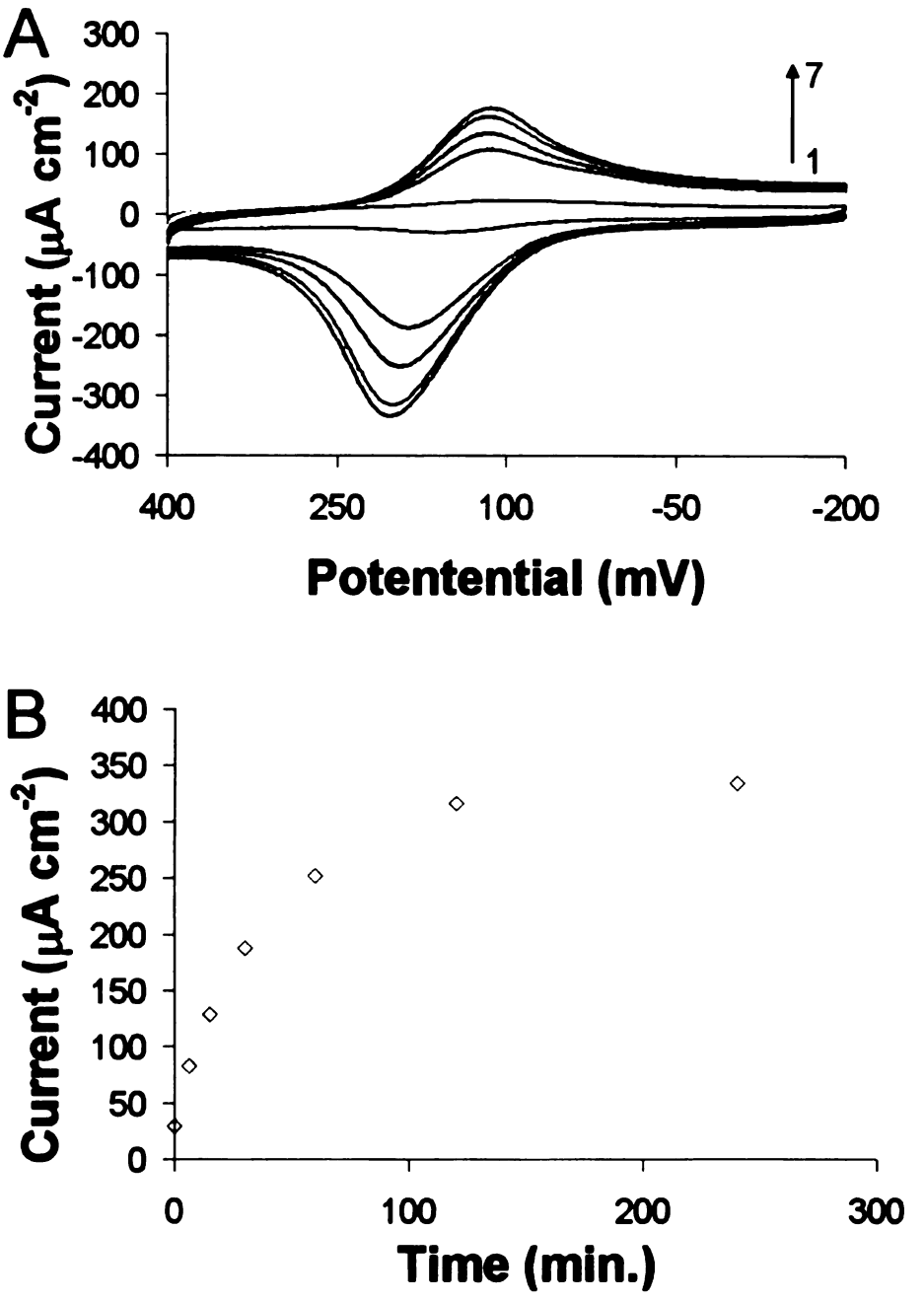

Figure 5.2: (A) Cyclic voltammograms of the Cys-TBO-$NADP^+$-functionalized gold coated polystyrene electrode following various times of 2^o ADH adsorption: (1) 0, (2) 6, (3) 15, (4) 30, (5) 60, (6) 120, and (7) 240 min. The data were recorded in room-temperature 100 mM PBS (pH 7.4) containing 25 mM 2-propanol, at a potential scan rate of 100 mV s^{-1}. (B) Peak electrocatalytic current vs. time of adsorption.

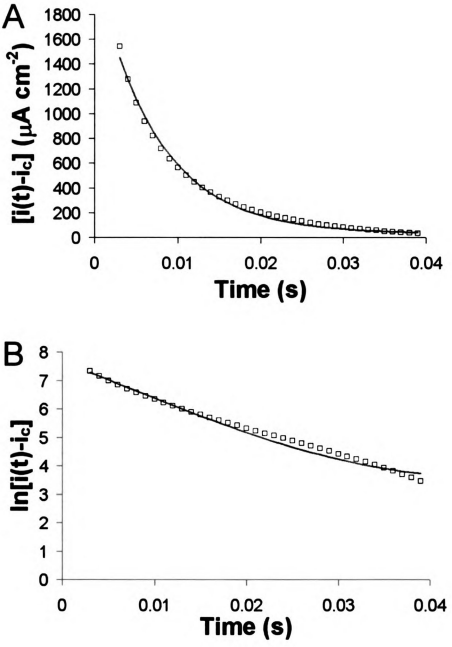

Figure 5.3: (A) Current transient for a potential step from -200 mV to 400 mV for a Cys-TBO-$NADP^+$-2° ADH-functionalized gold coated polystyrene in 100 mM PBS (pH 7.4) containing 25 mM 2-propanol at room temperature. (B) Shows the plots of $\log[i(t)-i_C]$ after double layer charging. The solid line represents the curve of best fit to the data.

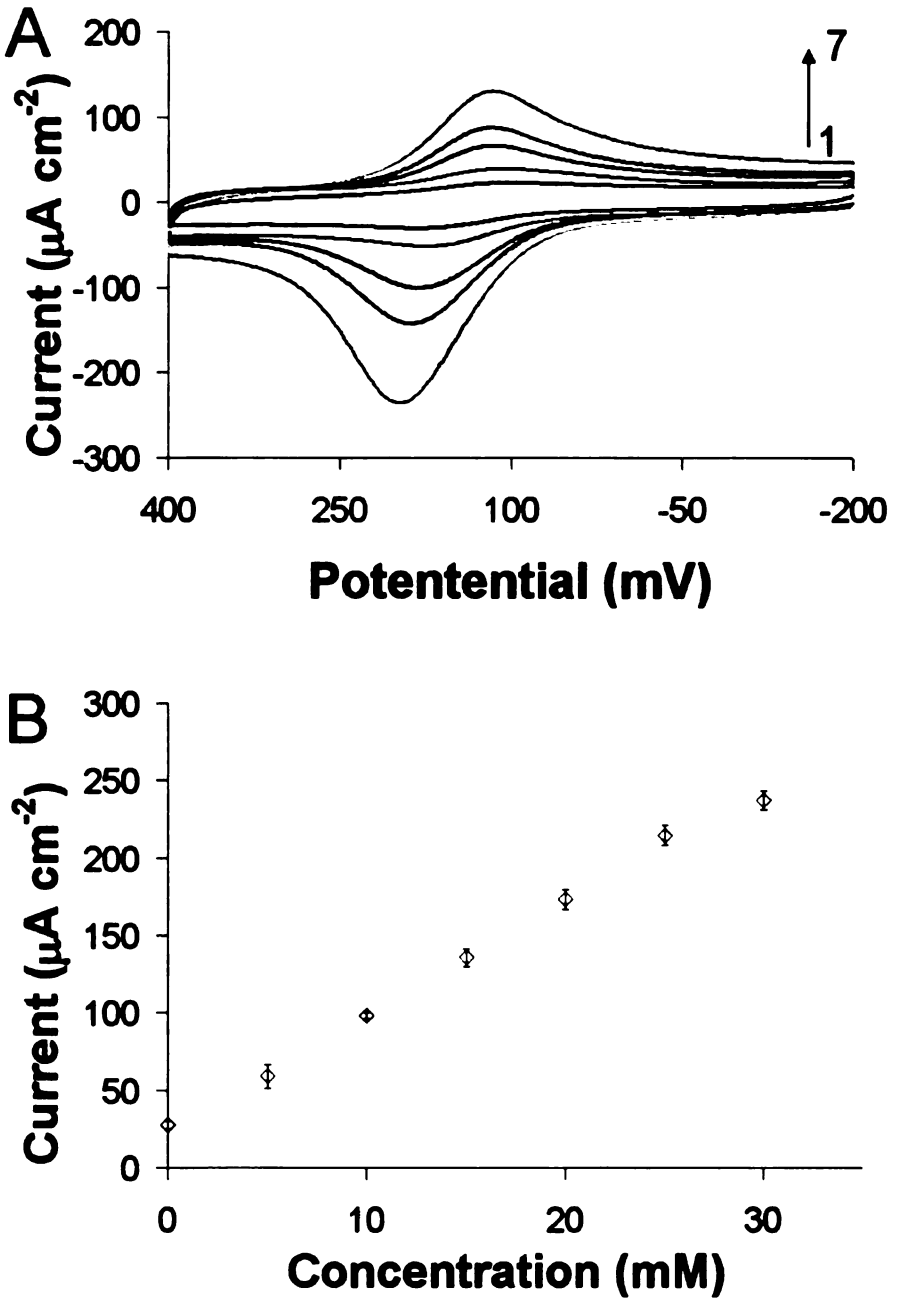

Figure 5.4: (A) Cyclic voltammograms for the Cys-TBO-$NADP^+$-2^o ADH-functionalized gold coated polystyrene electrode. The data were recorded in 100 mM PBS (pH 7.4) at room temperature containing (1) 0, (2) 5, (3) 10, (4) 15, (5) 20, (6) 25, and (7) 30 mM 2-propanol at a potential scan rate of 100 mV s^{-1}. (B) Peak electrocatalytic current at various 2-propanol concentrations. The error bars indicate the mean ± the standard deviation (n=3).

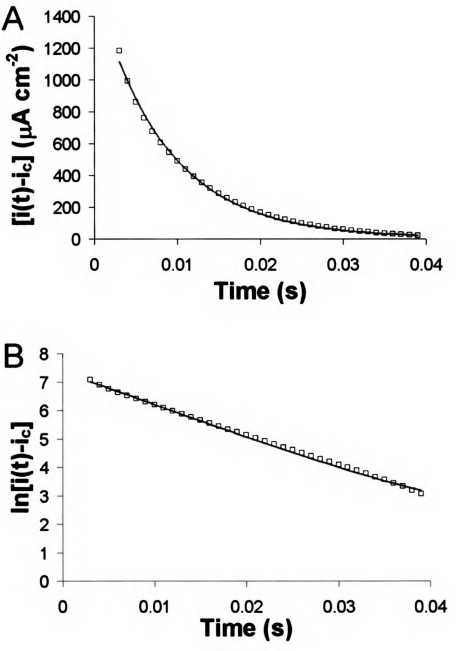

Figure 5.5: (A) Current transient for a potential step from -200 mV to 400 mV for a Cys-TBO-$NADP^+$-2^o ADH-functionalized gold coated Permanox® in 100 mM PBS (pH 7.4) containing 25 mM 2-propanol at room temperature. (B) Shows the plots of $\log[i(t)-i_C]$ after double layer charging. The solid line represents the curve of best fit to the data.

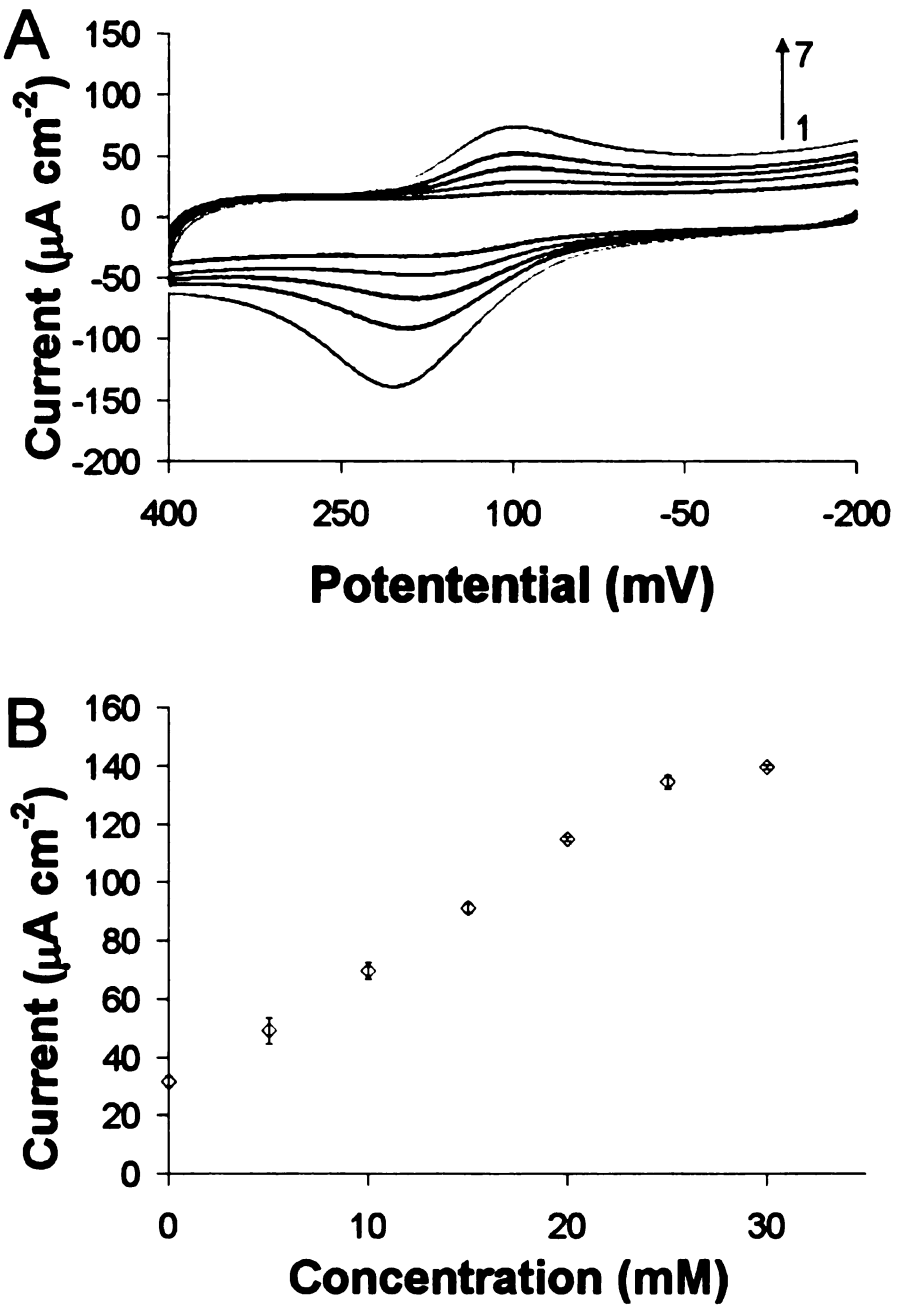

Figure 5.6: (A) Cyclic voltammograms for the Cys-TBO-$NADP^+$-2^o ADH-functionalized gold coated Permanox® electrode. The data were recorded in 100 mM PBS (pH 7.4) at room temperature containing (1) 0, (2) 5, (3) 10, (4) 15, (5) 20, (6) 25, and (7) 30 mM 2-propanol at a potential scan rate of 100 mV s^{-1}. (B) Peak electrocatalytic current at various 2-propanol concentrations. The error bars indicate the mean ± the standard deviation (n=3).

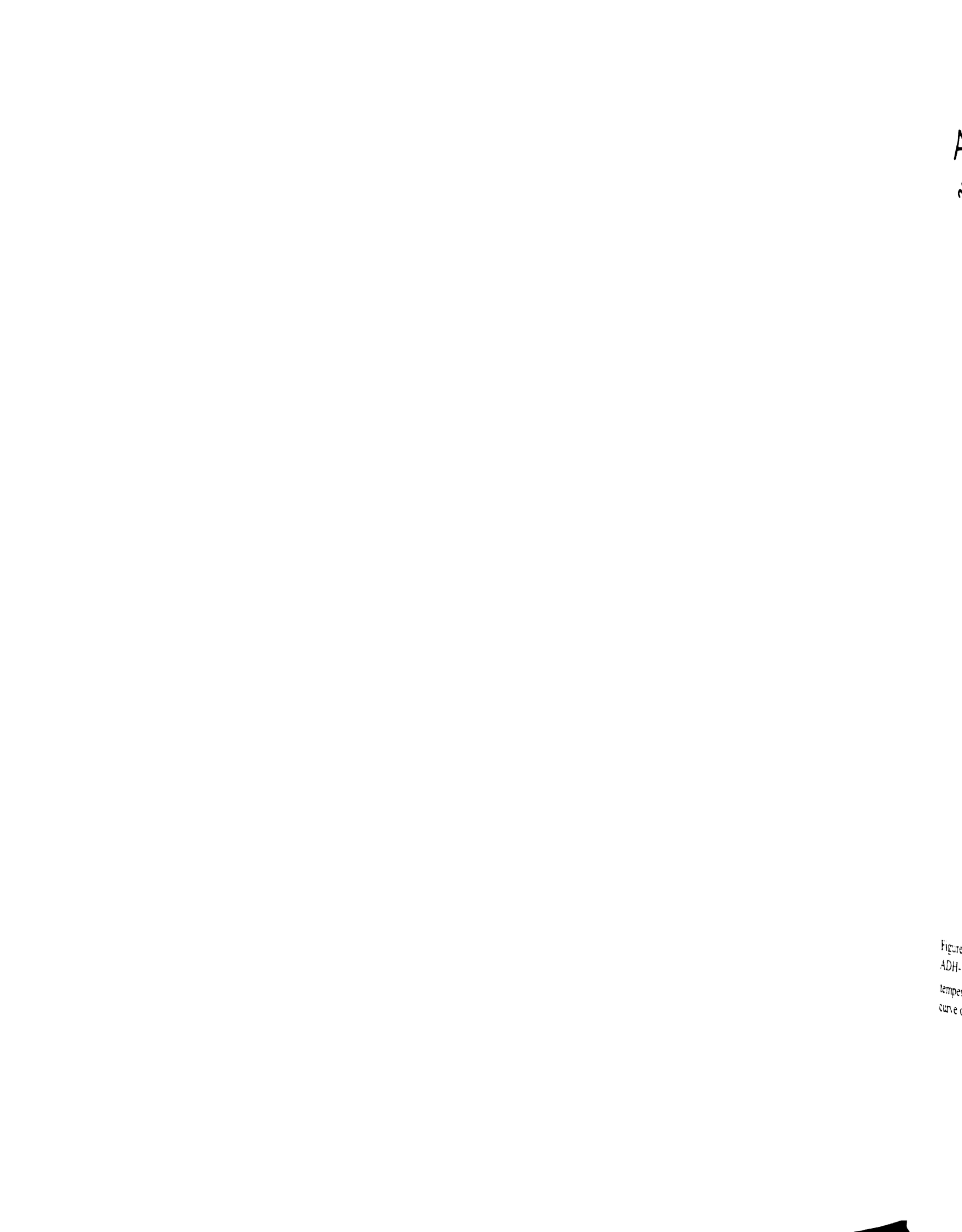

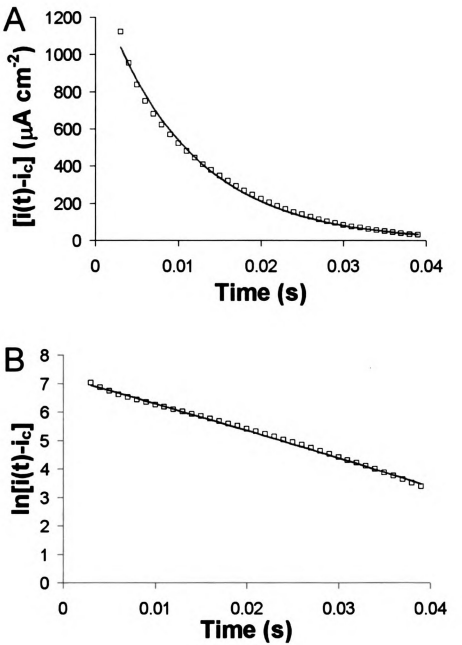

Figure 5.7: (A) Current transient for a potential step from -200 mV to 400 mV for a Cys-TBO-$NADP^{+}$-2^{O} ADH-functionalized gold coated glass in 100 mM PBS (pH 7.4) containing 25 mM 2-propanol at room temperature. (B) Shows the plots of $\log[i(t)-i_c]$ after double layer charging. The solid line represents the curve of best fit to the data.

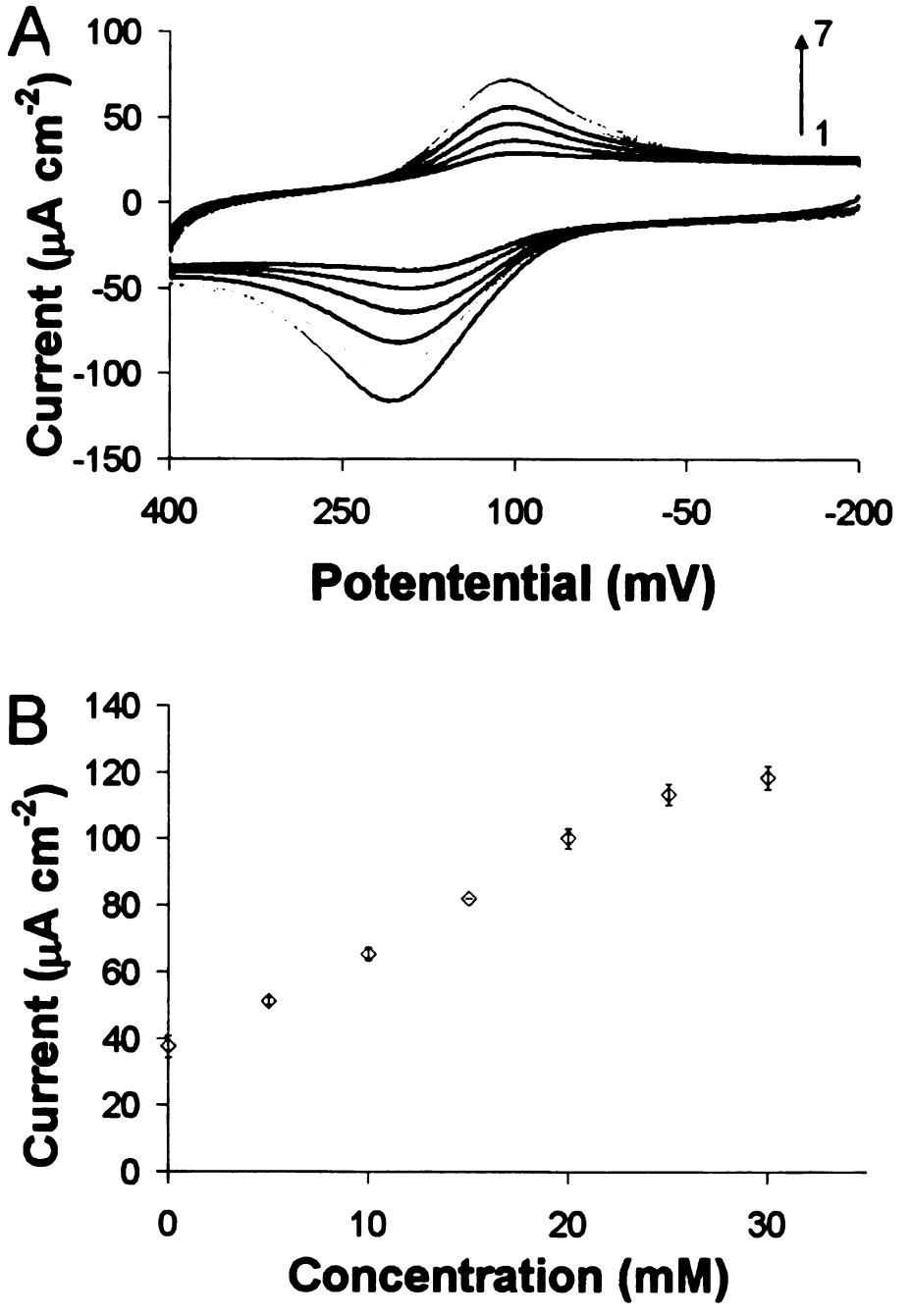

Figure 5.8: (A) Cyclic voltammograms for the Cys-TBO-$NADP^+$-2^o ADH-functionalized gold coated glass electrode. The data were recorded in 100 mM PBS (pH 7.4) at room temperature containing (1) 0, (2) 5, (3) 10, (4) 15, (5) 20, (6) 25, and (7) 30 mM 2-propanol at a potential scan rate of 100 mV s^{-1}. (B) Peak electrocatalytic current at various 2-propanol concentrations. The error bars indicate the mean ± the standard deviation (n=3).

6. RENEWABLE DEHYDROGENASE BASED INTERFACES FOR BIOELECTRONIC APPLICATIONS

6.1. Abstract

Bioelectronic interfaces that establish electrical communication between redox enzymes and electrodes have potential applications as biosensors, biocatalytic reactors, and biological fuel cells. However, these interfaces contain labile components (enzymes and cofactor) have limited lifetimes and must be replaced periodically to allow long-term operation. Current fabrication methods do not allow facile replacement of these components, thus limiting the useful lifetime of the interfaces. This chapter describes a versatile new fabrication approach that binds the enzymes and cofactors using reversible ionic interactions. This approach allows the interface to be removed *via* a simple pH change, and then replaced to fully regenerate the biocatalytic activity. Positively charged polyelectrolytes, poly(ethyleneimine) (PEI) and poly(allylamine hydrochloride) (PAH), were used to ionically bond a dehydrogenase enzyme and its cofactor to a gold electrode functionalized with 3-mercaptopropionic acid and the electron mediator toluidine blue O (TBO). By reducing the pH, the surface bound 3-mercaptopropionic acid (MPA) was protonated, disrupting the ionic bonds and releasing the enzyme-modified polyelectrolyte. After neutralization, fresh enzyme and cofactor were bound, regenerating the bioelectronic interface. Cyclic voltammetry, chronoamperometry, electrochemical impedance spectroscopy (EIS), and Fourier transform infrared spectroscopy (FTIR) analysis were used to characterize the bioelectronic interfaces. The reconstituted interface exhibited the similar surface coverage, electron transfer coefficient, and turnover rate as the original interface.

6.2. Introduction

Bioelectronic interfaces achieve electrical communication between redox enzymes and an electrode (Armstrong, Heering et al. 1997; Park, Laivenieks et al. 1999; Park and Zeikus 1999; Armstrong and Wilson 2000; Chen, Barton et al. 2001). Development of a bioelectronic interface is especially challenging for cofactor-dependent dehydrogenase enzymes, whose activity requires the presence of an electron carrying cofactor [e.g., β-nicotinamide adenine dinucleotide phosphate ($NADP^+$)] in the Rossmann fold of the enzyme. The cofactor transmits electrons between the electrode and the enzyme. Direct electron transfer between the cofactor and electrode is not kinetically favored, requiring the use of high overpotentials (Blaedel and Jenkins 1975; Schmakel, Santhanam et al. 1975) which may lead to cofactor degradation (Park, Laivenieks et al. 1999; Ramesh, Sivakumar et al. 2003). These problems can be circumvented by using an electron mediator to shuttle electrons between the electrode and cofactor at moderate potentials (Ozdemir and Tuncel 2000; Senel, Camli et al. 2002). Several approaches have been used to achieve mediated electron exchange, including immobilization of the enzymes in conductive polymers (Emr and Yacynych 1995; Chen, Barton et al. 2001) and redox relays that conduct electrons between the enzyme and electrode (Degani and Heller 1987; Zimmermann, Lindgren et al. 2000).

To achieve electron transfer, the mediator, cofactor, and enzyme were bound directly to the surface of the electrode (Zayats, Katz et al. 2002; Hassler and Worden 2006; Willner, Katz et al. 2006; Hassler, Dennis et al. 2007). This arrangement allowed unimpeded access of the cofactor to its binding site on the enzyme, provided efficient, multistep electron transfer, and prevented component loss due to diffusion. However,

many enzymes and cofactors have limited useful lifetimes, due to natural degradation processes (Burdette, Tchernajencko et al. 2000; Wang, Feng et al. 2003; De Temino, Hartmeier et al. 2005). The abovementioned interface fabrication methods involve covalent linkages and make no provision for removal and replacement of degraded components. For long-term operation, new interface-assembly methods must be developed that allow facile removal and replacement of the cofactor and enzyme.

Layer-by-layer (LbL) deposition provides a mechanism by which target molecules can be reversibly bound to an interface and later released (Wu, Guan et al. 2002; Yun, Song et al. 2005). Electrostatic attractions allow alternating layers of oppositely charged polyelectrolytes to be sequentially adsorbed onto virtually any surface (Decher and Hong 1991; Decher and Hong 1991; Decher, Hong et al. 1992). The resulting polyelectrolyte multilayers (PEMs) provide effective and economical organic thin films that have been extended to organic dyes (Masadome and Imato 2003; Qian, Suo et al. 2004), colloids (Lvov and Caruso 2001), cells (Berg, Yang et al. 2004; Kidambi, Lee et al. 2004), and biomaterials (Ai, Fang et al. 2002; Ai, Ihlemann et al. 2002). Proteins, including catalase (Shi, Lu et al. 2003; Wang and Caruso 2005; Shutava, Kommireddy et al. 2006), glucose oxidase (Antipov and Sukhorukov 2004; Zhao, Xu et al. 2005; Shutava, Kommireddy et al. 2006), and polyphenol oxidase (Forzani, Teijelo et al. 2003; Coche-Guerente, Desbrieres et al. 2005) have been incorporated into LbL films. However, dehydrogenase enzymes and their cofactors have yet to be incorporated.

This chapter presents a novel method based on LbL self assembly to fabricate a renewable bioelectronic interface in which the enzyme and cofactor can be removed and replaced. PEI and PAH were used to couple the electron mediator, cofactor, and enzyme

to a carboxylic-acid-modified gold electrode in such a way that mediated electron transfer was achieved. Decreasing the pH of the solution protonated the surface-bound carboxylic acid groups disrupting the ionic bonds and releasing the enzyme and cofactor. After neutralization, fresh enzyme and cofactor could be bound, allowing the interface to be reconstituted. Chronoamperometry, cyclic voltammetry, EIS, FTIR were used to characterize the interface. The original and reconstituted interfaces exhibited similar electrochemical properties.

6.3. Materials and methods

6.3.1. Media and strains

Escherichia coli (DH5α pADH B1M1-kan) culture containing a recombinant plasmid for 2° ADH from *Thermoaneorbactor ethanolicus* was grown, and purified as described in Chapter 2 (Hassler, Dennis et al. 2007).

6.3.2. Chemicals

1-ethyl-3-(3-dimethylaminopropyl) carbodiimide (EDC), 3-mercaptopropanoic acid (MPA), n-hydroxysuccinimide (NHS), TBO, PAH, PEI, 3-carboxy phenylboronic acid (CBA), $NADP^+$, glutaric dialdehyde (25% in water), 2-propanol, ethanol, 2-butanol, and 2-pentanol were obtained from Sigma-Aldrich (St. Louis, MO). Ultrapure water (18.2 MΩ) was supplied by a Barnstead Nanopure-UV four-stage purifier (Barnstead International, Dubuque, IA).

6.3.3. Interface formation

Cleaned gold electrodes were soaked in a 100 mM MPA solution in ethanol for 1 hr at room temperature (25±2°C) and thoroughly rinsed with ethanol and deionized water to remove weakly adsorbed MPA. The MPA-modified gold electrodes were incubated for 2 h in a 100 mM phosphate buffer solution (PBS) (pH 7.4) containing 10 mM NHS and

10 mM EDC, the EDC and NHS react with the carboxylic acid branch of the MPA forming a better leaving group on the surface of the Cys. The EDC/NHS-modified electrode was then reacted with the amine branch of TBO (1 mM TBO) resulting in the formation of an amide linkage between the TBO and the carboxylic group of the MPA (MPA-TBO). The MPA-TBO-modified electrodes were soaked in a 10 mM aqueous solution of PEI solution containing 100 mM NaCl (pH 7.0) forming a MPA-TBO-PEI-modified interface. It is proposed that the PEI adsorbs to the MPA-TBO-modified electrode through electrostatic interactions between the unreacted MPA and hydrophobic interactions with the TBO-modified interface. A 5 mM aqueous solution of CBA solution was activated at room temperature in the presence of 2 mM NHS and 2 mM EDC in 100 mM PBS for 2 h. The NHS-modified CBA was then reacted with the MPA-TBO-PEI-functionalized electrodes for 1 h at room temperature, resulting in an ester linkage between the CBA and the amine group of the PEI. The resulting MPA-TBO-PEI-CBA-modified electrodes were reacted with a 1 mM solution of $NADP^+$ in 100 mM PBS for 1 h and then washed with water. The MPA-TBO-PEI-$NADP^+$-functionalized gold electrodes were reacted with a 4.4 mg mL^{-1} solution of 2° ADH in 100 mM PBS for 1 h at room temperature and cross-linked with 25% (v/v) glutaric acid in water for 20 min. Scheme 6.1 illustrates the steps involved in functionalizing the electrode with MPA, TBO, PEI, $NADP^+$, and 2° ADH. The resulting 2° ADH-modified electrode was used for the biocatalytic oxidation of 2-propanol. Electrodes containing different polyelectrolytes (PAH) were fabricated in the manner described above, replacing PEI.

The cofactor and enzyme-functionalized PEI layer was removed by incubating the electrode in 10 mM HCl (pH 2.0) for 30 min. For values below the pKa of MPA

(pKa~4.3), the carboxylic acid group is protonated, thus decreasing the electrostatic interaction between the surface bound MPA and the 2° ADH-modified PEI and allowing the PEI to disengage from the surface. To reassemble the interface PEI, CBA, $NADP^+$, and 2° ADH were reattached onto the TBO-modified MPA monolayer using the protocol described above.

6.3.4. Electrochemical measurements

Cyclic voltammetry, chronoamperometry, and EIS were performed as described in Chapter 2 using an electrochemical analyzer (CHI660B, CH Instruments).

6.3.5. Surface characterization techniques

FTIR was performed with a Nicolet Magna 560 FTIR spectrometer using a PIKE grazing angle (80°) attachment. A background spectrum of each uncoated electrode was obtained prior to electrode modification.

6.4. Results

6.4.1. Interface formation

Figure 6.1 shows the FTIR spectra for gold electrodes modified with (A) MPA, (B) MPA-TBO, (C) MPA-TBO-PEI-$NADP^+$-2° ADH, respectively. Figure 6.1D shows the FTIR spectrum after the MPA-TBO-PEI-$NADP^+$ modified electrode was washed with 10 mM HCl, and Figure 6.1E shows the fully reconstituted MPA-TBO-PEI-$NADP^+$-2° ADH interface. The MPA-modified electrode (Figure 6.1A) shows peaks at 1710 and 1420 cm^{-1} corresponding to the stretching mode of the carboxylic acid group (C=O) vibration and C-H bend symmetric, respectively, confirming MPA adsorption to the electrode surface (Ihs and Liedberg 1991). The MPA-TBO-modified electrode (Figure 6.1B) shows absorption peaks at 1626 and 1450 cm^{-1}, which correspond to the amide I'

(C=O) stretching and amide II' (N-H) bending (Meersman, Wang et al. 2005), respectively, suggesting that MPA and TBO are linked by an amide bond. The MPA-TBO-$NADP^+$-2° ADH-modified electrode (Figure 6.1C) shows peaks at 1655 and 1540 cm^{-1}, corresponding to the carboxylic acid (C=O) vibration and amine (N-H) bending, respectively. These peaks are consistent with enzyme adsorption (Masuda, Hasegawa et al. 2004). The small shifts of amide I (1626-1655 cm^{-1}) and amide II (1450-1540 cm^{-1}) peaks upon 2° ADH adsorption suggest that the MPA-TBO-$NADP^+$-modified electrode surface does not undergo conformation changes upon 2° ADH adsorption (Liu and Cai 2007). The absorption peaks at 1655 and 1540 cm^{-1} of the MPA-TBO-PEI-$NADP^+$-2° ADH interface disappeared after washing with HCl (Figure 6.1D), while the peaks at 1626 and 1450 cm^{-1} remained, suggesting the removal of just the $NADP^+$-2° ADH-modified PEI. Upon the reattachment of the $NADP^+$-2° ADH-modified PEI, the absorption bands at 1655 and 1540 cm^{-1} reappeared (Figure 6.1E). Collectively, these results are consistent with the assembly of the MPA-TBO-PEI-$NADP^+$-2° ADH interface, removal of the $NADP^+$-2° ADH-modified PEI at reduced pH, and subsequent reconstitution of the interface.

Figure 6.2A shows the impedance spectra for the MPA, MPA-TBO, MPA-TBO-PEI, MPA-TBO-PEI-$NADP^+$, and MPA-TBO-PEI-$NADP^+$-2° ADH (Curves 1-5, respectively) modified electrodes. Fitting the equivalent-circuit model (Figure 2.1) to the (EIS) data gave charge transfer resistance (R_{CT}) values which increased with each subsequent layer, providing evidence of each step in the interface-fabrication process.

Figure 6.2B (Curve 1) shows the Nyquist plot for the MPA-TBO-PEI-$NADP^+$-2° ADH-modified electrodes after HCl treatment. The resulting R_{CT} (19.7±2.5 Ω cm^2) was approximately equal to the original MPA-TBO-modified electrode (20.3±1.3 Ω cm^2) suggesting that the HCl removed the PEI, $NADP^+$, and 2° ADH. After neutralizing the pH and subsequent readsorbtion of PEI, CBA, $NADP^+$, and 2° ADH, the R_{CT} (65.3±1.3 Ω cm^2) (Figure 6.2B, Curves 2-4) were consistent with the original MPA-TBO-PEI-$NADP^+$-2° ADH-modified electrode (62.5±5.0 Ω cm^2). The impedance measurements indicate that the bioelectronic interface could be removed by changing pH and then reconstituted.

6.4.2. Electrochemical characterization

6.4.2.1. MPA-TBO-PEI-$NADP^+$-2° ADH-modified electrode

Figure 6.3A shows the cyclic voltammograms at different times of 2° ADH adsorption on a MPA-TBO-PEI-$NADP^+$-modified electrode. Figure 6.3B shows the peak anodic current as a function of adsorption time. The pseudo-first-order adsorption time constant (τ_{PEI}) derived from the data was 40.1±2.7 min, a value similar to τ_{Cys} (49.2±1.0 min) suggesting that the enzyme adsorption kinetics are dependent on the cofactor bound to the surface of the electrode, while being independent of the underling surface modification.

Figure 6.4 shows the chronoamperometric response for the MPA-TBO-PEI-$NADP^+$-2° ADH-modified electrode. Fitting Eqs. 2.1 and 2.3 to the chronoamperometric data gave values for the an electron transfer rate constant (k_{et}) and an apparent enzymatic surface coverage (Γ_{enz}) of 125.6±5.3 s^{-1} and 2.3±0.2×10^{-11} mol cm^{-2}, respectively. The

measured Γ_{enz} is comparable to that measured for the Cys-TBO-NADP$^+$-2° ADH-modified gold coated silicon wafer ($2.6\pm0.1\times10^{-11}$ mol cm^{-2}) (Hassler, Dennis et al. 2007). Figure 6.5A shows the cyclic voltammograms of the MPA-TBO-PEI-NADP$^+$-2° ADH-modified electrode. The peak anoidic current increased linearly with 2-propanol concentration (Figure 6.5B) below 30 mM, with a sensitivity of 3.5 ± 0.1 μA mM^{-1} cm^{-2}. At 2-propanol concentrations above 30 mM, the anodic current reached a saturation current (I_{cat}^{sat}) of 134.2 ± 0.9 μA cm^{-2}. The maximum turnover rate (TR_{max}) was determined to be 21.2 ± 1.5 s^{-1}, according to Eq. 2.4. The values for I_{cat}^{sat}, sensitivity, and TR_{max} values are comparable to that measured for a Cys-TBO-NADP$^+$-2° ADH-modified gold electrode (129.0 ± 3.0 μA cm^{-2}, 3.8 ± 0.0 μA mM^{-1} cm^{-2}, and 19.8 ± 1.1 s^{-1}, respectively) (Hassler, Dennis et al. 2007).

The selectivity of the MPA-TBO-PEI-NADP$^+$-2° ADH-modified electrode was examined by testing alternative substrates. Table 6.1 shows the values of I_{cat}^{sat}, sensitivity, and TR_{max} for the MPA-TBO-PEI-NADP$^+$-2° ADH-modified electrode to 2-propanol, ethanol, 2-butanol, and pentanol. These data are consistent with the literature values for 2° ADH (Burdette and Zeikus 1994; Burdette, Secundo et al. 1997).

To confirm renewability of the interface, the performance properties of the MPA-TBO-PEI-NADP$^+$-2° ADH-modified electrode were measured before and after interface removal and reconstitution (Table 6.2). The values of Γ_{enz}, k_{et}, I_{cat}^{sat}, sensitivity, and TR_{max} values for the reconstituted interface were virtually identical to those for the MPA-

TBO-PEI-$NADP^+$-2° ADH-modified electrode before HCl treatment, confirming that the interface could be removed and reconstituted without and loss in performance.

6.4.2.2. MPA-TBO-PAH-$NADP^+$-2° ADH-modified electrode

Figure 6.6 shows the cyclic voltammograms at different times of 2° ADH adsorption on a MPA-TBO-PAH-$NADP^+$-modified electrode. Figure 6.3B shows the peak anodic current as a function of adsorption time. The pseudo-first-order adsorption time constant (τ_{PAH}) derived from the data was 43.1±0.6 min. The value of τ_{PAH} is consistent with τ_{PEI} (40.1±2.7 min) suggesting that the enzyme adsorption kinetics are dependent on the cofactor bound to the surface of the electrode.

Figure 6.7 shows the chronoamperometric response for the MPA-TBO-PAH-$NADP^+$-2° ADH-modified electrode. Fitting Eqs. 2.1 and 2.3 to the chronoamperometric data gave k_{et} and Γ_{enz} values of 120.4±2.4 s^{-1} and 2.8±0.0×10^{-11} mol cm^{-2}, respectively. Figure 6.8A shows the cyclic voltammograms of the MPA-TBO-PEI-$NADP^+$-2° ADH-modified electrode at various 2-propanpol concentrations. The peak anodic current increased linearly with 2-propanol concentration below 30 mM, with a sensitivity and I_{cat}^{sat} values of 3.5±0.1 μA mM^{-1} cm^{-2} and 134.8±1.2 μA cm^{-2}, respectively (Figure 6.8B). TR_{max} was determined to be 18.2±1.0 s^{-1}. The values of sensitivity of k_{et}, Γ_{enz}, I_{cat}^{sat}, sensitivity, and TR_{max} for the MPA-TBO-PAH-$NADP^+$-2° ADH-modified interface are consistent with then those for the MPA-TBO-PEI-$NADP^+$-2° ADH-modified (125.6.±5.3 s^{-1}, 2.3±0.2×10^{-11} mol cm^{-2}, 3.5±0.1 μA mM^{-1} cm^{-2}, 134.2±0.9 μA

cm^{-2}, and 21.2±1.5 s^{-1}, respectively) suggesting that the underlining polymer doesn't affect the performance of the bioelectronic interface.

The selectivity of the MPA-TBO-PAH-$NADP^+$-2° ADH-modified electrode was examined by testing alternative substrates. Table 6.3 shows the values of I_{cat}^{sat}, sensitivity, and TR_{max} for the MPA-TBO-PAH-$NADP^+$-2° ADH-modified electrode to 2-propanol, ethanol, 2-butanol, and pentanol. These data are consistent with the literature values for 2° ADH (Burdette and Zeikus 1994; Burdette, Secundo et al. 1997).

To confirm renewability of the interface, the performance properties of the MPA-TBO-PAH-$NADP^+$-2° ADH-modified electrode were measured before and after interface removal and reconstitution (Table 6.4). The values of Γ_{enz}, k_{et}, I_{cat}^{sat}, sensitivity, and TR_{max} values for the reconstituted interface were virtually identical to those for the MPA-TBO-PAH-$NADP^+$-2° ADH-modified electrode before HCl treatment, confirming that the interface could be removed and reconstituted without and loss in performance. The Γ_{enz}, sensitivity and I_{cat}^{sat} were found to be half of that found for the original interface, indicating that the interface isn't completely renewable. On the other hand, the TR_{max} was comparable to the MPA-TBO-PAH-$NADP^+$-2° ADH-modified electrode suggesting that the activity of the adsorbed 2° ADH remains constant.

6.5. Disucssion

Two amine terminated polycations (PEI and PAH) were examined. Chronoamperometry, cyclic voltammetry, electrochemical impedance spectroscopy, and FTIR were used to characterize the bioelectronic interfaces. Upon HCl treatment and

readsorption of the PEI, cofactor, and enzyme the Γ_{enz}, sensitivity and I_{cat}^{sat} are consistent with the original interface, indicating that the interface is completely renewable. The renewable bioelectronic interfaces are ideal for the long-term operation of bioelectronic interfaces. However, upon HCl treatment and readsorption of the PAH, cofactor, and enzyme the Γ_{enz}, sensitivity and I_{cat}^{sat} were found to be half of that found for the original interface, indicating that the interface isn't completely renewable. The differences in the performance properties of the interfaces can be explained by the molecular architecture of the polycation. The branched-PEI has primary, secondary, and tertiary amines within its backbone, while the PAH contains primary amines. At low-pH's (below the pKa of the amine functional group) the secondary and tertiary amines in the backbone could provide electrostatic repulsion, allowing the PEI to be removed from the surface. The decrease in activity on the PAH-modified electrode could be due to the enzyme denaturing on the surface of the electrode. The work described here could be expanded to include a second enzyme upon the readsorption process; this could be particular interest when more then one analyte needs to be detected.

The work on the renewable bioelectronic interface has been focused on the use of polycations on the surface of the electrode; the work could be extended to the use of polyanions on a positively charged electrode. It is believed that interfaces containing polyanions would exhibit similar renewable characteristics. The study of these interfaces will allow for the optimization of bioelectronic interface performance at low pH's were the PEI/PAH would degrade.

6.6. Conclusions

A novel bioelectronic interface for dehydrogenase enzymes has been developed, in which an electron mediator was first covalently bound to a negatively charged gold electrode, and then positively charged polyelectrolytes functionalized with the enzyme and its cofactor were bound by electrostatic interactions. Cyclic voltammetry, chronoamperometry, EIS, and FTIR analysis were used to demonstrate sequential assembly of the layers and to characterize the performance properties of the resulting bioelectronic interfaces. The labile components of the interface, the cofactor and enzyme, were able to be removed by a decrease in pH, and then reconstituted to regenerate the bioelectronic interface. The saturation current, sensitivity, and turnover rate for the MPA-TBO-PEI-$NADP^+$-2° ADH-modified interface before the removal were 3.5±0.1μA mM^{-1} cm^{-2}, 123.9±2.7 μA cm^{-2}, and 23.6±0.2 s^{-1}, respectively compared to 3.1±0.1 μA mM^{-1} cm^{-2}, 113.4±1.6 μA cm^{-2}, and 25.2±0.5 s^{-1}, respectively, for the reconstituted bioelectronic interface. Bioelectronic interfaces formed using PAH exhibited a comparable peak current and sensitivity (3.5±0.2 μA mM^{-1} cm^{-2}, 125.3±3.5 μA cm^{-2}, and 23.8±0.3 s^{-1}, respectively); however, the interface was not able to be reconstituted. The ability to renew bioelectronic interfaces is a novel capability that has potential applications for biosensors and biocatalytic reactors, and biological fuel cells.

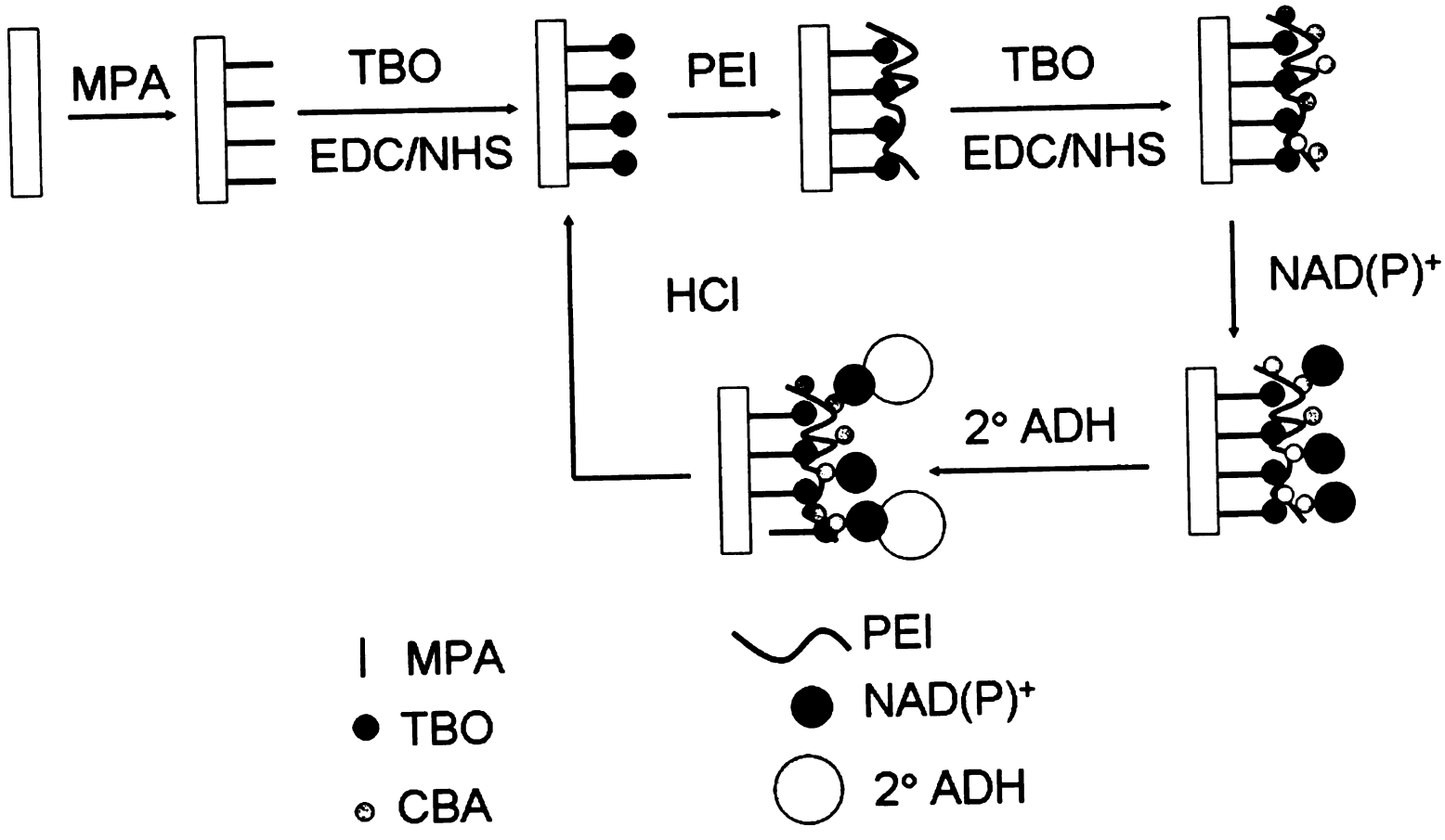

Scheme 6.1: Formation of cross-linked integrated MPA-TBO-PEI-$NADP^+$-2° ADH-functionalized gold electrode.

Table 6.1: Selectivity of the MPA-TBO-PEI-$NADP^+$-2°ADH-modified electrode to the substrates 2-propanol, ethanol, 2-butanol, and 2-pentanol

Compound	I_{cat}^{sat} ($\mu A\ cm^{-2}$)	Sensitivity ($\mu A\ mM^{-1}\ cm^{-2}$)	TR_{max} (s^{-1})
2-propanol	134.2±0.9	3.5±0.1	21.2±1.5
Ethanol	50.7±1.2	1.4±0.1	7.7±0.6
2-Butanol	50.2±0.2	1.2±0.0	7.0±0.5
2-Pentanol	51.1±1.2	1.1±0.1	6.5±0.5

Table 6.2: Comparison of performance of the MPA-TBO-PEI -$NADP^{+}$-2^{o} ADH-modified electrode before and after interface removal by HCl wash and reconstitution.

	Γ_{enz} ($\times 10^{-11}$ mol cm^{-2})	k_{et} (s^{-1})	I_{cat}^{sat} ($\mu A\ cm^{-2}$)	Sensitivity ($\mu A\ mM^{-1}\ cm^{-2}$)	TR_{max} (s^{-1})
Before HCl wash	2.3±0.2	125.6±5.3	134.2±0.9	3.5±0.1	21.2±1.5
After Reconstitution	2.5±0.2	118.9±1.40	120.3±2.6	3.1±0.1	17.6±1.6

Table 6.3: Selectivity of the MPA-TBO-PAH-$NADP^+$-2°ADH-modified electrode to the substrates 2-propanol, ethanol, 2-butanol, and 2-pentanol

Compound	I_{cat}^{sat} ($\mu A\ cm^{-2}$)	Sensitivity ($\mu A\ mM^{-1}\ cm^{-2}$)	TR_{max} (s^{-1})
2-propanol	134.8±1.2	3.5±0.1	18.2±1.0
Ethanol	65.1±8.6	1.0±0.0	5.5±2.0
2-Butanol	50.7±0.2	1.2±0.0	6.1±0.3
2-Pentanol	54.4±2.9	0.7±0.0	3.6±0.7

Table 6.4: Comparison of performance of the MPA-TBO-PAH-$NADP^{+}$-2^{o} ADH-modified electrode before and after interface removal by HCl wash and reconstitution

	Γ_{enz} ($\times 10^{-11}$ mol cm^{-2})	k_{et} (s^{-1})	I_{cat}^{sat} ($\mu A\ cm^{-2}$)	Sensitivity ($\mu A\ mM^{-1}\ cm^{-2}$)	TR_{max} (s^{-1})
Before HCl wash	2.8±0.0	120.4±2.4	134.8±1.2	3.5±0.1	18.2±1.0
After Reconstitution	1.5±0.4	111.5±4.8	83.8±1.2	1.7±0.0	17.9±5.0

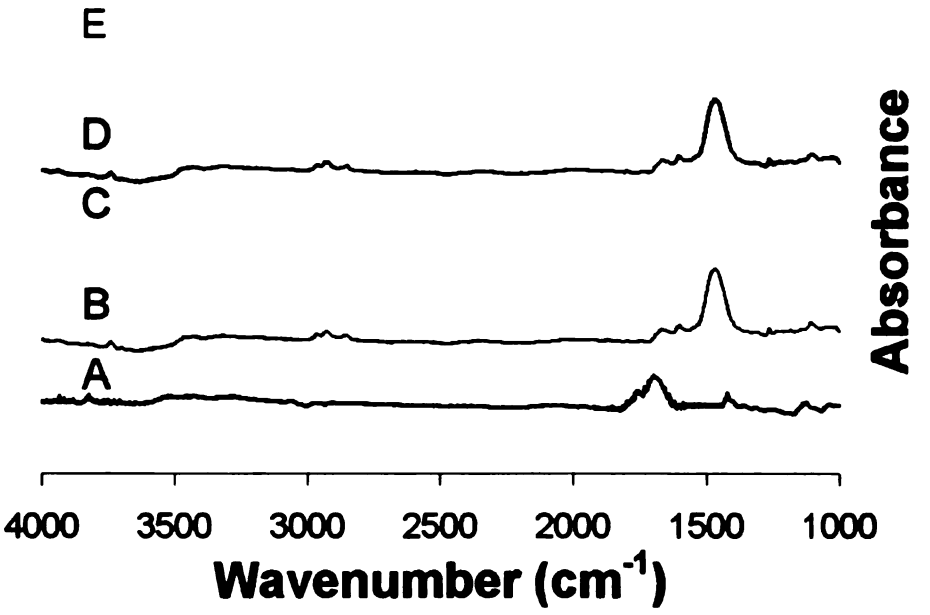

Figure 6.1: Average FTIR absorption spectra for the bioelectronic interface at several intermediate stages of assembly (A) MPA, (B) MPA-TBO, (C) MPA-TBO-PEI-$NADP^+$-2° ADH-modified electrodes, (D) MPA-TBO-PEI-$NADP^+$-2° ADH-modified electrode after HCl treatment, and (E) MPA-TBO-PEI-$NADP^+$-2° ADH after neutralization and subsequent readsorption of PEI, $NADP^+$, and 2° ADH.

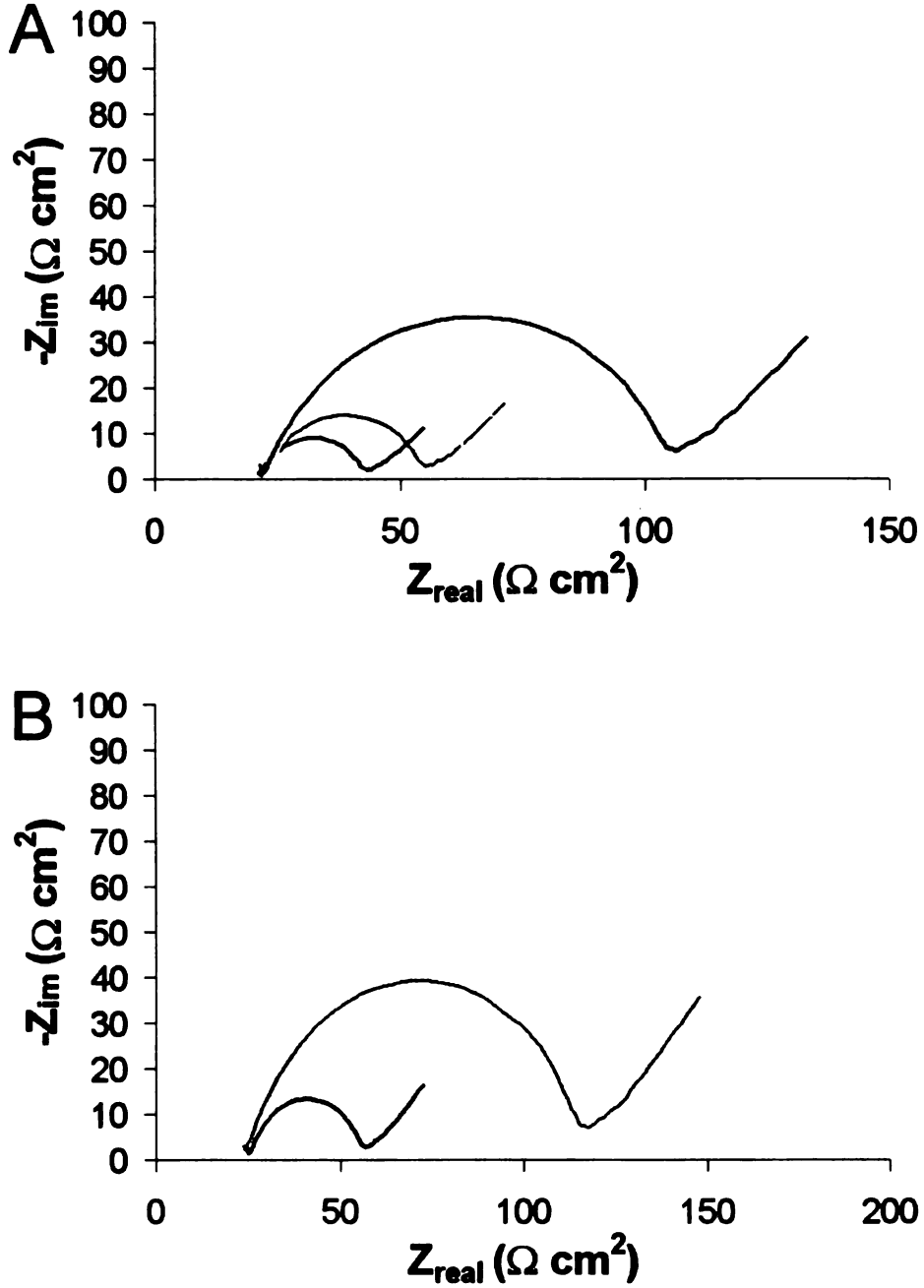

Figure 6.2: (A) Nyquist plots of (1) MPA, (2) MPA-TBO, (3) MPA-TBO-PEI, (4) MPA-TBO-PEI-$NADP^+$, and (5) MPA-TBO-PEI-$NADP^+$-2° ADH-modified electrode and (B) Nyquist plots for the (1) MPA-TBO-PEI-$NADP^+$-2° ADH-modified electrode after washing with 10 mM HCl and the (2) MPA-TBO-PEI-$NADP^+$-2° ADH-modified electrode after reconstitution. All impedance measurements were recorded in an equimolar 5 mM solution of $K_3[Fe(CN)_6]/K_4[Fe(CN)_6]$ in 100 mM PBS (pH 7.4) recorded at the electrodes open circuit potential (230 mV) and room temperature (25±2°C).

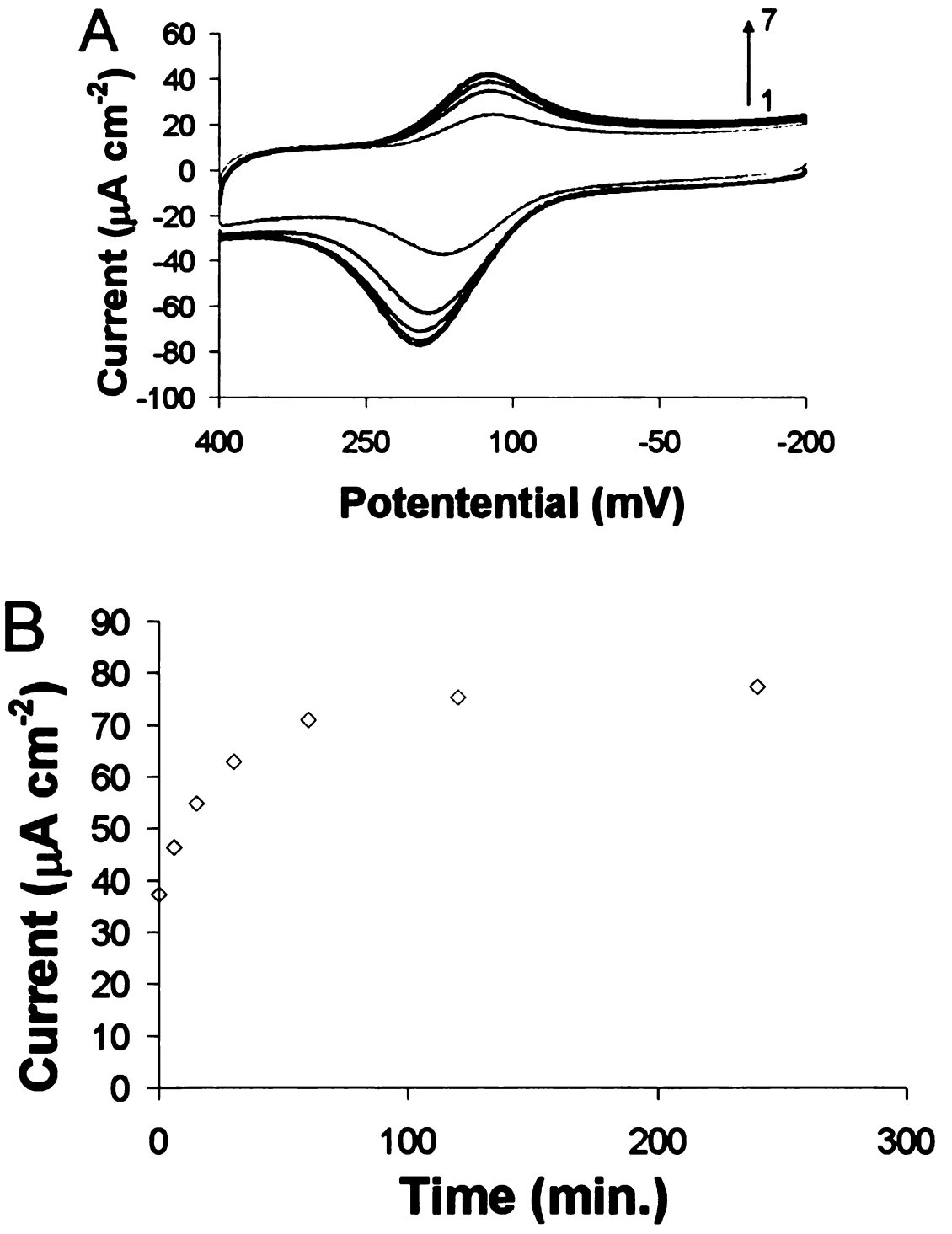

Figure 6.3: (A) Cyclic voltammograms of the MPA-TBO-PEI-$NADP^+$-2^o ADH-modified electrode following various times of 2^o ADH adsorption: (1) 0, (2) 6, (3) 15, (4) 30, (5) 60, (6) 120, and (7) 240 min. The data were recorded in room-temperature 100 mM PBS (pH 7.4) containing 25 mM 2-propanol, at a potential scan rate of 100 mV s^{-1}. (B) Peak electrocatalytic current vs. time of adsorption.

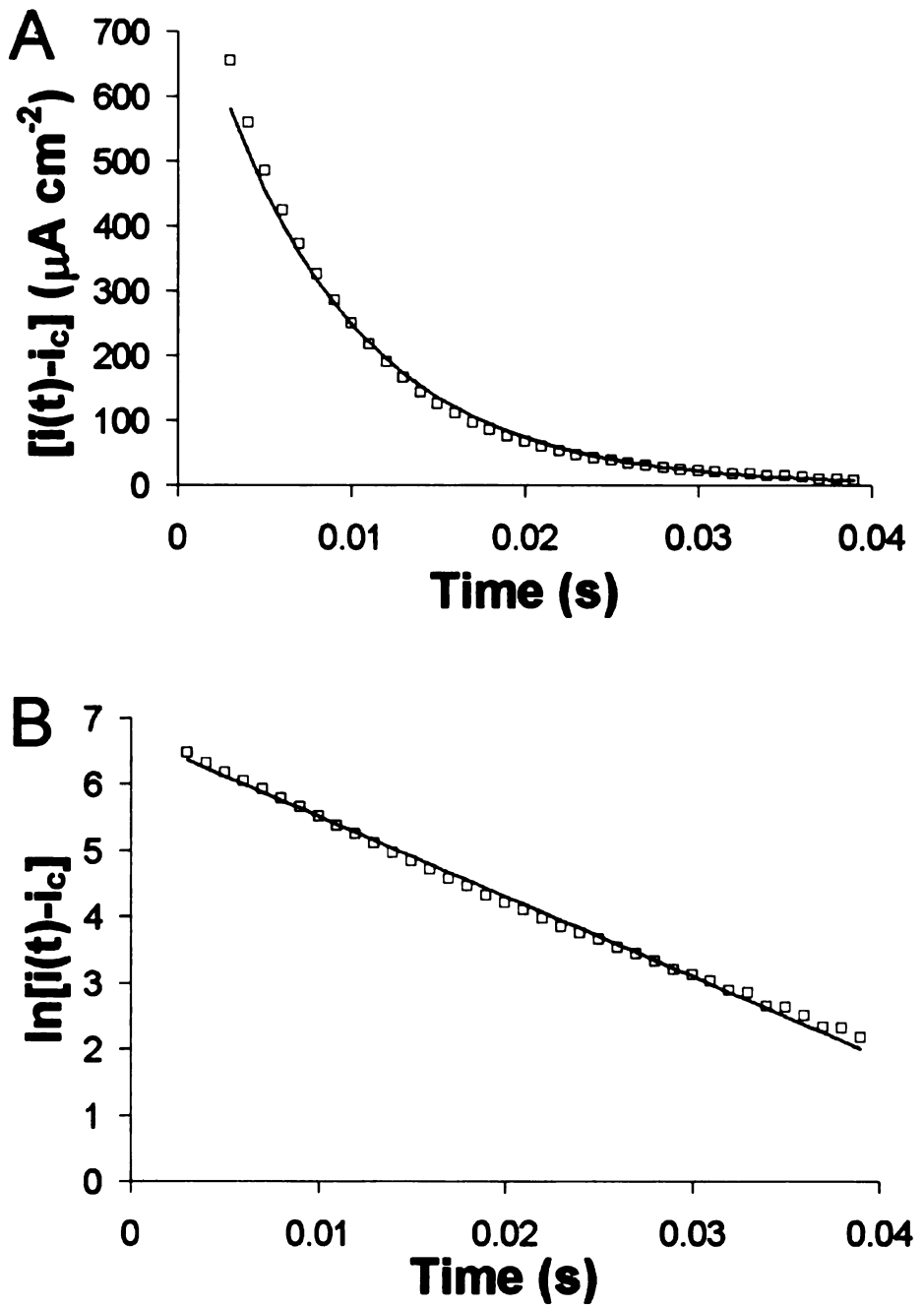

Figure 6.4: (A) Current transient for a potential step from -200 mV to 400 mV for a MPA-TBO-PEI-$NADP^{+}$-2° ADH-modified electrode in 100 mM PBS (pH 7.4) containing 25 mM 2-propanol at room temperature. (B) Shows the plots of $\log[i(t)-i_c]$ after double layer charging. The solid line represents the curve of best fit to the data.

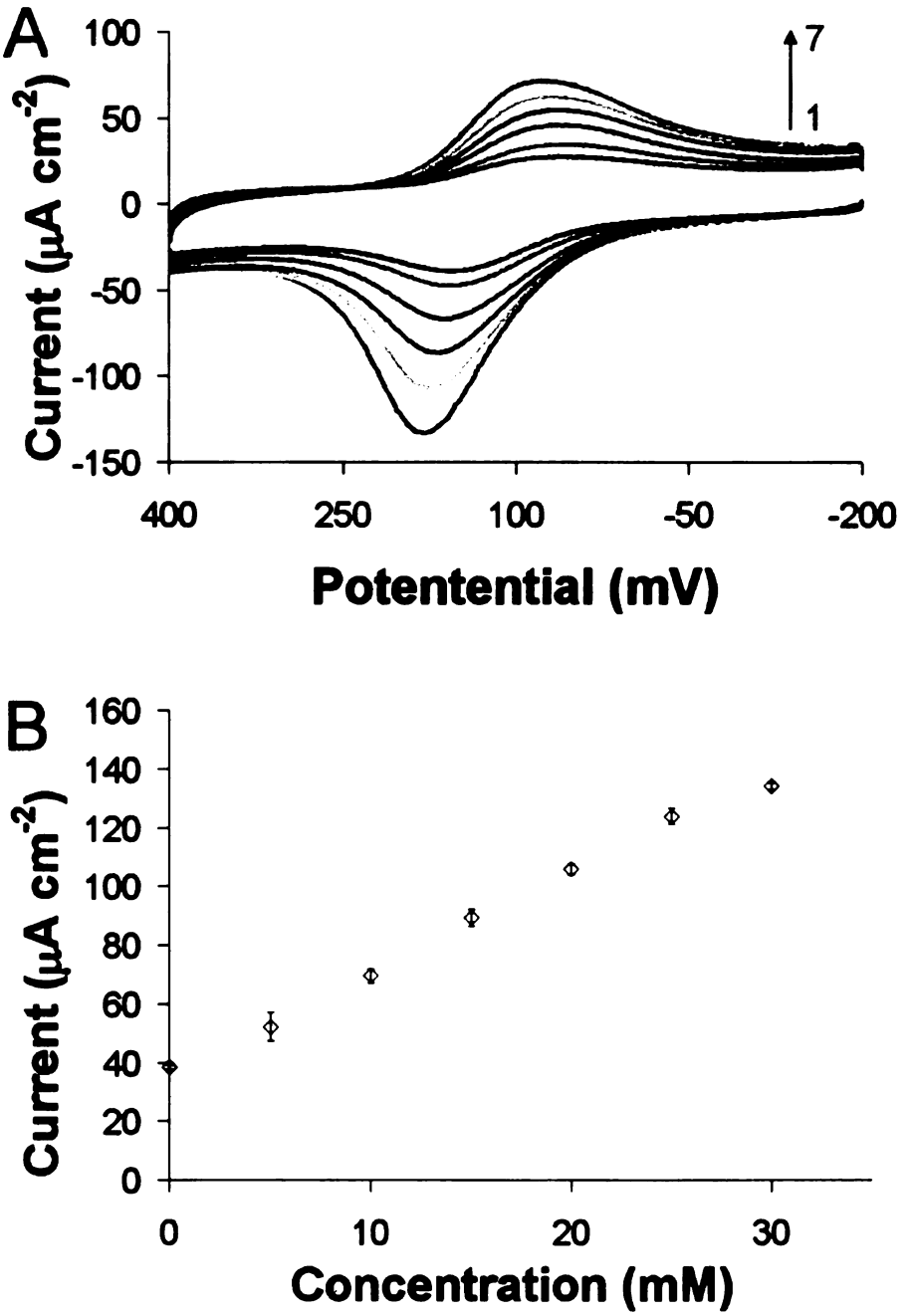

Figure 6.5: (A) Cyclic voltammograms for the MPA-TBO-PEI-$NADP^+$-2^o ADH-functionalized electrode. The data were recorded in 100 mM PBS (pH 7.4) at room temperature containing (1) 0, (2) 5, (3) 10, (4) 15, (5) 20, (6) 25, and (7) 30 mM 2-propanol at a potential scan rate of 100 mV s^{-1}. (B) Peak electrocatalytic current at various 2-propanol concentrations. The error bars indicate the mean ± the standard deviation (n=3).

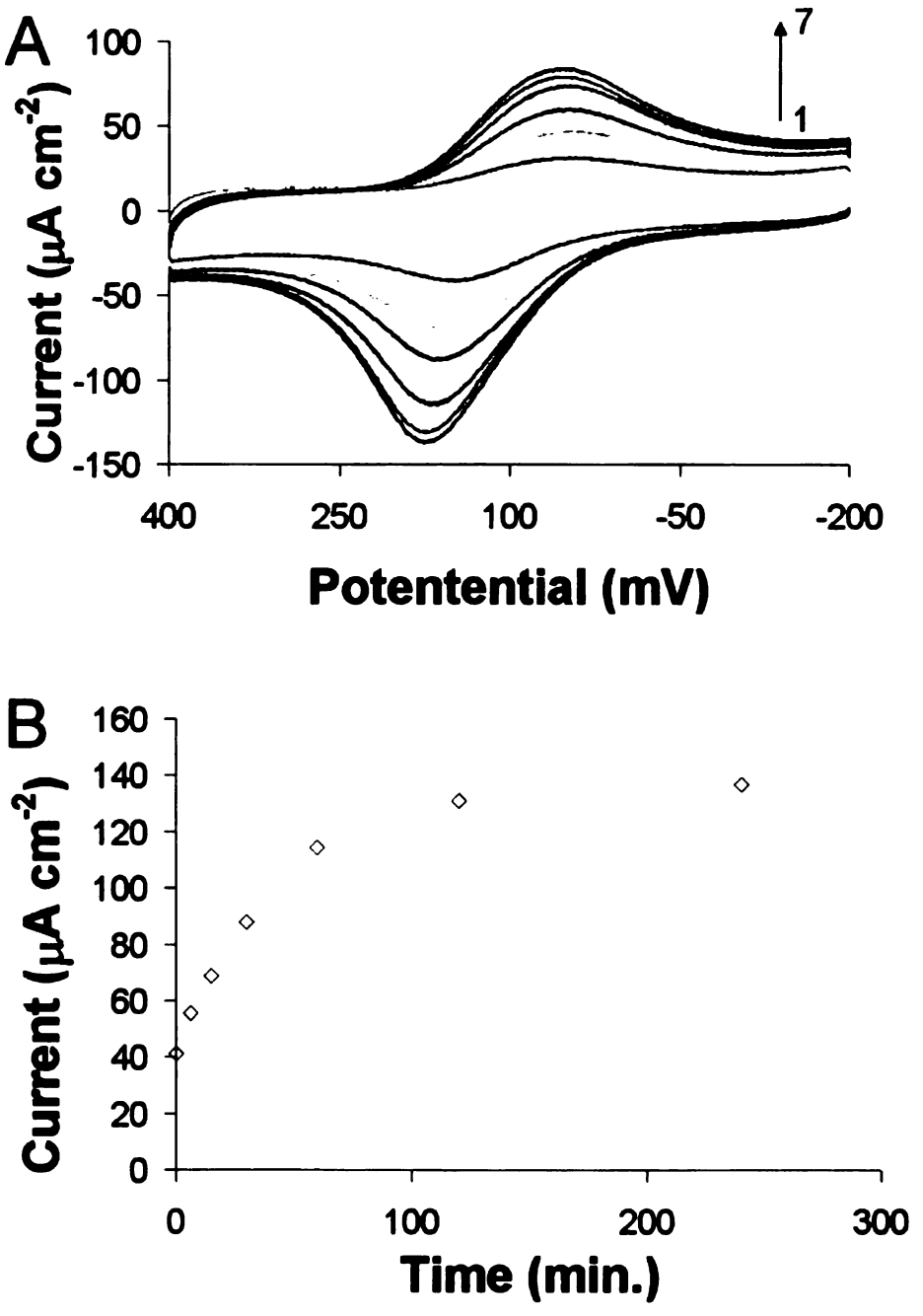

Figure 6.6: (A) Cyclic voltammograms of the MPA-TBO-PAH-$NADP^+$-modified electrode following various times of 2^o ADH adsorption: (1) 0, (2) 6, (3) 15, (4) 30, (5) 60, (6) 120, and (7) 240 min. The data were recorded in room-temperature 100 mM PBS (pH 7.4) containing 25 mM 2-propanol, at a potential scan rate of 100 mV s^{-1}. (B) Peak electrocatalytic current vs. time of adsorption.

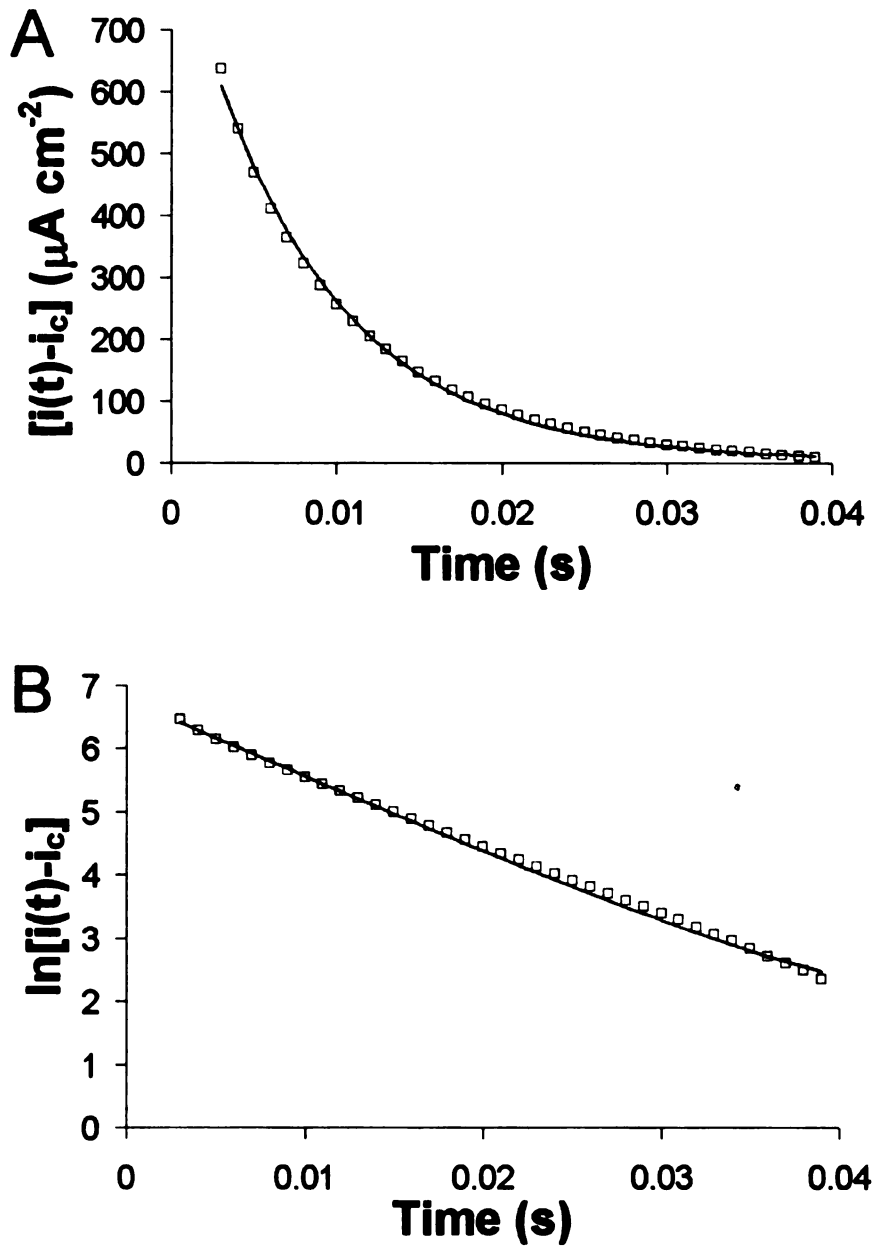

Figure 6.7: (A) Current transient for a potential step from -200 mV to 400 mV for a MPA-TBO-PAH-$NADP^{+}$-2° ADH-modified electrode in 100 mM PBS (pH 7.4) containing 25 mM 2-propanol at room temperature. (B) Shows the plots of $\log[i(t)-i_c]$ after double layer charging. The solid line represents the curve of best fit to the data.

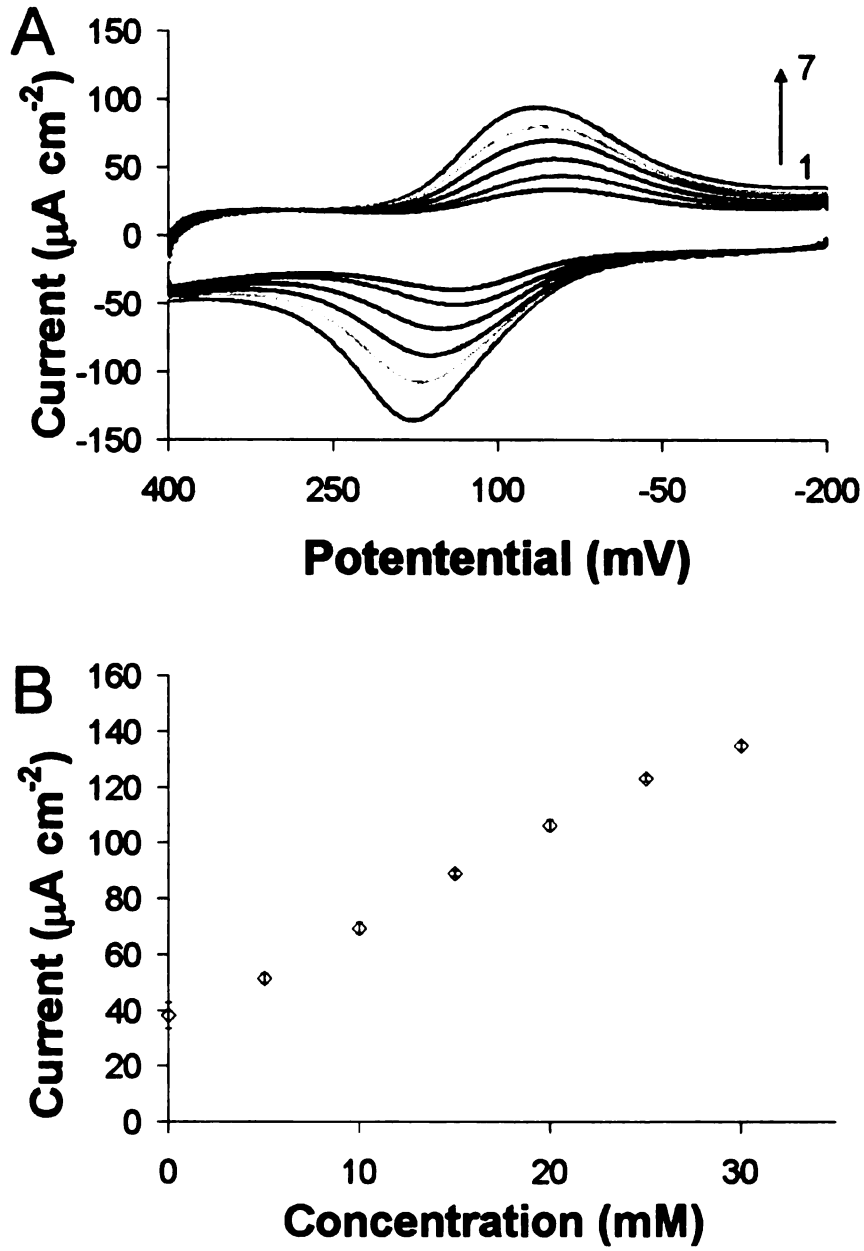

Figure 6.8: (A) Cyclic voltammograms for the MPA-TBO-PAH-$NADP^+$-2^o ADH-functionalized electrode. The data were recorded in 100 mM PBS (pH 7.4) at room temperature containing (1) 0, (2) 5, (3) 10, (4) 15, (5) 20, (6) 25, and (7) 30 mM 2-propanol at a potential scan rate of 100 mV s^{-1}. (B) Peak electrocatalytic current at various 2-propanol concentrations. The error bars indicate the mean ± the standard deviation (n=3).

7. CHARACTERIZATION OF RENEWABLE MULTILAYERED DEHYDROGENASE-BASED BIOELECTRONIC INTERFACES

7.1. Abstract

Bioelectronic interfaces that establish electron transfer between an electrode and enzyme have numerous potential applications as biocatalysts, biosensors, and biological fuel cells. These interfaces are commonly formed by binding a single bioelectronic cassette containing the electron mediator, cofactor, and dehydrogenase enzyme directly to the electrode surface. However, these interfaces are limited in their reaction capacity, because they contain only a single enzyme monolayer. This chapter describes a novel approach, in which multiple nanostructured bioelectronic cassettes are stacked in series to yield multilayered bioelectronic interfaces having higher reaction capacities. Atomic force microscopy (AFM), cyclic voltammetry, chronoamperometry, electrochemical impedance spectroscopy (EIS), and ellipsometry were used to characterize the study multilayered bioelectronic interfaces. The saturation current and sensitivity increased linearly up to four cassettes, and then decreased as additional layers were added indicating that the performance properties of these bioelectronic interfaces can be tuned by controlling the number of cassettes. Renewability of the multilayered bioelectronic interface was confirmed by using cyclic voltammetry and EIS.

7.2. Introduction

Two of the major challenges in the fabrication of bioelectronic interfaces are the process of establishing electrical communication between an electrode and an immobilized redox enzyme and the incorporatation of an electron carrying cofactor (e.g., β-nicotinamide adenine dinucleotide phosphate [$NADP^+$]) (Burdette and Zeikus 1994;

Burdette, Vieille et al. 1996; Burdette, Secundo et al. 1997; Park and Zeikus 1999; Burdette, Tchernajencko et al. 2000; Park and Zeikus 2000; Zayats, Katz et al. 2002; Hassler and Worden 2006). Direct electrochemical oxidation or reduction of $NADP^+$ requires the use of high over potentials (Blaedel and Jenkins 1975; Schmakel, Santhanam et al. 1975), which may lead to cofactor degradation or interference from compounds such as ascorbic acid and molecular oxygen (Park and Zeikus 1999; Ramesh, Sivakumar et al. 2003). Cofactor degradation can be circumvented by using an electron mediator to shuttle electrons between the electrode and cofactor at more moderate potentials (Burdette and Zeikus 1994; Ozdemir and Tuncel 2000; Senel, Camli et al. 2002). Several approaches have been used to achieve mediated electron exchange in bioelectronic interfaces, including immobilizing the enzymes on conductive polymers (Heller 1990; Emr and Yacynych 1995) and constructing a redox relay that conducts electrons between the enzyme and electrode (Degani and Heller 1987; Zimmermann, Lindgren et al. 2000).

Several molecular architectures have been developed to immobilize the electron mediator, cofactor, and enzyme in an orientation that affords multistep electron transfer while preventing component loss (Zayats, Katz et al. 2002; Hassler, Dennis et al. 2007; Hassler, Kohli et al. 2007). However, these methods involve covalent linkages and make no provision for periodic removal and replacement of cofactors and enzymes, whose activities degrade over time (Burdette, Tchernajencko et al. 2000; Wang, Feng et al. 2003; De Temino, Hartmeier et al. 2005). Long-term operation will require interface-assembly methods that allow facile removal and replacement of these labile components.

To address this need, we recently developed a renewable, nanostructured bioelectronic interface in which the enzyme and cofactor can be easily removed by

reducing the pH, and then replaced to regenerate the bioelectronic activity (Hassler, Kohli et al. 2007). This renewable interface is fabricated via layer-by-layer (LbL) self assembly, a technique first introduced by Decher (Decher and Hong 1991; Decher and Hong 1991; Decher, Hong et al. 1992). In LbL self assembly, alternating layers of oppositely charged polyelectrolytes are sequentially adsorbed to create a polyelectrolyte multilayer (PEM) film. In the renewable interface, molecular layers of an electron mediator, a cofactor, and a dehydrogenase enzyme are sequentially deposited to yield a bioelectronic cassette that efficiently transfers electrons between an electrode and the enzyme.

The deposition of multiple enzymes using PEMs films have been shown to increase the reaction rate for interfaces containing catalase (Shi, Lu et al. 2003; Wang and Caruso 2005; Shutava, Kommireddy et al. 2006), glucose oxidase (Antipov and Sukhorukov 2004; Zhao, Xu et al. 2005), and polyphenol oxidase (Forzani, Teijelo et al. 2003; Coche-Guerente, Desbrieres et al. 2005). However, the strategy of using multiple enzyme layers has not been investigated for systems containing cofactor-dependent dehydrogenase. Optimum performance of such systems requires not only efficient reactant mass transfer from the bulk liquid to the enzyme but also efficient electron transfer between the electrode and enzyme.

This chapter describes and characterizes a novel bioelectronic interface in which multiple bioelectronic cassettes containing cofactor-dependent dehydrogenases are stacked in series. The method integrates LbL deposition of polyelectrolytes and molecular self-assembly. The fabrication of multiple cassettes was characterized using AFM, EIS, and ellipsometry. The performance parameters including sensitivity, peak

current, and heterogenous rate constant for each cassette was characterized using cyclic voltammetry, chronoamperometry, and EIS. Electron transfer properties including the concentration of redox active sites and charge propagation diffusion coefficient (D_{app}) were also determined.

7.3. Materials and methods

7.3.1. Media and strains

Escherichia coli (DH5α pADH B1M1-kan) culture containing a recombinant plasmid for 2° ADH from *Thermoaneorbactor ethanolicus* was grown, and purified as described in Chapter 2 (Hassler, Dennis et al. 2007).

7.3.2. Chemicals

3-mercaptopropionic acid (MPA), 1-ethyl-3-(3-dimethylaminopropyl) carbodiimide (EDC), n-hydroxysuccinimide (NHS), toluidine blue O (TBO), Polyethyleneimine (PEI), polyacrylic acid (PAA), 3-carboxy phenylboronic acid (CBA), $NADP^+$, 2-propanol, ethanol, 2-butanol, 2-pentanol, were obtained from Sigma-Aldrich (St. Louis, MO). Ultrapure water (18.2 MΩ) was supplied by a Barnstead Nanopure-UV four-stage purifier (Barnstead International, Dubuque, IA).

7.3.3. Interface fabrication

The first bioelectronic cassette was fabricated as described previously (Hassler, Kohli et al. 2007). To add additional cassettes on top of the first, the 2° ADH-terminated interfaces were immersed in a 10 mM aqueous PEI solution containing 100 mM NaCl (pH 7.0), and washed with water to remove the residual PEI from the surface. The resulting PEI-modified electrodes were immersed in a 100 mM PAA solution (pH 5.5) and washed with water. The MPA-TBO-PEI-$NADP^+$-2° ADH-PEI-PAA-modified

electrodes were incubated for 2 h in 0.1 mM TBO in a 100 mM PBS in the presence of 2 mM NHS and 2 mM EDC, resulting in the formation of an amide linkage between the TBO and the PAA. The electrodes were then immersed in a 10 mM aqueous PEI solution (pH 7.0). The NHS-activated CBA was then reacted with MPA-TBO-PEI-$NADP^+$-2° ADH-PEI-PAA-TBO-PEI-functionalized electrodes for 1 h at room temperature. The resulting CBA-modified electrodes were reacted with a 1 mM $NADP^+$ solution in 100 mM PBS for 1 h and then washed with water. The second cassette was completed by immersing the electrodes in a 4.4 mg mL^{-1} 2° ADH solution in 100 mM PBS for 1 h at room temperature. As illustrated in Scheme 7.1, the assembly process described above for the second cassette was carried out a total of *m* times to adsorb *m* PAA-TBO/PEI-$NADP^+$-2° ADH cassettes on top of the first cassette, resulting in a total of *m*+1 bioelectronic cassettes in series.

The labile components of the interface were removed by incubating the electrode in 10 mM HCl (pH 2.0) for 30 min. At pH values below the pKa of MPA (pKa~4.3), the carboxylic acid groups become protonated decreasing the electrostatic interaction between the surface bound MPA (or PAA within the multilayered-structure) and the 2° ADH modified PEI allowing the PEI to disengage from the surface. To reassemble the interface, the PEI, CBA, $NADP^+$, PAA, TBO, and 2° ADH were reattached onto the TBO-modified MPA monolayer using the protocol described above.

7.3.4. Electrochemical techniques

Cyclic voltammetry, chronoamperometry, and electrochemical impedance spectroscopy were performed as described in Chapter 2 using an electrochemical analyzer (CHI660B, CH Instruments).

7.3.5. Surface characterization techniques

AFM and ellipsometry were performed as described in Chapter 2. To evaluate the reproducibility of the method, three bioelectronic interfaces were fabricated, and the current was measured for each at multiple 2-propanol concentrations.

7.4. Results

7.4.1. Interface assembly

The AFM images (Figure 7.1) show the surface morphology after successive deposition of bioelectronic cassettes and drying with N_2. Figure 7.1A shows the image of the film after deposition of the first cassette; the interface had a root mean square (RMS) roughness of 6.15±0.24 nm suggesting that the enzyme conglomerates on the surface of the electrode. Upon the adsorption of subsequent cassettes the RMS roughness decreased to to 4.54±1.63, 3.03±1.09, 2.02±0.13, 1.81±0.29, and 1.55±0.11 nm for two (Figure 7.1B), three (Figure 7.1C), four (Figure 7.1D), five (Figure 7.1E), and six cassettes (Figure 7.1F), respectively, suggesting that the [PAA-TBO/PEI-$NADP^+$-2° ADH]$_m$ fills the pores. The results are consistent with AFM studies of multilayers of horse radish peroxidase on a gold electrode (Liu, Jin et al. 2007).

In order to study the multilayer growth in more details, ellipsometric measurements were performed after each covalent assembly step. Film thickness was found to increase linearly with thickness of 7.4±1.3 nm $cassette^{-1}$ (Figure 7.2). The linear

increase in film thickness during the process indicates an orderly manner of layer growths.

Figure 7.3A compares the Nyquist plots of the impedance spectroscopy at different film- modified electrodes. Upon the stepwise adsorption of the [PAA-TBO/PEI-$NADP^+$-2° ADH]$_m$ cassettes, R_{CT} increased proportionally with the number of cassettes (57.6±7.0 Ω cm^2 $cassette^{-1}$) indicating a well-behaved LbL assembly process (Zhao and Ju 2006). Figure 7.3B, shows the Nyquist plot for the MPA-TBO-PEI-$NADP^+$-2° ADH-[PAA-TBO/PEI-$NADP^+$-2° ADH]$_m$-modified electrode after removal of the interface using with 10 mM HCl, and subsequent reassembly of the bioelectronic interface. The R_{CT} value after the HCl wash (20 Ω cm^2) was approximately equal to that for the original MPA-TBO-modified electrode, indicating that the HCl treatment removed all six [PAA-TBO/PEI-$NADP^+$-2° ADH] cassettes. As the assembly process used to deposit the six cassettes was carried out, R_{CT} increased at a rate of 58.7±2.1 Ω cm^2 $cassette^{-1}$. The increase in R_{CT} indicates that the bioelectronic-interface can be reconstituted.

7.4.2. Determination of redox site concentration

The redox site concentration (Γ_{med}) was estimated from the low frequency impedance using Eq. 2.7. The experimental data for the MPA-TBO-PEI-$NADP^+$-2° ADH-[PAA-TBO/PEI-$NADP^+$-2° ADH]$_m$-modified electrode was fit with the equivalent circuit, replacing the C_{DL} with a constant phase element (CPE) (Brug, Vandeneeden et al. 1984). Table 7.1 lists the resulting values for C_F and ω_{tr}. The surface coverage of the

toluidine blue (Γ_{TBO}) was determined by Eq. 2.7 (Table 7.1). The measured Γ_{TBO} value for a single cassette is comparable the surface coverage of TBO on a terephthaloyl-modified gold electrode ($6.8\pm0.1\times10^{-11}$ mol cm^{-2}) (Ju, Xiao et al. 2002). The measured Γ_{TBO} increases linearly with the number of cassettes indicating that Γ_{TBO} is independent of the number of cassettes (each cassette contributes the same amount of TBO redox centers). A model predicting that Γ_{TBO} is proportional to the film thickness was fit to the data and used to determine an average TBO concentration within the film of 126.4±8.0 mM.

7.4.3. Charge propagation diffusion coefficient

From the plot of ω_{tr}^{-1} vs. d^2 (Figure 7.4) the charge transport diffusion coefficient (D_{app}) was determined to be $7.9\pm0.5\times10^{-9}$ cm^2 s^{-1}. The calculated D_{app} should be considered a binary apparent diffusion coefficient, since two different species could be responsible for charge transport through the film (Tagliazucchi and Calvo 2007): the TBO_{ox}/TBO_{red} redox centers through an electron hopping mechanism or by counter ion diffusion. For the MPA-TBO-PEI-$NADP^+$-2° ADH-[PAA-TBO/PEI-$NADP^+$-2° ADH]$_m$-modified interface the resistance measured at 10 kHz varied by 2 Ω in the potential range -50 to 350 mV, indicating that D_{app} is governed by electron hopping (Tagliazucchi and Calvo 2007).

7.4.4. Interface characterization

Figure 7.5 shows a log(Y/ω) vs log(ω) plot at different stages of the self-assembly process for the MPA-TBO-PEI-$NADP^+$-2° ADH-[PAA-TBO/PEI-$NADP^+$-2° ADH]$_m$-modified electrode. After each adsorption step, the maximum of the low frequency

capacitance (Y/ω) we observe a shift of the transition frequency (ω_{tr}) to lower values as more [PAA-TBO/PEI-NADP$^+$-2° ADH] cassettes are added as expected from Eq. 2.8. The transition in ω_{tr} is consistent with those observed for multiple layers of glucose oxidase on gold (Tagliazucchi and Calvo 2007). For the MPA-TBO-PEI-NADP$^+$-2° ADH-[PAA-TBO/PEI-NADP$^+$-2° ADH]$_m$-modified electrodes at all frequencies the slope of log(Y/ω) vs log(ω) plot is smaller than the value 0.5 expected for a diffusional Warburg impedance, and increases slightly with the number of layers (Tagliazucchi and Calvo 2007).

Equation 2.2 was fit to the chronoamperometric data for MPA-TBO-PEI-NADP$^+$-2° ADH-[PAA-TBO/PEI-NADP$^+$-2° ADH]$_m$-modified electrodes in the presence of 100 mM PBS containing 25 mM 2-propanol following a step change in potential from -200 mV to 400 mV. The k_{et} value for the first cassette (142.3±1.1 s^{-1}) is comparable to that previously reported for the MPA-TBO-PEI-NADP$^+$-2° ADH-modified electrode (131.9±1.4 s^{-1}) (Hassler, Kohli et al. 2007), an interface identical to the bioelectronic interface containing a single cassette. Increasing the number of cassettes decreased k_{et} nonlinearly (Figure 7.6). The value of Γ_{enz} for the first cassette (2.2±0.0×10^{-11} mol cm^{-2}) is similar to that previously reported for an MPA-TBO-PEI-NADP$^+$-2° ADH-modified electrode (2.5±0.1×10^{-11} mol cm^{-2}) (Hassler, Kohli et al. 2007). Increasing the number of cassettes increased the apparent Γ_{enz} nonlinearly (Figure 7.6). The fractional increase in

electrocatalytic activity (A_c) contributed by each subsequent layer was calculated using Eq. 7.1,

$$A_c = \frac{\Gamma_{enz,m} - \Gamma_{enz,m-1}}{\Gamma_{enz,1}} \quad (7.1)$$

where $\Gamma_{enz,m}$, $\Gamma_{enz,m-1}$, and $\Gamma_{enz,1}$ are the total enzyme surface coverage values for the m^{th}, $(n-1)^{th}$, and first cassette, respectively. Upon the adsorption of the sixth [PAA-TBO/PEI-$NADP^+$-2° ADH]-cassette A_c was 41.8% (Zhao, Xu et al. 2005).

Figure 7.7 shows the saturation current (I_{cat}^{sat}) and sensitivity as a function of the number of bioelectronic cassettes. For the first cassette, the anodic I_{cat}^{sat} and sensitivity values (118.2±4.5 μA cm^{-2} and 3.4±0.2 μA mM^{-1} cm^{-2}, respectively) are comparable to those measured previously for the MPA-TBO-PEI-$NADP^+$-2° ADH-modified electrode (134.2±0.9 μA cm^{-2} and 3.5±0.1 μA mM^{-1} cm^{-2}) (Hassler, Kohli et al. 2007). As the number of cassettes increased, both I_{cat}^{sat} and sensitivity increased to maximum values at four cassettes, and then began decreasing (Figure 7.7). The TR_{max} value for the first cassette (20.5±1.6 s^{-1}) is comparable to that measured previously for an MPA-TBO-PEI-$NADP^+$-2° ADH modified electrode (21.2±1.5 s^{-1}) (Hassler, Kohli et al. 2007). Upon the adsorption of additional cassettes TR_{max} decreased (Figure 7.8).

To investigate the mechanism leadigng to the maximum in I_{cat}^{sat} (Figure 7.7) and the decrease in TR_{max} (Figure 7.8) the effect of scan rate (v) on electrochemical properties of electrodes containing four and five cassettes was investigated in 100 mM PBS

containing 25 mM 2-propanol. The peak current (I_P) values for the interface containing four cassettes were better correlated using a model predicting a linear relationship between I_P and v (R^2=0.999) (Figure 7.9A) than a model predicting a relationship between I_P and $v^{1/2}$ (R^2=0.982) (Figure 7.9B), suggesting that the rate-limiting factor was reaction kinetics of a surface-bound, redox active species (Malinauskas, Ruzgas et al. 2001). On the other hand, I_P values for the interface containing five cassettes were better correlated using $v^{1/2}$ (R^2=0.993) (Figure 7.10A) than v (R^2=0.970) (Figure 7.10B), suggesting that diffusion was the rate limiting factor (Malinauskas, Ruzgas et al. 2000). Comparison of the relationship between I_P and v suggests that the MPA-TBO-PEI-$NADP^+$-2° ADH-[PAA-TBO/PEI-$NADP^+$-2° ADH]$_m$-modified electrode transitions from a surface-bound-reaction-limited system to a diffusion-limited system upon the adsorption of the fifth cassette.

A transition from a surface-bound-reaction-limited system to a diffusion-limited system is consistent with the hypotheses that (1) I_{cat}^{sat} initially increases with the number of cassettes because the surface reaction capacity is rate limiting, and (2) I_{cat}^{sat} subsequently decreases with the number of cassettes because transport becomes rate limiting. Since the 2° ADH adsorption is reversible (Pham, Phillips et al. 1989; Pham and Phillips 1990), any one of three transport processes could be rate-limiting: substrate transport, product transport, and electron transport. We have developed a mathematical model (to be presented in Chapter 9) that describes the simultaneous diffusion and reaction of substrate, product, and electrons within the bioelectronic interface. The model extends the approach used by Bartlett et al. (Bartlett and Pratt 1995) to systems that have

multiple adsorbed cassettes, reversible enzyme kinetics, and mass-transfer resistance both within the bioelectronic interface and in a stagnant liquid film between the interface and the bulk liquid. The model predicts that I_{cat}^{sat} will increase with the number of adsorbed cassettes until either transport becomes rate limiting. When either substrate transport or electron transport (but not both) become rate limiting, I_{cat}^{sat} is predicted to reach a plateau. However, when increases in the number of cassettes result in significant transport limitation of both substrate and electrons, the model predicts that I_{cat}^{sat} will reach a maximum and then decrease, as was observed in Figure 7.7. This result suggests that transport of both substrate and electrons through the MPA-TBO-PEI-$NADP^+$-2° ADH-[PAA-TBO/PEI-$NADP^+$-2° ADH]$_m$-modified electrode are limiting for more than four cassettes.

The stability and reaction specificity of the MPA-TBO-PEI-$NADP^+$-2° ADH-[PAA-TBO/PEI-$NADP^+$-2° ADH]$_m$-modified electrode were also investigated. An interface containing four cassettes exhibited no measurable loss in performance when stored a 100 mM borate buffer (pH 7.5) at room temperature for two weeks. To understand the selectivity of the MPA-TBO-PEI-$NADP^+$-2° ADH-[PAA-TBO/PEI-$NADP^+$-2° ADH]$_m$-modified electrode containing four cassettes to alternative substrates. The sensitivities to 2-propanol, ethanol, 2-butanol, and 2-pentanol were 7.5±0.1, 2.7±0.1, 2.2±0.2, and 1.9±0.1 μA mM^{-1} cm^{-2}, respectively. The relative reaction rates for these substrates are consistent with literature values for *T. ethanolicus* 2° ADH which indicates

that 2° ADH activity decreases for alcohols larger then 2-propanol (Burdette, Secundo et al. 1997).

To confirm renewability of the interface, the performance properties of the MPA-TBO-PEI-$NADP^+$-2° ADH-[PAA-TBO/PEI-$NADP^+$-2° ADH]$_m$-modified electrode containing four cassettes were measured before and after interface removal by HCl wash and reconstitution of four [PAA-TBO/PEI-$NADP^+$-2° ADH] cassettes. The values of Γ_{enz}, k_{et}, I_{cat}^{sat}, sensitivity, and TR_{max} for the reconstituted MPA-TBO-PEI-$NADP^+$-2° ADH-[PAA-TBO/PEI-$NADP^+$-2° ADH]$_m$-modified electrode containing four cassettes ($6.8\pm0.2\times10^{-11}$ mol cm^{-2}, 134.3 ± 0.5 s^{-1}, 263.8 ± 11.8 μA cm^{-2}, 8.3 ± 0.2 μA mM^{-1} cm^{-2}, 16.1 ± 1.0 s^{-1}, respectively) were virtually identical to those for the MPA-TBO-PEI-$NADP^+$-2° ADH-[PAA-TBO/PEI-$NADP^+$-2° ADH]$_m$-modified electrode containing four cassettes before HCl treatment ($6.8\pm0.0\times10^{-11}$ mol cm^{-2}, 135.4 ± 0.8 s^{-1}, 236.6 ± 12.3 μA cm^{-2}, 7.5 ± 0.1 μA mM^{-1} cm^{-2}, 15.5 ± 1.0 s^{-1}, respectively), confirming that the interface could be removed and reconstituted without any loss in performance.

The results presented here demonstrate a novel approach to fabricate bioelectronic interfaces, in which nanostructured bioelectronic cassettes, each containing a mediator, a cofactor, and a dehydrogenase enzyme, are stacked in series. The strong dependence of sensitivity and I_{cat}^{sat} values on the number of cassettes provides a mechanism by which performance properties can be controlled. Also, the ability to quickly and inexpensively remove and reconstitute the interface without diminishing its performance could greatly extend the useful lifetime of biofuel cells, biosensors, and biocatalysts. Because the

fabrication method is based on molecular self-assembly of components from aqueous solutions, it is compatible with microfluidic processes and use in high throughput systems (e.g., biosensor arrays).

7.5. Discussion

Currently cofactor-dependent dehydrogenase based bioelectronic interfaces containing are limited in its reaction capacity, because the interfaces contain a single layer on the surface of the electrode. Systems containing multiple enzyme layers have been shown to increase the reaction rate. This chapter describes the fabrication of novel bioelectronic interface in which multiple nanostructured-bioelectronic cassettes are stacked in series yielding higher reaction activity. The values of I_{cat}^{sat} and sensitivity for the MPA-TBO-PEI-$NADP^+$-2° ADH-[PAA-TBO/PEI-$NADP^+$-2° ADH]$_m$-modified electrode increased with the number of cassettes, suggesting that the reaction capacitiy increased with the number of layers on the surface of the electrode. However, upon the adsorption of additional [PAA-TBO/PEI-$NADP^+$-2° ADH]-cassettes the I_{cat}^{sat} and sensitivity decreases. A mathematical model (Chapter 9) suggests that the decrease in the I_{cat}^{sat} and sensitivity is due to the system being limited by both substrate and mediator diffusion. The peak I_{cat}^{sat} and sensitivity suggests that the activity of MPA-TBO-PEI-$NADP^+$-2° ADH-[PAA-TBO/PEI-$NADP^+$-2° ADH]$_m$-modified electrode can be optimization for specific bioelectronic applications.

The system can be expanded to included nanoparticles (e.g., colloidal gold) or multiple enzymes. The inclusion of conductive nanoparticles would increase the conductivity through the film, decreasing mediator diffusion; however, the inclusion of

nanoparticles could effect the diffusion of the substrate/product through the film. The inclusion of multiple enzymes in the bioelectrronic interface allows for greater selection of reaction substrates. For a bioelectronic ineterface contain multiple enzymes the product of one enzyme will be substrate of the second enzyme.

7.6. Conclusions

Molecular self assembly was used to fabricate novel MPA-TBO-PEI-$NADP^+$-2° ADH-[PAA-TBO/PEI-$NADP^+$-2° ADH]$_m$-modified electrodes, in which nanostructured bioelectronic cassettes are stacked in series on a gold electrode. Ellipsometry data and the observation that total charge transfer resistance was directly proportional to the number of cassettes added, indicate that each cassette has a similar thickness and charge transfer resistance. Electrochemical impedance spectroscopy was used to determine Γ_{TBO} and D_{app} values. The k_{et}, A_c, and TR_{max} values decreased as the number of cassettes was added. The I_{cat}^{sat} and sensitivity values increased with the number of cassettes to a maximum at four cassettes, and then decreased as additional cassettes were added. Cyclic voltammetry data suggested that the peak coincides with a transition from a kinetically limited system to a transport-limited system. Labile components of the renewable interface--the cofactor and enzyme--could be easily removed by decreasing the pH, and then reconstituted to fully regenerate the biocatalytic activity.

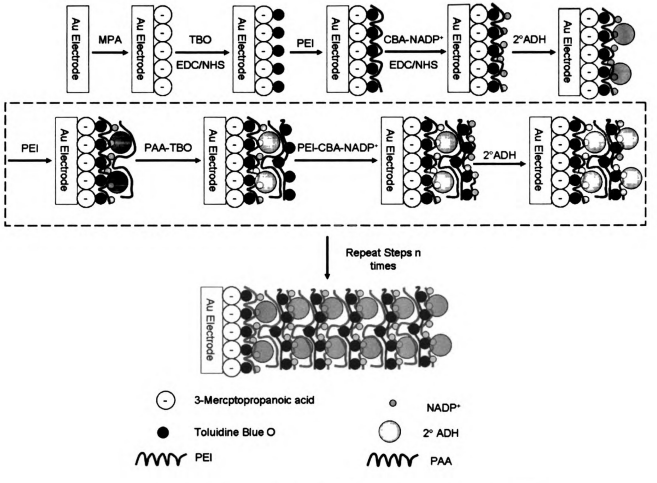

Scheme 7.1: Schematic diagram for the assembly of a MPA-TBO-PEI-$NADP^+$-2° ADH-$[PAA\text{-}TBO/PEI\text{-}NADP^+\text{-}2^\circ\ ADH]_m$-modified electrode on a gold electrode.

Table 7.1: Best fit parameters of the MPA-TBO-PEI-$NADP^+$-2° ADH-[PAA-TBO/PEI-$NADP^+$-2° ADH]$_m$-modified electrode containing m+1 cassettes.

Cassettes	C_F (μF)	ω_{tr} (Hz)	Γ_{MED} ($\times 10^{-10}$ mol cm^{-2})
1	65.2±1.4	3800±800	1.1±0.0
2	123.7±9.3	2000±150	2.1±0.2
3	184.5±9.3	1400±69	3.1±0.2
4	239.7±9.1	890±51	4.0±0.2
5	288.4±12.1	550±42	4.8±0.2
6	333.4±14.0	420±12	5.5±0.2

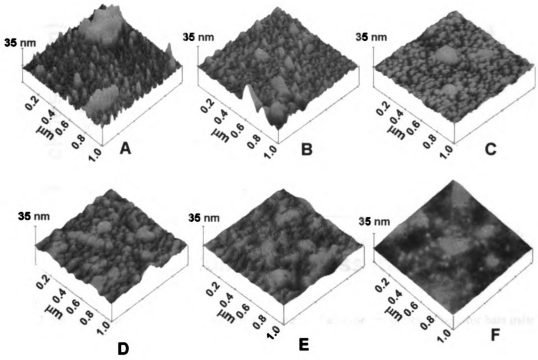

Figure 7.1: Atomic force microscopy images of the MPA-TBO-PEI-$NADP^+$-2° ADH-[PAA-TBO/PEI-$NADP^+$-2° $ADH]_m$-modified interface containing (A) one, (B) two, (C) three, (D) four, (E) five, and (F) six adsorbed cassettes. All images were recorded in air in tapping mode at room temperature (25±2° C).

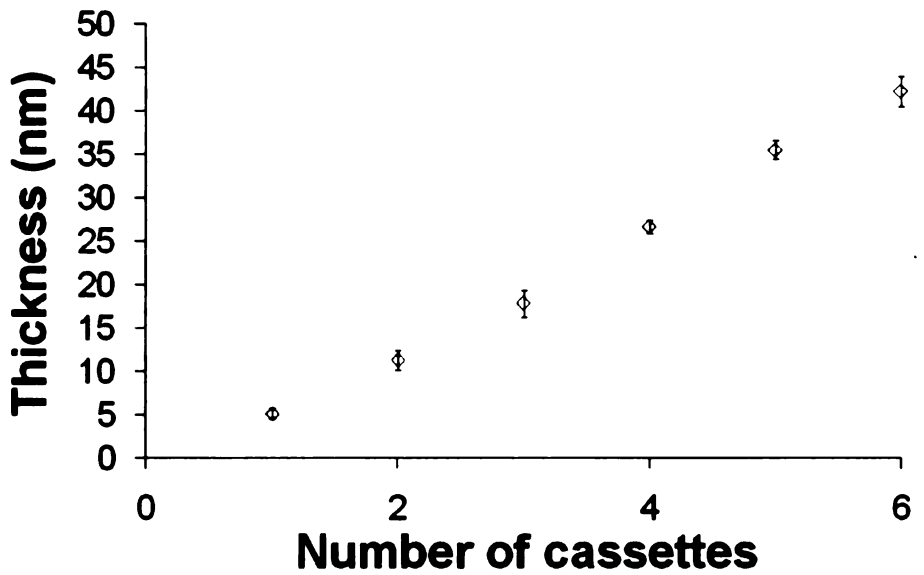

Figure 7.2: Plot of ellipsometric thickness (d) vs the number of adsorbed cassettes. The error bars indicate the mean ± the standard deviation (n=3).

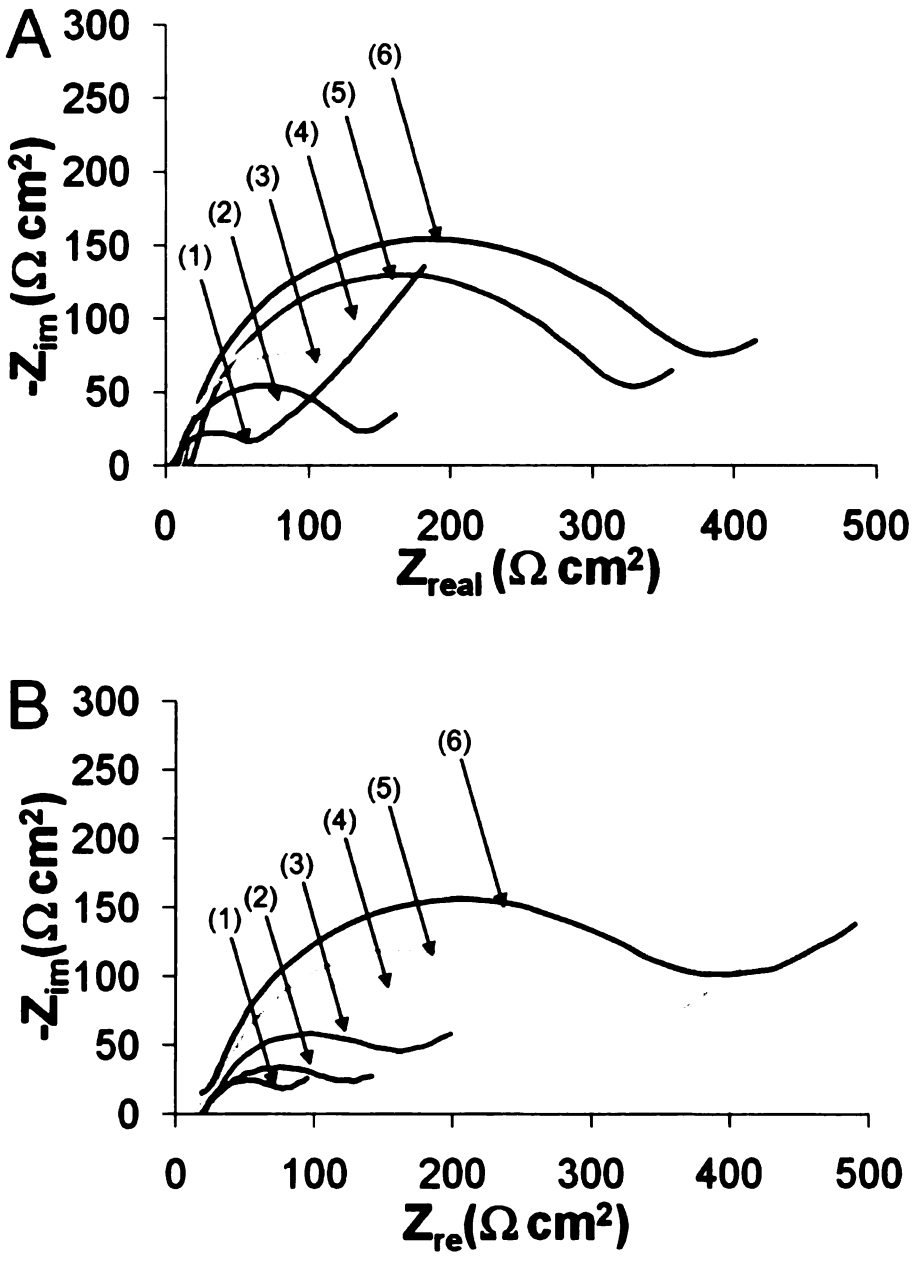

Figure 7.3: (A) Nyquist plots for the MPA-TBO-PEI-NADP$^+$-2° ADH-[PAA-TBO/PEI-NADP$^+$-2° **ADH**]$_m$-modified electrode containing (1) one, (2) two, (3) three, (4) four, (5) five, and (6) six adsorbed **cassettes** and (B) Nyquist plots for the the MPA-TBO-PEI-NADP$^+$-2° ADH-[PAA-TBO/PEI-NADP$^+$-2° **ADH**]$_m$-modified interface containing (1) one, (2) two, (3) three, (4) four, (5) five, and (6) six adsorbed **cassettes** after reconstitution. All impedance measurements were recorded in an equimolar 5 mM solution **of** $K_3[Fe(CN)_6]/K_4[Fe(CN)_6]$ in 100 mM PBS (pH 7.4) recorded at the electrodes open circuit potential **(230 mV)** and room temperature (25±2°).

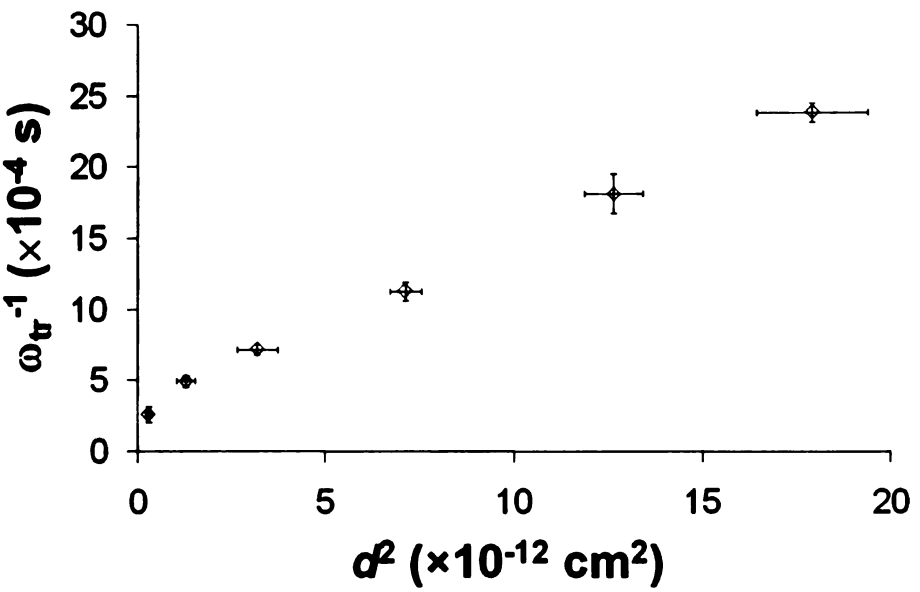

Figure 7.4: Plot of ω_{tr}^{-1} vs the square of ellipsometric thickness (d^2). The error bars indicate the mean ± the standard deviation (n=3).

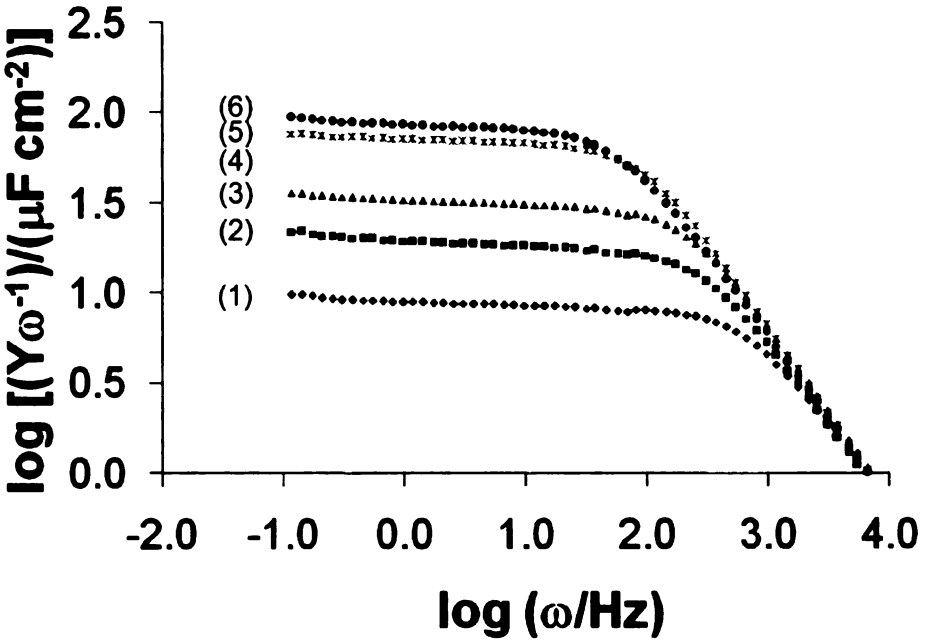

Figure 7.5: Plot of log(Y/ω) vs. log (ω) for the MPA-TBO-PEI-$NADP^+$-2° ADH-[PAA-TBO/PEI-$NADP^+$-2° ADH]$_m$-modified electrode containing (1) one, (2) two, (3) three, (4) four, (5) five, and (6) six adsorbed cassettes. The number to the left of each curve represents the number of adsorbed cassettes. All measurements were made in 100 mM PBS at the apparent E^0.

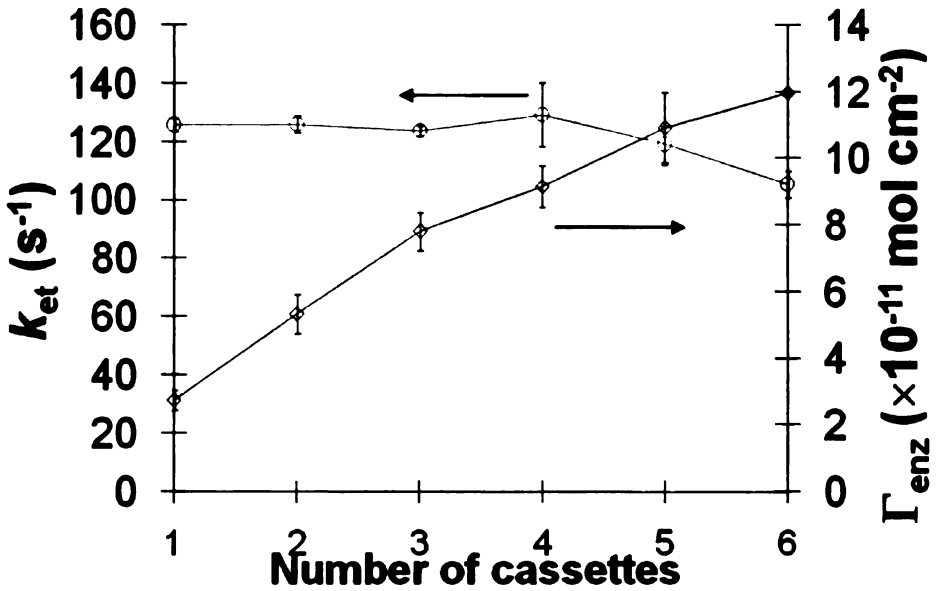

Figure 7.6: Plots of k_{et} (○) and surface coverage (◊) of electroactive 2^{o} ADH *vs.* the number of adsorbed cassettes. The error bars indicate the mean ± the standard deviation (n=3).

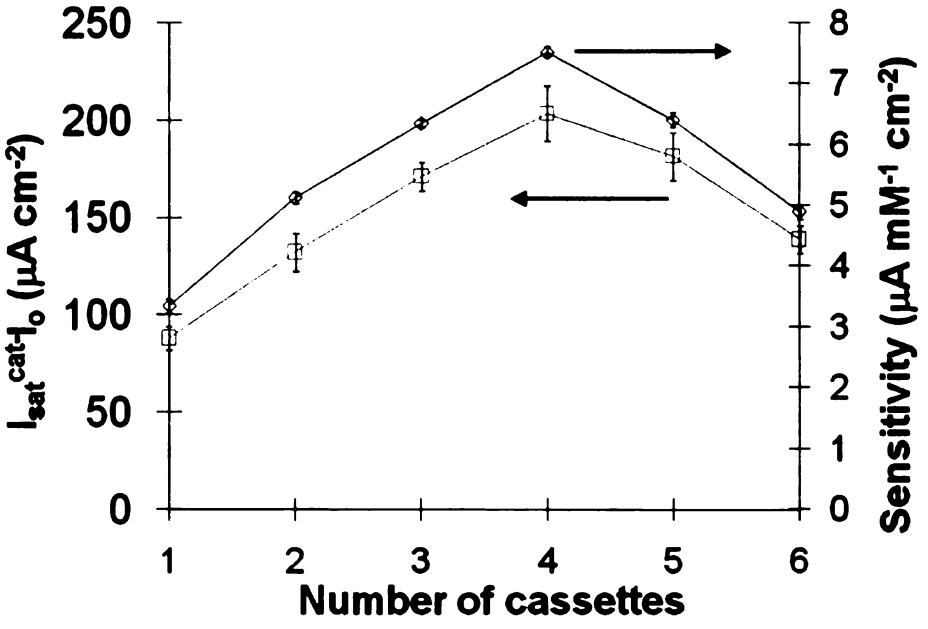

Figure 7.7: Saturation current (○) and sensitivity (◊) *vs.* the number of adsorbed cassettes. The error bars indicate the mean ± the standard deviation (n =3).

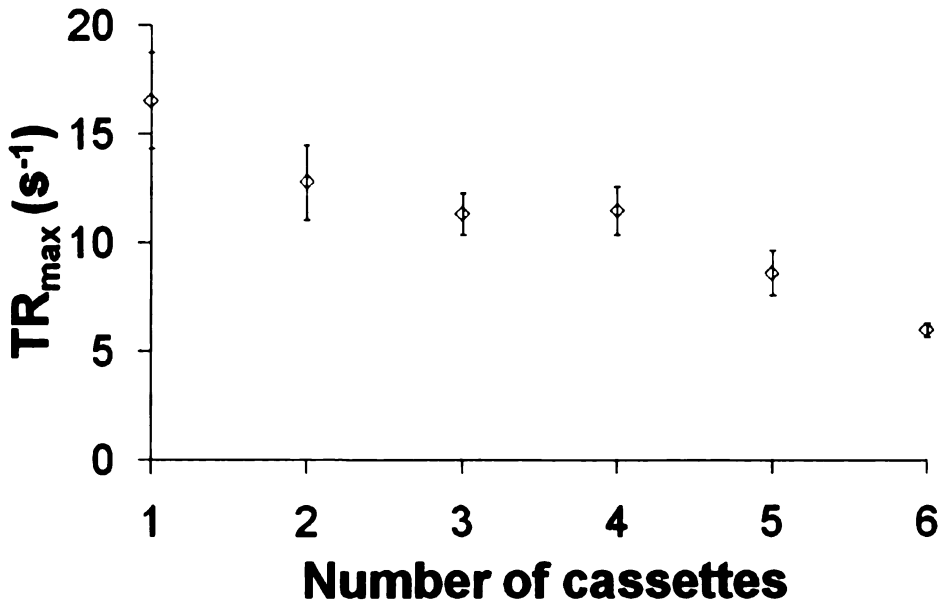

Figure 7.8: Plot of TR_{max} *vs.* the number of adsorbed cassettes. The error bars indicate the mean ± the standard deviation (n=3).

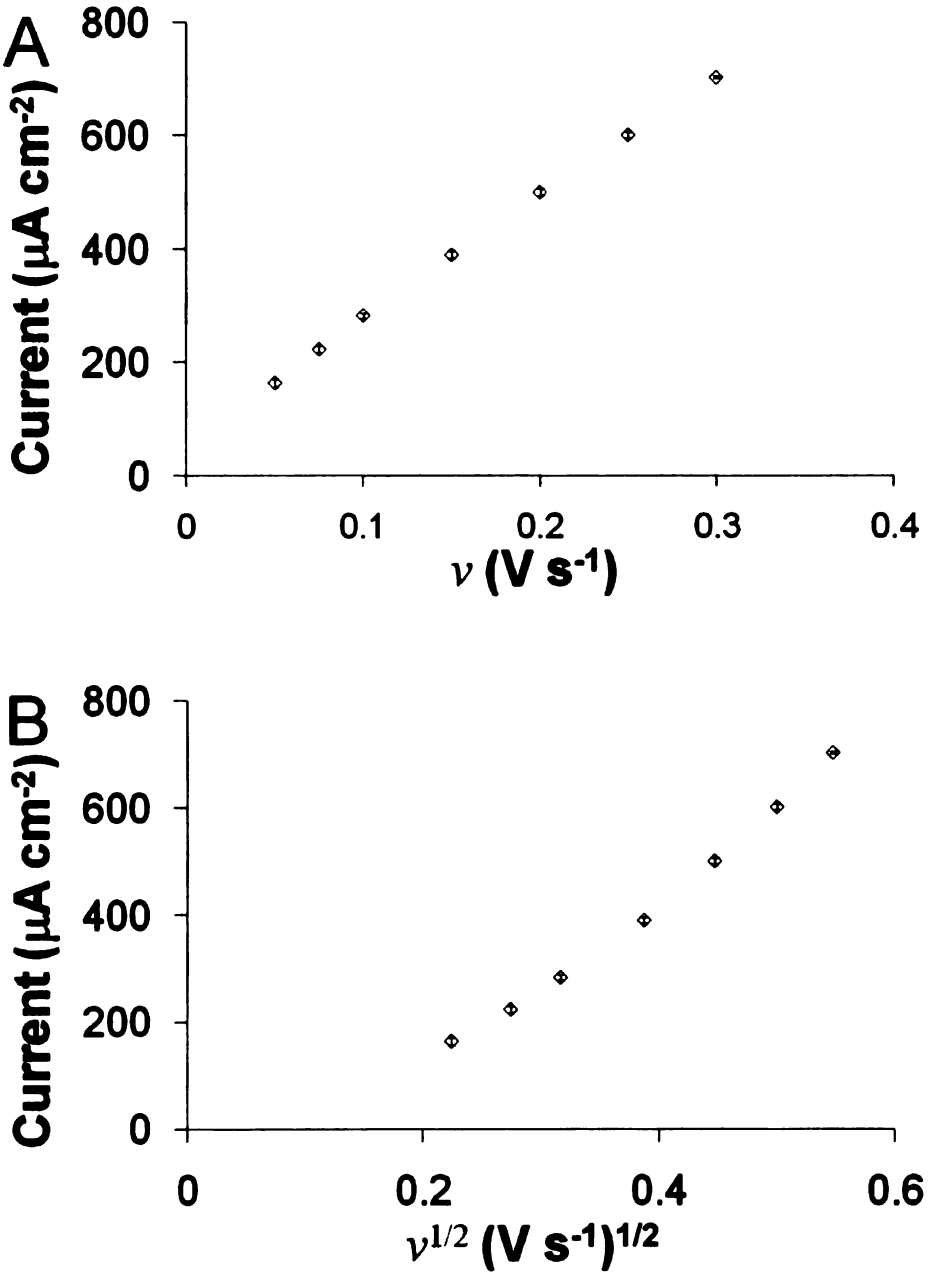

Figure 7.9: (A) The peak current (I_P) vs. scan rate (ν) and (B) I_P and $\nu^{1/2}$ a bioelectronic interface containing four cassettes.

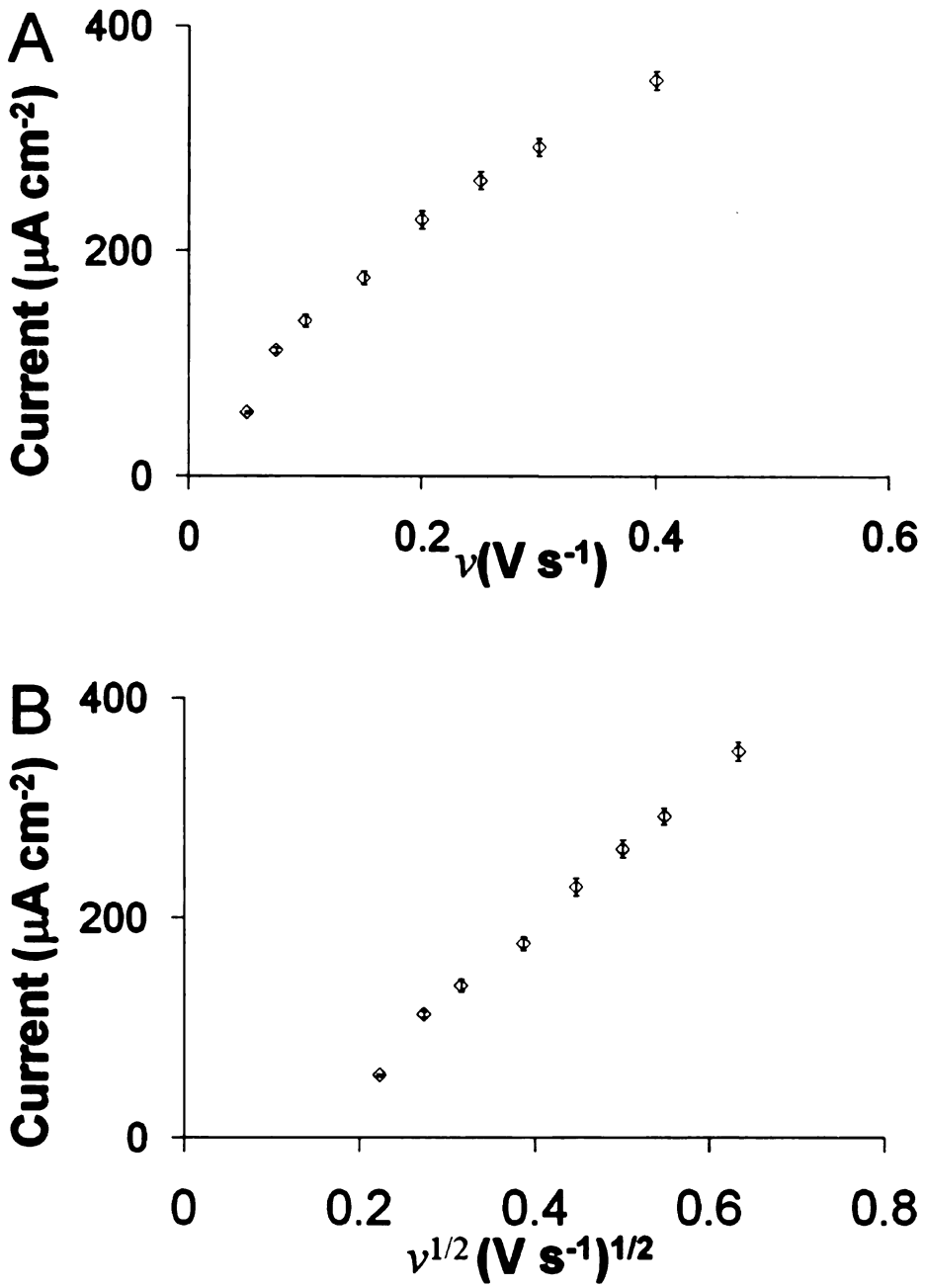

Figure 7.10: (A) The peak current (I_P) vs. square root of scan rate ($v^{1/2}$) and (B) I_P and v a bioelectronic interface containing five cassettes.

8. VERSATILE BIOELECTRONIC INTERFACES ON EXFOLIATED GRAPHITE SUPPORTS

8.1. Abstract

Bioelectronic interfaces that establish electrical communication between a redox enzyme and the electrode have potential applications as biosensors, biocatalytic reactors, and biological fuel cells. This chapter describes a versatile new fabrication method for bioelectronic interfaces using exfoliated graphite nanoplatelets (xGnP^{TM})-modified with poly(ethyleneimine) (PEI). The approach combines layer-by-layer (LbL) self assembly and directed molecular self assembly to yield a bioelectronic interface containing an electron mediator, xGnP, cofactor, and a dehydrogenase enzyme. The incorporation of xGnP into the interface increased the enzymatic surface coverage from $2.1\pm0.1\times10^{-11}$ mol cm^{-2} to $3.3\pm0.2\times10^{-11}$ mol cm^{-2}. The xGnP-modified interface exhibited a sensitivity of 5.6±0.1 μA mM^{-1} cm^{-2}, saturation current (I_{cat}^{sat}) of 184.8±5.1 μA cm^{-2}, and a turnover rate of 23.5±1.5 s^{-1}. The use of PEI allowed the interface to be removed via a simple pH change and then regenerated. Dyanamic light scattering (DLS) and zeta potential measurements were used to characterize the encapsulation of xGnP with PEI. Atomic force microscopy (AFM), chronoamperometry, cyclic voltammetry, electrochemical impedance spectroscopy (EIS), and field emission scanning electron microscopy (FE-SEM) were used to demonstrate the sequential assembly process and characterize the electrochemical properties of the bioelectronic interface. The original and regenerated interfaces exhibited virtually identical sensitivities, saturation currents, and turnover rates.

8.2. Introduction

Bioelectronic interfaces are able to achieve electrical communication between a bound redox enzyme and an electrode. Promising applications of bioelectronic interfaces include biosensors (Zayats, Katz et al. 2002; Hassler and Worden 2006; Hassler, Dennis et al. 2007; Hassler, Kohli et al. 2007), biocatalysts (Katz, Heleg-Shabtai et al. 1998; Diez-Perez, Guell et al. 2006), personal health monitors (Kricka 2001), and biofuel cells (Burdette and Zeikus 1994; Burdette, Secundo et al. 1997). Dehydrogenase enzymes are of particular interest for use in bioelectronic interface because they catalyze reactions that involve electron transfer. Dehydrogenases use a cofactor (e.g., β-nicotinamide adenine dinucleotide phosphate [$NADP^+$]) (Jornvall, Eklund et al. 1978) that needs to be electrochemically regenerated for continuous operation. Regeneration of the cofactor is not kinetically favored, requiring a high over potential, which can lead to cofactor degradation (Blaedel and Jenkins 1975; Schmakel, Santhanam et al. 1975). Electron mediators can circumvent this problem by shuttling electrons between the electrode and cofactor at moderate potentials (Ozdemir and Tuncel 2000; Senel, Camli et al. 2002).

Several molecular architectures have been used to bind the electron mediator, cofactor, and enzyme to the electrode in a manner that achieves multi-step electron transfer, including a linear electron transfer chain (Zayats, Katz et al. 2002), a branched electron transfer chain (Hassler and Worden 2006; Hassler, Dennis et al. 2007), and an imprinted polymer (Pogorelova, Zayats et al. 2003). However, these methods involve covalent linkages and make no provision for removal and replacement of labile components that degrade over time. To address this shortcoming, we developed a renewable bioelectronic interface via LbL-self assembly (Decher and Hong 1991; Decher

and Hong 1991; Decher, Hong et al. 1992) self assembly, in which the enzyme and cofactor can be easily removed by reducing the pH and reassembled to regenerate the activity of the interface (Hassler, Kohli et al. 2007).

LbL-self assembly is a versatile approach based on the alternating adsorption of materials containing oppositely charged functional groups (Decher and Hong 1991; Decher and Hong 1991; Decher, Hong et al. 1992), such as polyelectrolyte multilayers (PEMs) onto virtually any surface (Hammond 2004). The LbL approach has been extended to use attractive forces between layers other than ionic interactions including covalent bonding, hydrogen bonding, and other weak intermolecular interactions. Recently, proteins (Antipov and Sukhorukov 2004; Wang and Caruso 2005; Shutava, Kommireddy et al. 2006), colloidal particles (Chen, Yuan et al. 2006; Qi, Honma et al. 2006), cells (Kidambi, Lee et al. 2004), fullerenes (Guldi, Zilbermann et al. 2004), carbon nanotubes (Huang, Wang et al. 2006), and exfoliated graphite (Du, Xiao et al. 2004) have been incorporated into PEM films via LbL self-assembly.

The incorporation of graphene-based nanoparticles, including xGnP, carbon nanotubes, and fullerenes into polyelectrolyte films is significant due to their unique chemical, physical, and electronic properties (Luo, Killard et al. 2006). The chemical, physical, and electronic properties of xGnP are consistent with carbon nanotubes and fullerenes. The low production cost ($5/pound) and chemical, physical, and electronic properties make xGnP a suitable replacement for carbon nanotubes and fullerenes. Coating xGnP with polyelectrolytes not only increases the stability of the suspension, but also increases the surface charge of the xGnP, allowing them to self assemble in LbL films (Hendricks, Lu et al. 2008).

In this chapter we present a novel assembly method that incorporates polyelectrolyte-modified xGnP into a renewable bioelectronic interface. PEI was used to couple the xGnP, cofactor, and enzyme to the mediator-modified gold electrode in a configuration that allows electron transfer. Zeta potential was used to characterize the encapsulation of xGnP within PEI, and AFM, chronoamperometry, cyclic voltammetry, EIS, and FE-SEM were used to characterize the bioelectronic interface. Electron transfer properties including the concentration of redox active site and charge propagation diffusion coefficient (D_{app}) were also determined.

8.3. Materials and Methods

8.3.1. Media and strains

Escherichia coli (DH5α pADH B1M1-kan) culture containing a recombinant plasmid for 2° ADH from *Thermoaneorbactor ethanolicus* was grown, and purified as described in Chapter 2 (Hassler, Dennis et al. 2007).

8.3.2. Chemicals

All chemicals, including 3-mercaptopropionic acid (MPA), 1-ethyl-3-(3-dimethylaminopropyl) carbodiimide (EDC), n-hydroxysuccinimide (NHS), toluidine blue O (TBO), PEI, 3-carboxy phenylboronic acid (CBA), $NADP^+$, glutaric dialdehyde (25% in water), 2-propanol, ethanol, 2-butanol, and 2-pentanol were purchased from Sigma-Aldrich (St. Louis, MO). Ultrapure water (18.2 MΩ) was supplied by a Barnstead Nanopure-UV four-stage purifier (Barnstead International, Dubuque, IA).

8.3.3. Preparation of exfoliated graphite nanoplatelets

A 0.1 g sample of xGnP was dispersed in 1 g L^{-1} aqueous PEI solution (pH 7.0) containing 100 mM NaCl. The graphite dispersion was then tip-sonicated using a Branson B15 (Branson Ultrasonic Corporation, Danbury, CT) for 30 min (100 W, pulsed)

followed by stirring for 24 h. The PEI-coated-xGnP (PEI/xGnP) was then filtered using a 0.22-μm Millipore filter (Millipore, Billerica, MA) and washed three times with deionized water. The PEI/xGnP was collected and redispersed in 100 mL deionized water using tip sonication (50 W, pulsed) for 10 min.

8.3.4. Interface formation

The cleaned gold electrodes were soaked in a 100 mM MPA solution in ethanol for 1 h at room temperature (25±2°C) and thoroughly rinsed with ethanol and deionized water to remove weakly adsorbed MPA. The MPA-modified gold electrodes were incubated for 2 h in a 100 mM phosphate buffer solution (PBS) (pH 7.4) containing 10 mM NHS and 10 mM EDC, the EDC and NHS react with the carboxylic acid branch of the MPA forming a better leaving group on the surface of the MPA. The EDC/NHS-modified electrode was then reacted with the amine branch of TBO (1 mM TBO) resulting in the formation of an amide linkage between the TBO and the carboxylic group of the MPA (MPA-TBO). The MPA-TBO-modified electrodes were soaked in a 10 mM aqueous PEI/xGnP-solution, leading to the formation of an MPA-TBO-PEI/xGnP-functionalized electrode. A 5 mM aqueous CBA solution was activated at room temperature in the presence of 2 mM NHS and 2 mM EDC in 100 mM PBS for 2 h. The NHS-modified CBA was then reacted with the MPA-TBO-PEI/xGnP-functionalized electrodes for 1 h at room temperature, resulting in a MPA-TBO-PEI/xGnP-CBA-modified electrode. The MPA-TBO-PEI/xGnP-CBA-modified electrodes were then incubated in a 1 mM $NADP^+$ solution in 100 mM PBS for 1 h, resulting in the formation of a boronic acid linkage between the $NADP^+$ and the CBA (MPA-TBO-PEI/xGnP-$NADP^+$). The MPA-TBO-PEI/xGnP-$NADP^+$-functionalized gold electrodes were then

incubated in a 4.4 mg mL^{-1} solution of 2° ADH in 100 mM PBS for 1 h at room temperature and cross-linked with 25% (v/v) glutaric dialdehyde in water for 20 min. Scheme 8.1 illustrates the processes involved in functionalizing the electrode with MPA, TBO, PEI/xGnP, $NADP^+$, and 2° ADH. The resulting 2° ADH-modified interfaces were used for the biocatalytic oxidation of 2-propanol.

The cofactor and enzyme-functionalized PEI/xGnP was removed by incubating the electrode in 10 mM HCl (pH 2.0) for 30 min. For pH values below the pKa of MPA (pKa~4.3), MPA's unreacted carboxylic acid groups become protonated, decreasing the electrostatic interaction with the 2° ADH-modified PEI and allowing the PEI to disengage from the surface. To reassemble the interface, PEI/xGnP, CBA, $NADP^+$, and 2° ADH were readsorbed onto the TBO-modified MPA using the protocol described above.

8.3.5. Electrochemical techniques

Cyclic voltammetry, chronoamperometry, and electrochemical impedance spectroscopy were performed as described in Chapter 2 using an electrochemical analyzer (CHI660B, CH Instruments).

8.3.6. Surface characterization techniques

The zeta (ζ) potential of 1.0 mg mL^{-1} xGnP and PEI/xGnP samples were measured in 1 mM KCl solution at room temperature using a Zeta Plus ζ potential analyzer (Brookhaven Instrument Corporation, New York, New York, USA). AFM and ellipsometry were performed as described in Chapter 2.

8.4. Results

8.4.1. xGnP/PEI fabrication

Upon the adsorption of PEI, the ζ-potential for the xGnP shifted from -13.1±4.2 mV to +14.8±2.6 mV, indicating that the positively charged PEI binds to the negatively charged xGnP.

8.4.2. Interface fabrication

Figure 8.1A shows the impedance spectra for the MPA, MPA-TBO, MPA-TBO-PEI/xGnP, MPA-TBO-PEI/xGnP-$NADP^+$, and MPA-TBO-PEI/xGnP-$NADP^+$-2° ADH (Curves 1-5, respectively) modified electrodes. Fitting the equivalent-circuit model (Figure 2.1) to the impedance spectra using Z-view software gave R_{CT} values of 10.3±0.8, 24.5±2.5, 43.3±5.3, 49.7±5.1 and 80.2±7.2 Ω cm^2, for the MPA, MPA-TBO, MPA-TBO-PEI, MPA-TBO-PEI-$NADP^+$, and MPA-TBO-PEI-$NADP^+$-2° ADH-modified electrodes, respectively. The increase in R_{CT} with each sequential layer is consistent with the successive deposition of additional layers, thus providing evidence of electrode formation. Figure 8.1B (Curve 1) shows the Nyquist plot for the MPA-TBO-PEI-$NADP^+$-2° ADH-modified electrodes after HCl treatment. The resulting R_{CT} (19.7±2.5 Ω cm^2) was approximately equal to the original MPA-TBO-modified electrode suggesting that the HCl removed the PEI/xGnP, CBA, $NADP^+$, and 2° ADH. After neutralizing the pH and subsequent readsorbtion of PEI/xGnP, CBA, $NADP^+$, and 2° ADH, the R_{CT} (65.3±1.3 Ω cm^2) (Figure 8.1B, Curves 2-4) were consistent with the original MPA-TBO-PEI/xGnP-$NADP^+$-2° ADH-modified electrode. The impedance

measurements indicate that the bioelectronic interface could be removed by changing pH and then reconstituted.

Figure 8.2A shows AFM images of the MPA-TBO-PEI/xGnP-$NADP^+$-2° ADH-modified electrode; a terrace-type structure is present suggesting that the xGnP is bound to the surface. Upon treatment with HCl, the terrace-type structure disappeared (Figure 8.2B), indicating that the PEI/xGnP was removed. Upon readsorption of PEI/xGnP, $NADP^+$ and 2° ADH the terrace-type structure reappears (Figure 8.2C) suggesting that the PEI/xGnP was readsorbed onto the electrode. The AFM results are consistent with the EIS suggesting that the $NADP^+$-2° ADH-modified PEI/xGnP can be removed via a change in pH and subsequently readsorbed on the MPA-modified gold electrode.

8.4.3. Determination of redox site concentration

The redox site concentration (Γ_{med}) was estimated from the low frequency impedance using Eq. 2.7. The experimental data for the MPA-TBO-PEI/xGnP-$NADP^+$-2° ADH-modified electrode was fit with the equivalent circuit (Figure 2.2) (Brug, Vandeneeden et al. 1984). The best fit value for C_F was determined to be $5.2\pm0.3\times10^{-5}$ F. The surface coverage of TBO (Γ_{TBO}) was determined as $8.7\pm0.1\times10^{-11}$ mol cm^{-2}.

8.4.4. Determination of charge propagation diffusion coefficient

The ω_{tr} value was determined graphically from plots of $\log(Y/\omega)$ vs $\log(\omega)$ (Figure 8.3) to be 58.2±9.6 Hz; this value was used in Eq. 2.8 to calculate a D_{app} of $1.0\pm0.3\times10^{-10}$ cm^2 s^{-1}. The value of D_{app} should be considered a binary apparent diffusion coefficient, since at least two different species could be responsible for charge transfer inside the

film: the TBO_{ox}/TBO_{red} redox centers through an electron hopping mechanism and counter-ion diffusion (Tagliazucchi and Calvo 2007). The high frequency resistance (measured at 10 kHz) for the MPA-TBO-PEI/xGnP-$NADP^+$-2° ADH-modified electrode varied by 10% over the potential range -200 to 200 mV, indicating that D_{app} is governed by electron hopping (Tagliazucchi and Calvo 2007).

8.4.5. Interface characterization

8.4.5.1. Enzyme Adsorption Kinetics

Figure 8.4A shows the cyclic voltammograms at different times of 2° ADH adsorption on a MPA-TBO-PEI/xGnP-$NADP^+$-modified electrode obtained at a constant 2-propanol concentration (25 mM) in 100 mM PBS (pH 7.4) at room temperature. Figure 8.4B shows the peak anodic current as a function of adsorption time. The pseudo-first-order absorption time constant derived from the data was 49.2±1.0 min. The pseudo-first-order absorption time constant is higher than that obtained for 2° ADH adsorption on a MPA-TBO-PEI-$NADP^+$-modified electrode (40.1±2.7 min) (Hassler, Kohli et al. 2007) suggesting that the incorporation of the xGnP decreases the 2° ADHs affinity for the $NADP^+$ bound on the surface of the electrode.

8.4.5.2. Effects of pH changes

The influence of pH on the redox reactions is shown in Figure 8.5. The oxidation potentials varied linearly with pH, giving slopes of 58.8±2.7 mV $(pH\ unit)^{-1}$. According to the Nernst equation, the theoretical value of this slope should be 59.16 b/d mV $(pH\ unit)^{-1}$ (Wang, Li et al. 2006), where b and d correspond to the number of protons and electrons transferred during oxidation, respectively. The proximity of the measured values to those predicted by Nernst equation for the case where $b=d$ suggests that an

equal number of electrons and protons are exchanged during the anodic and cathodic sweeps, respectively.

8.4.5.3. Interface properties

Figure 8.6 shows the chronoamperometric response for the MPA-TBO-PEI/xGnP-$NADP^+$-2° ADH-modified electrode. Fitting Eqs. 2.1 and 2.3 to the chronoamperometric data gave values for the an electron transfer rate constant (k_{et}) and an apparent enzymatic surface coverage (Γ_{enz}) of 137.7±11.9 s^{-1} and of 3.3±0.1×10^{-11} mol cm^{-2}, respectively. The measured Γ_{enz} is 50% greater than that measured for the MPA-TBO-PEI-$NADP^+$-2° ADH-modified electrode without xGnP (2.1±0.1×10^{-11} mol cm^{-2}) (Hassler, Kohli et al. 2007). Figure 8.7A shows the cyclic voltammograms of the MPA-TBO-PEI/xGnP-$NADP^+$-2° ADH-modified electrode. The peak anoidic current increased linearly with 2-propanol concentration (Figure 8.7B) below 30 mM, with a sensitivity of 5.6±0.1 μA mM^{-1} cm^{-2}. At 2-propanol concentrations above 30 mM, the anodic current reached a saturation current (I_{cat}^{sat}) of 184.8±5.1 μA cm^{-2}. The sensitivity and I_{cat}^{sat} were found to be 50% greater than that found for the MPA-TBO-PEI-$NADP^+$-2° ADH-modified electrode (3.5±0.1 μA mM^{-1} cm^{-2} and 134.2±0.9 μA cm^{-2} μA cm^{-2}, respectively) (Hassler, Kohli et al. 2007). On the other hand, the TR_{max} (23.5±1.5 s^{-1}) was comparable to the MPA-TBO-PEI-$NADP^+$-2° ADH-modified electrode (21.2±1.5 s^{-1}) (Hassler, Kohli et al. 2007) suggesting the activity of the 2° ADH is unaffected by the presence of the xGnP.

The selectivity of the MPA-TBO-PEI/xGnP-$NADP^+$-2° ADH-modified electrode was examined by testing alternative substrates. Table 8.1 shows the values of I_{cat}^{sat}, sensitivity, and TR_{max} for the MPA-TBO-PEI/xGnP-$NADP^+$-2° ADH-modified electrode in the presence of 2-propanol, ethanol, 2-butanol, and pentanol. These data are consistent with the literature values for 2° ADH (Burdette, Secundo et al. 1997).

To confirm renewability of the interface, the performance properties of the MPA-TBO-PEI/xGnP-$NADP^+$-2° ADH-modified electrode were measured before and after interface removal and reconstitution (Table 8.2). The values of Γ_{enz}, k_{et}, I_{cat}^{sat}, sensitivity, and TR_{max} values for the reconstituted interface were virtually identical to those for the MPA-TBO-PEI/xGnP-$NADP^+$-2° ADH-modified electrode before HCl treatment, confirming that the interface could be removed and reconstituted without and loss in performance.

The results presented here demonstrate the fabrication of a bioelectronic interface containing xGnP. The sensitivity and I_{cat}^{sat} were found to be nearly twice that found for the MPA-TBO-PEI-$NADP^+$-2° ADH-modified electrode. The ability to quickly and inexpensively remove and reconstitute the interface without diminishing its performance could greatly extend the useful lifetime of biofuel cells, biosensors, and biocatalysts. Because the fabrication method is based on molecular self-assembly of components from aqueous solutions, it is compatible with microfluidic processes and use in high throughput systems (e.g., biosensor arrays).

8.5. Discussion

Recently, graphene-based nanoparticles, including xGnP, carbon nanotubes, and fullerenes have been incorporated into polyelectrolyte films (Luo, Killard et al. 2006). The chemical, physical, and electronic properties for xGnP are consistent with carbon nanotubes and fullerenes. The low production cost ($5/pound) and chemical, physical, and electronic properties make xGnP a suitable replacement for carbon nanotubes and fullerenes. The incorporation of xGnP into the bioelectronic interface is believed to increase Γ_{enz} and increase D_{app}. The Γ_{enz}, sensitivity and I_{cat}^{sat} were found to be 50% greater while TR_{max} was comparable to the MPA-TBO-PEI-$NADP^+$-2° ADH-modified electrode suggesting that the xGnP can be incorporated without decreasing bioelectronic activity. Huang and Yu suggests that if the xGnP where standing on end the Γ_{enz} would increases by a factor of 10 (Huang, Yu et al. 2009), suggesting that the 50% increase in Γ_{enz} is associated with the xGnP lying parallel to the surface of the gold electrode.

The research could be extended to control the binding of xGnP on the surface of the electrode; by controlling the mechanism for xGnP binding we could maximize Γ_{enz} while minimizing the effects on substrate/product diffusion. The current approach can also be extended to other nanoparticles including: fullerenes, carbon nanotubes, colloidal gold particles or other colloidal metals.

8.6. Conclusions

This chapter describes the fabrication of a novel xGnP-modified, dehydrogenase-based bioelectronic interface. The approach is renewable in that the labile components of the interface, including the polyelectrolyte-bound cofactor and enzyme could be removed by decreasing pH, and then reconstituted to regenerate the biocatalytic activity. Cyclic

voltammetry, chronoamperometry, and EIS were used to characterize the performance properties of the resulting bioelectronic interfaces. The I_{cat}^{sat}, sensitivity, and TR_{max} for the MPA-TBO-PEI/xGnP-$NADP^+$-2° ADH-modified interface before the removal were 184.6±5.1 μA cm^{-2}, 5.6±0.1 μA mM^{-1} cm^{-2}, and 23.5±1.5 s^{-1}, respectively, compared to 185.7±5.8 μA cm^{-2}, 5.6±0.3 μA mM^{-1} cm^{-2}, and 23.3±2.1 s^{-1}, respectively, for the reconstituted bioelectronic interface. With the incorporation of xGnP, the I_{cat}^{sat} and sensitivity doubled. The ability to renew bioelectronic interfaces is a novel capability that has potential applications for biosensors, biocatalytic reactors, and biological fuel cells.

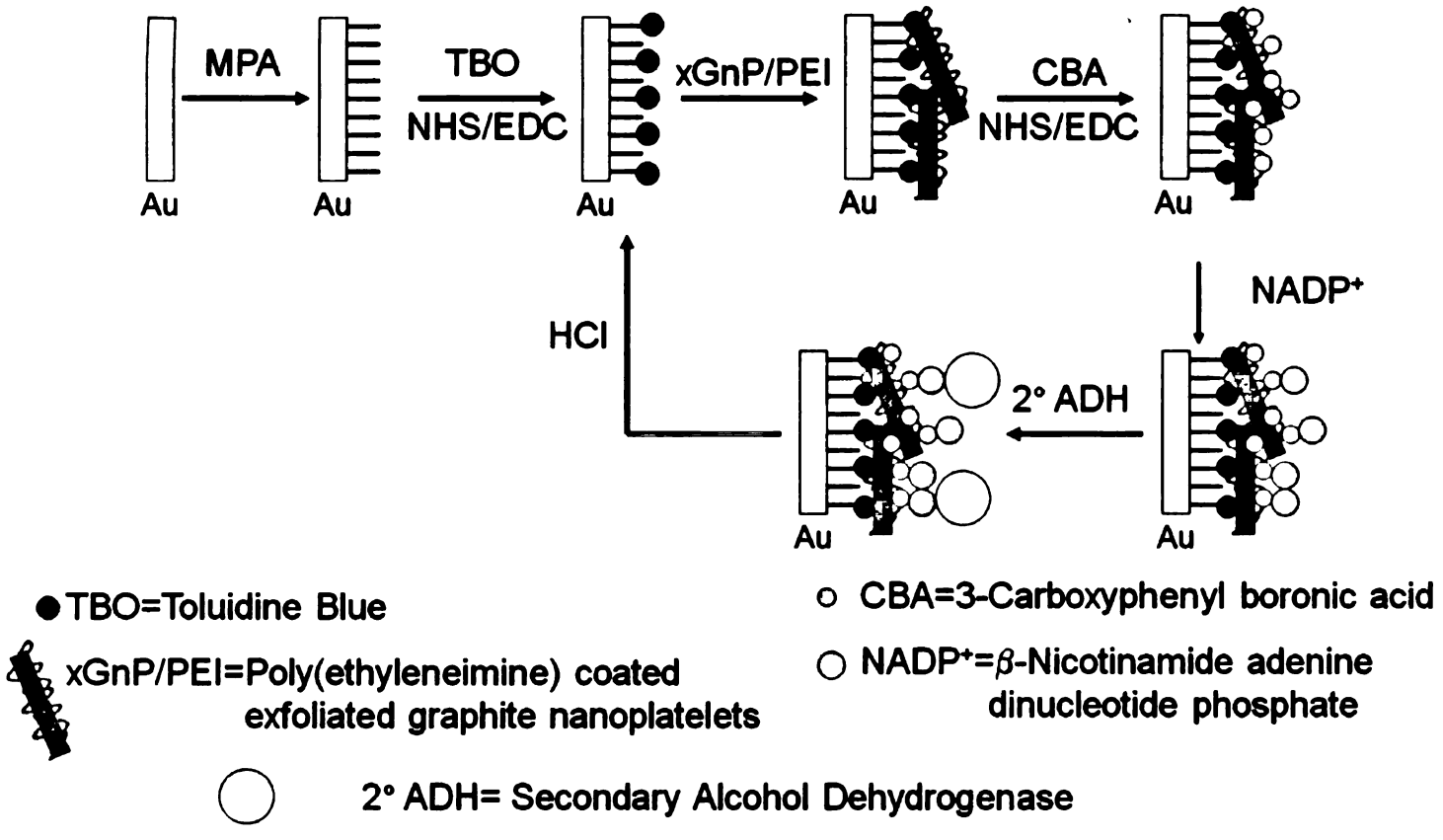

Scheme 8.1: Sequential steps in the formation of integrated MPA-TBO-PEI/xGnP-$NADP^{+}$-2° ADH functionalized gold electrode.

Table 8.1: Selectivity of the MPA-TBO-PEI/xGnP-$NADP^{+}$-2^{o} ADH-modified electrode to the substrates: 2-propanol, ethanol, 2-butanol, and 2-pentanol.

Compound	I_{cat}^{sat} ($\mu A\ cm^{-2}$)	Sensitivity ($\mu A\ mM^{-1}\ cm^{-2}$)	TR_{max} (s^{-1})
2-propanol	184.8±5.1	5.6±0.0	17.0±1.2
Ethanol	107.4±1.5	2.6±0.1	8.2±0.5
2-Butanol	88.8±0.8	2.5±0.1	7.2±0.4
2-Pentanol	82.8±2.8	2.3±0.1	6.5±0.6

Table 8.2: Comparison of performance of the MPA-TBO-PEI/xGnP-$NADP^{+}$-2^{o} ADH-modified electrode before and after interface removal by HCl wash and reconstitution.

	Γ_{enz} ($\times 10^{-11}$ mol cm^{-2})	k_{et} (s^{-1})	I_{cat}^{sat} ($\mu A\ cm^{-2}$)	Sensitivity ($\mu A\ mM^{-1}\ cm^{-2}$)	TR_{max} (s^{-1})
Before HCl wash	4.6±0.3	135.7±5.9	184.8±5.1	5.6±0.0	17.0±1.2
After Reconstitution	4.5±0.2	136.7±10.8	185.6±5.8	5.6±0.1	17.1±1.2

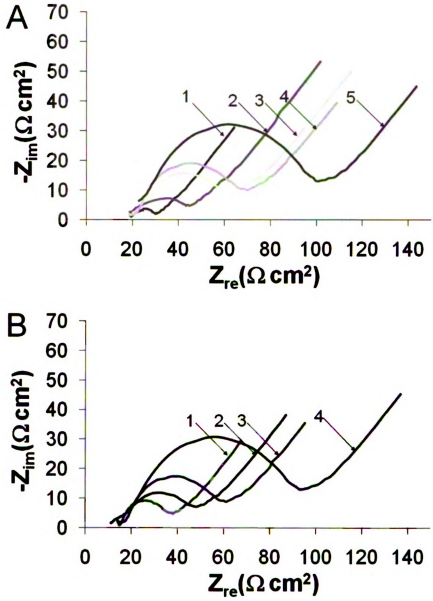

Figure 8.1: (A) Nyquist plots (1) MPA, (2) MPA-TBO, (3) MPA-TBO-PEI/xGnP, (4) MPA-TBO-PEI/xGnP-$NADP^+$, and (5) MPA-TBO-PEI/xGnP-$NADP^+$-2° ADH-modified electrode and (B) Nyquist plots for the (1) MPA-TBO-PEI/xGnP-$NADP^+$-2° ADH-modified electrode after washing with 10 mM HCl, and the reassembled (2) MPA-TBO-PEI/xGnP, (3) MPA-TBO-PEI/xGnP-$NADP^+$, and (4) MPA-TBO-PEI/xGnP-$NADP^+$-2° ADH-modified electrode after interface removal and reconstitution. All impedance measurements were recorded in an equimolar 5 mM solution of $K_3[Fe(CN)_6]/K_4[Fe(CN)_6]$ in 100 mM PBS (pH 7.4) recorded at the electrodes open circuit potential (230 mV) and room temperature (25±2°).

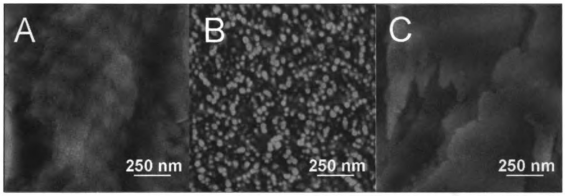

Figure 8.2: AFM characterization of the PEI/xGnP-modified electrode: (A) after deposition of the PEI-modified xGnP, (B) after HCl treatment, and (C) the MPA-TBO-PEI/xGnP-$NADP^{+}$-2^{o} ADH-functionalized electrode, after being reconstituted on the interface.

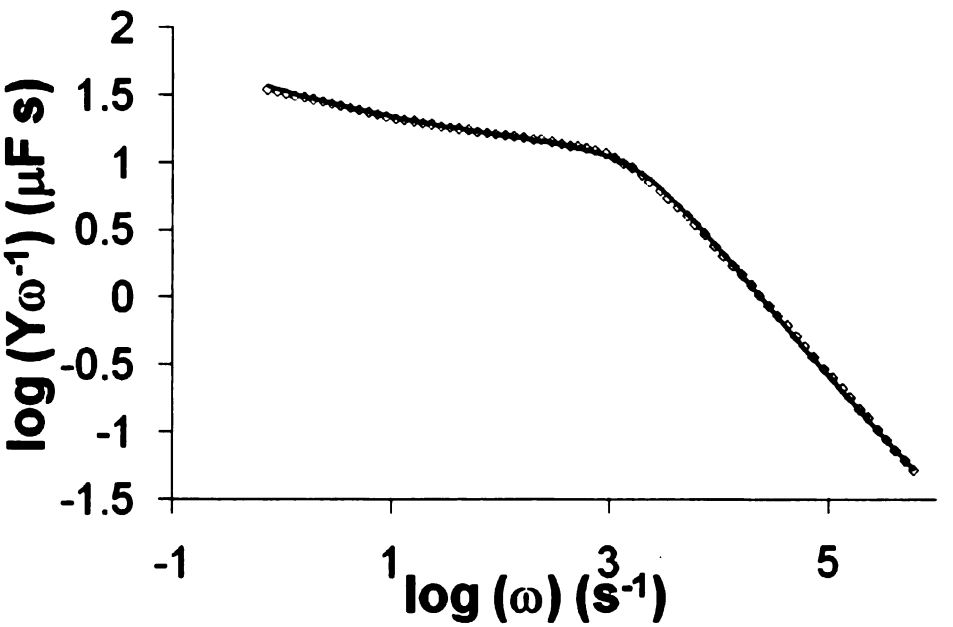

Figure 8.3: Log (Y/ω) vs log (ω) plots for the MPA-TBO-PEI/xGnP-$NADP^+$-2° ADH-functionalized electrode in 100 mM PBS (pH 7.4), E=-200 mV. Solid line represents the best fit of the circuit.

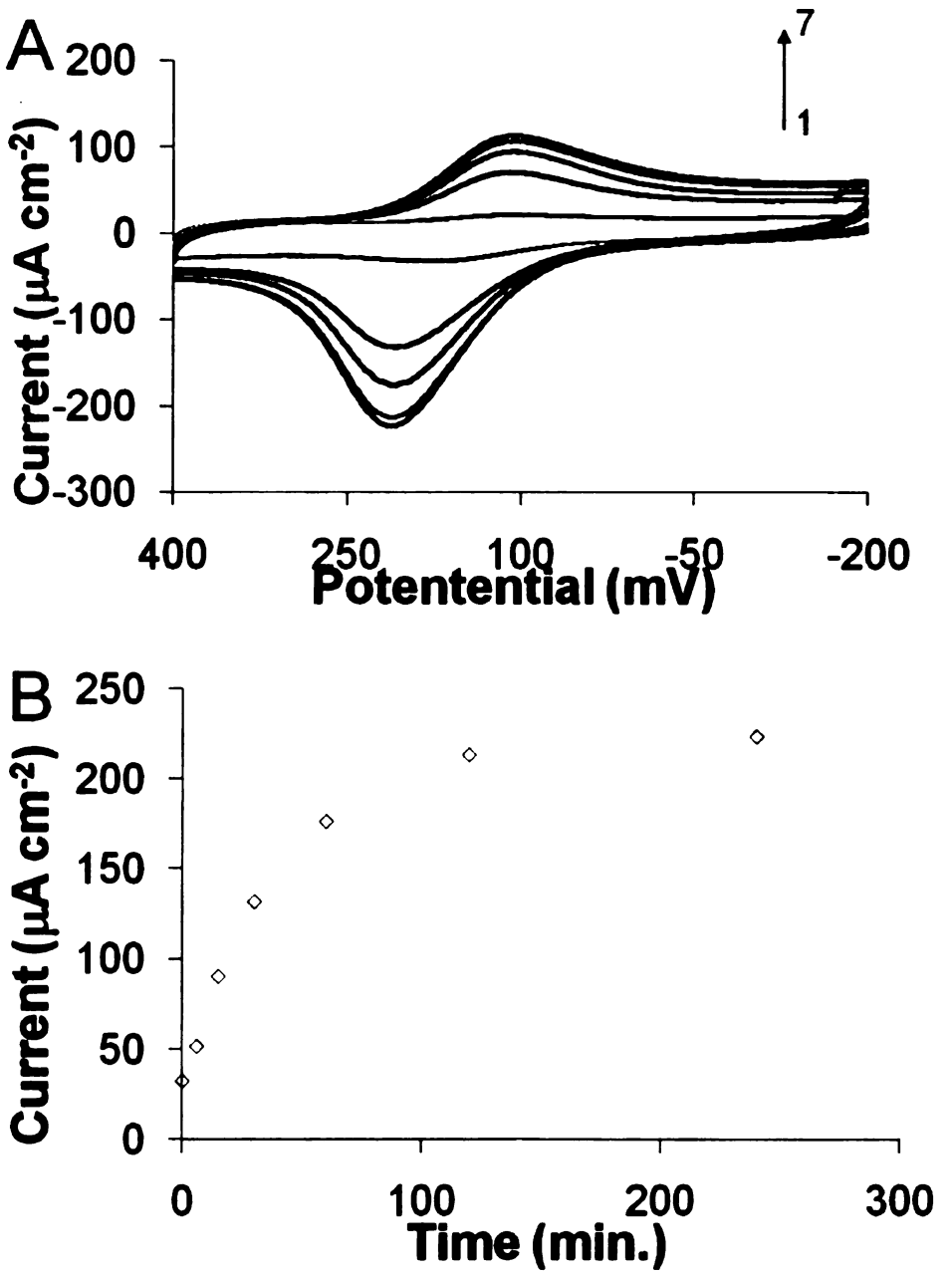

Figure 8.4: (A) Cyclic voltammograms of the MPA-TBO-PEI/xGnP-$NADP^+$-functionalized electrode after various times of 2° ADH of reconstitution: (1) 0, (2) 6, (3) 15, (4) 30, (5) 60, (6) 120, and (7) 240 min. The data were recorded in 100 mM PBS (pH 7.4) containing 25 mM 2-propanol at room temperature and a potential scan rate of 100 mV s^{-1}. (B) Peak electrocatalytic current at various time intervals.

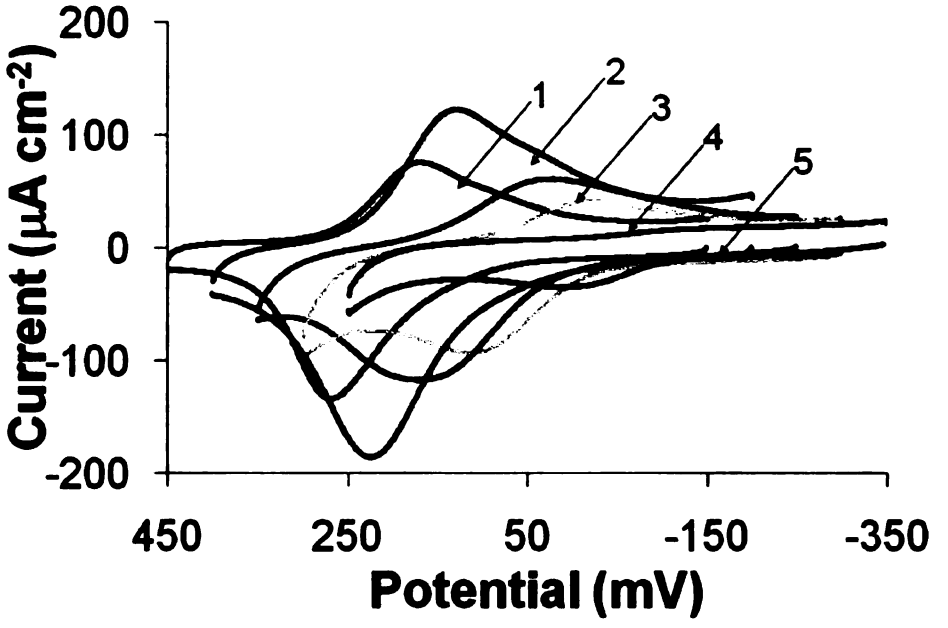

Figure 8.5: Cyclic voltammograms of the MPA-TBO-PEI/xGnP-$NADP^+$-2° ADH-functionalized electrode in 100 mM PBS containing 25 mM 2-propanol at room temperature, at various pH values: (1) 6.0, (2) 7.0, (3) 8.0, (4) 9.0, and (5) 10.0.

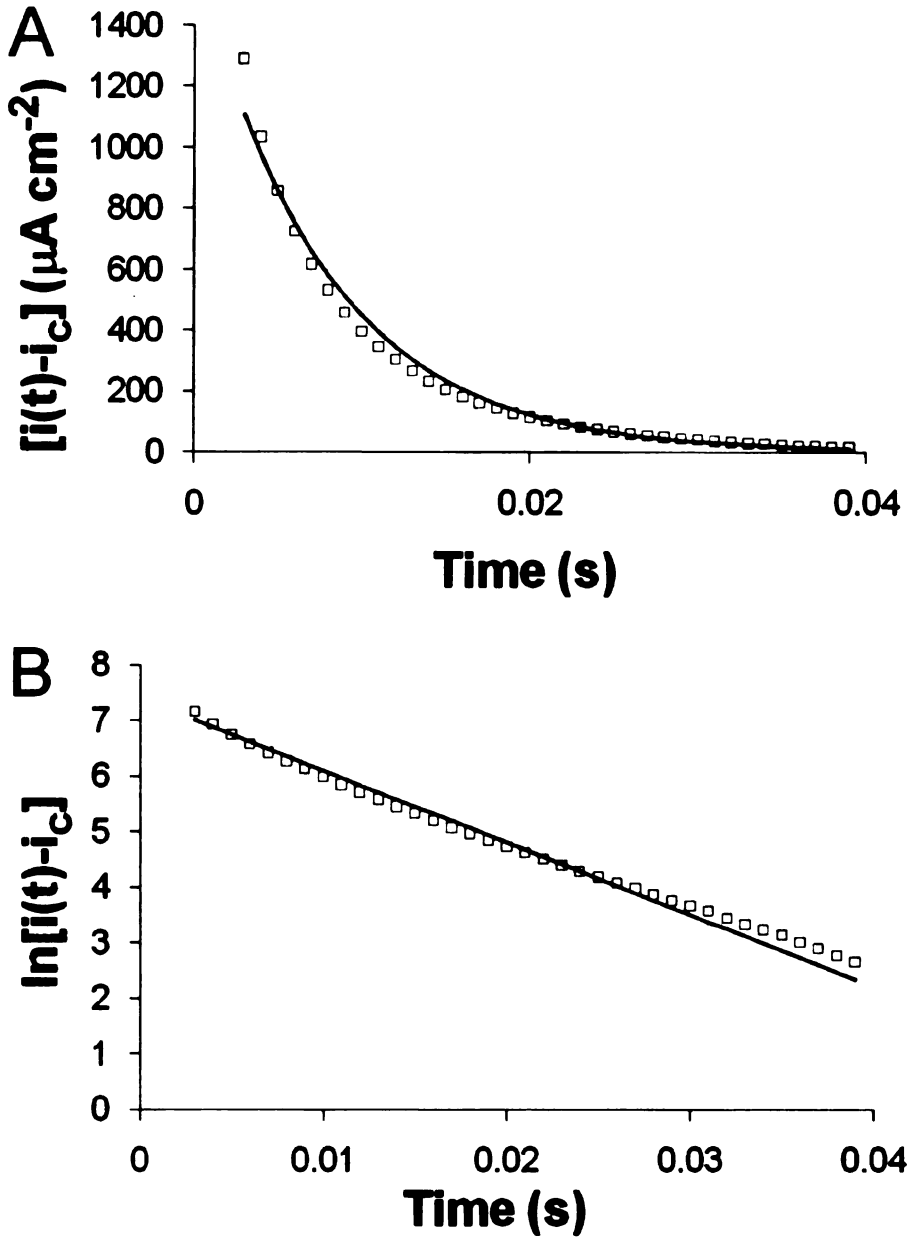

Figure 8.6: (A) Current transient for a potential step from -200 mV to 400 mV for a MPA-TBO-PEI/xGnP-$NADP^{+}$-2° ADH-functionalized electrode in 100 mM PBS (pH 7.4) containing 25 mM 2-propanol at room temperature (25±2°C). (B) Shows the plots of $\log[i(t)-i_c]$ after double layer charging. The solid line represents the curve of best fit to the data.

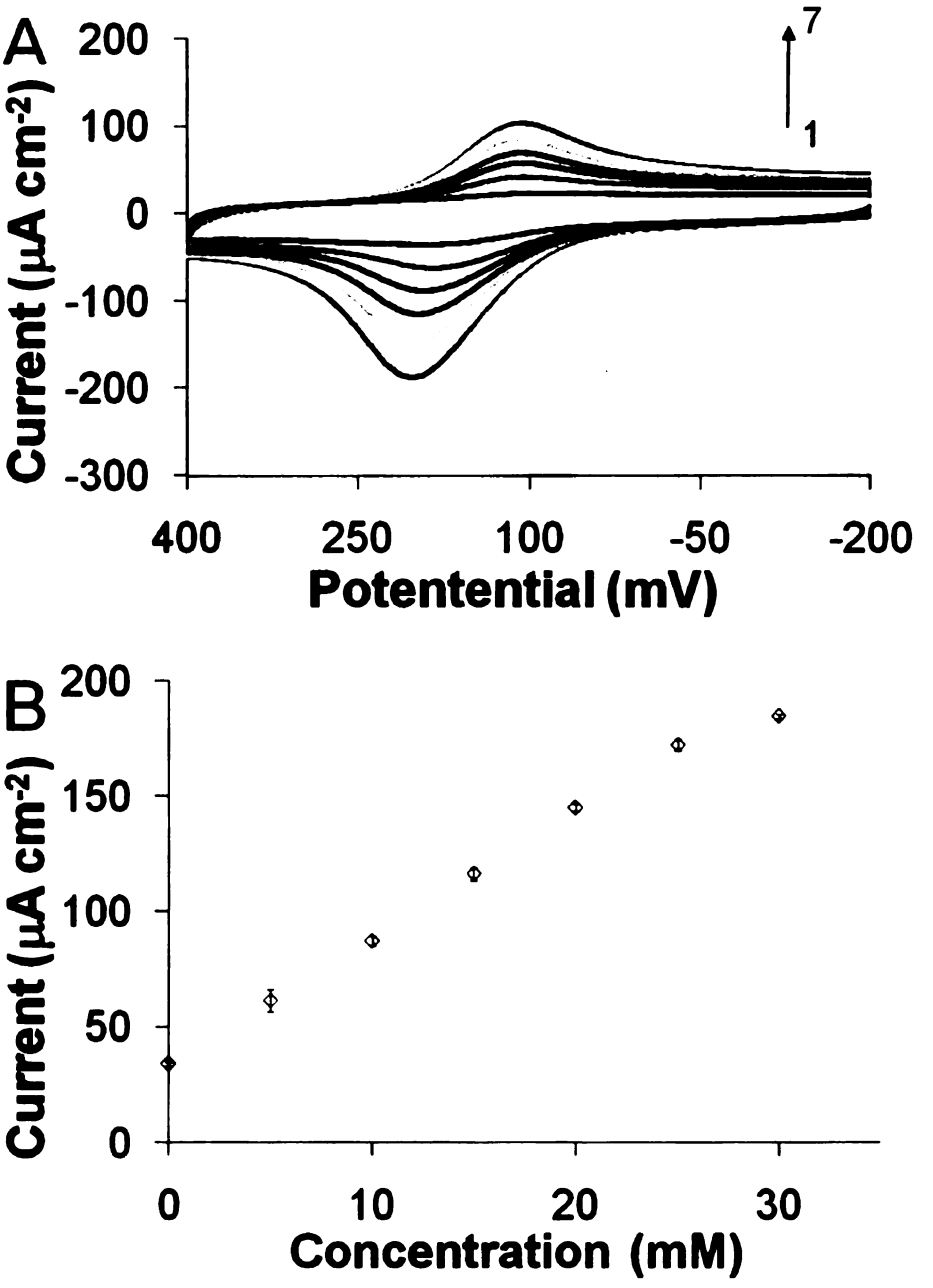

Figure 8.7: (A) Cyclic voltammograms of the MPA-TBO-PEI/xGnP-$NADP^+$-2° ADH-functionalized electrode in 100 mM PBS (pH 7.4) at room temperature in the presence of different 2-propanol concentrations: (1) 0, (2) 5, (3) 10, (4) 15, (5) 20, (6) 25, and (7) 30 mM. The data were recorded at a potential scan rate of 100 mV s^{-1}. (B) Peak electrocatalytic current at various fructose concentrations. The error bars indicate the mean ± the standard deviation (n=3).

9. THEORETICAL STUDY OF REVERSIBLE ENZYMES AT AN ELECTRODE SURFACE

9.1. Abstract

Bioelectronic interfaces containing dehydrogenases have potential utility in important applications including biosensors, biocatalytic reactors and biofuels cells. Engineering these systems is challenging, because their performance properties depend on a complex set of simultaneous molecular processes, including multistep electron exchange between an electrode, an electron mediator, a cofactor, and the enzyme; interphase and intraphase transport of the substrates, products, and electrons; and reversible bi-bi enzyme kinetics involving substrates, products, and electrons. This paper presents a mathematical model that captures these simultaneous processes and predicts their effects on the overall system performance. The steady-state model was expressed in terms of natural dimensionless groups and solved numerically to explore the effects of reversible enzyme and mediator kinetics, substrate, product, and electron diffusion, and substrate, product, and mediator concentration, and electrode potential on the overall reaction rate. The effects of substrate, product, and electron transport resistance on the overall reaction rate were correlated in terms of an effectiveness factor and an observable Thiele modulus. These results have utility in design and optimization of practical bioelectronic processes involving dehydrogenases.

9.2. Introduction

Bioelectronic interfaces have potential utility in important applications including biofuel cells (Barton, Gallaway et al. 2004), biocatalysis (Asuri, Karajanagi et al. 2006; Hassler, Dennis et al. 2007), and biosensors (Zayats, Katz et al. 2002; Hassler, Kohli et al. 2007). A major challenge in the formation of bioelectronic interfaces is establishing efficient electrical communication between an electrode and an immobilized redox enzyme (Park and Zeikus 1999; Park and Zeikus 2000; Zayats, Katz et al. 2002; Hassler, Dennis et al. 2007; Hassler, Kohli et al. 2007). The use of dehydrogenase-containing interfaces requires incorporation of a cofactor [e.g., β-nicotinamide adenine dinucleotide phosphate ($NADP^+$)] (Burdette and Zeikus 1994; Burdette, Vieille et al. 1996; Burdette, Secundo et al. 1997; Burdette, Tchernajencko et al. 2000) that transfers electrons to the enzyme's redox center. Direct electrochemical oxidation or reduction of nicotinamide cofactors requires the use of high overpotentials (Blaedel and Jenkins 1975; Schmakel, Santhanam et al. 1975), which can be minimized using an electron mediator (Ozdemir and Tuncel 2000; Senel, Camli et al. 2002). Several molecular architectures have been developed to immobilize the electron mediator, cofactor, and enzyme in an orientation that affords multistep electron transfer (Zayats, Katz et al. 2002; Hassler and Worden 2006; Hassler, Dennis et al. 2007; Hassler, Kohli et al. 2007). One shortcoming of these architectures is that they make no provision for periodic removal and replacement of the enzyme and cofactor, which have limited useful lifetimes (Burdette, Tchernajencko et al. 2000; Wang, Feng et al. 2003; De Temino, Hartmeier et al. 2005). To address this shortcoming, we recently developed a renewable bioelectronic interface in which the

enzyme and cofactor can be easily removed by reducing the pH, and then replaced to regenerate the bioelectronic activity (Hassler, Kohli et al. 2007).

Design and optimization of a bioelectronic interface for a specific application would be aided by a mathematical model able to quantitatively predict performance properties. Development of suitable models is challenging, because performance depends on a variety of potentially rate-limiting molecular and electronic processes, including interphase and intraphase transport of the substrates, products; multistep electron transfer between an electrode, an electron mediator, a cofactor, and the enzyme; and reversible electrochemical reactions that occur both at the enzyme active site and the electrode surface.

Models that describe subsets of these processes have been reported previously. Kinetic models have been developed to describe reaction of a soluble substrate with a mediator bound within an electrode-immobilized film (Andrieux, Dumasbouchiat et al. 1982; Scott and Bowden 1994; Rahamathunissa and Rajendran 2008). Bartlett and Pratt presented a comprehensive treatment of substrate diffusion and reaction within a uniform film containing immobilized enzyme and mediator at an electrode surface (Bartlett and Pratt 1995). However, this latter approach did not describe reversible reactions by either the enzyme or the mediator. It as also neglected interphase mass transfer resistance between the film and bulk liquid.

This paper extends the Bartlett and Pratt approach to include reversible, bi-bi enzyme reaction kinetics for the dehydrogenase, reversible kinetics for the mediator, and interphase mass transfer resistance. Dimensional analysis was used to determine key dimensionless groups that govern system behavior. The steady-state model was solved

numerically and used to explore the effects of reversible enzyme and mediator kinetics, substrate, product, and electron diffusion, and substrate, product, and mediator concentration on the overall reaction rate. Effects of key independent variables on system performance are shown, and methods by which the model could be applied to design and optimization of bioelectronic processes are described.

9.3. Model Development

Scheme 9.1 shows the conceptual framework underlying the model. A redox enzyme (E) that follows an ordered bi-bi mechanism (Segel 1993) reversibly converts an reduced substrate (S) into an oxidized product (P). The oxidized enzyme/cofactor complex (EC_1) and reduced enzyme-cofactor complex (EC_2) exchange electrons with the oxidized and reduced forms of the electron mediator (M_1 and M_2, respectively). The substrate and product diffuse through the film with diffusion coefficients D_S and D_P, respectively. Charge transport through the film is modeled after a diffusion process. The "mediator diffusion coefficient" (D_M) is assumed to describe electron transport through the film via either physical migration of soluble mediator molecules, or electron hopping between adjacent molecules of immobilized mediators. Partitioning of the substrate and product across the solution/membrane interface is modeled using the partition coefficients K_S and K_P, respectively. Interphase mass transfer resistances for substrate and product transport are described using mass transfer coefficients ($k_{x,S}$ and $k_{x,P}$, respectively). The enzyme (and in some cases mediator) is assumed to be immobilized, with a constant concentration across the thickness (l) of the membrane.

Based on this conceptual model, the following conservation equations for S, P, and M_1 describe the simultaneous transport and reaction within the film:

$$\frac{\partial S}{\partial t} = D_S \frac{\partial^2 S}{\partial x^2} + v_S \tag{9.1}$$

$$\frac{\partial P}{\partial t} = D_P \frac{\partial^2 P}{\partial x^2} + v_P \tag{9.2}$$

$$\frac{\partial [M_1]}{\partial t} = D_M \frac{\partial^2 [M_1]}{\partial x^2} + v_M \tag{9.3}$$

where v_S, v_P, and v_M are the volumetric reaction rates for the enzyme reaction with respect to S, P, and M_1, respectively. At steady state, Eqs. 9.1 through 9.3 simplify to

$$D_S \frac{\partial^2 S}{\partial x^2} = -v_S \tag{9.4}$$

$$D_P \frac{\partial^2 P}{\partial x^2} = -v_P \tag{9.5}$$

$$D_M \frac{\partial^2 [M_1]}{\partial x^2} = -v_M \tag{9.6}$$

The elementary step mechanism for the ordered bi-bi reaction of the enzyme with the substrate and cofactor is shown in Eq. 9.7

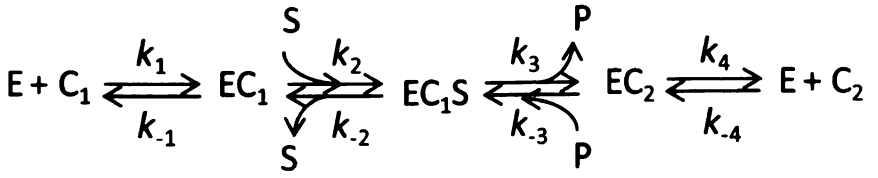

(9.7)

where k_1 and k_{-1} are the second order reaction rate constants describing the reversible reaction between E and the oxidized cofactor (C_1) to form EC_1; k_2 and k_{-2} are the second order rate constants describing the reversible reaction of EC_1 and S to form the enzyme/cofactor/substrate complex (EC_1S); k_3 and k_{-3} are the second order rate constants for the reversible breakdown of EC_1S into EC_2 and P; and k_4 and k_{-4} are the reaction rate constants describing the reversible breakdown of EC_2 into E and reduced cofactor (C_2). Since the enzyme is bound in an active conformation within the film, the association rate constants (k_1 and k_{-4}) are assumed to be much greater than the dissociation rate constants (k_{-1}, and k_4), suggesting the mechanism shown in Eq. 9.7 can be simplified to that shown in Eq. 9.8 (Mulcahy, O'Flaherty et al. 1999; Oakey and Mulcahy 2004).

$$\mathrm{EC_1 + S} \underset{k_{-2}}{\overset{k_2}{\rightleftarrows}} \mathrm{EC_1S} \underset{k_{-3}}{\overset{k_3}{\rightleftarrows}} \mathrm{EC_2 + P} \qquad \textbf{(9.8)}$$

The reaction between the mediator and enzyme-cofactor complex can be written as:

$$\mathrm{M_1 + EC_2} \underset{k_B}{\overset{k_A}{\rightleftarrows}} \mathrm{M_2 + EC_1} \qquad \textbf{(9.9)}$$

where k_A and k_B are the second order rate constants describing the reaction of M_1 and M_2 with EC_2 and EC_1, respectively. In this way, the ordered sequential bi-bi mechanism of Eq. 9.8 may be represented as a ping pong, bi-bi mechanism. Reversible oxidation or reduction of the mediator occurs at the electrode surface as shown in Eq. 9.10.

$$M_2 \rightleftarrows M_1 \qquad \textbf{(9.10)}$$

The rates of substrate, product, and mediator (M_1) formation are given by Eqs. 9.11 through 9.13, respectively.

$$v_S = k_{-2}\left[EC_1S\right] - k_2\left[EC_1\right] S \tag{9.11}$$

$$v_P = k_3\left[EC_1S\right] - k_{-3}\left[EC_2\right] P \tag{9.12}$$

$$v_M = k_B\left[M_2\right]\left[EC_1\right] - k_A\left[M_1\right]\left[EC_2\right] \tag{9.13}$$

At steady state, expressions for v_S and v_M can be written in terms of v_P (Eq. 9.14):

$$v_P = -v_S = -v_M \tag{9.14}$$

where v_M is counterbalanced by the rate of the mediator reaction at the electrode.

Development of the kinetic model begins with the unsteady state mass balances on EC_1S and EC_2 shown in Eqs. 9.15 and 9.16, respectively.

$$\frac{\partial\left[EC_1S\right]}{\partial t} = k_2\ S\ \left[EC_1\right] - k_{-2}\left[EC_1S\right] - v_P \tag{9.15}$$

$$\frac{\partial\left[EC_2\right]}{\partial t} = v_P - k_A\left[M_1\right]\left[EC_2\right] + k_B\left[M_2\right]\left[EC_1\right] \tag{9.16}$$

Assuming pseudo-steady-state for reaction intermediates (Segel 1993), substituting Eq. 9.12 into Eq. 9.15, and solving for $[EC_1S]$ gives

$$\left[EC_1S\right] = \frac{k_2\ S\ \left[E_T\right] + \left[EC_2\right]\ k_{-3}\ P - k_2\ S}{k_{-2} + k_3 + k_2\ S} \tag{9.17}$$

where the total concentration of immobilized enzyme is given by $[E_T]=[EC_1]+[EC_2]+[EC_1S]$. Substituting the expression for $[EC_1S]$ from Eq. 9.17 into Eq. 9.16 and solving for $[EC_2]$ gives:

$$\left[EC_2\right]=\frac{\left[E_T\right]\ k_3k_B\ \left[M_T\right]-\left[M_1\right]\ +k_{-2}k_B\ \left[M_T\right]-\left[M_1\right]\ +k_2k_3\ S}{S\ \ k_2k_3+k_2k_A\left[M_1\right]\ +\ P\ \ k_{-3}k_B\ \left[M_T\right]-\left[M_1\right]\ +k_{-2}k_{-3}\ +....} \qquad \textbf{(9.18)}$$
$$k_2k_{-3}\ S\ \ P\ +\ k_A\left[M_1\right]+k_B\ \left[M_T\right]-\left[M_1\right]\ \ k_{-2}+k_3$$

where the total mediator concentration is given by $[M_T]=[M_1]+[M_2]$. Substituting the expressions for $[EC_1S]$ and $[EC_2]$ into Eq. 9.12 gives the final kinetic model.

$$v_P=\frac{\left[E_T\right]\ k_2k_3k_A\left[M_1\right]\ S\ -k_{-2}k_{-3}k_B\ \left[M_T\right]-\left[M_1\right]\ \ P}{S\ \ k_2k_3+k_2k_A\left[M_1\right]\ +\ P\ \ k_{-3}k_B\ \left[M_T\right]-\left[M_1\right]\ +k_{-2}k_{-3}\ +....} \qquad \textbf{(9.19)}$$
$$k_2k_{-3}\ S\ \ P\ +\ k_A\left[M_1\right]+k_B\ \left[M_T\right]-\left[M_1\right]\ \ k_{-2}+k_3$$

Michaelis constants for the substrate and product are defined by Eqs. 9.20 and 9.21, respectively.

$$K_{M,S}=\frac{k_{-2}+k_3}{k_2} \qquad \textbf{(9.20)}$$

$$K_{M,P}=\frac{k_{-2}+k_3}{k_{-3}} \qquad \textbf{(9.21)}$$

9.4. Dimensional Analysis

Dimensional analysis was performed to express the model using the minimum number of variables and obtain physical insight into the system's behavior. The Buckingham-Pi approach yielded the dimensionless groups shown in Eqs. 9.22 through 9.35.

$$s = \frac{S}{K_S \; S_\infty} \tag{9.22}$$

$$p = \frac{P}{K_P \; P_\infty} \tag{9.23}$$

$$m = \frac{\left[M_1\right]}{\left[M_T\right]} \tag{9.24}$$

$$\chi = \frac{x}{l} \tag{9.25}$$

$$\phi = \frac{k_B}{k_A} \tag{9.26}$$

$$\mu = \frac{K_S \; S_\infty}{K_{M,S}} \tag{9.27}$$

$$\lambda = \frac{K_P \; P_\infty}{K_{M,P}} \tag{9.28}$$

$$\kappa^2 = \frac{k_A\left[E_T\right]\left[M_T\right]l^2}{D_M K_P \; P_\infty} \tag{9.29}$$

$$\omega = \frac{k_3}{k_A\left[M_T\right]} \tag{9.30}$$

$$\rho = \frac{k_{-2}}{k_A\left[M_T\right]} \tag{9.31}$$

$$\alpha = \frac{D_M}{D_P} \tag{9.32}$$

$$\beta = \frac{D_M}{D_S} \tag{9.33}$$

$$\theta = \frac{K_P\ P_\infty}{[M_T]} \tag{9.34}$$

$$\sigma = \frac{K_P\ P_\infty}{K_S\ S_\infty} \tag{9.35}$$

In these equations, the subscript ∞ denotes the value in the bulk solution; s, p, and m are the dimensionless concentrations of the substrate, product, and mediator, respectively, normalized with respect to the maximum concentrations of substrate ($K_S[S]_\infty$), product ($K_P[P]_\infty$), and mediator ($[M_T]$) present within the film. The dimensionless distance from the electrode is χ. The ratio of mediator reaction rates is ϕ. The substrate and product concentrations normalized to the substrate and product Michaelis constants are μ and λ, respectively; κ is a Thiele modulus for the mediator; ω and ρ are ratios of rate constants for product or substrate production, respectively, to that for cofactor regeneration; α and β are the ratios of mediator diffusivity to that of the substrate and product, respectively; θ and σ are the ratios of the bulk product concentration to the total mediator concentration and the bulk substrate concentration, respectively.

Substituting the dimensionless variables (Eqs. 9.22 through 9.35) into Eq. 9.19 gives:

$$\overline{v_P} = \frac{\kappa^2\alpha\left[s\mu\omega m - p\lambda\rho\phi\ 1-m\ \right]}{s\mu\ \omega+m\ +p\ \lambda\phi\ 1-m\ +\rho\lambda\ +ps\mu\lambda\ \omega+\rho\ +m+\phi\ 1-m} \tag{9.36}$$

where $\overline{v_P}$ is the reaction rate normalized with the $K_P[P]_\omega$, D_P and l and given by Eq. 9.37:

$$\overline{v_P} = \frac{l^2 v_P}{D_P K_P P_\infty} \tag{9.37}$$

Substituting the dimensionless variables into the transport equations (Eqs. 9.4 through 9.6) gives Eqs. 9.38 through 9.40.

$$\frac{\partial^2 s}{\partial \chi^2} = -\left(\frac{\sigma\beta}{\alpha}\right)\overline{v_P} \tag{9.38}$$

$$\frac{\partial^2 p}{\partial \chi^2} = \overline{v_P} \tag{9.39}$$

$$\frac{\partial^2 m}{\partial \chi^2} = -\left(\frac{\theta}{\alpha}\right)\overline{v_P} \tag{9.40}$$

9.5. Boundary Conditions

The interphase fluxes of S and P from the bulk solution to the biocatalytic film equal the fluxes into the film. The dimensionless substrate and product boundary conditions expressing this relation are given by Eqs. 9.41 and 9.42, respectively,

$$Bi_S \left(s|_{\chi=1} - 1\right) = -\left.\frac{ds}{d\chi}\right|_{\chi=1} \tag{9.41}$$

$$Bi_P \left(p|_{\chi=1} - 1\right) = -\left.\frac{dp}{d\chi}\right|_{\chi=1} \tag{9.42}$$

where the Biot number for mass transfer of component i (Bi_i) is defined as

$$Bi_i = \frac{k_{x,i} l}{D_i} \tag{9.43}$$

When the interphase mass-transfer resistance is negligible ($k_{x,i} \sim \infty$), Eqs. 9.41 and 9.42 reduce to

$$p|_{\chi=1} = s|_{\chi=1} = 1 \tag{9.44}$$

At the electrode/film interface (χ=0), there is no diffusion of substrate or product into the electrode, so the following no-flux boundary conditions apply.

$$\left.\frac{\partial s}{\partial \chi}\right|_{\chi=0} = \left.\frac{\partial p}{\partial \chi}\right|_{\chi=0} = 0 \tag{9.45}$$

At the electrode surface, an oxidation or reduction reaction regenerates the mediator. This reaction is assumed to be at electrochemical equilibrium, as described by the Nernst equation (Bartlett and Pratt 1995):

$$E_P = E_P^0 + \frac{RT}{nF} \ln \frac{[M_1]_0}{[M_2]_0} \tag{9.46}$$

where E_P is the electrochemical potential of the electrode, $E_P{}^0$ is the standard potential of the mediator, R is the ideal gas law constant, T is the absolute temperature, n is the number of electrons transferred during oxidation/reduction reaction, F is Faraday's constant, and $[M_1]_0$ and $[M_2]_0$ are the concentrations of the oxidized and reduced forms of the mediator at the electrode surface, respectively.

In terms of the dimensionless electrode potential (ε) defined in Eq. 9.47, the

$$\varepsilon = \frac{E_P - E_P^0 \; nF}{RT} \tag{9.47}$$

dimensionless boundary conditions for m at the electrode surface becomes

$$m|_{\chi=0} = \frac{1}{1+\exp(-\varepsilon)} \tag{9.48}$$

There is assumed to be no mediator loss or charge transfer into the bulk liquid, so the following no-flux boundary condition applies:

$$\left.\frac{\partial m}{\partial \chi}\right|_{\chi=1} = 0 \tag{9.49}$$

The rate of charge transported through the film via the mediator can be modeled as a mediator flux (J_M), which is related to the electrical current generated or consumed at the electrode, as shown by Eq. 9.50 (Bartlett and Pratt 1995).

$$J_M = \frac{I}{nFA} = D_M \left.\frac{d[M_1]}{dx}\right|_{x=0} \tag{9.50}$$

In dimensionless form, Eq. 9.50 becomes

$$j_M = \frac{J_M l}{D_M} = \left.\frac{dm}{d\chi}\right|_{\chi=0} = \frac{\sigma\beta}{\alpha}\left.\frac{ds}{d\chi}\right|_{\chi=1} - \frac{\theta}{\alpha}\left.\frac{dp}{d\chi}\right|_{\chi=1} \tag{9.51}$$

9.6. Properties of the Reversible Kinetic Model

In reversible enzymatic reactions, product accumulation can slow substrate conversion, resulting in apparent reaction inhibition. Graphical analysis methods can characterize enzyme inhibition patterns, including those arising from reaction reversibility. Rearranging Eq. 9.34 into the Henri-Michaelis-Menten form (Segel 1993) gives

$$\overline{v_P} = \frac{\overline{V_{\max}}\left(\mu - \frac{\lambda}{\overline{K_{eq}}}\right)}{\mu\left(1+\frac{\lambda}{\overline{K_{ii}}}\right) + \overline{K_{M,S}}\left(1+\frac{\lambda}{\overline{K_{ip}}}\right)} \tag{52}$$

where $\overline{V_{\max}}$, $\overline{K_{eq}}$, $\overline{K_{ii}}$, $\overline{K_{M,S}}$, and $\overline{K_{M,P}}$ are the dimensionless maximum reaction rate, equilibrium coefficient, iso-inhibition constant, substrate Michaelis constant, and product inhibition constant, respectively, are defined in Eqs. 9.53 through 9.57:

$$\overline{V_{\max}} = \frac{\kappa^2 \alpha \omega m}{\omega + m} \tag{9.53}$$

$$\overline{K_{eq}} = \frac{\omega m s}{p \rho \phi\ 1-m} \tag{9.54}$$

$$\overline{K_{ii}} = \frac{\omega + m}{p\ \omega + \rho} \tag{9.55}$$

$$\overline{K_{M,S}} = \frac{m + \phi\ 1-m}{s\ \omega + m} \tag{9.56}$$

$$\overline{K_{ip}} = \frac{m + \phi\ 1-m}{p\ \phi\ 1-m\ + \rho} \tag{9.57}$$

Following the approach described by Segel (Segel 1993), $\overline{K_{ii}}$ can be graphically determined by plotting $1/\overline{V_{\max,app}}$ *vs.* λ, where $\overline{V_{\max,app}}$ is the apparent maximum reaction rate. The equation for the line is given by Eq. 9.58 (Segel 1993).

$$\frac{1}{\overline{V_{\max,app}}} = \frac{1}{\overline{V_{\max}}\,\overline{K_{ii}}}\lambda + \frac{1}{\overline{V_{\max}}} \tag{9.58}$$

$K_{M,P}$ can be determined graphically by plotting the slopes of the double reciprocal plot ($slope_{1/\mu}$) vs λ. The equation for the line is given by Eq. 9.59 (Segel 1993).

$$slope_{1/\mu} = \frac{\mu \overline{\overline{K_{M,S}}}}{\overline{V_{\max}}\left(\mu - \frac{\lambda}{\overline{\overline{K_{eq}}}}\right)}\left(1 + \frac{\lambda}{\overline{\overline{K_{ip}}}}\right) \tag{9.59}$$

9.7. Effectiveness Factor

In porous heterogeneous catalysts, a dimensionless effectiveness factor (η) is used to assess whether mass-transfer resistance limits the overall reaction rate; η is defined as the observed reaction rate divided by the reaction rate in the absence of diffusional resistance (i.e., if the rate of reaction were evaluated using surface concentrations at (i.e., at χ=1). Based on this definition, η values for the biocatalytic film may be calculated using Eq. 9.60:

$$\eta_i = \frac{\int_{\chi=0}^{\chi=1} \overline{v_i} d\chi}{\overline{v_i}\big|_{\chi=1}} \tag{9.60}$$

where *i* indicates the reacting species of interest (*S*, *P*, or *M*). Effectiveness factor values can be calculated by first solving Eqs. 9.37 through 9.39 with the appropriate boundary conditions together with Eq. 9.60 and then plotting the results as η for the species of interest vs. a dimensionless Thiele modulus for that species *i*. The Thiele modulus is the ratio of the maximum reaction rate to the maximum diffusion rate for that species. For the results to be most useful, the Thiele modulus should be defined using variables that

are readily measured experimentally, rather than difficult-to-measure intrinsic kinetic constants. An observable Thiele modulus (Φ_i) is defined in Eq. 9.61.

$$\Phi_i = \frac{v_i l^2}{D_i K_i C_i} \tag{9.61}$$

where v_i, K_i, and C_i are the reaction rate with respect to component i, partition coefficient of component i at the bulk/film-interface, and concentration of species i at the liquid-film interface, respectively. Since the mediator is entrapped within the film and does not partition, $K_i C_i$, is replaced by M_T.

9.8. Results

9.8.1. Comparison to Bartlett and Pratt Model

The model developed by Bartlett and Pratt (Bartlett and Pratt 1995), assumed irreversible enzyme and mediator reactions. These assumptions can be implemented in the present model by setting k_{-3}=0 and k_B=0, yielding Eqs. 9.62 through 9.64, respectively.

$$\frac{\partial^2 s}{\partial \chi^2} = \frac{\kappa^2 B\beta \; s\mu\omega m}{s\mu \; \omega + m \; + m} \tag{9.62}$$

$$\frac{\partial^2 p}{\partial \chi^2} = 0 \tag{9.63}$$

$$\frac{\partial^2 m}{\partial \chi^2} = \frac{A\kappa^2 \; s\mu\omega m}{s\mu \; \omega + m \; + m} \tag{9.64}$$

Following rearrangement Eqs. 9.62 and 9.64 become:

$$\frac{\partial^2 s}{\partial \chi^2} = \frac{\gamma \xi^{-1} \tau^2 ms}{\gamma m\ 1+\mu s\ +s} \tag{9.65}$$

and

$$\frac{\partial^2 m}{\partial \chi^2} = \frac{\tau^2 ms}{\gamma m\ 1+\mu s\ +s} \tag{9.66}$$

where

$$\tau = \sqrt{\frac{k_A \left[E_T\right] l^2}{D_A}} \tag{9.67}$$

$$\xi = \frac{D_S k_S\ k_{-2} + k_3}{D_S k_3 k_2} \tag{9.68}$$

and

$$\gamma = \frac{\left[M_T\right] k_A\ k_{-2} + k_3}{k_2 k_3 K_S\ S_\infty} \tag{9.69}$$

Eqs. 9.65 through 9.69 match the analogous equations developed by Bartlett and Pratt (Bartlett and Pratt 1995), indicating that the new model is a more general version of the previously published one.

9.8.2. Polarization curves

Steady-state polarization curves can be obtained experimentally by slowly varying the electrode's potential while measuring the resulting current. These curves typically have three main regions: (1) oxidation current plateau at positive applied overpotentials (difference between the applied potential and the potential at which the redox event is experimentally observed) (Bard and Faulkner 2001), (2) reduction current

plateau at negative applied overpotentials, and (3) transition between the oxidation and the reduction current plateaus. The model was used to predict effects of key parameters (μ, λ, ϕ, ω, ρ, Bi_S and Bi_P) on polarization curves, with emphasis on illustrating phenomena arising from the reversible kinetics. Three physically realistic cases were simulated: (1) where the forward and reverse reactions are equally favored (μ=1.0, λ=1.0, ϕ=1.0, κ=4.6, $\omega=1.5\times10^{-3}$, $\rho=1.5\times10^{-3}$, α=1.0, β=1.0, $Bi_S=1.2\times10^{5}$, and $Bi_P=1.2\times10^{5}$); (2) where the forward reaction of the enzyme and mediator reactions are kinetically favored over the reverse reaction (μ=1.0, λ=1.0, $\phi=1.7\times10^{-1}$, κ=6.5, $\omega=1.6\times10^{-2}$, $\rho=3.1\times10^{-4}$, $\alpha=5.7\times10^{-1}$, $\beta=2.8\times10^{-1}$, $Bi_S=6.9\times10^{3}$, and $Bi_P=1.4\times10^{4}$); and (3) where the reverse reactions of the enzyme and mediator are kinetically favored (μ=1.0, λ=1.0, $\phi=6.8\times10^{-1}$, κ=3.3, $\omega=2.9\times10^{-3}$, $\rho=1.8\times10^{-2}$, α=2.5, β=1.8, $Bi_S=1.1\times10^{5}$, and $Bi_P=1.5\times10^{5}$). For each of these cases, the product formation rate was calculated over a range of bulk substrate and product concentrations.

9.8.2.1. Apparent reaction inhibition due to reaction reversibility

Simulations for Case 1 performed for a wide variety of bulk substrate concentrations and four bulk product concentrations were performed. The Lineweaver-Burk plot in Figure 9.1A shows the predicted patterns of inhibition for Case 1. Despite the complexity of the system, the predicted reaction rates for each bulk product concentration are highly linear (R^2>0.999). Moreover, the lines intersect at a point that is not on either the $1/\mu$ or $1/\sqrt{v_P}$ axes, indicating a pattern characteristic of mixed inhibition (Segel 1993). As the product concentration increases, the lines pivot clockwise around the point of intersection, and their slopes become steeper, indicating stronger

apparent inhibition. The $\overline{K_{ii}}$ and $\overline{K_{ip}}$ values were determined to be 5.74×10^{2} and 3.30×10^{2} from the x-intercepts of the plots of slope *vs.* λ (Figure 9.1B) and $1/\overline{v_P}$ *vs.* λ (Figure 9.1C), respectively. The $\overline{V_{\max}}$, and $\overline{K_{eq}}$ values were estimated to be 6.5×10^{-4} and 6.2×10^{3}, respectively. The inhibition constants for Cases 2 and 3 were also determined in this way for all three cases are presented in Table 1. The increase of $\overline{V_{\max}}$, $\overline{K_{eq}}$, $\overline{K_{ii}}$, and $\overline{K_{ip}}$ from Case 2 to Case 3 indicates that the systems parameters affect the apparent reaction inhibition.

Under conditions where the concentration of the substrate, product, and mediator across the film is consistent across the film adherence to Eq. 9.52 is observed. However, when a concentration gradient of either the substrate, product, or mediator (or any combination) is observed the system no longer adheres to Eq. 9.52. Under a given set of reaction conditions Lineweaver-type of behavior maybe obsereved.

9.8.2.2. Effects of substrate and product concentration

Figure 9.2A shows the predicted effects of bulk substrate concentration on the polarization curves for Case 1. At μ values less than 0.1 the oxidation current increases proportionately to μ, suggesting that the system is limited by availability of the substrate. As μ increases to about 5, the oxidation current approaches a plateau, consistent with Michaelis-Menten saturation kinetics. However, at higher values of μ ($\mu>10$) the reduction current decreases suggesting that the increased concentration inhibits the formation of additional substrate via reaction with the available product.

Figure 3B shows the effects of dimensionless bulk product concentration on the reduction current. Under these conditions, the product would be converted to substrate. At λ values below 0.1, the reduction current increases proportionately with λ, suggesting that the current is limited by availability of the product. The reduction current approaches a plateau as λ reaches a value of about 3, indicating that the reverse reaction rate is becoming significant enough to reduce the net reaction rate. At higher values of λ (λ>10) the oxidation current decreases suggesting that the increased concentration inhibits the formation of additional substrate via reaction with the available product. The symmetry between Figures 3A and 3B suggests that μ and λ have equal effects on the oxidation and reduction current, respectively.

The predicted response for Cases 2 and 3 were also examined. At low values of μ and λ (μ and λ<0.1) the oxidation and reduction current increases proportionately to μ and λ, respectively (results not shown). For Cases 2 and 3, the oxidation and reduction current approaches a plateau as μ and λ approaches 5 (results not shown). The decrease in the reduction (oxidation) current upon further increases in μ (λ) above 10 was also apparent in Cases 2 and 3.

9.8.2.3. Effects of cofactor-regeneration kinetics

The kinetics of *EC* regeneration by the mediator are reflected by the parameter ϕ. As shown in Figure 9.3, for ϕ values between 0.1 and 100, the oxidation and reduction currents calculated for Case 1 remain stable., and the predicted half-wave potential (E_{app}^{0}, the potential giving a current half way between the oxidation and reduction currents) varied with ϕ as described in Eq. 9.70.

$$E^0_{app} - E^0_P = \left(\frac{RT}{nF}\right)\ln\phi \tag{70}$$

However, for ϕ values above 100, the oxidation current decreases, and for ϕ values below 0.1, the reduction current decreases. The decrease in current suggests that the kinetics of mediator-catalyzed cofactor regeneration becomes rate-limiting under these conditions.

9.8.2.4. Effects of enzyme kinetics

Figure 9.4 shows the effects of the ratio of dehydrogenase-catalyzed reaction rate to regeneration rate on the polarization curve. Figure 9.4A shows that the oxidation current increases proportionally with ω. Similarly, Figure 9.4B shows that the reduction current increases proportionally with ρ/ϕ. The simulations suggest that for Case 1 enzyme kinetics are rate limiting. Similar behavior was also observed for Cases 2 and 3.

9.8.2.5. Effects of interphase transport resistance

Figure 9.5 shows the effects of interphase mass transfer resistance on the oxidation and reduction currents for Case 1. At Bi_S values greater than 1.2, the oxidation/reduction current remains constant (Figure 9.5A), indicating that interphase mass transfer is not limiting. As the Bi_S value decreases below about 1, the oxidation current begins decreasing, but the reduction current stays relatively constant. Examination of the concentration profiles suggests that the decrease in the oxidation current is associated with a subsequent decrease in the concentration of the substrate at the film/bulk solution interface ($\chi=1$), as would be expected when interphase mass transfer resistance is rate limiting. As the Bi_S drops into the range of 0.01, the reduction current also begins to decrease. This asymmetric response between the oxidation and reduction curves is attributed to a much higher value of Bi_P than Bi_S, resulting in the

substrate being highly rate limiting for the oxidation reaction but the product being in ample supply for the reduction reaction. The decrease in reduction current observed as Bi_S less than 0.01 is attributed to accumulation of substrate in the film, causing apparent inhibition of the reversible enzyme. Such behavior would not be expected from a model that did not include enzyme reversibility. Figure 9.5B shows the effects of Bi_p on the reduction current. At high values of Bi_P (Bi_P>1.2) the reduction current the oxidation/reduction current remains constant; however as Bi_p is decreased (Bi_P>1.2) the reduction current decreases. At lower values of Bi_P ($Bi_P<6.0\times10^{-4}$) the oxidation current also began to decrease.

The current response for Cases 2 and 3 were also examined. The oxidation and reduction current decreased with decreasing Bi_S and Bi_P, respectively (results not shown). Similar trends were observed to those shown in Figure 9.5, suggesting that the rate-limiting effects of Bi_S and Bi_P are relatively insensitive to the kinetic parameters of the bioelectronic interface.

9.8.2.6. Effects of intraphase transport resistance

Transport of three different reacting species within the biocatalytic film could be rate-limiting: electrons, substrate, and product. The degree to which each is rate limiting can be quantified through its effectiveness factor. Observable Thiele moduli for substrate (Φ_S) and product (Φ_P), analogous to that defined for the mediator in Eq. 9.27, can be defined and used for effectiveness factor plots. Figure 9.6A shows the effect of α on η for reaction Case 1 at various values of μ determined by measuring the oxidation current. As expected, when Φ_S<0.1, η approaches unity, indicating that the bioelectronic interface

is kinetically limited. For $\Phi_S>1$, η decreases rapidly indicating that the system is substrate diffusion limited. The minor shift in η curves to higher Φ_S values as bulk substrate concentration increases is typical for immobilized enzyme systems; it reflects the transition from apparent first order kinetics to zero order kinetics as the increasing substrate concentration saturates the enzyme. The decrease in η associated with reduction current is believed to be due to the formation of a concentration gradient of across the film (Figure 9.6B) caused by changes in α.

Figure 9.7A shows the effect of β on η for Case 1 at varies values of λ determined by measuring the reduction current. As in Figure 9.7A, the bioelectronic interface transitions from a kinetics limited regime to a diffusion limited regime as Φ_P approaches 0.1. Comparison of the plots of η vs. Φ_P and η vs. Φ_S suggests that a single curve can represent the behavior of a bioelectronic interface for a range of bulk concentration and reaction conditions suitable of biocatalytic experiments. The decrease in η associated with reduction current is believed to be due to the formation of a concentration gradient of across the film (Figure 9.7B) caused by increases in β. To explore the extent to which the effectiveness factor curves are independent of the system parameters, simulations were also generated for reaction Cases 2 and 3 (results not shown). Similar behavior was also observed for Cases 2 and 3.

Figure 9.8A shows η vs. observable mediator Thiele modulus (Φ_M) for Case 1 at various values of D_M. A minor shift in the effectiveness factor curves as bulk substrate or product concentration reflects the transition from apparent first order kinetics to zero order kinetics as the increasing substrate concentration saturates the enzyme. Similarity

between the plots of η vs. Φ_M suggests that the bioelectronic interface transitions from the kinetic limited to the diffusion limited regime are independent of M_T. Since the plots of η vs. Φ_M for Case 1 overlap, a single curve can represent the behavior of the bioelectronic interface. The decrease in η associated with reduction current is believed to be due to the formation of a concentration gradient of across the film (Figure 9.8B) caused by increases in D_M. At low values of D_M the value of m only decreased to 0.50, suggesting that even at high values of ε at low values of D_M the film is only expirencing a value of ε=0, according to Eq. 9.48. Cases 2 and 3 were also examined (results not shown).

9.9. Discussion

The bioelectronic interface model presented here extends the work of Bartlett and Pratt, allowing the effects of reversible enzyme and mediator kinetics on system behavior to be explored. Although in the model's formulation, the reduced species was arbitrarily called the "substrate" and the oxidized species was called the "product", the model can just as easily describe reversible reduction of an oxidized species, as shown in the polarization curves (Figures 9.2 through 9.5).

Because of the large number of variables involved and space limitations, only a limited range of the parameter space could be examined in this paper. However, the simulations shown illustrate the model's ability to predict effects of substrate/product concentration, enzyme kinetics, mediator kinetics, substrate/product diffusion, charge transfer diffusion, and mass transfer from the bulk to film interface on the overall reaction rate. The prediction that the system should exhibit apparent mixed inhibition kinetics (Figure 9.1) provides a framework by which experimental data could be

analyzed, and the effects of product inhibition predicted. A variety of operating regimes were illustrated, along with ranges of the dimensionless groups associated with those regimes. For example, under all the reaction conditions studied, the oxidation and reduction current consistently began to reach a plateau at substrate of product values of $\mu \sim 3$ and $\lambda \sim 3$, respectively, above which the system was no longer substrate limited. The system's apparent oxidation potential was predicted to be strongly affected by cofactor regeneration kinetics (Figure 9.3), with a trend that could be correlated through ϕ using Eq. 70. Reactant concentration (Figure 9.2) and mass-transfer resistance were predicted to have a weaker, but significant effect on the apparent oxidation potential (Figure 9.5). The oxidation/reduction current generated by the bioelectronic interface was predicted to depend strongly on enzyme kinetics, as well as mediator-regeneration kinetics (Figure 9.4). The key dimensionless groups determining which of these steps was most flux-controlling were μ and ω. Effectiveness factor correlations (Figures 9.6 and 9.7) in terms of observable Thiele moduli for substrate, product, and mediator allow the predicted results for a wide range of parameter space to graphically correlated, providing a simple means to determine whether intraphase mass transfer resistance limits system performance.

The utility of the new model lies in its capability to predict performance properties of the bioelectronic interface and identify rate-limiting variables. This capability will aid in engineering dehydrogenase-containing bioelectronic interfaces for applications in which significant quantities of both substrate and product may be present, such as electrobiocatalytic reactors that oxidize or reduce a substrate to form a high-value product or biocatalytic films thick enough that significant conversion is achieved across

the film. In such systems, a calibrated model would enable design and optimization studies to be conducted *in-silico*, thereby reducing costs and saving time.

9.10. Conclusions

The first steady-state model of a dehydrogenase-containing bioelectronic interface that incorporates reversible kinetics of both the enzyme and mediator has been developed, expressed in dimensionless form, and solved numerically. The model allows the overall reaction rate to be predicted as a function of the key independent variables (enzyme kinetics, mediator kinetics, substrate/product diffusion, mediator diffusion, substrate/product concentration, mediator concentration and electrode potential). Dimensional analysis allowed key dimensionless groups that control system response to be identified. Lineweaver-Burk analysis predicted that the bioelectronic interface would exhibit apparent mixed-inhibition kinetics with respect to product concentration. The sensitivity of the polarization curve to bulk substrate and product concentrations, relative rates of enzyme reaction and mediator regeneration, and mediator reaction rates was explored. The apparent redox potential of the interface was predicted to be strongly dependent on cofactor regeneration kinetics and weakly dependent on transport limitations. Conditions under which the interface's reaction is limited by transport of substrate, product and mediator were correlated in plots of effectiveness factor vs. observable Thiele modulus. This model provides a mechanism to design and optimize bioelectronic interface performance for applications in biosensors, biocatalytic reactors, and biological fuel cells.

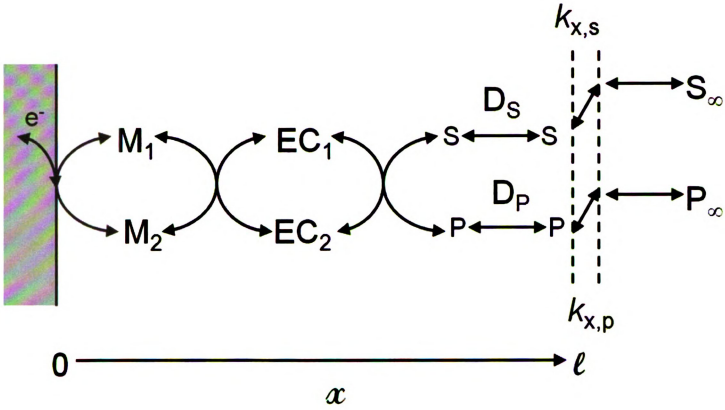

Scheme 9.1: Schematic of a typical enzyme-membrane electrode showing the processes considered in the model.

Table 9.1: Kinetic parameters estimated from the initial reaction rate expression for Case 1 (ϕ=1.0, κ=4.6, ω=1.5×10^{-3}, ρ=1.5×10^{-3}, α=1.0, β=1.0, Bi$_S$=1.2×10^{5}, and Bi$_P$=1.2×10^{5}), Case 2 (ϕ=1.7×10^{-1}, κ=6.5, ω=1.6×10^{-2}, ρ=3.1×10^{-4}, α=5.7×10^{-1}, β=2.8×10^{-1}, Bi$_S$=6.9×10^{3}, and Bi$_P$=1.4×10^{4}), and Case 3 (ϕ=6.8×10^{-1}, κ=3.3, ω=2.9×10^{-3}, ρ=1.8×10^{-2}, α=2.5, β=1.8, Bi$_S$=1.1×10^{5}, and Bi$_P$=1.5×10^{5}).

	$\overline{V_{\max}}$	$\overline{K_{eq}}$	$\overline{K_{M,S}}$	$\overline{K_{ii}}$	$\overline{K_{ip}}$
Case 1	6.51E-04	6.19E+03	9.99E-01	5.74E+02	3.30E+02
Case 2	1.41E-03	8.45E+04	9.99E-01	2.82E+03	5.11E+02
Case 3	6.29E-04	5.83E+01	1.00E+00	3.19E+01	4.74E+01

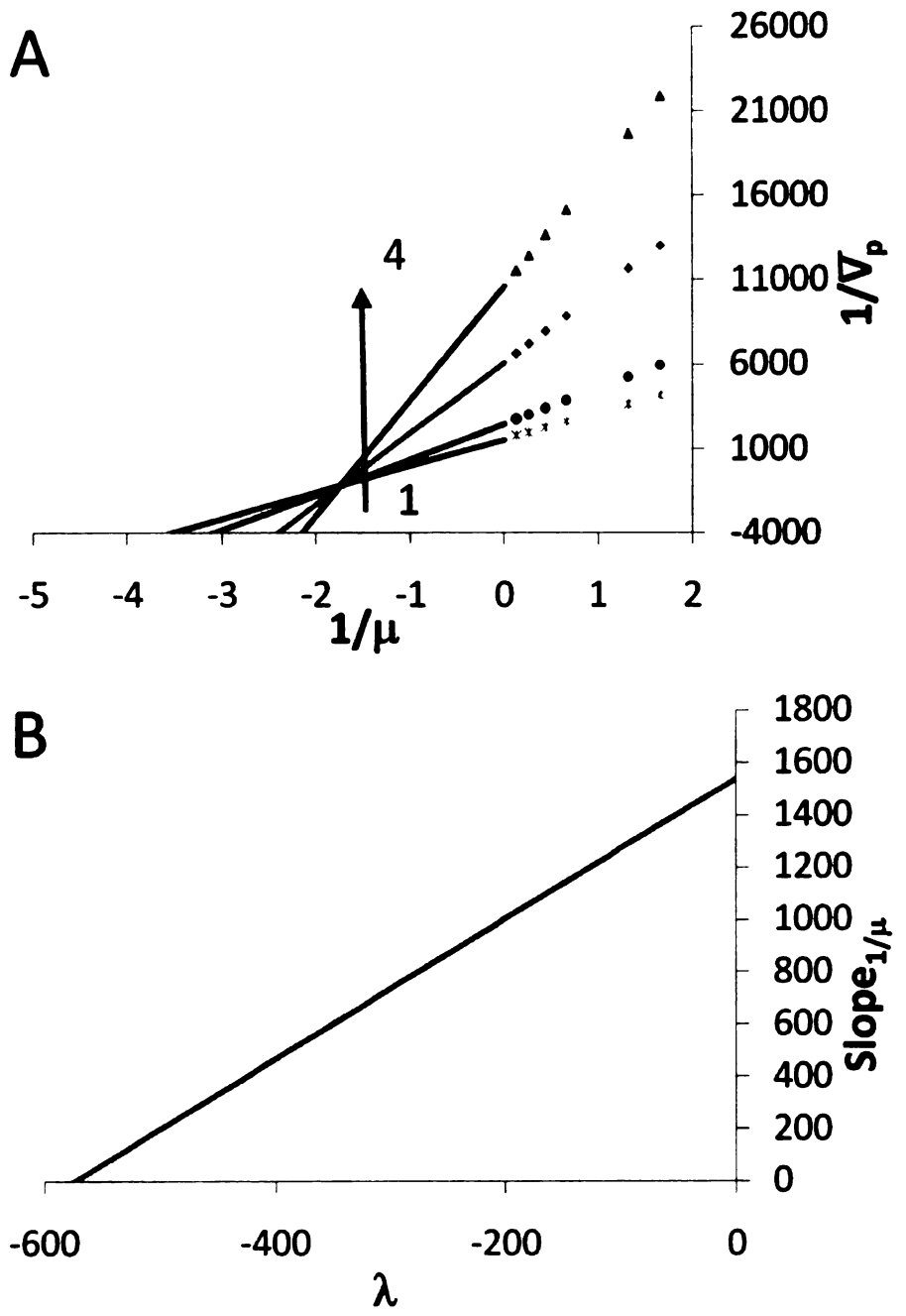

Figure 9.1: (A) Lineweaver Burk plot of $1/\sqrt{v_P}$ versus 1/μ in the presence of different fixed values of λ: (1) λ =0, (2) λ=2, (3) λ=20, and (4) λ=200 when 1.0, κ=4.6, ω=1.5×10^{-3}, ρ=1.5×10^{-3}, α=1.0, β=1.0, Bi$_S$=1.2×10^5, and Bip=1.2×10^5. Single points represent the simulated data while the lines represent the extrapolation to negative values of μ (B) Replot of the slope of the double reciprocal plot vs. λ, and (C) replot of $1/\sqrt{v_{\max,app}}$ vs. λ.

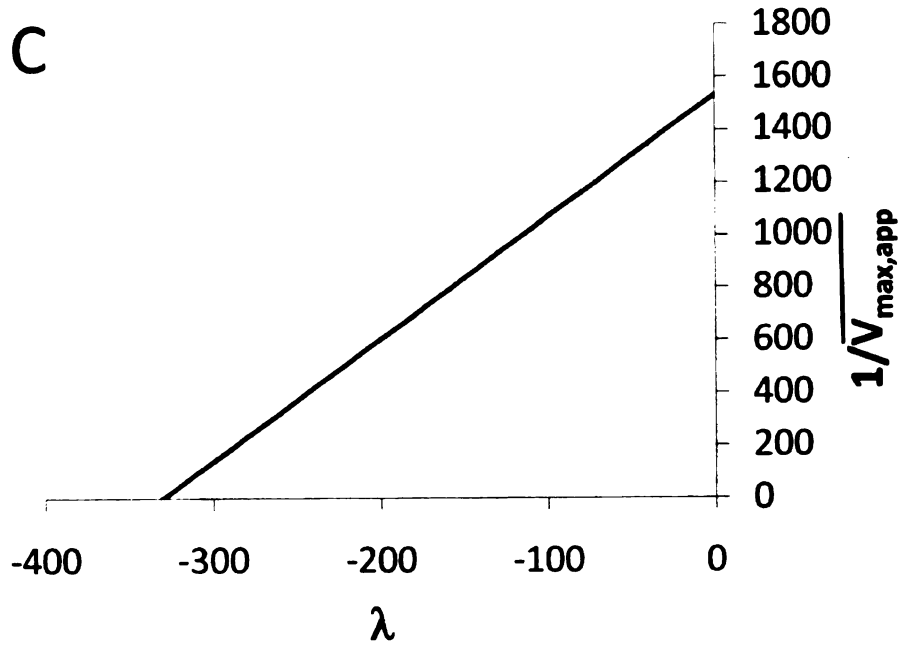

Figure 9.1 continued.

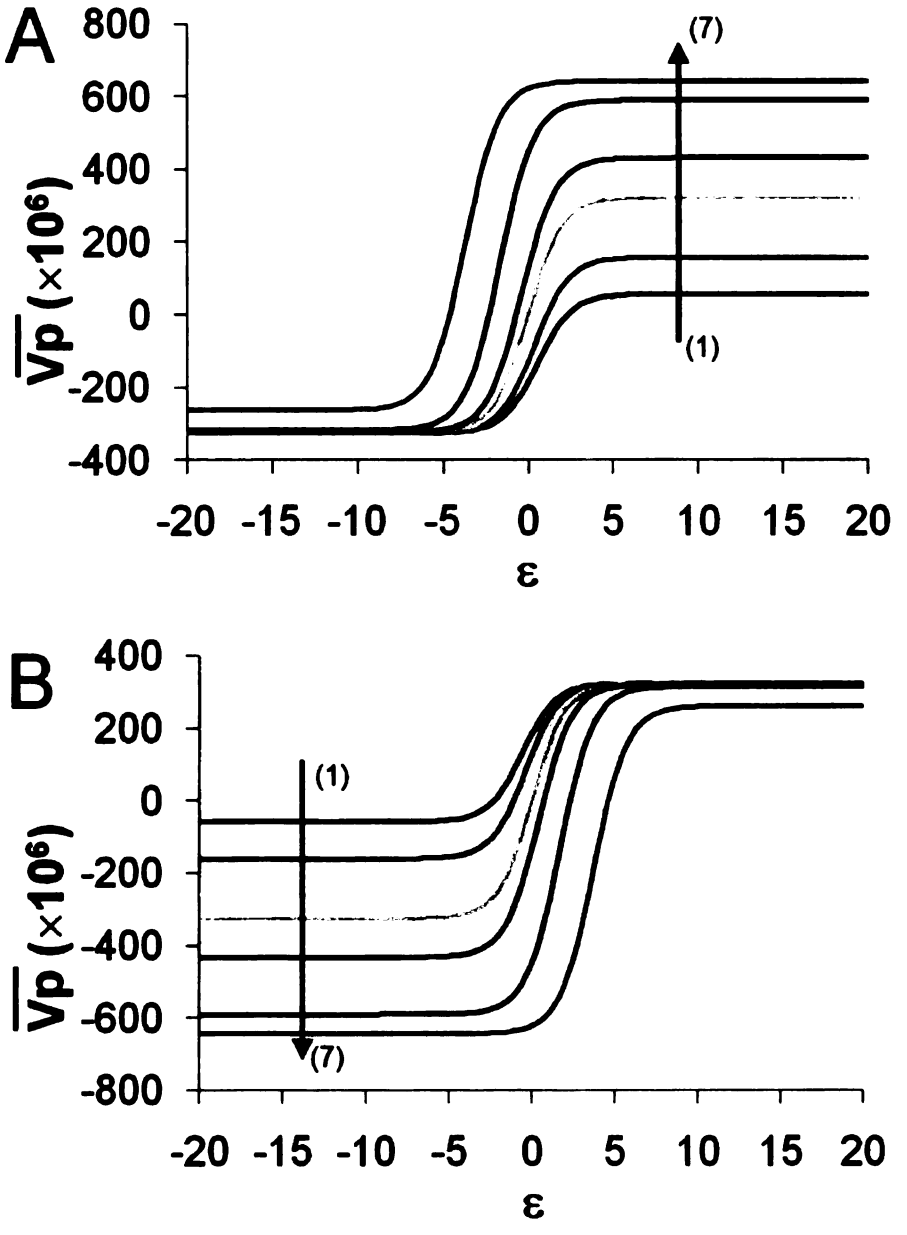

Figure 9.2: Dimensionless steady state voltammograms where ϕ=1.0, κ=4.6, $\omega=1.5\times10^{-3}$, $\rho=1.5\times10^{-3}$, α=1.0, β=1.0, $Bi_S=1.2\times10^{5}$, and $Bi_P=1.2\times10^{5}$ when [A] (1) $\mu=1.0\times10^{-1}$, (2) $\mu=3.3\times10^{-1}$, (3) $\mu=6.6\times10^{-1}$, (4) μ=1.0, (5) μ=2.0, (6) μ=3.0, and (7) μ=4.0 and [B] (1) $\lambda=1.0\times10^{-1}$, (2) $\lambda=3.3\times10^{-1}$, (3) $\lambda=6.6\times10^{-1}$, (4) λ=1.0, (5) λ=2.0, (6) λ=3.0, and (7) λ=4.0.

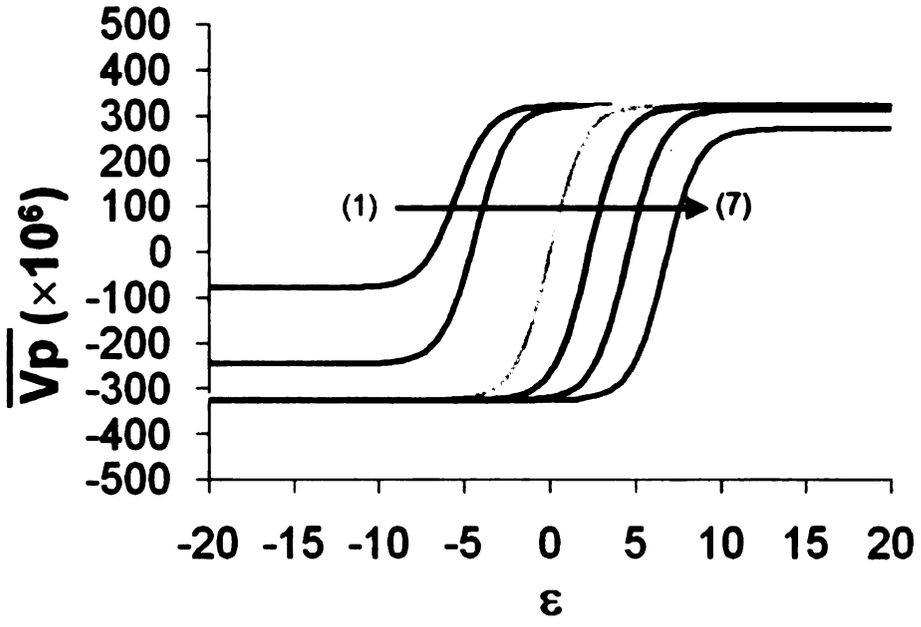

Figure 9.3: Dimensionless steady state voltammograms where μ=1.0, λ=1.0, κ=4.6, $\omega=1.5\times10^{-3}$, $\rho=1.5\times10^{-3}$, α=1.0, β=1.0, $Bi_S=1.2\times10^{5}$, and $Bi_P=1.2\times10^{5}$ when (1) $\phi=1.0\times10^{-3}$, (2) $\phi=1.0\times10^{-2}$, (3) $\phi=1.0\times10^{-1}$, (4) ϕ=1.0, (5) $\phi=1.0\times10^{1}$, (6) $\phi=1.0\times10^{2}$, and (7) $\phi=1.0\times10^{3}$.

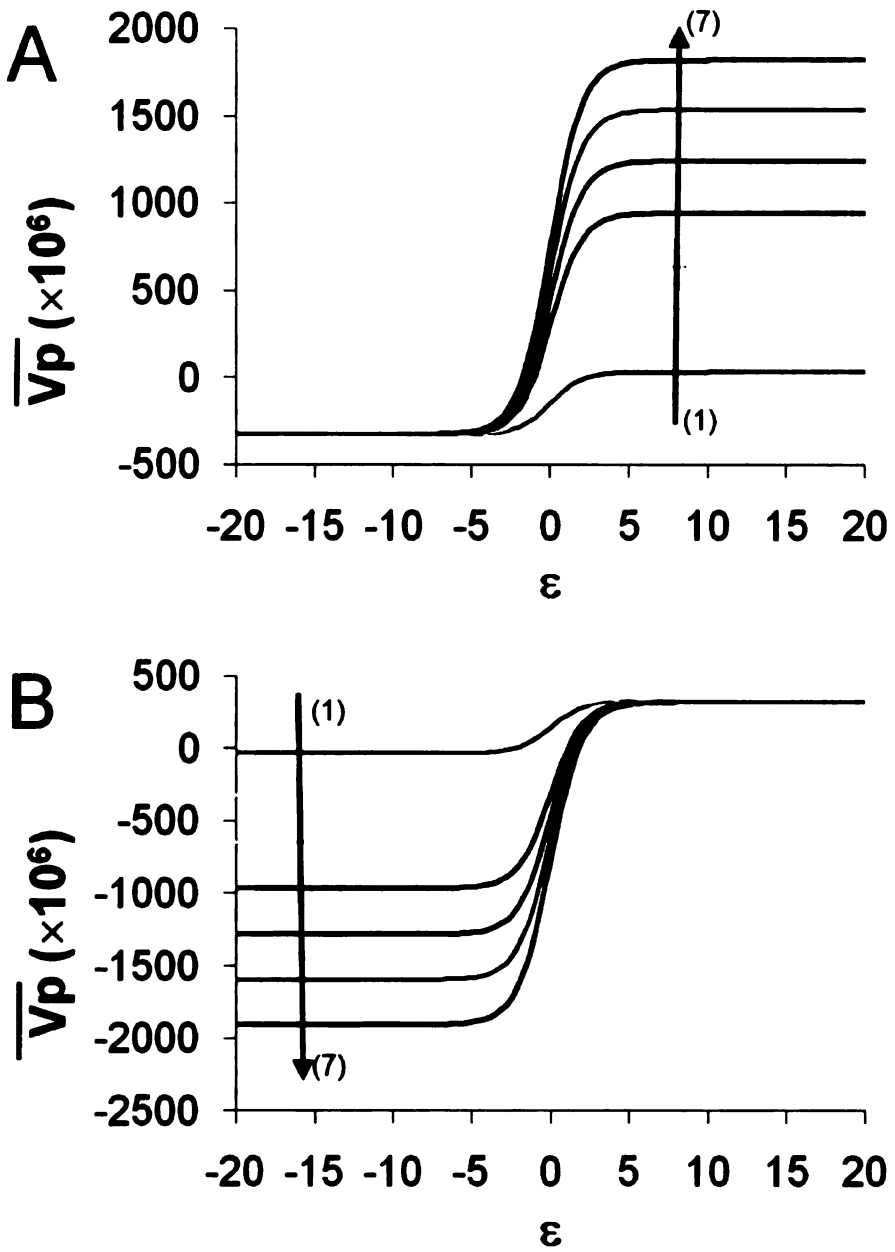

Figure 9.4: Dimensionless steady state voltammograms where μ=1.0, λ=1.0, ϕ=1.0, κ=4.6, α=1.0, β=1.0, $Bi_S=1.2\times10^{5}$, and $Bi_S=1.2\times10^{5}$ when [A] (1) $\omega=1.5\times10^{-4}$, (2) $\omega=1.5\times10^{-3}$, (3) $\omega=3.0\times10^{-3}$, (4) $\omega=4.6\times10^{-3}$, (5) $\omega=6.1\times10^{-3}$, (6) $\omega=7.6\times10^{-4}$, and (7) $\omega=9.1\times10^{-4}$ and [B] (1) $\rho/\phi=1.5\times10^{-4}$, (2) $\rho/\phi=1.5\times10^{-3}$, (3) $\rho/\phi=3.0\times10^{-3}$, (4) $\rho/\phi=4.6\times10^{-3}$, (5) $\rho/\phi=6.1\times10^{-3}$, (6) $\rho/\phi=7.6\times10^{-4}$, and (7) $\rho/\phi=9.1\times10^{-4}$.

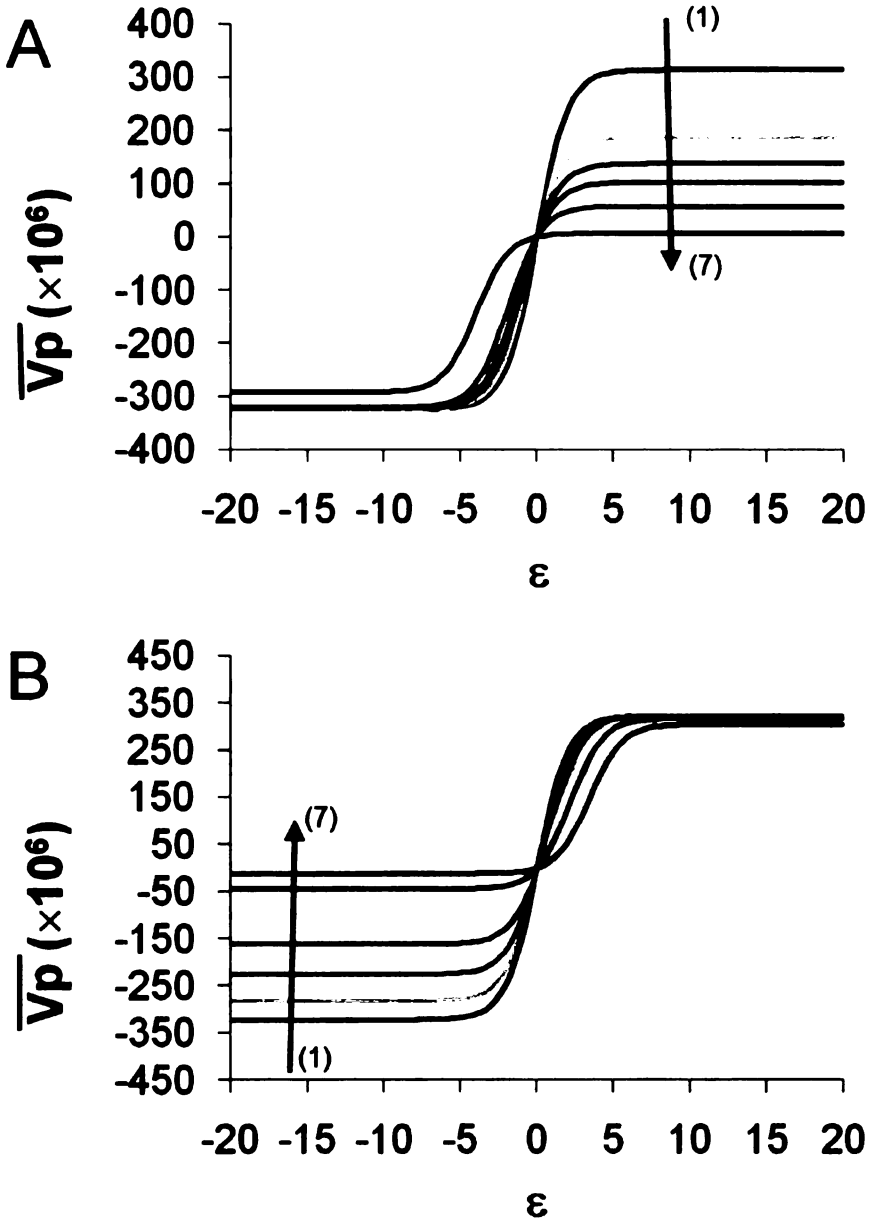

Figure 9.5: [A] Dimensionless steady state voltammograms where μ=1.0, λ=1.0, ϕ=1.0, κ=4.6, α=1.0, β=1.0, and Bi_P=1.2 where (1) Bi_S=1.2, (2) $Bi_S=1.2\times10^{-1}$, (3) $Bi_S=6.0\times10^{-2}$, (4) $Bi_S=3.6\times10^{-2}$, (5) $Bi_S=2.4\times10^{-2}$, (6) $Bi_S=1.2\times10^{-2}$, and (7) $Bi_S=1.2\times10^{-3}$ and [B] Dimensionless steady state voltammograms where μ=1.0, λ=1.0, ϕ=1.0, κ=4.6, $\omega=1.5\times10^{-3}$, $\rho=1.5\times10^{-3}$, α=1.0, β=1.0, and Bi_S=1.2 where (1) Bi_P=1.2, (2) $Bi_P=6.0\times10^{-2}$, (3) $Bi_P=2.4\times10^{-2}$, (4) $Bi_P=1.2\times10^{-2}$, (5) $Bi_P=6.0\times10^{-3}$, (6) $Bi_P=2.4\times10^{-3}$, and (7) $Bi_P=6.0\times10^{-4}$.

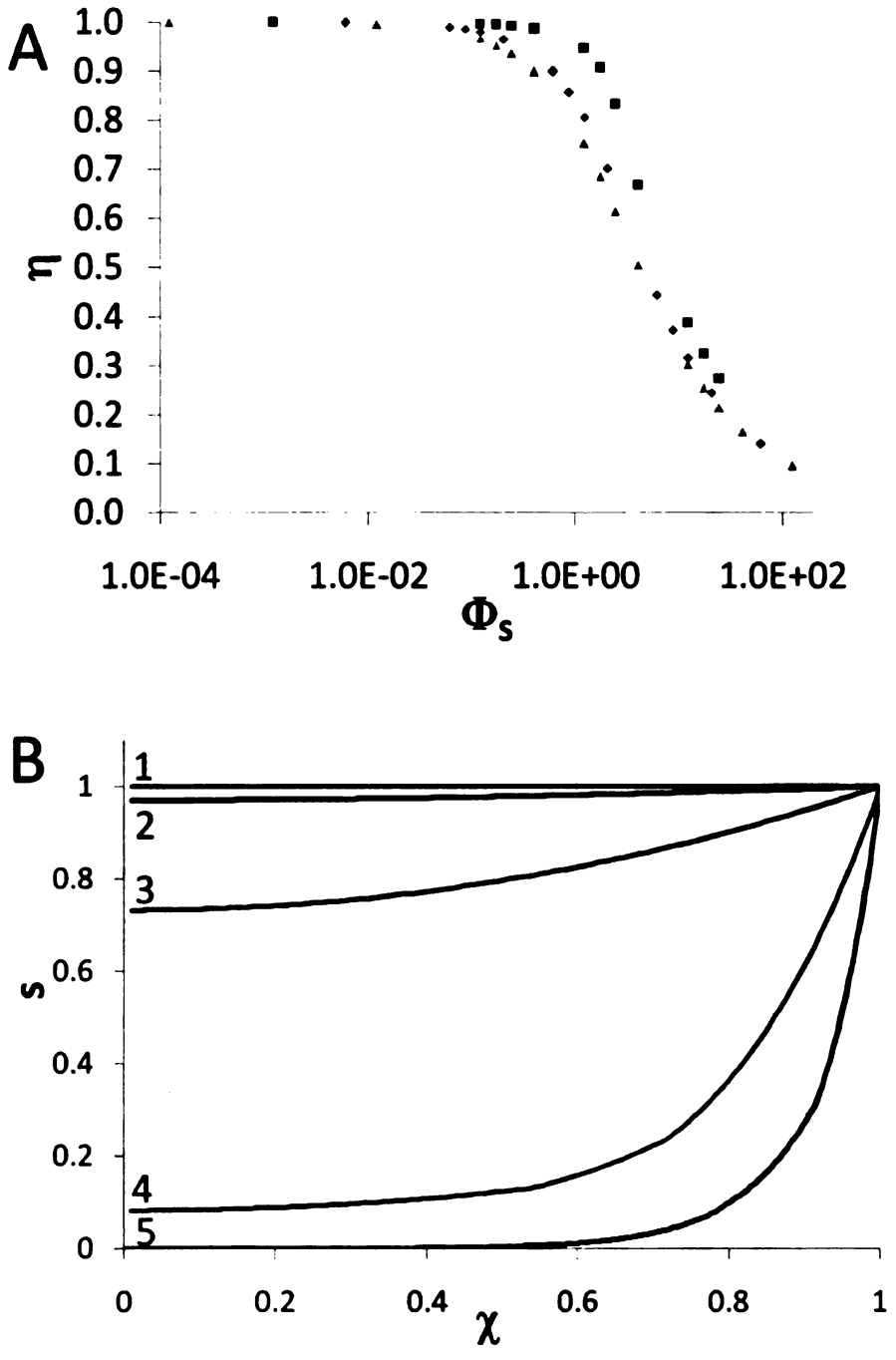

Figure 9.6: Effectiveness factor (η) as a function of the observed-Thiele modulus with respect to the substrate (Φ_S) when ϕ=1.0, κ=4.6, $\omega=1.5\times10^{-3}$, $\rho=1.5\times10^{-3}$, $Bi_S=1.2\times10^{5}$, and $Bi_P=1.2\times10^{5}$ measuring the effects of (A) D_S on the bioelectronic interface performance when (♦) μ=1, (■) μ=10 and (▲) and μ=100 and (B) Concentration profile of s through the film when (1) $\beta=1\times10^{-10}$, (2) β=1.0, (3) β=10, (4) β=100, and (5) β=1000.

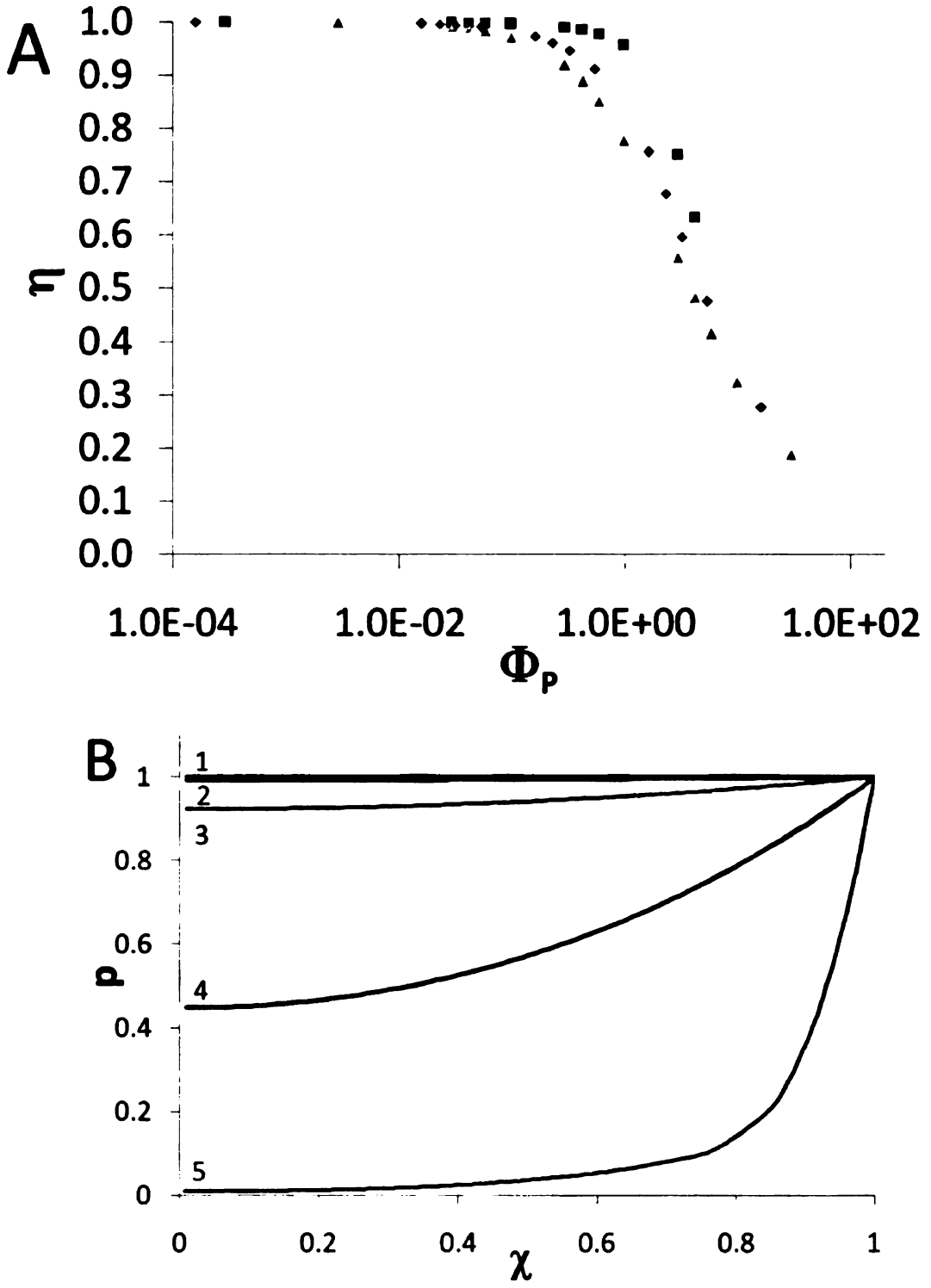

Figure 9.7: Effectiveness factor (η) as a function of the observed-Thiele modulus with respect to the substrate (Φ_P) when ϕ=1.0, κ=4.6, , $\omega=1.5\times10^{-3}$, $\rho=1.5\times10^{-3}$, $Bi_S=1.2\times10^{5}$, and $Bi_P=1.2\times10^{5}$ measuring the effects of (A) D_P on the bioelectronic interface performance when (♦) λ=1, (■) λ=10 and (▲) and λ=100 and (B) Concentration profile of s through the film when (1) $\alpha=1\times10^{-10}$, (2) α=1.0, (3) α=10, (4) α=100, and (5) α=1000.

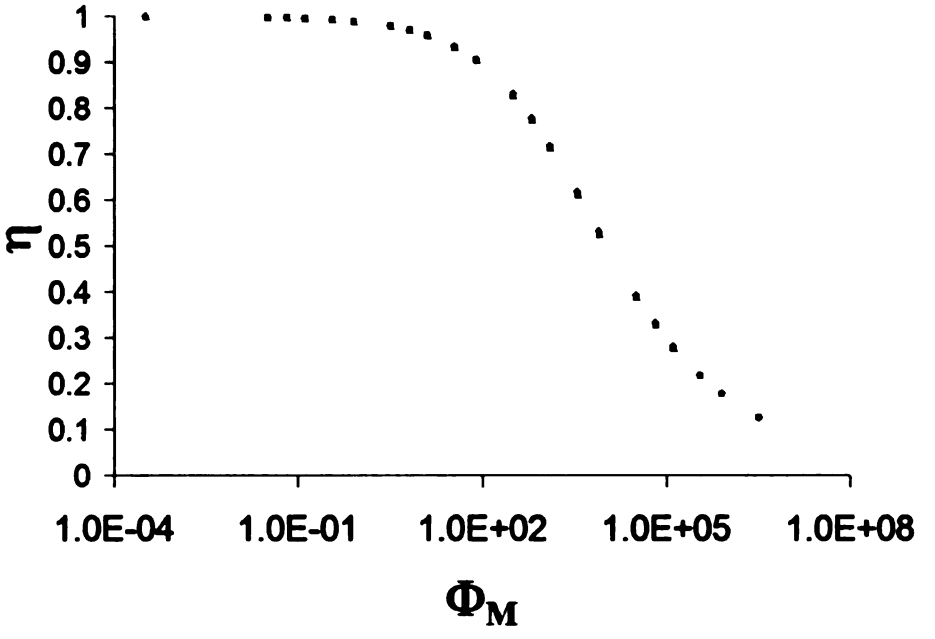

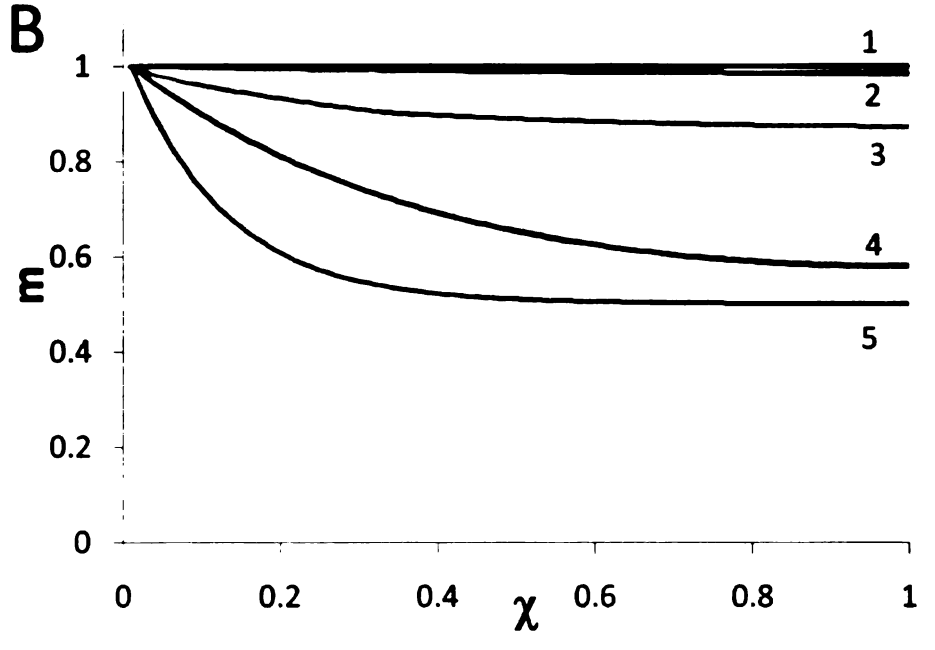

Figure 9.8: Effectiveness factor of the bioelectronic interface as a function of the observed-Thiele modulus; measuring the effects of D_M (Φ_M) on the bioelectronic interface when (♦) m=1, (■) m=10 and (▲) and m=100 when μ=1.0, λ=1.0, ϕ=1.0, κ=4.6, , $\omega=1.5\times10^{-3}$, $\rho=1.5\times10^{-3}$, $Bi_S=1.2\times10^{5}$, and $Bi_p=1.2\times10^{5}$ and (B) Concentration profile of s through the film when (1) D_M =1, (2) $D_M=1\times10^{-12}$, (3) $D_M=1\times10^{-13}$, (4) D_M 1×10^{-14}, and (5) $D_M=1\times10^{-15}$.

10. COVALENT MODIFICATION OF GLASSY CARBON ELECTRODES WITH MANNITOL DEHYDROGENASE FOR DETERMINATION OF FRUCTOSE

10.1. Abstract

Bioelectronic interfaces that establish electrical communication between a redox enzyme and electrodes have potential applications as biosensors, biocatalytic reactors, and biological fuel cells. Many bioelectronic interfaces contain enzymes and cofactors that have a limited lifetime and must be replaced periodically to allow long term operation. This chapter describes the fabrication of a novel bioelectronic interface containing an electron mediator, cofactor, and enzyme on a glassy carbon electrode (GCE). Interface fabrication is based on molecular self-assembly via reversible, pH-dependent ionic interactions, allowing the cofactor and enzyme to be removed via a decrease in pH, and then replaced to regenerate the biocatalytic activity. Chronoamperometry, cyclic voltammetry, electrochemical impedance spectroscopy (EIS) and X-ray photoelectron spectroscopy (XPS) were used to demonstrate the sequential assembly process and characterize the electrochemical properties of the bioelectronic interfaces. The original and regenerated interfaces exhibited virtually identical sensitivities, saturation currents, and turnover rates.

10.2. Introduction

Bioelectronic interfaces that achieve electrical communication between redox enzymes and an electrode have potential applications as biosensors (Armstrong, Heering et al. 1997; Zayats, Katz et al. 2002; Halbhuber, Petrmichlova et al. 2003), biocatalysts (Park, Laivenieks et al. 1999; Park and Zeikus 1999; Tsujimura, Fujita et al. 2001; Park, Vieille et al. 2003), and biofuel cells (Chen, Barton et al. 2001; Park and Zeikus 2003). Development of bioelectronic interfaces is especially challenging for dehydrogenase

enzymes, whose activity requires the presence of an electron carrying cofactor [e.g., β-nicotinamide adenine dinucleotide (NADH)] in the Rossmann fold of the enzyme. The cofactor facilitates the transfer of electrons between the redox center of the enzyme and the electrode. However, direct electrochemical oxidation of NADH requires the use of high overpotentials, which may lead to cofactor degradation (Blaedel and Jenkins 1975; Schmakel, Santhanam et al. 1975). Cofactor degradation can be circumvented using an electron mediator, such as toluidine blue O (TBO), Nile blue A, or neutral red, to shuttle electrons between the electrode and cofactor at moderate potentials (Molina, Boujtita et al. 1999; Pasco, Jeffries et al. 1999).

Several approaches have been used to achieve mediated electron exchange, including the development of linear (Zayats, Katz et al. 2002) and branched (Hassler and Worden 2006; Hassler, Dennis et al. 2007) molecular architectures that simultaneously hold the electrode, mediator, cofactor, and enzyme in close proximity; allow unimpeded access of the cofactor to its binding site on the enzyme; provide multistep electron transfer; and prevent component loss due to diffusion. However, these fabrication methods involve covalent linkages and make no provision for removal and replacement of labile components, such as the enzyme and cofactor, which have limited lifetimes. Long-term operation will require interface assembly methods that allow periodic removal and replacement of these components.

To address this need we recently developed a method to fabricate renewable bioelectronic interface on gold electrodes (Hassler, Kohli et al. 2007), which allows facile removal and replacement of the cofactor and enzyme. The approach uses layer-by-layer deposition of polyelectrolytes to reversibly bind the cofactor and enzyme, so that they can

be removed by reducing pH and then replaced to regenerate the bioelectronic activity (Hassler, Kohli et al. 2007).

Popular chemistries suitable to anchor bioelectronic interfaces to electrodes include alkane thiol self-assembly onto gold (Ulman 1996), addition of silanes to metal oxide surfaces (Ulman 1996), and linkage of alkenes to highly doped silicon (Barrelet, Robinson et al. 2001). The gold-thiol system allows facile production of well-ordered monolayers on which to build customized interfaces. However, the high cost of gold restricts the commercial application of these interfaces. Alkoxy-terminated silanes can react with surface hydroxyl groups on metal-oxide electrodes to form a polysiloxane linkage (Quan, Kim et al. 2004; Curran, Chen et al. 2005), but metal oxide substrates are not stable during anodic potential cycling, due to the anodic dissolution of the metal-oxide coating (Kraft, Hennig et al. 1994). The abovementioned disadvantages can be circumvented by fabricating the bioelectronic interface on a glassy carbon electrode (GCE) using a carbon-nitrogen bond (Adams 1969; Woodward 1985). Reticulated vitreous carbon is an open-pore foam of glassy carbon (Friedrich, Ponce-De-Leon et al. 2004) that offers advantages of low electrical resistance, large surface area, and customizable pore structure, making it well suited for applications involving fluid flow (Strohl and Curran 1979; Strohl and Curran 1979).

To date, the advantages offered by the renewable bioelectronic interface concept have not been extended to GCE. This paper describes for the first time molecular self assembly of a renewable bioelectronic interfaces on a GCE. Glycine (Gly) and poly(ethyleneimine) (PEI) were used to couple the electron mediator (TBO), cofactor (NADH), and enzyme [mannitol dehydrogenase, (TmMtDH)] to a GCE in such a way

that mediated electron transfer was achieved. The enzyme and cofactor can be removed by decreasing pH, thereby protonating the surface-bound carboxylic acid and disrupting the electrostatic interactions between the GCE and the cofactor- and enzyme-modified PEI. Fresh cofactor and enzyme could then be reattached to regenerate bioelectronic activity. Chronoamperometry, cyclic voltammetry, EIS, and XPS were used to demonstrate the assembly process and characterize the electrochemical activity of the resulting bioelectronic interface. EIS was also used to determine the electron transfer properties including the surface coverage of the electron mediator (Γ_{med}) and charge propagation diffusion coefficient (D_{app}) were also determined.

10.3. Materials and Methods

10.3.1. Media and Strains

Escherichia coli BL21(DE3) (Novagen, Madison, WI) culture containing a recombinant plasmid for TmMtDH from *Thermotoga maritima* was grown, and purified as described in Chapter 2 (Song, Ahluwalia et al. 2008).

10.3.2. Chemicals

Gly, n-hydroxysuccinimide (NHS), 1-ethyl-3-(3-dimethylaminopropyl) carbodiimide (EDC), TBO, 3-carboxyphenyl boronic acid (CBA), NADH, PEI, glutaric dialdehyde (25% in water), D-fructose, D-glucose, sorbose, and arbinose were purchased from Sigma-Aldrich (St. Louis, MO). Ultrapure water (18.2 MΩ) was supplied by a Barnstead Nanopure-UV four-stage purifier (Barnstead International, Dubuque, IA).

10.3.3. Surface Modification

Polished GCEs were modified with Gly by cycling the applied potential between 2500 mV and -1500 mV at a scan rate (ν) of 100 mV s^{-1} in a 100 mM phosphate buffer

solution (PBS) (pH 7.4) containing 100 mM Gly. The GCEs were then washed with distilled water to remove any physically adsorbed material and dried with nitrogen.

The Gly-modified GCEs were incubated for 1 h in 0.1 mM TBO in 100 mM PBS (pH 7.4) in the presence of 10 mM NHS and 10 mM EDC, resulting in formation of an amide linkage between the amine group of the TBO and the carboxylic acid group of the Gly (Gly-TBO). The Gly-TBO-modified electrodes were soaked in a 10 mM aqueous solution of PEI containing 100 mM NaCl (pH 7.0) to form a Gly-TBO-PEI-modified interface. A 5 mM aqueous CBA solution was activated at room temperature (25±2 °C) in the presence of 10 mM NHS and 10 mM EDS for 2 h. The NHS-modified CBA was then reacted with Gly-TBO-PEI-functionalized electrodes at room temperature for 1 h, resulting in an amide linkage between the carboxylic acid group of the CBA and the amine group of the PEI. The CBA-modified electrodes were then reacted with a 1 mM NADH solution in 100 mM PBS (pH 7.4) for 1 h. Since NADH has two ribose units available for reaction two binding modes are available. The Gly-TBO-PEI-NADH-functionalized GCE were reacted with a 4.4 mg mL^{-1} solution of TmMtDH in 100 mM PBS (pH 7.4) for 1 h at room temperature and cross-linked with 25 % (v/v) glutaric dialdehyde in water for 20 min. The resulting TmMtDH-modified electrodes were used for either the biocatalytic reduction of fructose or oxidation of mannitol.

The functionalized PEI layer was removed from the electrode by immersion in 10 mM HCl (pH 2.0) at room temperature for 30 min. For pH values below the pKa of Gly (pKa~4.3) the unreacted carboxylic acid groups of Gly become protonated, decreasing electrostatic interaction between the Gly-TBO modified electrode and the TmMtDH-modified PEI, allowing PEI to disengage from the surface. To reconstitute the

bioelectronic interface PEI, CBA, NADH, and TmMtDH were deposited onto the TBO-modified Gly monolayer using the protocol described above.

10.3.4. Electrochemical Techniques

Cyclic voltammetry, chronoamperometry, and electrochemical impedance spectroscopy were performed using an electrochemical analyzer (CHI660B, CH Instruments) as described in Chapter 2.

10.3.5. Surface Characterization

10.3.5.1. Ellipsometry

After deposition of each layer, the bioelectronic interface was dried with N_2 and its ellipsometric thickness was measured using a rotating analyzer ellipsometer (model M-44, J. A. Woollam, Lincoln, NE, USA) and WVASE32 software. A film refractive index of 1.5 was assumed for all thickness measurements.

10.3.5.2. X-ray Photoelectron Spectroscopy

Binding of Gly to the GCE was confirmed by XPS (Ma, Gao et al. 2005) using a Perkin-Elmer Physical Electronics PHI 5400 X-ray photoelectron spectrometer equipped with a Mg X-ray source operated at 300 W (15 kV, 20 mA). The elemental nitrogen-to-carbon (N/C) ratio was calculated by dividing the total number of counts under the N(ls) band by that under the C(ls) (284.6 eV) band and multiplying the results by 100.

10.4. Results

10.4.1. Interface Assembly

The cyclic voltammetry plots (Figure 10.1) depict the anodic immobilization of Gly onto GCE in 100 mM PBS (pH 7.4) containing 100 mM Gly at a scan rate of 100 mV s^{-1}. An oxidation peak observed at 1300 mV in the anodic direction represents the one-electron oxidation of the amino group into its corresponding cation radical (Zhang

2008). The magnitude of the oxidation peak increased with each successive scan, suggesting the cation radicals form carbon-nitrogen linkages at the glassy carbon surface (Zhang and Lin 2001; Zhang and Sun 2001; Zhang 2008). A reduction peak at -420 mV, increased with each successive scan. The increases in both the oxidation and reduction peaks are consistent with an electroconductive film being formed on the electrode surface (Wang, Li et al. 2006).

10.4.2. Interface Characterization

Figure 10.2 shows the XPS spectrum of the N1s region for the freshly polished GCE (Figure 10.2A), GCE after soaking in 100 mM Gly for 1 h (Figure 10.2B), and after redox cycling potential between 2500 mV and -1500 mV in a 100 mM Gly solution (Figure 10.2C). The N1s peak (399.4 eV) provides evidence that a carbon-nitrogen bond was formed between the amine radical and an aromatic moiety of the GCE (Ma, Gao et al. 2005; Wang, Li et al. 2006). The freshly polished GCE exhibited an N/C peak ratio of 1.0 (Figure 10.2A). Upon soaking in 100 mM Gly for 1 h the N/C ratio increased to 1.8 (Figure 10.2B) suggesting that Gly weakly binds to the GCE, possibly due to physical adsorption (Zhang 2008). Upon cycling potential between 2500 mV and -1500 mV in the presence of 100 mM Gly the N/C ratio increased to 4.1 (Figure 10.2C). This increase in the N/C ratio relative to the polished electrode provides strong evidence for formation of carbon-nitrogen bonds on the GCE (Zhang 2008).

Figure 10.3A shows the impedance spectra for the Gly, Gly-TBO, Gly-TBO-PEI, Gly-TBO-PEI-NADH, and Gly-TBO-PEI-NADH-TmMtDH (Curves 1-5, respectively) modified electrodes. R_{CT} increased with each subsequent layer, providing evidence of interface assembly a well-behaved LBL assembly process (Zhao and Ju 2006). Figure

10.3B (Curve 1) shows the Nyquist plot after the Gly-TBO-PEI-NADH-TmMtDH-modified electrodes was immersed in 10 mM HCl, and subsequent reassembly of the bioelectronic interface. The R_{CT} value after the HCl wash (780±0.9 Ω cm^2) was approximately equal to that for the original Gly-TBO-modified electrode (760±1.0 Ω cm^2), suggesting that the HCl removed the PEI, NADH and TmMtDH layers. After neutralizing the pH and subsequent readsorption of PEI, NADH, and TmMtDH, the R_{CT} (2500±21 Ω cm^2) (Figure 10.3B, Curve 2) was consistent with the original Gly-TBO-PEI-NADH-TmMtDH-modified electrode (2300±20. Ω cm^2), indicating that the bioelectronic interface could be removed by changing pH then reconstituted.

10.4.3. Determination of redox site concentration

The redox site concentration (Γ_{med}) was estimated from the low frequency impedance using Eq. 2.7. The experimental data for the Gly-TBO-PEI-NADH-TmMtDH-modified GCE was fit with the equivalent circuit, replacing the C_{DL} with a constant phase element (CPE) (Brug, Vandeneeden et al. 1984). The best fit value for C_F was determined to be $3.7\pm0.3\times10^{-4}$ F. The surface coverage of toluidine blue (Γ_{TBO}) was determined as $1.4\pm0.1\times10^{-9}$ mol cm^{-2} by Eq. 2.7. The ellipsometric film thickness was determined to be 13.3±3.2 nm. A model predicting that Γ_{TBO} is proportional to the film thickness was fit to the data and used to determine an average TBO concentration within the film (C_{TBO}) of 126.4±8.0 mol cm^{-3}.

10.4.4. Determination of charge propagation diffusion coefficient

The ω_{tr} value was determined graphically from plots of $\log(Y/\omega)$ vs $\log(\omega)$ (Figure 10.4) to be 58.2±9.6 Hz; this value was used in Eq. 2.8 to calculate a D_{app} of $1.0\pm0.3\times10^{-10}$ cm^2 s^{-1}. The value of D_{app} should be considered a binary apparent diffusion coefficient, since at least two different species could be responsible for charge transfer inside the film: the TBO_{ox}/TBO_{red} redox centers through an electron hopping mechanism and counter-ion diffusion (Tagliazucchi and Calvo 2007). The high frequency resistance (measured at 10 kHz) for the Gly-TBO-PEI-NADH-TmMtDH-modified electrode varied by 10% over the potential range -200 to 200 mV, indicating that D_{app} is governed by electron hopping (Tagliazucchi and Calvo 2007).

10.4.5. Electrochemical Characterization

10.4.5.1. Enzyme Adsorption Kinetics

Figure 10.5A shows cyclic voltammograms at different times of TmMtDH adsorption on a Gly-TBO-PEI-NADH-modified electrode obtained at a constant fructose concentration (250 mM) in 100 mM PBS (pH 6.0) at 60 °C. Figure 10.5B shows the peak cathodic current at various adsorption times. A first-order kinetic model was fit to the peak-cathodic-current vs. time data, yielding a time constant of 56.4±1.3 min.

10.4.5.2. Effects of pH changes

The influence of pH on the redox reactions is shown in Figure 10.6. The oxidation potentials varied linearly with pH, giving a sensitivity of 58.8±2.7 mV $(pH\ unit)^{-1}$. According to the Nernst equation, the theoretical value of this slope should be 59.16 b/d mV $(pH\ unit)^{-1}$ (Wang, Li et al. 2006), where b and d are the number of protons and electrons transferred during oxidation, respectively. The similarity of the measured value

to that predicted by Nernst equation assuming $b=d$ suggests that an equal number of electrons and protons are exchanged during the anodic and cathodic sweeps, respectively.

10.4.5.3. Interface Properties

Figure 10.7 shows the chronoamperometric current response for the Gly-TBO-PEI-NADH-TmMtDH-modified electrode following a step change in potential from 100 to -600 mV, measured in 100 mM PBS (pH 6.0) containing 250 mM fructose at 60°C. Fitting Eq. 2.1 to the chronoamperometric data, gave k'_{et} and $k''_{et,}$ values of 260.5±3.7 and 112.8±2.2 s^{-1} for the two binding modes. The differences in k'_{et} and $k''_{et,}$ suggest that one of the two NADH-TmMtDH-complexes decays twice as fast as the other. The Γ_{enz} values, for the two binding modes were calculated to be $1.1\pm0.1\times10^{-11}$ mol cm^{-2} and $1.0\pm0.1\times10^{-11}$ mol cm^{-2} using Eq. 2.3.

Figure 10.8A shows the cyclic voltammograms of the Gly-TBO-PEI-NADH-TmMtDH-modified electrode at various fructose concentrations in 100 mM PBS (pH 6.0) at 60 °C. The peak cathodic current increased linearly with fructose concentration (Figure 10.8B) below 250 mM, indicating that the interface could be used as a fructose biosensor. The slope of the calibration curve (0.71±0.02 μA mM^{-1} cm^{-2}) is a measure of the biosensor's sensitivity. At fructose concentrations above 300 mM, the cathodic current reached a saturation value (I_{cat}^{sat}=734.9±7.2 μA cm^{-2}). The calculated TR_{max} was found to be 55.1±7.2 s^{-1}, using Eq. 2.4 (Eisenwiener and Schulz 1969).

The selectivity of the Gly-TBO-PEI-NADH-TmMtDH-modified electrode was examined by testing alternative substrates. Table 10.1 shows the values of I_{cat}^{sat}, sensitivity and TR_{max} values of the Gly-TBO-PEI-NADH-TmMtDH-modified electrode

in the presence of fructose, glucose, arbinose, and sorbose. These data are consistent with the published selectivity values for the free enzyme (Song, Ahluwalia et al. 2008).

To confirm renewability of the interface, the performance properties of the Gly-TBO-PEI-NADH-TmMtDH-modified electrode were measured before and after interface removal and reconstitution (Table 10.2). The Γ_{enz}, k'_{et}, k''_{et}, I_{cat}^{sat}, sensitivity, and TR_{max} for the reconstituted interface were virtually identical to those for the Gly-TBO-PEI-NADH-TmMtDH-modified electrode, indicating that the interface could be removed and reconstituted with virtually no performance loss.

The results presented here demonstrate for the first time fabrication of a renewable, dehydrogenase-based bioelectronic interface on a GCE. The approach uses functionalized polyelectrolytes that can be removed by a simple pH change, and then reconstituted. The ability to reconstitute dehydrogenase-based bioelectronic interfaces without performance loss can greatly reduce the useful lifetime, and hence operating costs, of bioelectronic processes. It would allow porous carbon electrode matrix to be renewed in-situ within a packed-bed electrobioreactor. The NADH-TmMtDH–modified PEI can be removed by a decrease in pH and then reconstituted for bioreactor and biofuel cell applications.

10.5. Discussion

The most popular chemistries for bioelectronic interface formation is alkane thiol self-assembly onto gold (Ulman 1996) allowing well ordered monolayers easily to easily form on the surface of the electrode. However, the high cost of gold and low surface area (typically limited to a two-dimensional structure on the surface of the electrode), restricts the use of these interfaces for commercial applications. The fabrication of novel

bioelectronic interface on a GCE is presented. The interfaces developed on the glassy carbon have been shown have an Γ_{enz} comparable to that found for a gold electrode. It is shown that an applied potential is required to catalyze the formation of the C-N bond on the surface of the electrode; however, it is know that the adsorption of Gly can be controlled by the number of sweeps during the adsorption process. Understanding the effects of the applied potential on the performance parameters of the electrode could be essential in the optimization for bioelectronic interface fabrication.

Even though the GCEs used in this study were two-dimensional with a controlled area, the development of the interface on carbon provides a mechanistic understanding for the fabrication of cofactor-dependent dehydrogenase enzymes on reticulated vitreous carbon electrodes (RVC). RVC is a poreous carbon substrate (electrode) whose high surface area (upto 70 cm^{-1} [surface area per unit volume]), low cost, high themal stability, and its ability to fit into a modular reactor make it attractive material for future development as a catalyst.

10.6. Conclusions

The first renewable, dehydrogenase-containing bioelectronic interface for glassy carbon electrodes has been developed. An electron mediator was first covalently bound to a GCE, followed by adsorption of a positively charged polyelectrolyte functionalized with its cofactor. Finally the enzyme (mannitol dehydrogenase) was adsorbed by electrostatic interactions. AFM, chronoamperometry, cyclic voltammetry, EIS, and XPS were used to demonstrate sequential assembly of the layers and to characterize the multistep electron transfer between the enzyme and electrode. Renewability was demonstrated by removing the labile components of the interface via a decrease in pH

and then reconstituting the interface to regenerate full functionality. The sensitivity, I_{cat}^{sat}, and TR_{max} of the reconstituted interface (0.7±0.1 μA mM^{-1} cm^{-2}, 734.2±16.9 μA cm^{-2}, and 52.1±4.2 s^{-1}, respectively) were comparable to those of the original (0.7±0.0 μA mM^{-1} cm^{-2}, 740.9±11.6 μA cm^{-2}, and 57.5±2.8 s^{-1}, respectively). The ability to develop a bioelectronic interface on a GCE has potential applications for biosensors and biocatalytic reactors, and biological fuel cells.

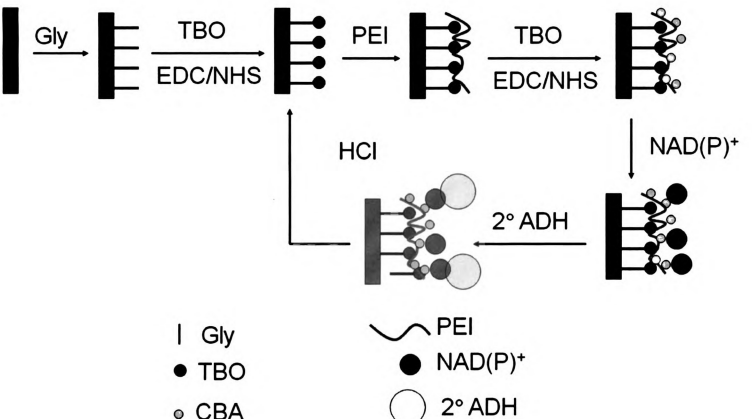

Scheme 10.1: Sequential steps in the formation of integrated Gly-TBO-PEI-NADH-TmMtDH- functionalized glassy carbon electrode.

Table 10.1: Selectivity of the Gly-TBO-PEI-NADH-TmMtDH-modified electrode to the substrates: fructose, glucose, arbinose, and sorbose.

Compound	I_{cat}^{sat} ($\mu A\ cm^{-2}$)	Sensitivity ($\mu A\ mM^{-1}\ cm^{-2}$)	TR_{max} (s^{-1})
Fructose	734.9±7.2	0.71±0.02	44.8±2.5
Glucose	530.7±2.2	0.18±0.00	10.3±0.8
Arabinose	542.8±9.1	0.26±0.00	15.2±2.1

Table 10.2: Comparison of performance of the Gly-TBO-PEI-NADH-TmMtDH-modified electrode containing before and after interface removal by HCl wash and reconstitution.

	Γ_{enz} ($\times 10^{-11}$ mol cm^{-2})		k_{et} (s^{-1})		I_{cat}^{sat} ($\mu A\ cm^{-2}$)	Sensitivity ($\mu A\ mM^{-1}\ cm^{-2}$)	TR_{max} (s^{-1})
Before HCl wash	0.9±0.1	1.8±0.1	471.3±15.6	84.1±1.7	784.9±7.2	0.71±0.02	44.8±2.5
After Reconstitution	0.6±0.0	2.2±0.1	471.8±9.6	73.9±0.1	734.2±16.9	0.62±0.01	39.1±3.5

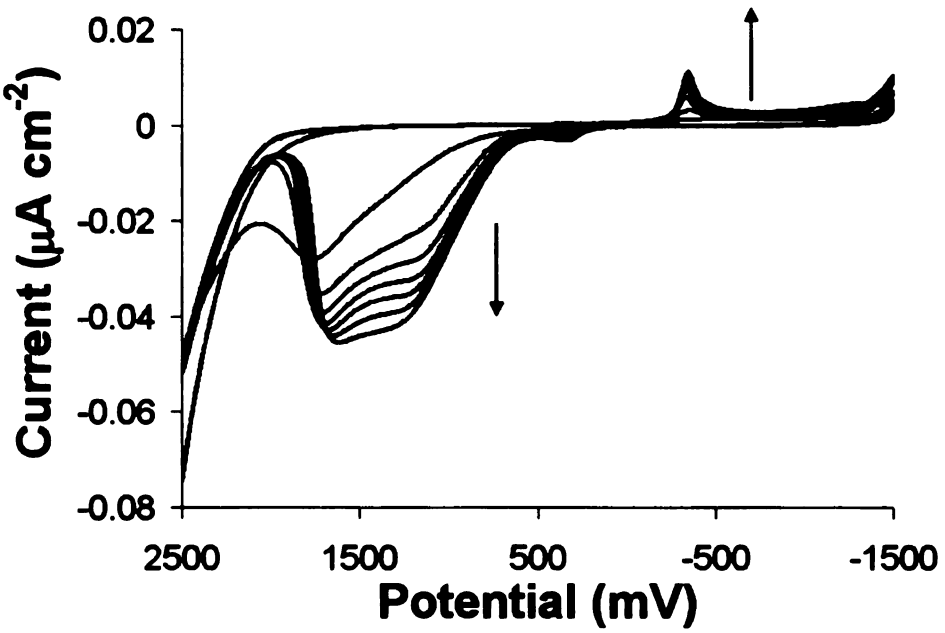

Figure 10.1: Cyclic voltammogram for the preparation of a Gly-modified GCE. Scan Rate 100 mV s^{-1}; supporting electrolyte: phosphate buffer solution (pH 7.4)

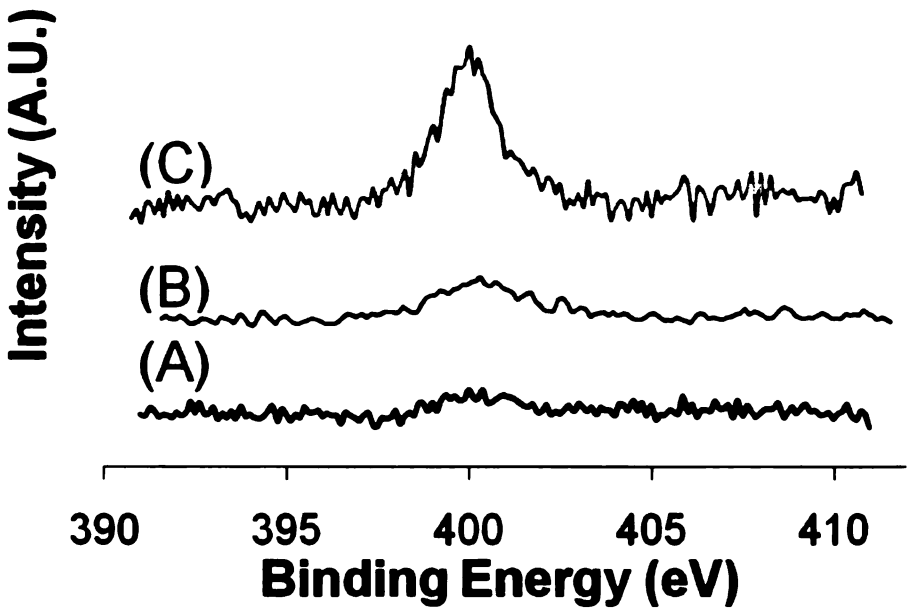

Figure 10.2: The N(1s) region of the XPS spectrum of the (A) bare GCE, (B) GCE after soaking in 100 mM Gly for 1 h, and (C) GCE after being electrooxidized by cyclic voltammetry between -1500 mV and 2500 mV in a 50 mM Gly solution for 14 cycles.

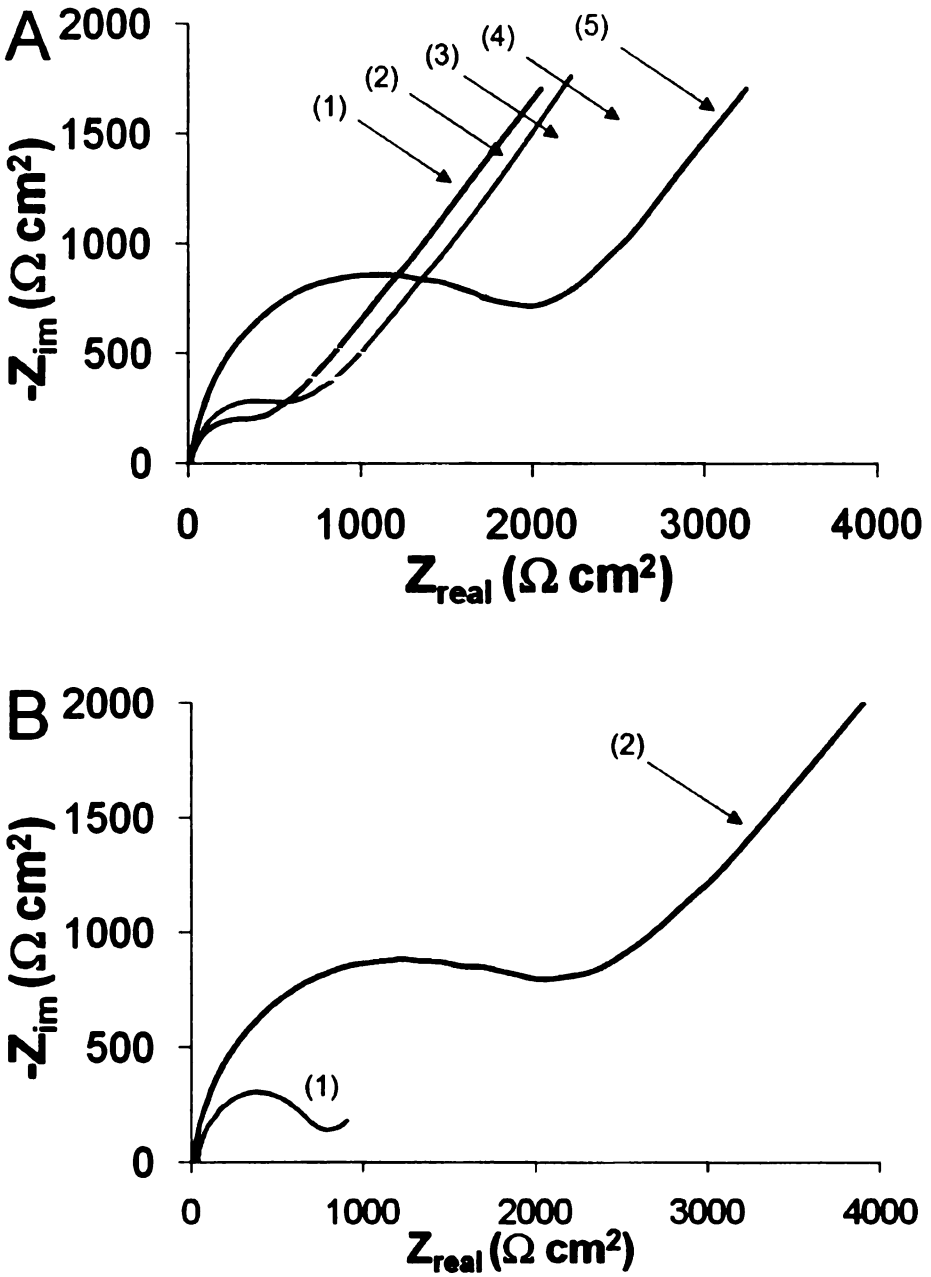

Figure 10.3: (A) (1) Gly, (2) Gly-TBO, (3) Gly-TBO-PEI, (4) Gly-TBO-PEI-NADH, and (5) Gly-TBO-PEI-NADH-TmMtDH-modified electrode and (B) Nyquist plots for the (1) Gly-TBO-PEI-NADH-TmMtDH-modified electrode after washing with 10 mM HCl and the (2) Gly-TBO-PEI-NADH-TmMtDH-modified electrode after interface removal and reconstitution. All impedance measurements were recorded in an equimolar 5 mM solution of $K_3[Fe(CN)_6]/K_4[Fe(CN)_6]$ in 100 mM PBS (pH 7.4) recorded at the electrodes open circuit potential (230 mV) and room temperature (25±2°).

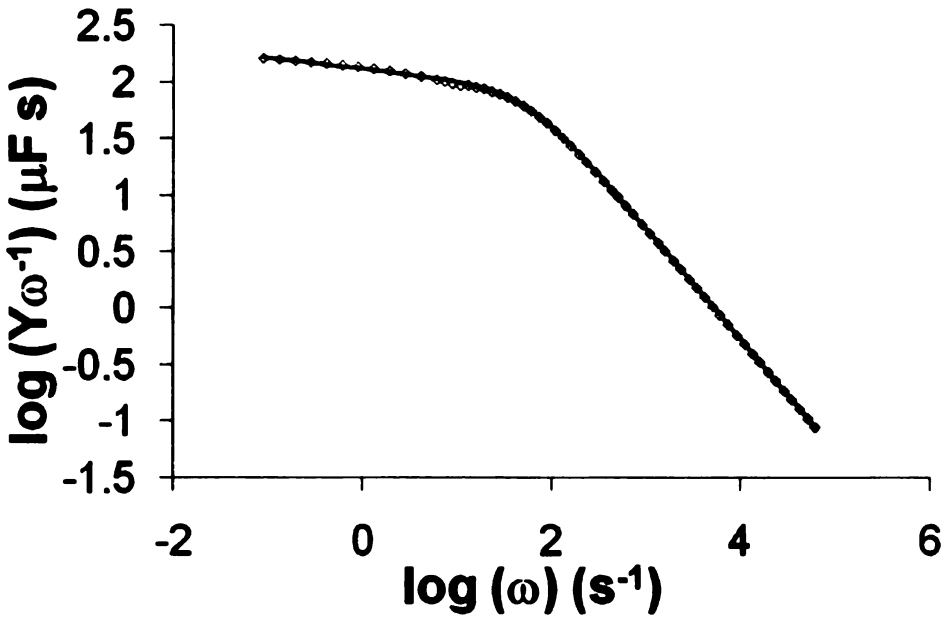

Figure 10.4: Log (Y"/ω) vs log (ω) plots for the Gly-TBO-PEI-NADH-TmMtDH-functionalized GCE in 100 mM PBS (pH 6.0) measured at a potential of -200 mV. Solid line represents the best fit of the circuit.

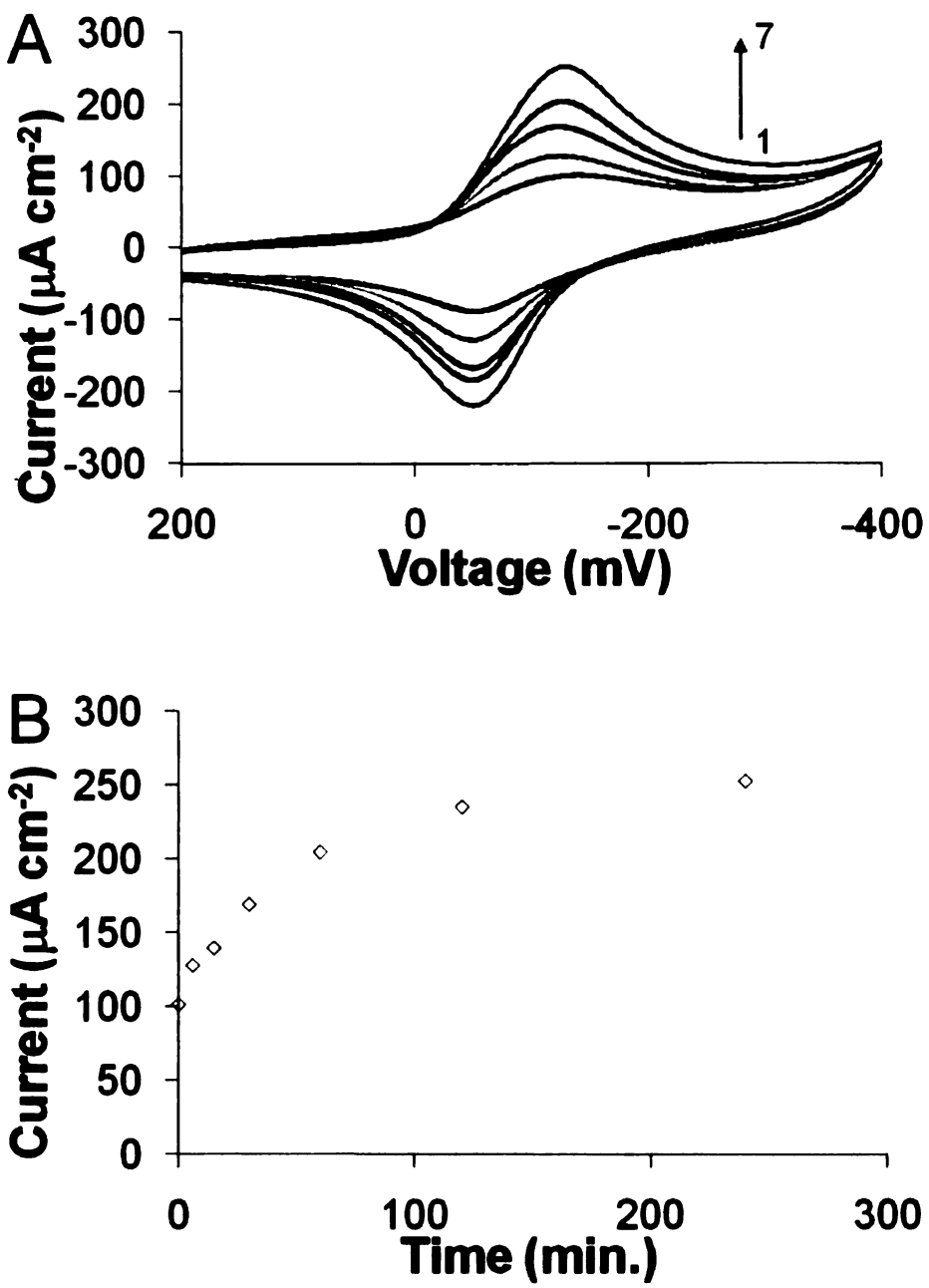

Figure 10.5: (A) Cyclic voltammograms of the Gly-TBO-PEI-NADH-functionalized electrode at various times of TmMtDH of reconstitution: (1) 0, (2) 6, (3) 15, (4) 30, (5) 60, (6) 120 and (7) 240 min. The data were recorded in 100 mM PBS (pH 6.0) containing 250 mM fructose at 60°C, and potential scan rate of 100 mV s^{-1}. (B) Peak electrocatalytic current at various time intervals.

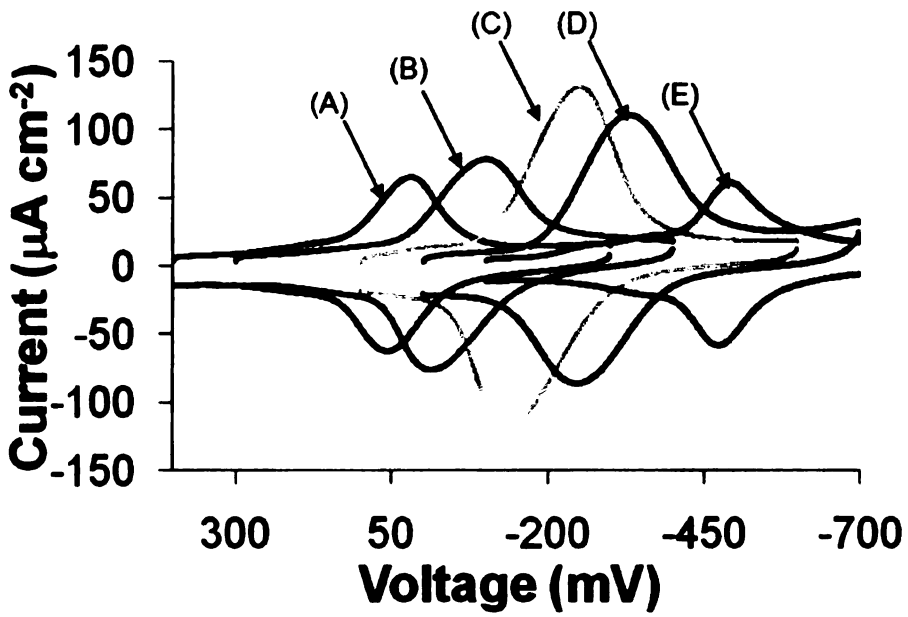

Figure 10.6: Cyclic Voltammograms of the Gly-TBO-PEI-NADH-TmMtDH-functionalized electrode in 100 mM PBS containing 250 mM fructose at 60°C, at various pHs: (A) 2.0, (B) 4.0, (C) 6.0, (D) 8.0, and (E) 10.0. The data were recorded in 100 mM PBS (pH 6.0) containing 250 mM fructose at 60°C at a potential scan rate of 100 mV s^{-1}.

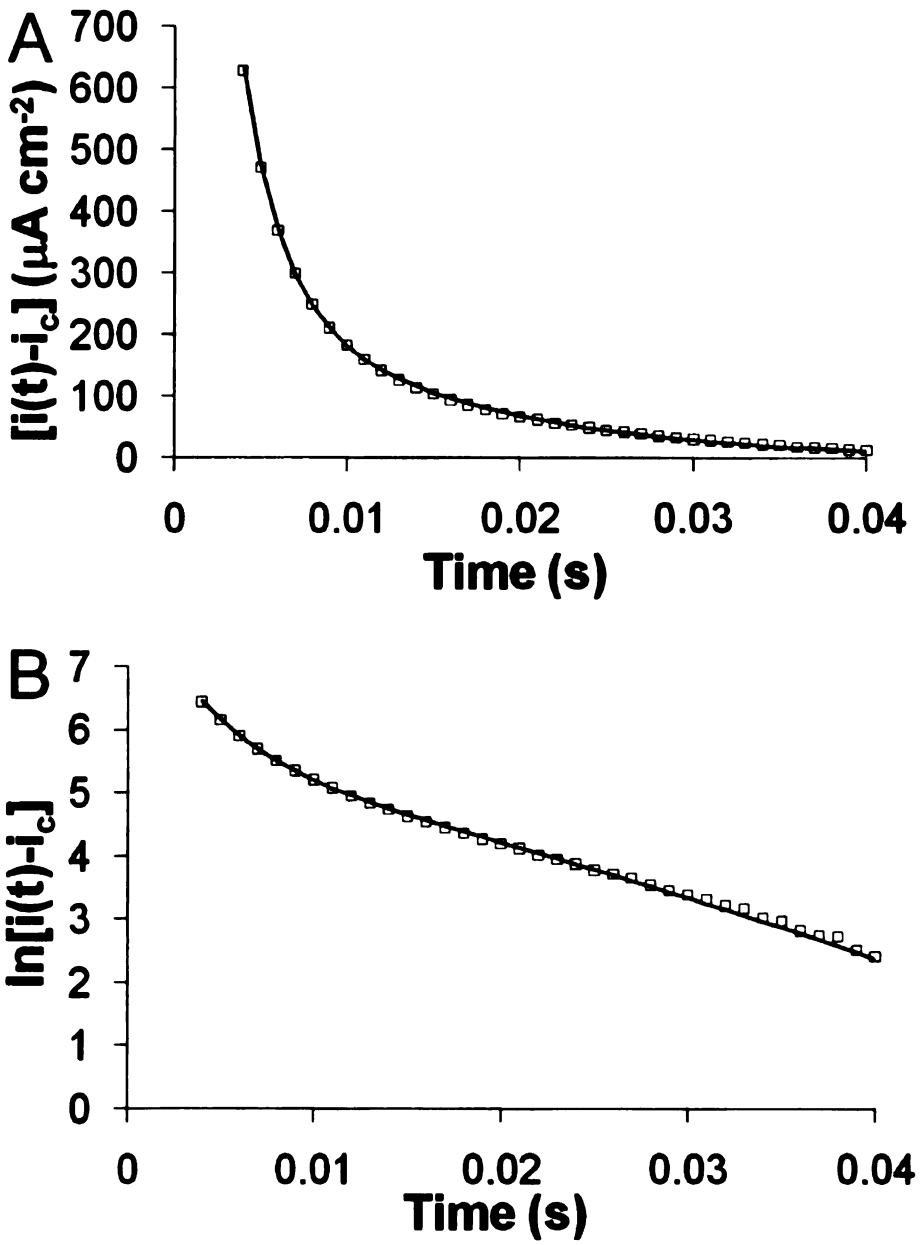

Figure 10.7: (A) Current transient for a potential step from -200 mV to 400 mV for a Gly-TBO-PEI-NADH-TmMtDH-functionalized electrode in 100 mM PBS (pH 7.4) containing 25 mM 2-propanol at room temperature. (B) Shows the plots of $\log[i(t)-i_c]$ after double layer charging. The solid line represents the curve of best fit to the data.

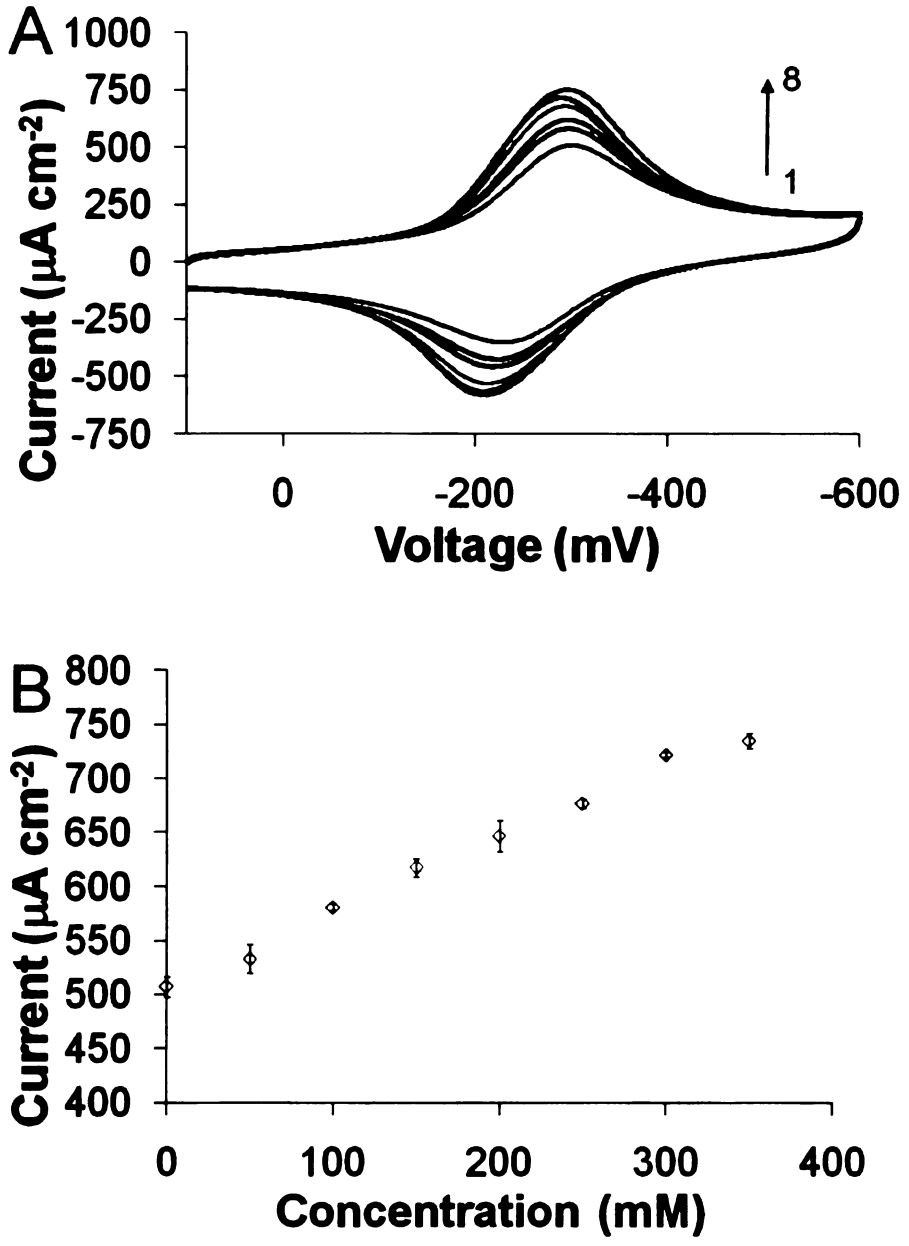

Figure 10.8: (A) Cyclic voltammograms of the Gly-TBO-PEI-NADH-TmMtDH-functionalized electrode in the presence of different concentrations of fructose in 100 mM PBS (pH 6.0) at 60°C: (1) 0, (2) 50, (3) 100, (4) 150, (5) 200, (6) 250, (7) 300, and (8) 350 mM. The data were recorded at a potential scan rate of 100 mV s^{-1}. (B) Peak electrocatalytic current at various fructose concentrations. The error bars indicate the mean ± the standard deviation (n=3).

11. REFERENCES

Adams, R. N. (1969). Electrochemistry at Solid Electrodes. New York, New York, Marcel Dekker.

Ai, H., M. Fang, et al. (2002). "Electrostatic layer-by-layer nanoassembly on biological microtemplates: Platelets." Biomacromolecules **3**(3): 560-564.

Ai, H., J. Ihlemann, et al. (2002). "Effect of fiber type and nutritional state on AICAR- and contraction-stimulated glucose transport in rat muscle." American Journal of Physiology-Endocrinology and Metabolism **282**(6): E1291-E1300.

Andrieux, C. P., J. M. Dumasbouchiat, et al. (1982). "Catalysis of Electrochemical Reactions at Redox Polymer Electrodes - Kinetic-Model for Stationary Voltammetric Techniques." Journal of Electroanalytical Chemistry **131**(JAN): 1-35.

Antipov, A. A. and G. B. Sukhorukov (2004). "Polyelectrolyte multilayer capsules as vehicles with tunable permeability." Advances in Colloid and Interface Science **111**(1-2): 49-61.

Armstrong, F. A., H. A. Heering, et al. (1997). "Reactions of complex metalloproteins studied by protein-film voltammetry." Chemical Society Reviews **26**(3): 169-179.

Armstrong, F. A. and G. S. Wilson (2000). "Recent developments in faradaic bioelectrochemistry." Electrochimica Acta **45**(15-16): 2623-2645.

Asuri, P., S. S. Karajanagi, et al. (2006). "Directed assembly of carbon nanotubes at liquid-liquid interfaces: Nanoscale conveyors for interfacial biocatalysis." Journal of the American Chemical Society **128**(4): 1046-1047.

Ausubel, F. M., R. Brent, et al. (1993). Current protocols in Molecular Biology. New York, NY, Greene Publishing and Wiley-Interscience.

Badia, A., R. Carlini, et al. (1993). "Intramolecular Electron-Transfer Rates in Ferrocene-Derivatized Glucose-Oxidase." Journal of the American Chemical Society **115**(16): 7053-7060.

Banta, S. and S. Anderson (2002). "Verification of a novel NADH-binding motif: Combinatorial mutagenesis of three amino acids in the cofactor-binding pocket of Corynebacterium 2,5-diketo-D-gluconic acid reductase." Journal of Molecular Evolution **55**(6): 623-631.

Bard, A. and L. Faulkner (2001). Electrochemical Methods Fundementals and Applications. Hoboken, NJ, John Wiley and Sons.

Barlett, P. N., P. Tebutt, et al. (1991). Prog. React. Kinet. **16**: 55-155.

Barrelet, C. J., D. B. Robinson, et al. (2001). "Surface characterization and electrochemical properties of alkyl, fluorinated alkyl, and alkoxy monolayers on silicon." Langmuir **17**(11): 3460-3465.

Bartlett, P. N. and K. F. E. Pratt (1995). "Theoretical Treatment of Diffusion and Kinetics in Amperometric Immobilized Enzyme Electrodes .1. Redox Mediator Entrapped within the Film." Journal of Electroanalytical Chemistry **397**(1-2): 61-78.

Barton, S. C., J. Gallaway, et al. (2004). "Enzymatic biofuel cells for Implantable and microscale devices." Chemical Reviews **104**(10): 4867-4886.

Berg, M. C., S. Y. Yang, et al. (2004). "Controlling mammalian cell interactions on patterned polyelectrolyte multilayer surfaces." Langmuir **20**(4): 1362-1368.

Blaedel, W. J. and R. A. Jenkins (1975). "Study of Electrochemical Oxidation of Reduced Nicotinamide Adenine-Dinucleotide." Analytical Chemistry **47**(8): 1337-1343.

Brooks, S. P. J. (1992). "A Simple Computer-Program with Statistical Tests for the Analysis of Enzyme-Kinetics." Biotechniques **13**(6): 906-911.

Brown, K. R., L. A. Lyon, et al. (2000). "Hydroxylamine seeding of colloidal au nanoparticles. 3. Controlled formation of conductive Au films." Chemistry of Materials **12**(2): 314-323.

Brug, G. J., A. L. G. Vandeneeden, et al. (1984). "The Analysis of Electrode Impedances Complicated by the Presence of a Constant Phase Element." Journal of Electroanalytical Chemistry **176**(1-2): 275-295.

Burdette, D. and J. G. Zeikus (1994). "Purification of Acetaldehyde Dehydrogenase and Alcohol Dehydrogenases from Thermoanaerobacter-Ethanolicus 39e and Characterization of the Secondary-Alcohol Dehydrogenase (2-Degrees Adh) as a Bifunctional Alcohol-Dehydrogenase Acetyl-Coa Reductive Thioesterase." Biochemical Journal **302**: 163-170.

Burdette, D. S., F. Secundo, et al. (1997). "Biophysical and mutagenic analysis of Thermoanaerobacter ethanolicus secondary alcohol dehydrogenase activity and specificity." Biochemical Journal **326**: 717-724.

Burdette, D. S., V. Tchernajencko, et al. (2000). "Effect of thermal and chemical denaturants on Thermoanaerobacter ethanolicus secondary-alcohol dehydrogenase stability and activity." Enzyme and Microbial Technology **27**(1-2): 11-18.

Burdette, D. S., C. Vieille, et al. (1996). "Cloning and expression of the gene encoding the Thermoanaerobacter ethanolicus 39E secondary-alcohol dehydrogenase and biochemical characterization of the enzyme." Biochemical Journal **316**: 115-122.

Chen, S. H., R. Yuan, et al. (2006). "Amperometric hydrogen peroxide biosensor based on the immobilization of horseradish peroxidase (HRP) on the layer-by-layer assembly films of gold colloidal nanoparticles and toluidine blue." Electroanalysis **18**(5): 471-477.

Chen, T., S. C. Barton, et al. (2001). "A miniature biofuel cell." Journal of the American Chemical Society **123**(35): 8630-8631.

Clark, S. L., M. F. Montague, et al. (1997). "Ionic effects of sodium chloride on the templated deposition of polyelectrolytes using layer-by-layer ionic assembly." Macromolecules **30**(23): 7237-7244.

Coche-Guerente, L., J. Desbrieres, et al. (2005). "Physicochemical characterization of the layer-by-layer self-assembly of polyphenol oxidase and chitosan on glassy carbon electrode." Electrochimica Acta **50**(14): 2865-2877.

Curran, J. M., R. Chen, et al. (2005). "Controlling the phenotype and function of mesenchymal stem cells in vitro by adhesion to silane-modified clean glass surfaces." Biomaterials **26**(34): 7057-7067.

De Temino, D. M., W. Hartmeier, et al. (2005). "Entrapment of the alcohol dehydrogenase from Lactobacillus kefir in polyvinyl alcohol for the synthesis of chiral hydrophobic alcohols in organic solvents." Enzyme and Microbial Technology **36**(1): 3-9.

Decher, G. and J. D. Hong (1991). "Buildup of Ultrathin Multilayer Films by a Self-Assembly Process .1. Consecutive Adsorption of Anionic and Cationic Bipolar Amphiphiles on Charged Surfaces." Makromolekulare Chemie-Macromolecular Symposia **46**: 321-327.

Decher, G. and J. D. Hong (1991). "Buildup of Ultrathin Multilayer Films by a Self-Assembly Process .2. Consecutive Adsorption of Anionic and Cationic Bipolar Amphiphiles and Polyelectrolytes on Charged Surfaces." Berichte Der Bunsen-Gesellschaft-Physical Chemistry Chemical Physics **95**(11): 1430-1434.

Decher, G., J. D. Hong, et al. (1992). "Buildup of Ultrathin Multilayer Films by a Self-Assembly Process .3. Consecutively Alternating Adsorption of Anionic and Cationic Polyelectrolytes on Charged Surfaces." Thin Solid Films **210**(1-2): 831-835.

Degani, Y. and A. Heller (1987). "Direct Electrical Communication between Chemically Modified Enzymes and Metal-Electrodes .1. Electron-Transfer from Glucose-Oxidase to Metal-Electrodes Via Electron Relays, Bound Covalently to the Enzyme." Journal of Physical Chemistry **91**(6): 1285-1289.

Diez-Perez, I., A. G. Guell, et al. (2006). "Conductance maps by electrochemical tunneling spectroscopy to fingerprint the electrode electronic structure." Analytical Chemistry **78**(20): 7325-7329.

Du, X. S., M. Xiao, et al. (2004). "Synthesis and characterization of polyaniline/graphite conducting nanocomposites." Journal of Polymer Science Part B-Polymer Physics **42**(10): 1972-1978.

Eisenwiener, H. G. and G. V. Schulz (1969). "Activity Mechanism of Glucose Oxidases from Aspergillus Niger and Penicillium Notatum." Naturwissenschaften **56**(11): 563-&.

Emr, S. A. and A. M. Yacynych (1995). Electroanalysis **7**: 913-923.

Emr, S. A. and A. M. Yacynych (1995). "Use of Polymer-Films in Amperometric Biosensors." Electroanalysis **7**(10): 913-923.

Forzani, E. S., M. L. Teijelo, et al. (2003). "Effect of the polycation nature on the structure of layer-by-layer electrostatically self-assembled multilayers of polyphenol oxidase." Biomacromolecules **4**(4): 869-879.

Friedrich, J. M., C. Ponce-De-Leon, et al. (2004). "Reticulated vitreous carbon as an electrode material." Journal of Electroanalytical Chemistry **561**(1-2): 203-217.

Gabrielli, C., O. Haas, et al. (1987). "Impedance Analysis of Electrodes Modified with a Reversible Redox Polymer Film." Journal of Applied Electrochemistry **17**(1): 82-90.

Guldi, D. M., I. Zilbermann, et al. (2004). "Langmuir-Blodgett and layer-by-layer films of photoactive fullerene-porphyrin dyads." Journal of Materials Chemistry **14**(3): 303-309.

Habermuller, L., M. Mosbach, et al. (2000). "Electron-transfer mechanisms in amperometric biosensors." Fresenius Journal of Analytical Chemistry **366**(6-7): 560-568.

Halbhuber, Z., Z. Petrmichlova, et al. (2003). "Overexpression and purification of recombinant membrane PsbH protein in Escherichia coli." Protein Expression and Purification **32**(1): 18-27.

Hammond, P. T. (2004). "Form and function in multilayer assembly: New applications at the nanoscale." Advanced Materials **16**(15): 1271-1293.

Hassler, B. L., M. Dennis, et al. (2007). "Mutation of Tyr-218 to Phe in Thermoanaerobacter ethanolicus secondary alcohol dehydrogenase: Effects on bioelectronic interface performance." Applied Biochemistry and Biotechnology **143**(1): 1-15.

Hassler, B. L., N. Kohli, et al. (2007). "Renewable dehydrogenase-based interfaces for bioelectronic applications." Langmuir **23**(13): 7127-7133.

Hassler, B. L. and R. M. Worden (2006). "Versatile bioelectronic interfaces based on heterotrifunctional linking molecules." Biosensors & Bioelectronics **21**(11): 2146-2154.

Heiss, C., M. Laivenieks, et al. (2001). "Mutation of cysteine-295 to alanine in secondary alcohol dehydrogenase from Thermoanaerobacter ethanolicus affects the enantioselectivity and substrate specificity of ketone reductions." Bioorganic & Medicinal Chemistry **9**(7): 1659-1666.

Heller, A. (1990). Acc. Chem. Res. **23**: 128-134.

Heller, A. (1990). "Electrical Wiring of Redox Enzymes." Accounts of Chemical Research **23**(5): 128-134.

Hendricks, T. R., J. Lu, et al. (2008). "Intact pattern transfer of conductive exfoliated graphite nanoplatelet composite films to polyelectrolyte multilayer platforms." Advanced Materials **20**(10): 2008-+.

Huang, G., B. Wang, et al. (2006). "Material characterization and modeling of single-wall carbon nanotube/polyelectrolyte multilayer nanocomposites." Journal of Applied Mechanics-Transactions of the Asme **73**(5): 737-744.

Huang, X. J., A. G. Yu, et al. (2009). "Surface modification of nanofibrous poly(acrylonitrile-co-acrylic acid) membrane with biomacromolecules for lipase immobilization." Journal of Molecular Catalysis B-Enzymatic **57**(1-4): 250-256.

Ihs, A. and B. Liedberg (1991). "Chemisorption of L-Cysteine and 3-Mercaptopropionic Acid on Gold and Copper Surfaces - an Infrared Reflection Absorption Study." Journal of Colloid and Interface Science **144**(1): 282-292.

Jornvall, H., H. Eklund, et al. (1978). "Subunit Conformation of Yeast Alcohol-Dehydrogenase." Journal of Biological Chemistry **253**(23): 8414-8419.

Ju, H. X., Y. Xiao, et al. (2002). "Electrooxidative coupling of a toluidine blue O terminated self-assembled monolayer studied by electrochemistry and surface enhanced Raman spectroscopy." Journal of Electroanalytical Chemistry **518**(2): 123-130.

Katz, E., V. Heleg-Shabtai, et al. (1998). "Surface reconstitution of a de novo synthesized hemoprotein for bioelectronic applications." Angewandte Chemie-International Edition **37**(23): 3253-3256.

Katz, E. and I. Willner (1997). "Kinetic separation of amperometric responses of composite redox-active monolayers assembled onto Au electrodes: Implications to the monolayers' structure and composition." Langmuir **13**(13): 3364-3373.

Keinan, E., E. K. Hafeli, et al. (1986). "Thermostable Enzymes in Organic-Synthesis .2. Asymmetric Reduction of Ketones with Alcohol-Dehydrogenase from Thermoanaerobium-Brockii." Journal of the American Chemical Society **108**(1): 162-169.

Keinan, E., K. K. Seth, et al. (1987). "Synthetic Applications of Alcohol-Dehydrogenase from Thermoanaerobium-Brockii." Annals of the New York Academy of Sciences **501**: 130-149.

Kidambi, S., C. Chan, et al. (2004). "Selective depositions on polyelectrolyte multilayers: Self-assembled monolayers of m-dPEG acid as molecular template." Journal of the American Chemical Society **126**(14): 4697-4703.

Kidambi, S., I. Lee, et al. (2004). "Controlling primary hepatocyte adhesion and spreading on protein-free polyelectrolyte multilayer films." Journal of the American Chemical Society **126**(50): 16286-16287.

Kleifeld, O., A. Frenkel, et al. (2000). "Spectroscopic studies of inhibited alcohol dehydrogenase from Thermoanaerobacter brockii: Proposed structure for the catalytic intermediate state." Biochemistry **39**(26): 7702-7711.

Korkhin, Y., A. J. Kalb, et al. (1998). "NADP-dependent bacterial alcohol dehydrogenases: Crystal structure, cofactor-binding and cofactor specificity of the ADHs of Clostridium beijerinckii and Thermoanaerobacter brockii." Journal of Molecular Biology **278**(5): 967-981.

Kosjek, B., W. Stampfer, et al. (2004). "Purification and characterization of a chemotolerant alcohol dehydrogenase applicable to coupled redox reactions." Biotechnology and Bioengineering **86**(1): 55-62.

Kraft, A., H. Hennig, et al. (1994). "Changes in Electrochemical and Photoelectrochemical Properties of Tin-Doped Indium Oxide Layers after Strong Anodic Polarization." Journal of Electroanalytical Chemistry **365**(1-2): 191-196.

Kricka, L. J. (2001). "Microchips, microarrays, biochips and nanochips: personal laboratories for the 21st century." Clinica Chimica Acta **307**(1-2): 219-223.

Kurita, R., H. Tabei, et al. (2000). "Fabrication and electrochemical properties of an interdigitated array electrode in a microfabricated wall-jet cell." Sensors and Actuators B-Chemical **71**(1-2): 82-89.

Lang, G. and G. Inzelt (1991). "Some Problems Connected with Impedance Analysis of Polymer Film Electrodes - Effect of the Film Thickness and the Thickness Distribution." Electrochimica Acta **36**(5-6): 847-854.

Li, C. Y., J. Y. Han, et al. (2007). "Flexible biosensors on spirally rolled micro tube for cardiovascular in vivo monitoring." Biosensors & Bioelectronics **22**(9-10): 1988-1993.

Lindholm, B., M. Sharp, et al. (1987). "Ac-Impedance Studies of Carbon Electrodes Coated with Poly-4-Vinylpyridine Films Containing the Fe(Cn)6(3-/4-) Redox Couple." Journal of Electroanalytical Chemistry **235**(1-2): 169-177.

Liu, J. Y., Y. D. Jin, et al. (2004). "Fabrication and characterization of DNA/QPVP-Os redox-active multilayer film." Electroanalysis **16**(23): 1931-1937.

Liu, L. J., X. Jin, et al. (2007). "A highly sensitive biosensor with (Con A/HRP)(n) multilayer films based on layer-by-layer technique for the detection of reduced thiols." Biosensors & Bioelectronics **22**(12): 3210-3216.

Liu, S. N. and C. X. Cai (2007). "Immobilization and characterization of alcohol dehydrogenase on single-walled carbon nanotubes and its application in sensing ethanol." Journal of Electroanalytical Chemistry **602**(1): 103-114.

Lu, C. Q., Z. Y. Jiang, et al. (2004). "Progress in regeneration of NAD(P)(+) and NAD(P)H." Chinese Journal of Organic Chemistry **24**(11): 1366-1379.

Luo, X. L., A. J. Killard, et al. (2006). "Reagentless glucose biosensor based on the direct electrochemistry of glucose oxidase on carbon nanotube-modified electrodes." Electroanalysis **18**(11): 1131-1134.

Lvov, Y. and F. Caruso (2001). "Biocolloids with ordered urease multilayer shells as enzymatic reactors." Analytical Chemistry **73**(17): 4212-4217.

Ma, Y., Q. Gao, et al. (2005). "Immobilization of glycosylated enzymes on carbon electrodes, and its application in biosensors." Microchimica Acta **150**(1): 21-26.

Malinauskas, A., T. Ruzgas, et al. (2000). "Electrochemical study of the redox dyes Nile Blue and Toluidine Blue adsorbed on graphite and zirconium phosphate modified graphite." Journal of Electroanalytical Chemistry **484**(1): 55-63.

Malinauskas, A., T. Ruzgas, et al. (2001). "Electrochemical study of glassy carbon electrodes modified with zirconium phosphate and some azine-type redox dyes." Journal of Solid State Electrochemistry **5**(4): 287-292.

Masadome, T. and T. Imato (2003). "Use of marker ion and cationic surfactant plastic membrane electrode for potentiometric titration of cationic polyelectrolytes." Talanta **60**(4): 663-668.

Masuda, S., K. Hasegawa, et al. (2004). "Light-induced structural changes in a putative blue-light receptor with a novel FAD binding fold sensor of blue-light using FAD (BLUF); Slr1694 of Synechocystis sp PCC6803." Biochemistry **43**(18): 5304-5313.

Mathias, M. F. and O. Haas (1992). "An Alternating-Current Impedance Model Including Migration and Redox-Site Interactions at Polymer-Modified Electrodes." Journal of Physical Chemistry **96**(7): 3174-3182.

Meersman, F., J. Wang, et al. (2005). "Pressure effect on the hydration properties of poly(N-isopropylacrylamide) in aqueous solution studied by FTIR spectroscopy." Macromolecules **38**(21): 8923-8928.

Molina, C. R., M. Boujtita, et al. (1999). "A carbon paste electrode modified by entrapped toluidine blue-O for amperometric determination of L-lactate." Analytica Chimica Acta **401**(1-2): 155-162.

Mulcahy, P., M. O'Flaherty, et al. (1999). "Effect of accessible immobilized NAD(+) concentration on the bioaffinity chromatographic behavior of NAD(+)- dependent dehydrogenases using the kinetic locking-on strategy." Protein Expression and Purification **16**(2): 261-275.

Oakey, L. and P. Mulcahy (2004). "Immobilized cofactor derivatives for kinetic-based enzyme capture strategies: direct coupling of NAD(P)(+)." Analytical Biochemistry **335**(2): 316-325.

Oka, A., H. Sugisaki, et al. (1981). "Nucleotide-Sequence of the Kanamycin Resistance Transposon Tn903." Journal of Molecular Biology **147**(2): 217-226.

Ozdemir, A. and A. Tuncel (2000). "Boronic acid-functionalized HEMA-based gels for nucleotide adsorption." Journal of Applied Polymer Science **78**(2): 268-277.

Park, D. H., M. Laivenieks, et al. (1999). "Microbial utilization of electrically reduced neutral red as the sole electron donor for growth and metabolite production." Applied and Environmental Microbiology **65**(7): 2912-2917.

Park, D. H., C. Vieille, et al. (2003). "Bioelectrocatalysts - Engineered oxidoreductase system for utilization of fumarate reductase in chemical synthesis, detection, and fuel cells." Applied Biochemistry and Biotechnology **111**(1): 41-53.

Park, D. H. and J. G. Zeikus (1999). "Utilization of electrically reduced neutral red by Actinobacillus succinogenes: Physiological function of neutral red in membrane-driven fumarate reduction and energy conservation." Journal of Bacteriology **181**(8): 2403-2410.

Park, D. H. and J. G. Zeikus (2000). "Electricity generation in microbial fuel cells using neutral red as an electronophore." Applied and Environmental Microbiology **66**(4): 1292-1297.

Park, D. H. and J. G. Zeikus (2003). "Improved fuel cell and electrode designs for producing electricity from microbial degradation." Biotechnology and Bioengineering **81**(3): 348-355.

Pasco, N., C. Jeffries, et al. (1999). "Characterisation of a thermophilic L-glutamate dehydrogenase biosensor for amperometric determination of L-glutamate by flow injection analysis." Biosensors & Bioelectronics **14**(2): 171-178.

Peretz, M., O. Bogin, et al. (1997). "Molecular cloning, nucleotide sequencing, and expression of genes encoding alcohol dehydrogenases from the thermophile Thermoanaerobacter brockii and the mesophile Clostridium beijerinckii." Anaerobe **3**(4): 259-270.

Pham, V. T. and R. S. Phillips (1990). "Effects of Substrate Structure and Temperature on the Stereospecificity of Secondary Alcohol-Dehydrogenase from Thermoanaerobacter-Ethanolicus." Journal of the American Chemical Society **112**(9): 3629-3632.

Pham, V. T., R. S. Phillips, et al. (1989). "Temperature-Dependent Enantiospecificity of Secondary Alcohol-Dehydrogenase from Thermoanaerobacter-Ethanolicus." Journal of the American Chemical Society **111**(5): 1935-1936.

Pogorelova, S. P., M. Zayats, et al. (2003). "Analysis of HAD(P)(+)/NAD(P)H cofactors by imprinted polymer membranes associated with ion-sensitive field-effect transistor devices and Au-quartz crystals." Analytical Chemistry **75**(3): 509-517.

Prodromidis, M. I. and M. I. Karayannis (2002). "Enzyme based amperometric Biosensors for food analysis." Electroanalysis **14**(4): 241-261.

Qi, Z. M., I. Honma, et al. (2006). "Layer-by-layer fabrication and characterization of gold-nanoparticle/myoglobin nanocomposite films." Advanced Functional Materials **16**(3): 377-386.

Qian, J. M., A. L. Suo, et al. (2004). "Polyelectrolyte-stabilized glucose biosensor based on woodceramics as electrode." Clinical Biochemistry **37**(2): 155-161.

Quan, D., Y. Kim, et al. (2004). "Characterization of an amperometric laccase electrode covalently immobilized on platinum surface." Journal of Electroanalytical Chemistry **561**(1-2): 181-189.

Rahamathunissa, G. and L. Rajendran (2008). "Modeling of nonlinear reaction-diffusion processes of amperometric polymer-modified electrodes." Journal of Theoretical & Computational Chemistry **7**: 113-138.

Raitman, O. A., F. Patolsky, et al. (2002). "Electrical contacting of glucose dehydrogenase by the reconstitution of a pyrroloquinoline quinone-functionalized

polyaniline film associated with an Au-electrode: an in situ electrochemical SPR study." Chemical Communications(17): 1936-1937.

Ramesh, P., P. Sivakumar, et al. (2003). "Phenoxazine functionalized, exfoliated graphite based electrodes for NADH oxidation and ethanol biosensing." Electroanalysis **15**(23-24): 1850-1858.

Riklin, A., E. Katz, et al. (1995). "Improving Enzyme-Electrode Contacts by Redox Modification of Cofactors." Nature **376**(6542): 672-675.

Sambrook, J. and D. W. Russell. (1989). Molecular Cloning: A Laboratory Manual. New York, NY, Cold Spring Harbor Laboratory Press.

Schmakel, C. O., K. S. V. Santhanam, et al. (1975). "Nicotinamide Adenine-Dinucleotide (Nad+) and Related Compounds - Electrochemical Redox Pattern and Allied Chemical Behavior." Journal of the American Chemical Society **97**(18): 5083-5092.

Schuhmann, W., T. J. Ohara, et al. (1991). "Electron-Transfer between Glucose-Oxidase and Electrodes Via Redox Mediators Bound with Flexible Chains to the Enzyme Surface." Journal of the American Chemical Society **113**(4): 1394-1397.

Scott, D. L. and E. F. Bowden (1994). "Enzyme-Substrate Kinetics of Adsorbed Cytochrome-C Peroxidase on Pyrolytic-Graphite Electrodes." Analytical Chemistry **66**(8): 1217-1223.

Segel, I. (1993). Enzyme Kinetics: Behavior and Analysis of Rapid Equilibrium and Steady-State Enzyme Systems. New York, New York, John Wiley and Sons.

Senel, S., S. T. Camli, et al. (2002). "Nucleotide adsorption-desorption behaviour of boronic acid functionalized uniform-porous particles." Journal of Chromatography B-Analytical Technologies in the Biomedical and Life Sciences **769**(2): 283-295.

Serban, S. and N. El Murr (2004). "Synergetic effect for NADH oxidation of ferrocene and zeolite in modified carbon paste electrodes - New approach for dehydrogenase based biosensors." Biosensors & Bioelectronics **20**(2): 161-166.

Shi, L. X., Y. X. Lu, et al. (2003). "Site-selective lateral multilayer assembly of bienzyme with polyelectrolyte on ITO electrode based on electric field-induced directly layer-by-layer deposition." Biomacromolecules **4**(5): 1161-1167.

Shutava, T. G., D. S. Kommireddy, et al. (2006). "Layer-by-layer enzyme/polyelectrolyte films as a functional protective barrier in oxidizing media." Journal of the American Chemical Society **128**(30): 9926-9934.

Song, S. H., N. Ahluwalia, et al. (2008). "Thermotoga maritima TM0298 is a highly thermostable mannitol dehydrogenase." Applied Microbiology and Biotechnology **81**(3): 485-495.

Strohl, A. N. and D. J. Curran (1979). "Controlled Potential Coulometry with the Flow-through Reticulated Vitreous Carbon Electrode." Analytical Chemistry **51**(7): 1050-1053.

Strohl, A. N. and D. J. Curran (1979). "Flow Injection Analysis with Reticulated Vitreous Carbon Flow-through Electrodes." Analytical Chemistry **51**(7): 1045-1049.

Supriya, L. and R. O. Claus (2004). "Solution-based assembly of conductive gold film on flexible polymer substrates." Langmuir **20**(20): 8870-8876.

Tagliazucchi, M. E. and E. J. Calvo (2007). "Surface charge effects on the redox switching of LbL self-assembled redox polyelectrolyte multilayers." Journal of Electroanalytical Chemistry **599**(2): 249-259.

Tisone, T. C. and J. Drobek (1972). "Diffusion in Thin-Film Ti-Au, Ti-Pd, and Ti-Pt Couples." Journal of Vacuum Science & Technology **9**(1): 271-&.

Tripp, A. E., D. S. Burdette, et al. (1998). "Mutation of Serine-39 to threonine in thermostable secondary alcohol dehydrogenase from Thermoanaerobacter ethanolicus changes enantiospecificity." Journal of the American Chemical Society **120**(21): 5137-5141.

Tsujimura, S., M. Fujita, et al. (2001). "Bioelectrocatalysis-based dihydrogen/dioxygen fuel cell operating at physiological pH." Physical Chemistry Chemical Physics **3**(7): 1331-1335.

Ulman, A. (1996). "Formation and structure of self-assembled monolayers." Chemical Reviews **96**(4): 1533-1554.

Uvdal, K. and T. P. Vikinge (2001). "Chemisorption of the dipeptide Arg-Cys on a gold surface and the selectivity of G-protein adsorption." Langmuir **17**(6): 2008-2012.

Wang, C. H., C. Y. Li, et al. (2006). "Covalent modification of glassy carbon electrode with L-cysteine for the determination of acetaminophen." Microchimica Acta **155**(3-4): 365-371.

Wang, S. Y., Y. Feng, et al. (2003). "Heat effect on the structure and activity of the recombinant glutamate dehydrogenase from a hyperthermophilic archaeon Pyrococcus horikoshii." Archives of Biochemistry and Biophysics **411**(1): 56-62.

Wang, Y. J. and F. Caruso (2005). "Mesoporous silica spheres as supports for enzyme immobilization and encapsulation." Chemistry of Materials **17**(5): 953-961.

Willner, B., E. Katz, et al. (2006). "Electrical contacting of redox proteins by nanotechnological means." Current Opinion in Biotechnology **17**(6): 589-596.

Woodward, J. (1985). Immobilized Cells and Enzymes a Practical Approach. Eynsham, Oxford, England, IRL Press Limited.

Wu, Z. Y., L. R. Guan, et al. (2002). "Renewable urea sensor based on a self-assembled polyelectrolyte layer." Analyst **127**(3): 391-395.

Yun, D. H., M. J. Song, et al. (2005). "Highly sensitive and renewable amperometric urea sensor based on self-assembled monolayer using porous silicon substrate." Journal of the Korean Physical Society **47**: S445-S449.

Zayats, M., E. Katz, et al. (2002). "Electrical contacting of flavoenzymes and NAD(P)(+)-dependent enzymes by reconstitution and affinity interactions on phenylboronic acid monolayers associated with Au-electrodes." Journal of the American Chemical Society **124**(49): 14724-14735.

Zhang, L. (2008). "Covalent modification of glassy carbon electrode with cysteine for the determination of dopamine in the presence of ascorbic acid." Microchimica Acta **161**(1-2): 191-200.

Zhang, L. and X. Q. Lin (2001). "Covalent modification of glassy carbon electrodes with glycine for voltammetric separation of dopamine and ascorbic acid." Fresenius Journal of Analytical Chemistry **370**(7): 956-962.

Zhang, L. and Y. G. Sun (2001). "Covalent modification of glassy carbon electrodes with beta-alanine for voltammetric separation of dopamine and ascorbic acid." Analytical Sciences **17**(8): 939-943.

Zhao, H. T. and H. X. Ju (2006). "Multilayer membranes for glucose biosensing via layer-by-layer assembly of multiwall carbon nanotubes and glucose oxidase." Analytical Biochemistry **350**(1): 138-144.

Zhao, W., J. J. Xu, et al. (2005). "Multilayer membranes via layer-by-layer deposition of organic polymer protected Prussian blue nanoparticles and glucose oxidase for glucose biosensing." Langmuir **21**(21): 9630-9634.

Zimmermann, H., A. Lindgren, et al. (2000). "Anisotropic orientation of horseradish peroxidase by reconstitution on a thiol-modified gold electrode." Chemistry-a European Journal **6**(4): 592-599.